Western&Graduate&PostdoctoralStudies

7-12-2022 10:30 AM

Compound flooding analysis over the Canadian coastal regions

Farshad Jalili Pirani, *The University of Western Ontario*

Supervisor: Mohammad Reza Najafi, *The University of Western Ontario*
A thesis submitted in partial fulfillment of the requirements for the Doctor of Philosophy degree
in Civil and Environmental Engineering
© Farshad Jalili Pirani 2022

Follow this and additional works at: https://ir.lib.uwo.ca/etd

Part of the Environmental Engineering Commons

Recommended Citation

Abstract

The communities settling in the Canadian coastal regions are threatened by multiple flood-generating mechanisms including riverine, pluvial, and sea level forces. Reliable design flood estimation and risk assessment in these regions demand characterization of the interrelationships between different drivers as well as the corresponding compounding effects. In this study, as our first step, we assess the compound flood risks across Canada's coasts considering eight bivariate flooding scenarios acquired from four flooding drivers including total water level (TWL), streamflow (Q), precipitation (Pr) and the skew surge (S) at 41 sites located at the three main regions of the Pacific, the Great Lakes (GL) and the Atlantic. For each scenario, an initial dependence test based on Kendall's Tau is conducted. Their joint probability is constructed using copulas. Further, compound flood risks and the failure probabilities are analyzed considering the OR, AND, Kendall, conditional hazard scenarios and the Compound Hazard Ratio (CHR) index. Results suggest that most locations can be affected by compound flooding associated with at least two types of bivariate events.

In the second step, we characterize the dependence structure between the three drivers of total water level, streamflow and precipitation based on the C-vine copula statistical approach and create their multivariate joint distribution for different locations. This is followed by calculating the OR, AND, and Kendall compound flooding joint return periods (JRPs) and their corresponding failure probabilities (FPs) and comparing them with the univariate and independent JRP values. Further, the CHR index is applied to quantify possible under- or overestimations of the flooding risks when individual drivers are assessed, independently. The results show that multivariate JRPs are less than those of univariate and independent multivariate hazard estimates.

In our third objective, we try to explore the univariate and multivariate trends of four flooding drivers at all sites. The univariate Mann-Kendall trend test and its extension to the multivariate case namely the Covariance Inversion Test (CIT), Covariance Sum Test (CST), and Covariance Eigenvalue Tests (CET) are applied to see the univariate (change in the intensity and frequency) and joint nonstationary behavior of the three drivers, respectively. The results show increased risks of individual and compound flooding over the Atlantic coast, and various trends in the Pacific and the GL regions.

Finally, we assess the compound flooding hazard under a nonstationary framework for all the locations. To this end, the time-varying behavior of the three drivers of step 2 and also the interdependencies between them are captured using linear and polynomial models. This process leads to producing a time-dependent joint occurrence/probability of the drivers. Then, the temporal variations of the compound flood hazard are assessed concerning the OR, and AND hazard scenarios and the CHR index. The results show the decline and increase in the AND JRPs and CHR values over time at 23 locations, especially in the Atlantic region. This study highlights that reliable flooding hazard analysis over the Canadian coastal regions is obtained considering all the flooding drivers and the corresponding interconnections. The Atlantic region is most susceptible considering the potential role of extra-tropical cyclones. The obtained results can support the operating agencies/decision makers to update the design levels/resilience strategies with respect to the multivariate hazard estimates. Besides, the time-varying analysis can lead to more sustainable and long-lasting protective infrastructures.

Keywords

Summary for Lay Audience

Approximately half of the global population lives within 200km of coastlines. The communities and infrastructure systems in the coastal environments are at risk of flooding caused by one or multiple mechanisms. Understanding the compounding effects of the drivers of flooding and quantifying the corresponding uncertainties are critical for flood risk analysis and the development of effective resilience strategies. To address this objective, we investigate compound flood events considering terrestrial (both precipitation, and streamflow which reflects the effects of snow/ice melt in addition to rainfall) and coastal mechanisms across Canada's Atlantic, Pacific and Great Lakes' coasts, with distinct hydroclimatic characteristics, based on a state-of-the-art statistical approach. The proposed design flood estimation method addresses the limitations in traditional approaches that neglect the interdependencies between two or multiple drivers of flooding. Further, the proposed approach identifies areas that are at high risk of compound flooding and identifies the main contributing factors. We also investigate whether the frequency and intensity of the co-occurrence of these flooding sources have altered from 1960 to 2015 or not. The results suggest that the risk of flooding can increase up to 50% if flood mechanisms are analyzed holistically and the interrelationships are accounted for, compared to estimates from the traditional approach. Precipitation and sea levels are the major factors that contribute to compound flooding, in particular on the Atlantic coast. The obtained findings of this research help coastal managers with designing more sustainable and long-lasting coastal protective infrastructures, strategies, policies and regulations concerning all three flooding sources, and the interconnection between them. Moreover, the flood mitigation and resilience strategies, regulations and management policies can also be updated concerning new flood hazard estimates.

Co-Authorship Statement

This thesis has been prepared according to the regulations set by the School of Graduate and Postdoctoral Studies (SGPS) at Western University for an Integrated Article format thesis. The co-authorship statements of the thesis chapters are as follows:

Chapter 2 is a journal article submitted and currently under review in the journal of Hydrology under the co-authorship of Farshad Jalili Pirani, and Mohammad Reza Najafi.

Chapter 3 is a journal article published in the journal of Earth's future. It is co-authored by Farshad Jalili Pirani and Mohammad Reza Najafi.

Chapter 4 is a journal article published in the Journal of Water Resources Research. It is co-authored by Farshad Jalili Pirani and Mohammad Reza Najafi.

Chapter 5 is a journal article and will be submitted for publication in the Journal of Water Resources Research under the co-authorship of Farshad Jalili Pirani, and Mohammad Reza Najafi.

Farshad Jalili Pirani executed all the analysis including data processing, risk calculations, presenting the result, and writing the manuscript. Mohammad Reza Najafi supervised the whole research and revised the manuscript.

Acknowledgments

Table of Contents

List of Tables

List of Figures

List of Appendices

Appendix B: List of supplementary Figures

Nomenclature

AHCCD	Adjusted and Homogenized Canadian Climate Data
AIC	Akaike Information Criterion
BBS	Block Bootstrap Sampling
BC	British Columbia
CDF	Cumulative Probability Distribution
CET	Covariance Eigenvalue Test
CF	Compound Flooding
CHR	Compound Hazard Ratio
CIT	Covariance Inversion Test
C-vine	Canonical Vine
CST	Covariance Sum Test
D-vine	Drawable Vines
ENSO	El Ni~no-Southern Oscillation
FP	Failure Probability
GEV	Generalized Extreme Value
GL	Great Lakes
GPD	Generalized Pareto Distribution
ICLR	Catastrophic Loss Reduction

IPCC	Intergovernmental Panel on Climate Change
JRP	Joint Return Period
KS	Kolmogorov-Smirnov
MCMC	Markov Chain Monte Carlo
MK	Mann Kendall
mpr	marginal precipitation
mq	marginal streamflow
mtwl	marginal total water level
NSERC	Natural Sciences and Engineering Research Council
PDF	Probability Density Function
POT	Peak Over Threshold
Pr	Precipitation
PS	Probability Summation
Q	Streamflow
RP	Return Period
S	Skew Surge
TWL	Total Water Level
WL	Water Level
WAIC	Widely Applicable Information Criterion

Chapter 1

1.   Introduction and background

1.1. General introduction

The communities settling on low-lying coastal areas are threatened by compound flooding. According to Intergovernmental Panel on Climate Change (IPCC), compound flooding is the simultaneous or successive occurrence of multiple drivers of riverine, rainfall, and sea level (IPCC, 2012) which has an extreme impact and leads to more significant socioeconomic damages than the occurrence of each driver in isolation. Such events happen when a low-pressure system like a tropical cyclone or a hurricane passing over the coast generates storm surges and high waves and at the same time is along with heavy rainfall and possible river overflows (Couasnon et al., 2019; Paprotny et al., 2018; Svensson and Jones, 2002). One example is hurricane Katrina (2005) which caused $125 billion damage on south Florida. The number of people living in coastal areas is anticipated to reach 949 million by the 2030s and 1.4 billion by the 2060s (Neumann et al., 2015), indicating larger exposure to different types of flood hazards in these regions in the future. Therefore, it is critical to understand and predict the mechanisms that drive flooding, including intense rainfall, high seawater levels, and river overflows, as well as their interactions, and interrelationships to develop effective flood mitigation and adaptation strategies.

Conventional approaches to studying such joint events are based on the assumption that the drivers of flooding are independent of one another. However, recent studies show strong evidence for the interactions between drivers of floods, especially in coastal areas around the world (Eilander et al., 2020; Hendry et al., 2019; Moftakhari et al., 2017; Nasr et al., 2021; Robins et al., 2021; Wahl et al., 2015; Ward et al., 2018). Thus, there has been a growing interest in the study of compound flood events in recent years at global (Eilander et al., 2020; Ward et al., 2018), continental (Ganguli and Merz, 2019; Paprotny et al., 2020), national (Ghanbari et al., 2021; Jalili Pirani and Najafi, 2020) and regional scales (Valle-Levinson et al., 2020; van Berchum et al., 2020) using statistical and process-based

approaches (Hao et al., 2018). These analyses include characterizing the statistical interrelationships between drivers of flooding based on Bayesian networks (Couasnon et al., 2018; Sebastian et al., 2017), copula theory (Bevacqua et al., 2017; Gori et al., 2020; Moftakhari et al., 2017; Paprotny et al., 2018; Xu et al., 2014), bivariate extreme value distributions (Zheng et al., 2014), correlation and linear regression (Robins et al., 2021), bivariate logistic threshold-excess model (Zheng et al., 2013) among others. Most of these analyses are limited to two drivers and limited scenarios (Paprotny et al., 2018; Ward et al., 2018). For example, Ward et al. 2018 and Whal et al. (2015) assessed the interrelationship between high river discharge and sea level and storm surges and precipitation using copulas, respectively. Bevacqua et al. (2019) and Moftakhari et al. (2017) applied copulas to study changes in the bivariate behavior (dependence) of storm surge/precipitation and fluvial flooding/sea level using historical and projected data, respectively. Only a few studies have investigated the effects of multiple (more than two) flood drivers including Liu et al. (2018) who investigated the joint effect of precipitation and surface runoff with the El Ni~no-Southern Oscillation (ENSO) and rising temperatures as underlying conditions in Texas, USA. Jane et al. (2020) applied Vine-Copulas to characterize the dependency between three variables of rainfall, Ocean-side WL, and groundwater level for coastal areas of Miami-Dade County (southeast Florida).

These studies concluded that analyzing flooding hazards over the coastal regions concerning individual flooding drivers can lead to an underestimation of the associated risks. Besides, the associated time-varying risks are under researched.

1.2. Motivation and objectives

Canada has the longest coastal line in the world which has settled over 7 million people in itself. Extratropical cyclones have already caused problems for these coastal areas, especially in the Pacific and Atlantic regions. Water levels vary due to melting glaciers and vertical land movement has worsened the situation. Yen Kuo et al. (2008) reported land uplifts in Lake Superior, Lake Huron, Lake Ontario, and the upper part of Lake Michigan

and Lake Erie and subsidence in the lower part of Lake Michigan and Lake Erie. Furthermore, the increasing water levels observed over the Atlantic coasts can be attributed to the thermal expansion and glacier melts due to climate change, and land subsidences (Karegar et al., 2016). Therefore, communities and infrastructure systems across Canada's coasts are at increased risk of flooding. Conventionally, the operating agencies and the decision makers analyze individual drivers of flooding in the Canadian coastal areaswithout considering the associated interdepenencies. Besides, studies on the probabilistic risks associated with compound flooding, the corresponding design floods, and the nonstationary behavior across Canada's coasts are lacking.

As the first of it its kind, this research was initiated with the aim to address the research gaps in the coastal flood risk assessments by developing a novel multivariate statistical framework to characterize and assess the flooding risk and estimate the corresponding design levels over the Canadian coastal regions. At first, unlike many previous studies focusing on only one type of bivariate event, we analyze the compound flooding with respect to a suite of bivariate combinations of the flooding drivers and will compare the results with univariate results. Secondly, we conduct the analysis considering all the existing dependencies (which can not be seen in bivariate cases) between the drivers in a trivariate scenario which is lacking in the literature. In the third step, we investigate whether either of the flooding scenarios and also their joint occurrence (bivariate and trivariate) have a time-varying behavior and we propose a new index namely the probability summation (PS) index to capture the joint trend of flooding drivers. And finally, according to the nonstationarity results of the flooding drives, we account for compound flooding risk and the design levels in a changing environment. To capture such nonstationarity in either the flooding drivers and their interdependencies, we developed different link functions. The results of this research would help the policymakers to update and develop more robust technical and non-technical flood mitigation and resilience measures such as upstream reservoirs, flood barriers, dykes (technical measures), and building regulations and guidelines, educating people to be prepared for these type of joint events, emergency preparedness to protect lives, and reduce damages (non-technical measures). Resilience is defined as the capacity of a system (here a coastal community) on

the earth to sustain feedbacks and interactions that enable the system to remain in its current state (Falkenmark et al., 2019).

1.3. Thesis layout

The present thesis is written in the "integrated-article" format as per Western University's thesis regulations. The thesis has six chapters out of which four are journal articles. Chapter 1 outlines a general introduction and background about compound flooding and the motivation behind the current study. Chapter 2 focuses on the flood risk analysis and its uncertainty from the perspective of different joints of four flooding drivers including skew surge, total water level, streamflow, and precipitation. This study helps with recognizing the locations which are at higher risk of flooding than other parts considering all the scenarios. Chapter 3 is a tri-variate analysis of the flood hazard and the associated uncertainty with respect to three flooding drivers of total water level, streamflow, and precipitation. Chapter 4 provides a comprehensive study of the time-varying behavior of compound flooding characteristics (intensity and frequency) over the Canadian coastal areas. Chapter 5 is an investigation of the flooding hazard in a tri-variate case under the nonstationary framework. Chapter 6 portrays the conclusions derived from the present study and the recommendations for future work.

References

Bevacqua E, Maraun D, Hobæk Haff I, Widmann M, Vrac M. Multivariate statistical modelling of compound events via pair-copula constructions: analysis of floods in Ravenna (Italy). *Hydrology and Earth System Sciences* 2017; 21: 2701-2723.

Bevacqua E, Maraun D, Vousdoukas MI, Voukouvalas E, Vrac M, Mentaschi L, et al. Higher probability of compound flooding from precipitation and storm surge in Europe under anthropogenic climate change. *Science advances* 2019; 5: eaaw5531.

Couasnon A, Eilander D, Muis S, Veldkamp TI, Haigh ID, Wahl T, et al. Measuring compound flood potential from river discharge and storm surge extremes at the global scale and its implications for flood hazard. 2019.

Couasnon A, Sebastian A, Morales-Nápoles O. A copula-based Bayesian network for modeling compound flood hazard from riverine and coastal interactions at the catchment scale: An application to the Houston Ship Channel, Texas. *Water* 2018; 10: 1190.

Eilander D, Couasnon A, Ikeuchi H, Muis S, Yamazaki D, Winsemius H, et al. The effect of surge on riverine flood hazard and impact in deltas globally. 2020.

Falkenmark, M., Wang-Erlandsson, L., Rockström, J., 2019. Understanding of water resilience in the Anthropocene. *Journal of Hydrology* X, 2: 100009.

Ganguli P, Merz B. Trends in Compound Flooding in Northwestern Europe During 1901–2014. *Geophysical Research Letters* 2019; 46: 10810-10820.

Ghanbari M, Arabi M, Kao SC, Obeysekera J, Sweet W. Climate Change and Changes in Compound Coastal-Riverine Flooding Hazard Along the US Coasts. *Earth's Future* 2021: e2021EF002055.

Gori A, Lin N, Xi D. Tropical cyclone compound flood hazard assessment: from investigating dependence to quantifying impacts. *Earth and Space Science Open Archive* ESSOAr 2020.

Hao Z, Singh V, Hao F. Compound extremes in hydroclimatology: a review. *Water* 2018; 10: 718.

Hendry A, Haigh I, Nicholls R, Winter H, Neal R, Wahl T, et al. Assessing the characteristics and drivers of compound flooding events around the UK coast. *Hydrology and Earth System Sciences* 2019; 23: 3117-3139.

Jalili Pirani F, Najafi M. Recent trends in individual and multivariate compound flood drivers in Canada's coasts. *Water Resources Research* 2020; 56: e2020WR027785.

Jane R, Cadavid L, Obeysekera J, Wahl T. Multivariate statistical modelling of the drivers of compound flood events in south Florida. *Natural Hazards and Earth System Sciences* 2020; 20: 2681-2699.

Karegar MA, Dixon TH, Engelhart SE. Subsidence along the Atlantic Coast of North America: Insights from GPS and late Holocene relative sea level data. *Geophysical Research Letters* 2016; 43: 3126-3133.

Lavell A, Oppenheimer M, Diop C, Hess J, Lempert R, Li J, et al. Managing the risks of extreme events and disasters to advance climate change adaptation. A Special Report of Working Groups I and II of the Intergovernmental Panel on Climate Change (IPCC) 2012: 25-64.

Liu Z, Cheng L, Hao Z, Li J, Thorstensen A, Gao H. A framework for exploring joint effects of conditional factors on compound floods. *Water Resources Research* 2018; 54: 2681-2696.

Moftakhari HR, Salvadori G, AghaKouchak A, Sanders BF, Matthew RA. Compounding effects of sea level rise and fluvial flooding. *Proceedings of the National Academy of Sciences* 2017; 114: 9785-9790.

Nasr AA, Wahl T, Rashid MM, Camus P, Haigh ID. Assessing the dependence structure between oceanographic, fluvial, and pluvial flooding drivers along the United States coastline. *Hydrology and Earth System Sciences Discussions* 2021: 1-31.

Neumann B, Vafeidis AT, Zimmermann J, Nicholls RJ. Future coastal population growth and exposure to sea-level rise and coastal flooding-a global assessment. *PloS one* 2015; 10: e0118571.

Paprotny D, Vousdoukas MI, Morales-Nápoles O, Jonkman SN, Feyen L. Compound flood potential in Europe. *Hydrol. Earth Syst. Sci. Discuss* 2018; 2018: 1-34.

Paprotny D, Vousdoukas MI, Morales-Nápoles O, Jonkman SN, Feyen L. Pan-European hydrodynamic models and their ability to identify compound floods. *Natural Hazards* 2020: 1-25.

Robins PE, Lewis MJ, Elnahrawi M, Lyddon C, Dickson N, Coulthard TJ. Compound flooding: Dependence at sub-daily scales between extreme storm surge and fluvial flow. *Frontiers in Built Environment* 2021: 116.

Santos VM, Casas-Prat M, Poschlod B, Ragno E, van den Hurk B, Hao Z, et al. Multivariate statistical modelling of extreme coastal water levels and the effect of climate variability: a case study in the Netherlands. *Hydrology and Earth System Sciences Discussions* 2020: 1-25.

Sebastian A, Dupuits E, Morales-Nápoles O. Applying a Bayesian network based on Gaussian copulas to model the hydraulic boundary conditions for hurricane flood risk analysis in a coastal watershed. *Coastal Engineering* 2017; 125: 42-50.

Seneviratne SI, Nicholls N, Easterling D, Goodess CM, Kanae S, Kossin J, et al. Changes in climate extremes and their impacts on the natural physical environment. Managing the risks of extreme events and disasters to advance climate change adaptation: *Special report of the Intergovernmental Panel on Climate Change*. Cambridge University Press, 2012, pp. 109-230.

Svensson C, Jones DA. Dependence between extreme sea surge, river flow and precipitation in eastern Britain. International Journal of Climatology: *A Journal of the Royal Meteorological Society* 2002; 22: 1149-1168.

Valle-Levinson A, Olabarrieta M, Heilman L. Compound flooding in Houston-Galveston Bay during Hurricane Harvey. *Science of The Total Environment* 2020; 747: 141272.

van Berchum EC, van Ledden M, Timmermans JS, Kwakkel JH, Jonkman SN. Rapid flood risk screening model for compound flood events in Beira, Mozambique. *Natural Hazards and Earth System Sciences* 2020; 20: 2633-2646.

Wahl T, Jain S, Bender J, Meyers SD, Luther ME. Increasing risk of compound flooding from storm surge and rainfall for major US cities. *Nature Climate Change* 2015; 5: 1093-1097.

Ward PJ, Couasnon A, Eilander D, Haigh ID, Hendry A, Muis S, et al. Dependence between high sea-level and high river discharge increases flood hazard in global deltas and estuaries. *Environmental Research Letters* 2018; 13: 084012.

White T, Wolf J, Anslow F, Werner A, Creative R. Indicators of climate change for British Columbia. 2016 update. British Columbia Ministry of Environment, Victoria, BC 2016.

Xu K, Ma C, Lian J, Bin L. Joint probability analysis of extreme precipitation and storm tide in a coastal city under changing environment. PLoS One 2014; 9: e109341.

Zheng F, Westra S, Leonard M, Sisson SA. Modeling dependence between extreme rainfall and storm surge to estimate coastal flooding risk. *Water Resources Research* 2014; 50: 2050-2071.

Zheng F, Westra S, Sisson SA. Quantifying the dependence between extreme rainfall and storm surge in the coastal zone. *Journal of hydrology* 2013; 505: 172-187.

Chapter 2

2. Characterizing compound flooding potential and the corresponding driving mechanisms across coastal environments

2.1. Introduction

Communities settling in the low-lying coastal zones are threatened by flood risks associated with high tides, surges, waves, river overflows, extreme precipitation, and mean sea level rise, among others (Kew et al., 2013; Lian et al., 2013). With an increasing trend over the past three decades, the average annual losses due to coastal floods are estimated to be around US$6 billion for the 136 largest coastal cities worldwide (Hallegatte et al., 2013). This trend is expected to continue in the future because of population growth, with the projected number of people residing in coastal zones exceeding one billion by 2050 (IPCC, 2019), urban development, and the effects of climate change on the intensity and frequency of flood-generating weather systems (Mokrech et al., 2007; Ranson et al., 2014). Glacier melts and land subsidence can further lead to the rise of the global sea levels exacerbating the flood risks in coastal environments (Dutton et al., 2015; Rodolfo and Siringan, 2006).

The simultaneous or successive occurrence of two or more flood mechanisms can lead to more adverse environmental and socio-economic impacts compared to the occurrence of a single driver (IPCC, 2012). Recent studies have highlighted the importance of assessing flood risks associated with the compounding effects of multiple drivers including precipitation, streamflow, storm tide, and Total Water Level (TWL) (combination of the astronomical tide, surge, and mean sea level) (Ganguli and Merz, 2019; Kew et al., 2013; Svensson and Jones, 2002). Multiple mechanisms can trigger or intensify compound flooding (CF) across coastal areas. Passage of a low-pressure system, e.g., a hurricane, can raise the water levels that subsequently propagate into the watershed. This, combined with excessive rainfall associated with the same weather system can cause catastrophic

flooding. Additionally, heightened total water levels can block the river drainage causing backwater effects and local flooding close to the river mouth. Further, a destructive storm surge can be accompanied by moderate rainfall that further increases the flood depth and/or extent of the inundated area (Wahl et al., 2015; Zhang et al., 2020). CF can also occur when precipitation falls on the wet ground with saturated soil due to a preceding storm surge (Bevacqua et al., 2019b).

Recent studies have investigated the dependence structure between flood-generating mechanisms by quantifying their joint probabilities along with their joint return levels/periods and assessed the corresponding impacts on the global (Bevacqua et al., 2020b; Bevacqua et al., 2020c; Couasnon et al., 2019; Eilander et al., 2020), continental (Bevacqua et al., 2019a; Camus et al., 2021; Ganguli and Merz, 2019; Paprotny et al., 2020), national (Fang et al., 2020; Jalili Pirani and Najafi, 2020; Wu et al., 2018) and locals scales (Ai et al., 2018; Zhang and Najafi, 2020). Xu et al. (2018) analyzed the joint probability of extreme precipitation and storm tide in the coastal city of Fuzhou, China. Jang and Chang (2022) studied the joint occurrence of rainfall and tide using copulas and multiple regression and assessed the corresponding risk of compound flooding. Lu et al. (2022) investigated the compound flooding risk in coastal-estuarine regions of Southeastern China using copulas. Moftakhari et al. (2017) and Ward et al. (2018) modeled the joint annual maximum streamflow and the associated water levels using copulas for major coastal cities in the U.S and the globe, respectively. Liu et al. (2018) investigated the joint effects of precipitation and surface runoff with the El Nino-Southern Oscillation (ENSO) and rising temperatures as underlying conditions in Texas, USA. Jane et al. (2020) applied vine-copulas to characterize the dependencies between three variables of rainfall, TWL, and groundwater level for coastal areas of Miami-Dade County (southeast Florida). However, the effects of major hydrologic factors such as soil moisture and snowpack might be overlooked when precipitation is considered as a proxy for streamflow, especially over Canadian watersheds (Biron et al., 1999; Macrae et al., 2010). Ward et al. (2018) estimated the average time between discharge gauging stations and the outlet near the coast within a maximum period of 14 days in studying the compounding effects of streamflow and seawater levels.

Only a few studies have conducted a comprehensive investigation of different mechanisms that can lead to compound flooding in coastal areas. In a recent study, Nasr et al., (2021) analyzed the interdependencies corresponding to 12 joint events acquired from four drivers including precipitation, surge, streamflow, and wave along the US coasts. They found higher dependencies between surge-wave and surge-precipitation than in other scenarios. Such analyses are crucial to better understand the compound flood characteristics and to develop possible flood scenarios along with the underlying uncertainties in flood risk assessments. Canada has the longest coastline in the world with distinct characteristics on the east (Atlantic), west (Pacific), and inland (Great Lakes). The communities in coastal zones are at risk of compound flooding caused by different drivers. The recent hurricane Larry in September 2021 that passed over Nova Scotia and the east U.S in 2020 led to three deaths and $80 million (2021 USD) in damage. Other destructive hurricanes striking the area include Hurricane Teddy in 2020 with 35 million (2020 USD), hurricane Dorian in 2019 with over 5.1, and Hurricane Matthew in 2016 with 16.47 billion in damages. However, understanding of the flood mechanisms on Canada's coasts in particular the corresponding interdependencies and combined risks is quite limited. In this study, we investigate the compound flood risks associated with eight bivariate joint events driven by four flooding mechanisms including rainfall, streamflow, skew surge, and total water level across Canada's coasts. To this end, firstly, we define eight types of the bivariate event of four flooding drivers and then develop their corresponding bivariate distribution using copulas The distributions' parameters are estimated using the Bayes theorem. Then, the flooding hazard is assessed using the Return Period (RP), Failure Probability (FP), and Compound Hazard Ratio index (CHR) methods over the Canadian coastal regions. Besides, the hotspot locations that are at a higher risk of compound flooding compared to other coastal regions are identified.

The remainder of the paper is as follows. Section 2 describes the study area and data followed by the discussion of the statistical approach in Section 3. The results and conclusions are presented in Sections 4 and 5, respectively.

2.2. Study area and data

Canada has a diverse climate regime with annual precipitation varying from almost 3000 mm at the west coast to 300 mm in parts of the Prairies and about 200 mm in the far north (Canada, 1995). It has the longest coastal line in the world (around 243,042 kilometers) extending from 43°N to 83°N latitude, which settles almost 7 million people. More than $400 billion of goods are shipped annually through Canadian ports in coastal areas (Association of Canadian Port Authorities, 2013). All provinces and territories, except Alberta and Saskatchewan, have marine coasts that are at risk of flooding with different levels of potential damage. This threat is increasing over time partly because of land-use change, land subsidence, and impacts of climate change, especially at the Atlantic coast (Couture and Manson, 2016; Lane et al., 2013; Lemmen, 2016). The magnitude and frequency of Total Water Level (TWL) extremes are projected to increase especially at the Atlantic coast in the future at a higher rate compared to the global mean (Bush and Lemmen, 2019a).
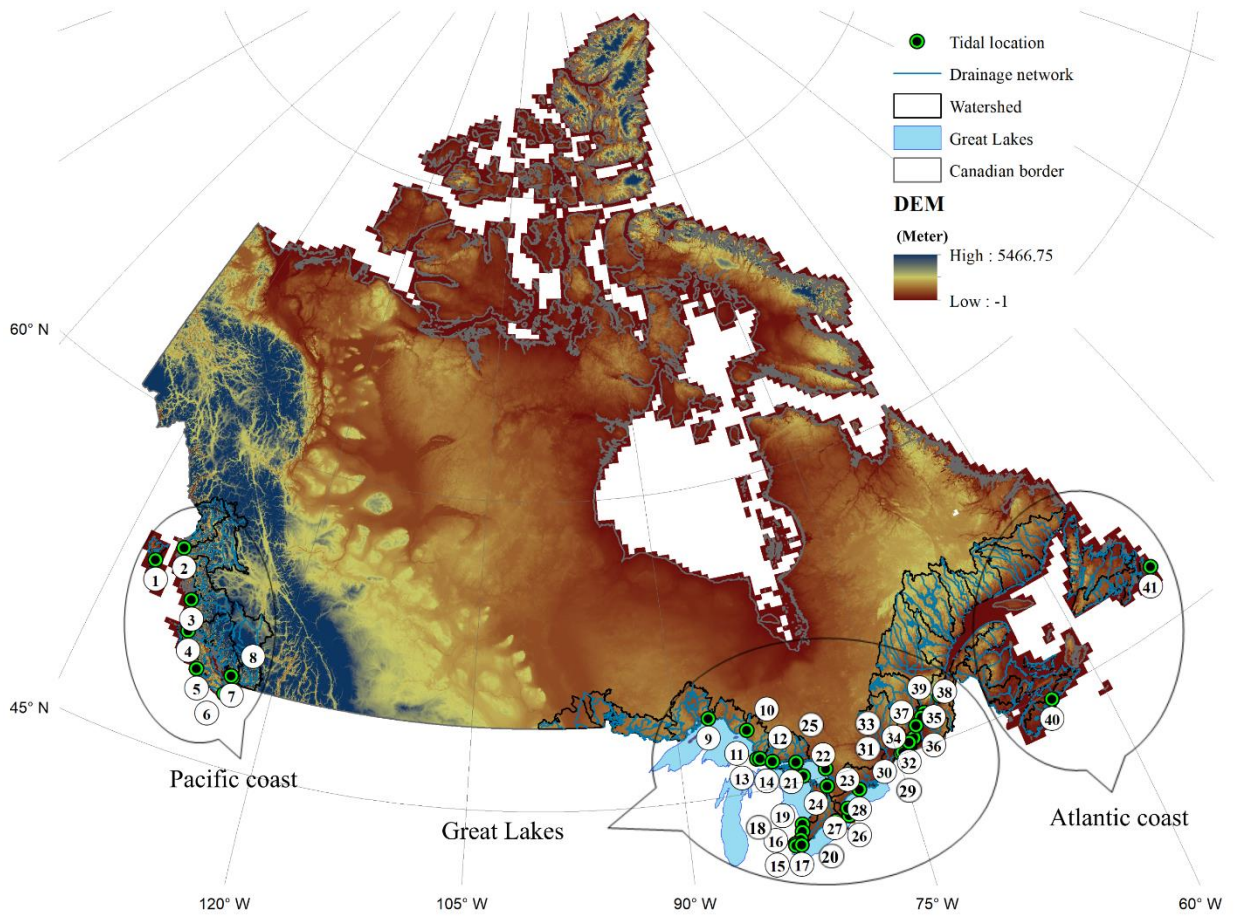
Figure 2.1) The study area along with the location of tidal gauges across the three regions of the Pacific, Atlantic, and the Great Lakes coasts.

The hourly TWL records are obtained from tidal gauges across Canada's coasts from 1960 to 2015. There are over 1000 tidal gauges available, however many of them are inactive or have large missing data. Daily mean streamflow denoted as Q and accumulated Precipitation (Pr) are acquired from the water survey of Canada, and Adjusted and Homogenized Canadian Climate Data (AHCCD) (Mekis and Vincent, 2011), respectively (Table S2.1).

Data records (TWL) are selected according to the following filtering criteria:

(1) Each year having more than 20 percent of missing data is removed for each tidal gauge.

(2) Tidal gauges with more than 20 percent of missing data over the entire period are removed, which leads to about 61 remaining gauges. This threshold of missing values was selected so that we have a balance between the number of locations and our statistical analysis which should not be affected by missing values. A level of more than 20 percent for missing values leads to only 7 gauges mostly at the GL and a level lower than 20 might questioned the reliability of our results.

(3) Precipitation and streamflow gauges that lie within a radius of 0.5° (about 55 km) from each tidal gauge are identified followed by the application of steps 1&2 on each record. In addition to the physical distance of streamflow gauges, flow routes are tracked to make sure they are directed towards the tidal gauge (Ward et al., 2018). In cases where several precipitation or streamflow gauges exist within the specified radius, the closest and most downstream ones are selected. If no hydroclimatic gauges exist within this distance (including gauges 2, 3, 19, 15, and 17 in Figure 4.1), the radius is increased to 100 km to identify at least one precipitation and one streamflow gauge (Wu et al., 2018). The choice of the distance is to ensure that gauges are representative of the homogeneous hydro-climatic conditions of their locations (Ward et al., 2018).

(4) Only the locations that have more than 80 percent overlap between T, skew surge, precipitation, and streamflow data records are retained.

Forty-one coastal locations (2 on the Atlantic Coast, 7 in the Pacific, and 32 on the Great Lakes) are selected after assessing the data (Figure 4.1). All locations include one tidal gauge; however, precipitation and streamflow data could be matched with two different tidal gauges because of physical proximity (resulting in 27 and 25 selected stations, respectively). Besides, to analyze the coincidence of multiple drivers of flooding the three data records are temporally matched. Following Ward et al. (2018) we shift the streamflow data for five hydrometric stations that are located > 55 km upstream of the coast. We use the Kirpich equation to estimate the corresponding time lag (Mata-Lima et al., 2007):

$$T_c = KL^{0.770}S^{-0.385} , \qquad\qquad (4.1)$$

where T_c is the time of concentration, K is a unit conversion coefficient and K=0.0195 in SI units, L is the channel flow length in feet or meters as dictated by K and S is the dimensionless main-channel slope. The range of T_C for these five gauges ranges between 18 to 36 hours. We further applied the Pickering method and noticed minor differences in the estimated time lags.

The skew surge data are derived by subtracting the high tide from maximum TWL regardless of their timing within 24-hour intervals. S has a higher flood potential than the conventional daily maximum storm surge that might be superimposed on low or high tide. This is due to the fact that the maximum storm surge happening on the low tide has less flood potential than a moderate storm surge happening on the high tide. In this study, the 24-hour maximum values of TWL together with S, and daily values of Pr and Q are considered for further analysis.

We tried to focus on the main flooding drivers (pluvial, pluvial and sea level rise) over the Canadian coastal regions and the four selected drivers represent these flooding sources. Other types of flooding drivers including groundwater flooding can also be incorporated into the analysis; however, we did not have access to these data. Different bivariate combinations of the four drivers that can cause compound flooding in the coastal areas are investigated. The extreme Pr and Q events are extracted using the peak over threshold (POT) method and are paired with the corresponding maximum values of TWL and S within ± 1 day of these events. The same approach is considered to couple the TWL and S extreme events with associated Pr and Q values. The threshold values are determined based on the 95th percentile of the data records. This procedure leads to eight bivariate scenarios denoted as ($Pr_{e\_0.95}$, S), ($Pr_{e\_0.95}$, TWL), ($Q_{e\_0.95}$, S), ($Q_{e\_0.95}$, TWL), ($TWL_{e\_0.95}$, Pr), ($TWL_{e\_0.95}$, Q), ($S_{e\_0.95}$, Pr), ($S_{e\_0.95}$, Q). e_0.95 refers to the extreme events higher than quantile 0.95 in a time series, for example, $Pr_{e\_0.95}$ refers to extreme precipitation events higher than quantile 0.95. The autocorrelation between extreme events is removed by selecting the peaks of 3-day intervals (Ghanbari et al., 2021). We ended up with around 700 samples for each bivariate scenario at each location. Regarding the scenarios ($TWL_{e\_0.95}$, Pr) and ($S_{e\_0.95}$, Pr), there exist several events with zero values for Pr that are discarded as they do not represent compound flood events.

2.3. Methodology

2.3.1. Dependencies between drivers of flooding

Multivariate statistical analysis based on copulas was introduced to the field of hydrology by Michele and Salvadori (2003). Copula functions link together the marginal distributions to form multivariate distribution functions and characterize the dependence structure (linear, non-linear, tail dependence) (Genest and Favre, 2007). A detailed discussion of the copula functions is provided in Joe (1997) and Nelson (1998).

Prior to analyzing the bivariate distributions using copulas, the Kendall correlation test is applied and the significance of the dependencies between the drivers is assessed at a 5% significance level (Genest and Favre, 2007). In comparison with the Pearson method which considers a linear relationship between two variables, Kendal's Tau measure a monotonic relationship (either linear or non-linear) between the variables. The test statistic is as follows:

$$\tau = \sqrt{\frac{9n(n-1)}{2(2n+5)}} |\tau_n|, \tag{2.1}$$

where τ is the test statistic which follows the standard normal distribution, τ_n is the Kendall correlation value between two variables. P-values are calculated as $2p(Z > \tau)$.

Marginal distributions are determined for each variable at each location, corresponding to each compound flood scenario. The Generalized Pareto Distribution (GPD) is fitted to the POT data, e.g. $Pr_{e\_0.95}$ in ($Pr_{e\_0.95}$, S), and the Akaike Information Criterion (AIC) is used to select the best-fitted distribution among the Normal, Lognormal, Gamma, Gumbel, Exponential, Generalized Extreme Value (GEV), Generalized Pareto Distribution (GPD), Weibull, Logistic, and Cauchy distributions using the ML method. AIC (Akaike, 1974) is defined as:

$$AIC = 2k - 2\ln(L), \tag{2.2}$$

15

where k is the number of parameters and L is the maximum value of the likelihood function for the model. The selected distribution is further evaluated using the Kolmogorov-Smirnov (KS) goodness-of-fit test (Chakravarty et al., 1967) considering a 5% significance level. The parameters of the best-fitted distributions are estimated based on the maximum likelihood approach. The data records corresponding to each driver are then converted into the (0, 1] space based on the corresponding CDFs. This is followed by selecting the best-fitted copula (among 41 functions) (Schepsmeier et al., 2015) including Gaussian, Student t, Frank, Joe, Clayton, Gumbel, Clayton-Gumbel (BB1), Joe-Gumbel (BB6), Joe-Clayton (BB7), Joe-Frank (BB8), Tawn type 1, and Tawn type 2 along with their rotational models (90, 180, and 360 degrees) to represent the dependence structures and determine the bivariate distributions. The lists of the univariate distributions, copula families, and the associated parameter ranges are provided in Tables S2.2 and S2.3, respectively.

AIC is a comparison-based approach for selecting a model. In other words, AIC helps with selecting a model which is the best fit among a few other fitted models; however, it does not show us whether this selected model is significant or not. Therefore the goodness-of-fit test proposed by Genest et al. (2006) is applied to further evaluate the best-fitted copula functions. The test is based on two variants, S_n and T_n of the Cramér–von Mises statistic, which are improvements over the previous works of Genest and Rivest (1993) and Wang and Wells (2000):

$$S_n = \int_0^1 |(K_n(w)|^2 \, k_{\theta_n}(w)dw, \tag{2.3}$$

$$T_n = \sup_{0 \leq w \leq 1} |K_n(w)|, \tag{2.4}$$

where $\mathbb{K}_n(w) = \sqrt{n}\{K_n(w) - K_{\theta_n}(w)\}$. K_n is the empirical cumulative distribution of the data and K_{θ_n} refers to the theoretical cumulative distribution of samples taken from the fitted copula and k_{θ_n} is the corresponding density. These relatively simple statistics are not limited to Archimedean copulas contrary to the Cramér–von Mises statistic. Further, p-values associated with these statistics can be obtained by bootstrapping. According to Genest et al. (2006), comparing raw values of S_n and T_n could be just as misleading as Cramér–von Mises statistic in model selection in some cases. H_0 To deal with this problem,

16

they proposed a bootstrap method to calculate the P-values under the null hypothesis, $H_0: C_\theta \in \mathcal{C}_\theta$ where C_θ is the underlying empirical copula belongs to a parametric family of copulas ($\mathcal{C}_\theta$) under consideration. This family of copulas depends on a parameter that has to be estimated. Therefore, Genest et al. (2006) proposed a bootstrap method to assess the evidence against the null. In this process, a large number, N, of independent samples of size n are generated from $\mathcal{C}_\theta$ and the corresponding values of S_n^* and T_n^* are computed to obtain the distribution of the statistics. The p-value is obtained as follows: For T_n, the p-value is computed in a similar way (Genest et al., 2006).

$$p - \text{value} = \frac{1}{N} \sum_{k=1}^{N} 1(S_{n,k}^* > S_n),$$

$\hspace{12cm}$ (2.5)

The number of iterations (N) in this study is 1000. S_n is the statistic value for the original data and $S_{n,k}^*$ is the statistic value for the kth bootstrap sample.

2.3.2. Uncertainty analysis of the bivariate distribution

In this study, the uncertainties in the copula and the marginal parameters are characterized based on the Bayesian inference approach (McElreach, 2018), which combines the knowledge brought by the prior distribution with the observations to generate the joint posterior distribution of the corresponding parameters. Considering n bivariate observations $(x_1, y_1),..., (x_n, y_n)$ representing the driving mechanisms, the joint posterior pdf is determined as follows (Smith, 2011):

$$f(\phi_c, \theta_m | (x_1, y_1), (x_2, y_2), \ldots, (x_n, y_n)) \propto$$
$$p(\theta_m) \cdot p(\phi_c) \cdot \prod_{i=1}^{n} c(x_i, y_i | \phi_c) \cdot f(x_i | \theta_m) \cdot f(y_i | \theta_m),$$

$\hspace{10cm}$ (2.6)

where $f(\phi_c, \theta_m | (x_1, y_1), (x_2, y_2), \ldots, (x_n, y_n))$ is the joint posterior density function of ϕ_c, θ_m, which are the parameter sets of copula and marginals, respectively. $p(\theta_m), p(\phi_c)$ are the prior distributions of θ_m, ϕ_c, and $c(x_i, y_i | \phi_c)$ is the copula density of x and y. $f(x_i)$ and $f(y_i)$ represent the marginal densities of x and y, respectively. As there is no

prior knowledge of the parameters, uninformative uniform distributions are considered in this study.

The Metropolis-Hastings method of the Markov Chain Monte Carlo (MCMC) algorithm is applied for sampling from the joint posterior distribution (Hastings, 1970). Each MCMC chain includes 10000 iterations with a burn-in period of 5000 to acquire full convergence and remove the effects of initial sampling. Next, following the method proposed by Geweke (1991) we test the convergence of the second half of the chain by comparing the mean of the first 10% of the chain against the second half of the chain. If the two means are equal, the chain is converged and the test statistic (standard Z-score) has standard Gaussian distribution. From the estimated joint posterior distributions, the median, and 95% credible interval of the parameters (ϕ_c, θ_m) are extracted to create the bivariate distributions followed by analyzing the flood risks and the corresponding uncertainties. The sampling algorithm was coded in the RStudio and the corresponding script is available in the GitHub link: "https://github.com/fjalilip?tab=repositories".

2.3.3. Joint Return Period (JRP)

Robust water resources management and sustainable engineering design require understanding the high-impact events and their probability of occurrence each year and during the lifetime of the project(s). Risk is mainly considered as the hydrologic risk in this study.

The return period refers to the average recurrence time between natural hazard disasters (earthquake, flood, drought, etc). The RP of a hazard corresponds to the average interarrival time between the occurrences divided by the exceedance probability. In multivariate analysis of extremes, the following risk scenarios are commonly considered for estimating the joint return periods of the driving mechanisms: either driver exceeds the extreme threshold (OR scenario), both drivers exceed the respective thresholds (AND scenario), the joint probability of two or more drivers exceeds a level of probability (Kendall scenario), and the joint probability of two drivers overtakes a survival level of

probability (Survival Kendall scenario) (Salvadori and De Michele, 2004; Salvadori et al., 2007; Shiau, 2006). Considering the compound flood event associated with (Pr$_{e\_0.95}$, TWL), as an example, with Pr and TWL as pluvial and coastal flood driving mechanisms, the exceedance probability and the corresponding JRP of the OR scenario similar to other studies can be defined as:

$$P_{or} = P\big((Pr > pr) \cup (TWL > twl)\big) = 1 - C(F_{Pr}(pr|\theta_{mpr}), F_{TWL}(twl|\theta_{mtwl})|\phi_c),$$
(2.7)

$$JRP_{or} = \frac{\mu}{P_{or}},$$
(2.8)

where P_{or} is the OR exceedance probability, θ_{mpr} and θ_{mtwl} are the set of marginal parameters for Pr and TWL, respectively. P and C(copula function) are the same and refer to the joint probability of TWL and Pr when both are lower than their respective thresholds. $F_{Pr}(pr|\theta_{mpr})$ and $F_{TWL}(twl|\theta_{mtwl})$ are the univariate cumulative probabilities of Pr, TWL given the set of parameters θ_{mpr}, and θ_{mtwl} respectively. ϕ_c is the copula parameter and μ is the average interarrival time between the events.

The AND exceedance probability and the corresponding JRP are computed as follows:

$$P_{and} = P\big((P > pr) \cap (TWL > twl)\big) = 1 - F_{Pr}\big(pr\big|\theta_{mpr}\big) - F_{TWL}(twl|\theta_{mtwl}) +$$
$$C(F_{Pr}(pr|\theta_{mpr}), F_{TWL}(q|\theta_{mtwl})|\phi_c),$$
(2.9)

$$JRP_{and} = \frac{\mu}{P_{and}},$$
(2.10)

where P_{and} AND P are the AND exceedance probability or the probability of two drivers when both TWL Pr are higher than their respective thresholds.

The (unrealistic) independence OR and AND JRPs are estimated based on:

$$JRP_{or} = \frac{\mu}{1 - (F_{Pr}(pr|\theta_{mpr}) \times F_{TWL}(twl|\theta_{mtwl}))},$$
(2.11)

$$JRP_{and} = \frac{\mu}{1 - F_{Pr}(pr|\theta_{mpr}) - F_{TWL}(twl|\theta_{mtwl}) + (F_{Pr}(pr|\theta_{mpr}) \times F_{TWL}(twl|\theta_{mtwl}))},$$
(2.12)

Previous studies such as Salvadori et al. (2011, 2016) and Xu et al. (2019) have shown that OR and AND JRPs may not identify the risk zone, properly. They point to some major events with a larger RP than the events in the dangerous regions defined by the AND or OR scenarios, which can cause under- or over-estimation of the engineering designs. To address this issue, Salvadori and De Michele (2010) proposed the Kendall JRP based on the Kendall distribution function. In this type of JRP, the probability space is divided into three parts including a critical probability layer called p (a line in 2D and a surface in 3D probability space), a dangerous region denoted as S_p^d that includes all the events with joint probabilities more than p, a safe region denoted as S_p^s, which includes all the events with joint probabilities less than p. d and s denote dangerous and safe regions, respectively (Salvadori et al., 2016). The JRP corresponding to the dangerous region is defined as follows:

$$JRP_{Kendall} = \frac{\mu}{P[C(F_{Pr}(pr|\theta_{mpr}), F_{TWL}(twl|\theta_{mtwl})|\phi_c) > p]} = \frac{\mu}{1 - K_c(p)},$$ (2.13)

where $K_c(p) = P[C(F_{Pr}(pr|\theta_{mpr}), F_{TWL}(twl|\theta_{mtwl})|\phi_c) \le p]$ (Salvadori et al., 2016),

According to Salvadori et al. (2016), the Kendall scenario does not have a direct physical/structural interpretation and should be used for the preliminary risk assessments. Overall, selecting a specific JRP scenario depends on the aim of the study and the past flooding events.

Further, we assess the conditional RPs representing the design floods corresponding to one driver conditional on the other. For example, considering the Q and TWL:

$$P_{cond} = P(Q \ge q|TW \ge Ltwl) = 1 - \frac{F_Q(q|\theta_{mq}) - C(F_q(q|\theta_{mq}), F_{TWL}(twl|\theta_{mtwl})|\phi_c)}{1 - F_{TWL}(twl|\theta_{mtwl})},$$ (2.14)

$$RP_{cond} = \frac{\mu}{P_{cond}},$$ (2.15)

where P_{cond} is the probability of Q given the non-exceedance probability of TWL.

For all the scenarios at each location, the univariate RP when the exceedance probability is 0.01 is compared with those of conditional, AND (dependence and independence), OR (dependence and independence), and Kendall scenarios.

The univariate RP is also calculated as dividing the average interarrival time by the exceedance probability of 0.01 for each location.

RP is not tied to the sustainability of a design level. In other words, the RP can not determine whether a designed level is sustainable by the next few years (for example, 10, 100 … etc years). To tackle this problem, we use the failure probability concept as follows.

2.3.4. Failure Probability (FP)

The hydrologic risk is assessed by considering the probability of a potential flood event happening at least once in a given project's lifetime (Salvadori et al., 2016; Xu et al., 2019a; Xu et al., 2019b) or in other words, the hydrologic risk of failure of infrastructure within a specific period. While the results can be calculated for all the hazard scenarios, here the comparison is made between the copula-based FPs OR and its counterpart independence scenario and the univariate analysis.

The failure probability (Xu et al ., 2019b) is estimated by:

$$FP = 1 - \prod_{i=1}^{T} F(Pr_i, TWL_i), \tag{2.16}$$

F represents the non-exceedance probability, which is calculated based on Equation 8 for the OR scenario. T is the project lifetime in the case of annual max data (in which the number of events is the same as the project lifetime). However, in the case of the POT approach, this number of events (N) is obtained by dividing T (the project lifetime) by μ (average interarrival time between the events) as follows.

$$N = \frac{T}{\mu}, \tag{2.17}$$

Considering the dependence between the drivers, the OR FP can be estimated based on Equation 18:

$$FP_{or} = 1 - \prod_{i=1}^{N} C(F_{Pr}(pr|\theta_{mp}^i), F_Q(q|\theta_{mq}^i)|\phi_c^i), \qquad (2.18)$$

In this study, the bivariate hydrologic risk is quantified by comparing the FPs corresponding to the (Pr$_{e\_0.95}$, TWL) OR scenario (independence and dependence) with a univariate scenario for RPs of 100 and 10 years and lifetimes ranging from 1 to 100 years. Furthermore, the bivariate hydrologic risk for different levels of each driver with the other driver having RPs of 20 and 100 years are assessed for lifetimes from 1 to 50 years.

We also estimate and suggest the optimum design levels of Pr$_{e\_0.95}$ and TWL using the FPs for location #40 as an example. To this end, we calculate the bivariate FPs for different levels of Pr$_{e\_0.95}$ and 20 and 100 year levels of TWL. And, we do the same for TWL with 20 and 100-year levels of Pr$_{e\_0.95}$. This helps us to see at what levels the bivariate hydrologic risk decreases and whether the design is safe. Besides, it provides us with the levels of both drivers at which the design is superfluous. However, if the design level should be just regarding the streamflow which is affected by the sea level rise upstream, the RP and FP can not be applied. We came up with this problem using the CHR index as follows.

2.3.5. Compound Hazard Ratio (CHR) index

Ganguli et al. (2019) proposed the CHR index to compare the T-year return level of seasonal (November-March) streamflow discharge, conditional on annual maximum water level, with the unconditional T-year fluvial event. We apply the CHR index to investigate the extent and direction (decrease or increase) to which the discharge rate variations are dependent on TWL, and vice versa, regarding two scenarios of (Q$_{e\_0.95}$, TWL) and (TWL$_{e\_0.95}$, Q). Given *Q* and *TWL* as the fluvial and coastal flood drivers, the CHR is estimated as follows:

22

$$CHR = \frac{Q'_T}{Q_T} = \frac{C_{Q|TWL=twl}^{-1}\left[1-\frac{\mu}{T_{Q|TWL=twl}(q|twl)}\right]}{F_Q^{-1}\left[1-\frac{\mu}{T_Q(q)}\right]}$$ (Ganguli et al., 2019), (2.19)

Q'_T and Q_T are conditional (copula-based) and unconditional return levels of *discharge* given a 100-year total water level. $C_{Q|TWL=twl}^{-1}$ and F_Q^{-1} denote inverse quantile transformations of copula-based and univariate distributions, respectively. μ is the average interarrival time between the events. $T_{Q|TWL=twl}(q|twl)$ and $T_Q(q)$ are the conditional and unconditional return periods of q (streamflow). The CHR index varies from 0 to infinity with values more than 1 indicating the positive interdependency between the TWL on Q.

Finally, we identify the locations that are at higher risk of compound flooding according to the 8 scenarios. For example, at each location we assess whether the AND JRP is lower than the one estimated based on the independence assumption and the CHR index is over 1. We repeat this analysis for the other seven joint scenarios and along with the AND results, we count the number of times, out of 8, this criterion is met for the site. For example, a value of 6 indicates that 6 compound flood scenarios out of 8 can potentially impact the location. Three thresholds of 2, 4, and 6 (#scenarios) are considered to identify the low-, medium- and high-risk locations.

2.4. Results and discussion

2.4.1. Marginal distributions

For each scenario, extremes selected based on the POT approach are represented by the GPD distribution. The second marginal distribution of the joint pair is selected from ten distributions using the AIC metric followed by the KS significance test, as discussed in the previous section. Considering the scenarios (Pre_0.95, S), (Pre_0.95, TWL), (Qe_0.95, TWL), and (Qe_0.95, S), Gumbel and Logistic distributions are the overall best fits for S over the three regions, and Gamma and Normal distributions are selected for TWL across

all locations. Besides, GPD is the dominant marginal distribution in ($TWL_{e\_0.95}$, Pr), ($TWL_{e\_0.95}$, Q), ($S_{e\_0.95}$, Pr), and ($S_{e\_0.95}$, Q) compound events especially in the Pacific and GL regions. Considering all the scenarios, over 80% of the selected distributions passed the KS test (Figure S2. 1).

2.4.2. Dependence analysis

The results of Kendall's Tau underline the positive and most statistically significant dependency between the drivers of the ($Pr_{e\_0.95}$, TWL) scenario at the majority of the locations (35 out of 41) across the three regions. This is also true, with a few exceptions, for ($Pr_{e\_0.95}$, S) particularly on the Pacific and Atlantic coasts. For the scenarios ($Q_{e\_0.95}$, TWL) and ($Q_{e\_0.95}$, S), 17 locations indicate significant positive dependencies on the Pacific/GL areas, and over the three regions respectively. The number of locations that show statistically significant positive dependencies is 22 (mainly at the GL), 32 (South Pacific, the GL, and Atlantic), 21 (mostly southern and eastern GL), and 31 (relatively more in two coastal areas) corresponding to the ($S_{e\_0.95}$, Q), ($S_{e\_0.95}$, Pr), ($TWL_{e\_0.95}$, Q), and ($TWL_{e\_0.95}$, Pr) joint events (Figure 2.2). Concerning all the scenarios and sites, the interdependence between the drivers varies from -0.2 to over +0.3. The locations that experience positive dependencies are at higher risk of compound flooding. Overall, the Atlantic region shows a higher positive dependency between the drivers followed by the Pacific and the GL regions. From a flooding driver perspective, the highest dependence is found between $TWL_{e\_0.95}$ and Pr followed by bivariate events ($S_{e\_0.95}$, Pr), ($Pr_{e\_0.95}$, S), ($Pr_{e\_0.95}$, TWL), ($Q_{e\_0.95}$, S), ($Q_{e\_0.95}$, TWL), ($S_{e\_0.95}$, Q) and ($TWL_{e\_0.95}$, Q). Moreover, the dependence analysis highlights the important role of extreme precipitation and TWL and S over the Atlantic coast. This might be associated with the extratropical cyclones historically affecting this area. However, the coincidence of flow with sea-related drivers is more remarkable on the Pacific coast, which can be associated with the more rapid response of the hydrological basins outflowing to the estuaries in this area than in the other two regions. At the GL, extreme S plays a major role. Although this region is less affected by the tidal forces and tropical cyclones than the other two coasts, due to the seiche events in this area, the joint occurrence of $S_{e\_0.95}$ with Pr and Q is more likely.

Characterizing such interdependencies between different drivers in the three regions lead to more in-depth risk analysis as they highly affect the joint probabilities of major flooding types.
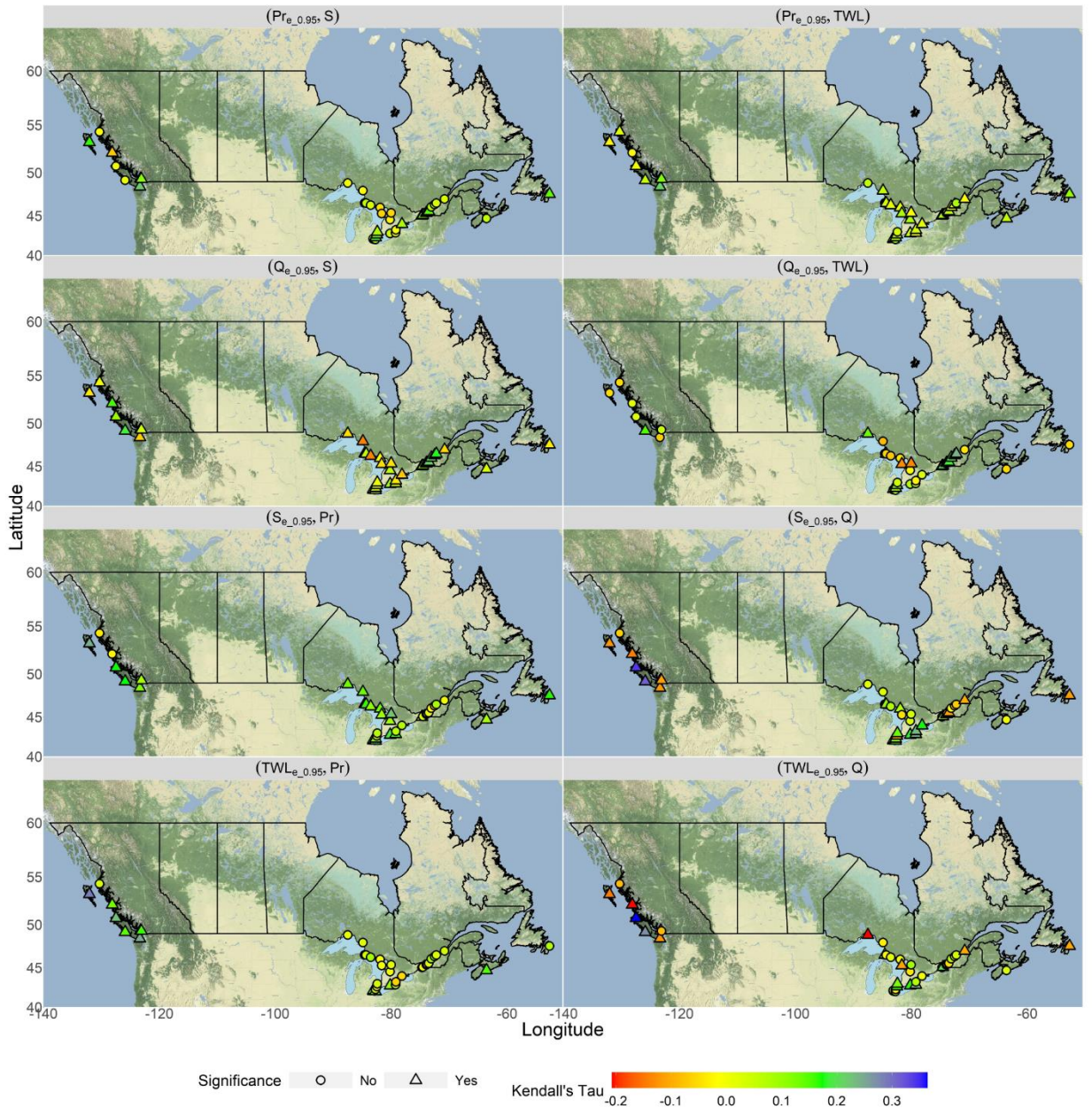
Figure 2.2) The Kendall's Tau results and the associated significance status for different scenarios at various locations across the Canadian coastal line.

2.4.3. Copula models

The selected copula families, the corresponding AIC values, and the significance test results are shown in Tables S2.4 to S2.7. Frank, Rotated Tawn type 2 (90 degrees) and Gaussian copulas are mainly selected for different bivariate scenarios. At some locations across the GL and the Pacific coast, extreme copulas including Tawn type 1 and 2, and their rotations are selected because there are higher dependencies in the upper tails of the joint events. The same copula types are selected in the Atlantic area regarding scenarios ($TWL_{e\_0.95}$, Q) and ($TWL_{e\_0.95}$, Pr). Table S2.8 presents the number of locations corresponding to each region in which the best-fitted copulas pass the goodness of fit test concerning each scenario. Close to 90% of the selected copulas pass the significance test, especially for scenarios ($Pr_{e\_0.95}$, TWL), ($Pr_{e\_0.95}$, S), ($Q_{e\_0.95}$, TWL) and ($Q_{e\_0.95}$, S).

2.4.4. Return Period (RP)

The JRPs and the corresponding uncertainties are estimated for the OR, AND, Kendall, and conditional scenarios for the bivariate events and compared with their counterpart univariate RP and unrealistic independence scenarios. Figure 2.3 shows the results for the ($Pr_{e\_0.95}$, TWL) and ($Pr_{e\_0.95}$, S) bivariate events. Generally, the results of the joint events are different from those of univariate and bivariate independent events at all locations in both scenarios. The JRPs estimated for the OR scenario are 5-11 years smaller than the univariate RPs across different locations suggesting that the probability of either pluvial or sea-level drivers causing flooding is higher than the one corresponding to each driver when studied in isolation. Besides, not considering the dependency between the drivers leads to the underestimation of JRPs regarding the OR scenario.

The AND JRPs are also influenced by the interrelationship between the drivers. Figure 2.3a illustrates how the positive dependency reduces the AND JRP (overall, lower than 500 years, and 100 years at some locations) in contrast to the independence scenario (varying from 577 to 662 years). The uncertainties also diverge accordingly. The performance of Kendall JRPs with the dependency is analogous to AND JRPS. The higher positive dependency leads to a lower Kendall JRP, changing from 10 years

(location 41 in the Atlantic region) to 56 years (location 26 at the GL). The results of the $(Pr_{e\_0.95}, S)$ scenario are similar to those of $(TWL_{e\_0.95}, S)$ considering the effects of dependency on JRPs. Concerning both scenarios, the results highlight the dominance of surge drivers over both coasts and TWL in the GL area. Relatively, more locations on both coasts show decreased AND JRPs than the GL area. This could be explained by the fact that these regions (specifically the Atlantic region) are prone to extra-tropical weather systems with the potential to cause simultaneous high S (TWL) and Pr and subsequently, more compound flooding events. Further, TWL at the GL is mainly affected by the flow to the lake and water leaving the lake as a function of over-lake precipitation, over-lake temperature, and streamflow from the outflowing basins (Nandanwar, 2022), especially at the locations near the basins with a high hydrological response as it results in the co-occurrence of TWL and Pr and a higher chance of joint events.

The estimated RPs for other scenarios show similar behavior to $(Pr_{e\_0.95}, TWL)$ regarding the effects of dependency between the drivers. Figure 2.3b shows the JRP results of OR, AND, and Kendall scenarios for the $(Pr_{e\_0.95}, S)$ bivariate event. At all the locations where the dependencies between the drivers are positive, the joint RPs for the AND, and Kendall scenarios are smaller than those considering the unrealistic independence assumption indicating that the flood risks are underestimated if such interrelationships are not characterized. These changes are more noticeable at locations 31, 32, 37 (northern Lake Ontario), and 41 (north Atlantic coast). Other bivariate events are shown in Figures S2. 2-S2. 4. Overall, several sites such as 15-20, 24, and 26 at the GL show a higher likelihood of compound flood events (if the dependencies are considered) considering the $(Q_{e\_0.95}, TWL)$ scenario. Scenario $(TWL_{e\_0.95}, Q)$ presents fewer critical locations compared to others. The analyses of $(TWL_{e\_0.95}, Pr)$ also accentuate the effects of positive interconnection between the drivers on JRP. Almost 25 locations have AND JRP smaller than the ones from the independence assumption, and the situation is perilous respecting locations 16, 24, and 29 (Lakes Huron and Superior) (JRPs less than 100) (Figure S2. 3b). The two drivers in the $(S_{e\_0.95}, Pr)$ joint event show positive dependencies in many

locations, especially at 6 (south BC), 9, 1, 13, 14, 18, 21, 22, 24 (eastern Ontario), and 41(North Atlantic) (Figure S2. 4b).
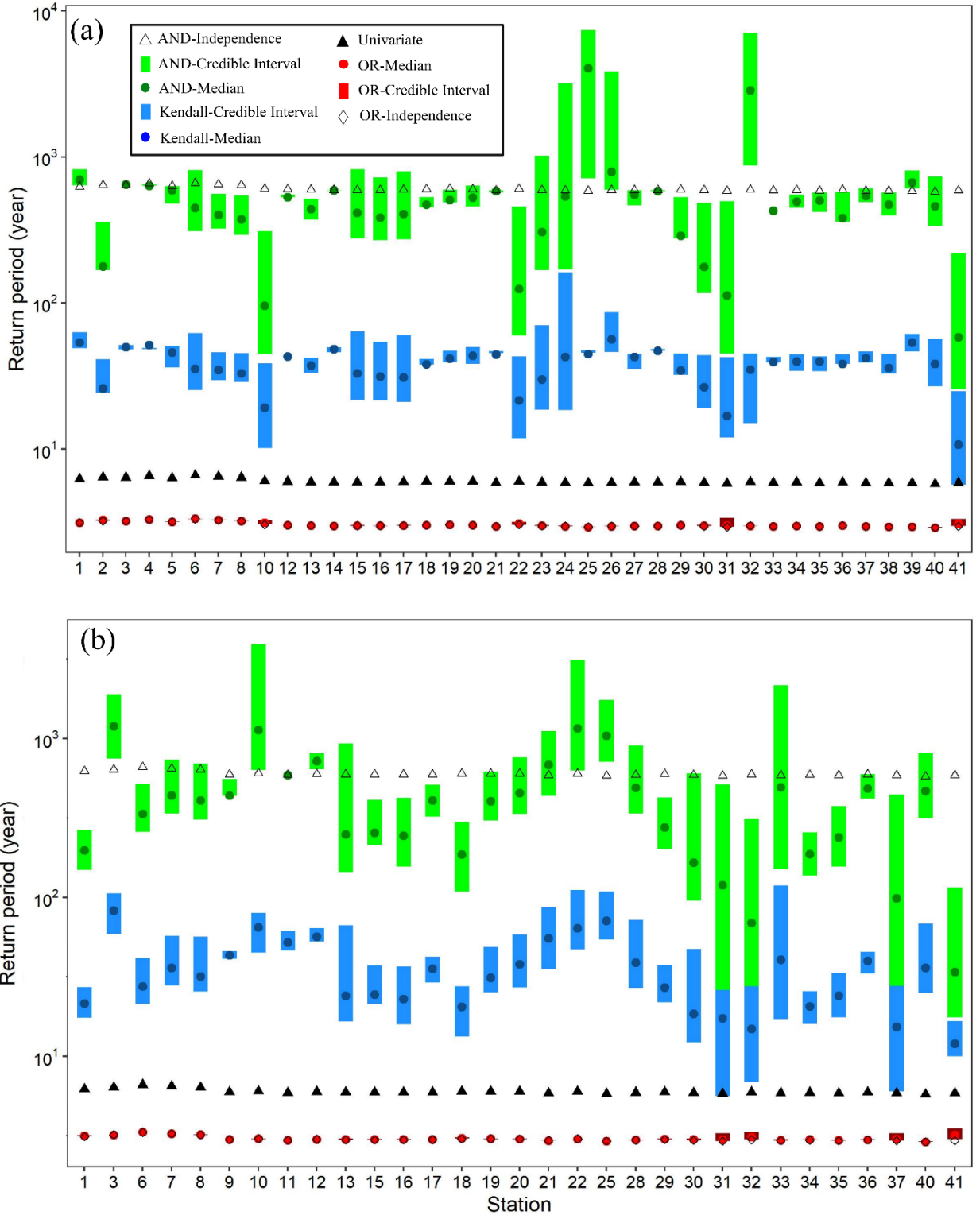
Figure 2.3) The estimated OR, AND, and Kendall JRPs for different locations in comparison with univariate RP and independence OR and AND JRPs related to scenarios (Pr$_{e\_0.95}$, TWL) and (Pr$_{e\_0.95}$, S).

29

2.4.5. CHR index

Further, we investigate the variations in the 100-year return level of fluvial flood driving mechanism conditional on the TWL (with a return period of 100 years) and compare it with the unconditional (univariate) estimate using the CHR index. This allows us to quantify how much the streamflow levels may change conditional on the sea level component. The median CHR values for the scenario ($Q_{e\_0.95}$, TWL) are above one for over half of the locations on both south and north of the Pacific coast, western and eastern GL, and southern Atlantic (Figure 2.4). They suggest that the 100-year streamflow levels conditioned on TWL are more severe by ~ 0.5 % at the Pacific to ~86 % at the GL compared to those of the unconditional estimates. Besides, results highlight the higher correlation between TWL and Q at the GL area compared to the other two coastal regions. In South Pacific, southern GL (Canadian side), and northern Atlantic where the index falls below unity, the extreme streamflow events tend to occur when TWLs are relatively low (indicating lower risks of compound flooding associated with high Q and TWLs). Additionally, the uncertainty range varies subject to the location with the lowest and highest at locations 2 at the Pacific and 17 at the south GL. Besides, 39% of the locations distributed on the eastern GL areas indicate CHR index above unity regarding scenario ($TWL_{e\_0.95}$, Q) (Figure S2. 5). Table 2.1 provides the number of locations with CHR more than unity for different scenarios in three regions. It shows that concerning scenarios ($Pr_{e\_0.95}$, TWL), ($Pr_{e\_0.95}$, S), ($TWL_{e\_0.95}$, Pr), and ($S_{e\_0.95}$, Pr), all three regions have sites with CHR of more than 1. Regarding the Atlantic area, both locations show CHR > 1 for multiple bivariate scenarios. This highlights the consistency of S and TWL in this area (when the S occurs on the high tide). In other words, the joint occurrence probability of pluvial and coastal flooding drivers is high which has been observed during the past hurricane events in this area as well. These results, however, do not imply causality, e.g., for the occurrence of precipitation conditioned on coastal water levels. Rather, they suggest higher chances of intense precipitation events during high water levels. Concerning the GL over half of the stations (mostly on eastern GL) have CHR > 1. Although the dependence of streamflow on the GL water level is stronger than with Pr, however, more locations are at flooding risk regarding the joint extreme Pr and TWL than other bivariate events in this area. These locations are mainly over Lake Erie and Lake Ontario. Such behavior is also observed over the Pacific area regarding the aforementioned scenarios and ($Q_{e\_0.95}$, S) events. Besides, the watersheds outflowing into the sea in this area have a rapid hydrological response and therefore, an extreme precipitation event can lead to the occurrence of pluvial flooding and fluvial flooding with a short time lag. This might justify the positive correlation of both Pr and Q

with sea-level components in the Pacific region. All these results highlight that not taking into account the mutual impacts of the drivers might lead to the underestimation of the design levels.

Table 2.1) The number of locations at each region with CHR index above unity considering different bivariate compound events.

Region / Scenario	Pacific	GL	Atlantic
$(Pr_{e\_0.95}, TWL)$	6/8	25/31	2/2
$(Pr_{e\_0.95}, S)$	4/8	18/31	2/2
$(Q_{e\_0.95}, TWL)$	3/8	19/31	0/2
$(Q_{e\_0.95}, S)$	5/8	15/31	1/2
$(TWL_{e\_0.95}, Q)$	2/8	14/31	0/2
$(TWL_{e\_0.95}, Pr)$	8/8	16/31	2/2
$(S_{e\_0.95}, TWL)$	2/8	18/31	0/2
$(S_{e\_0.95}, Pr)$	6/8	21/31	2/2
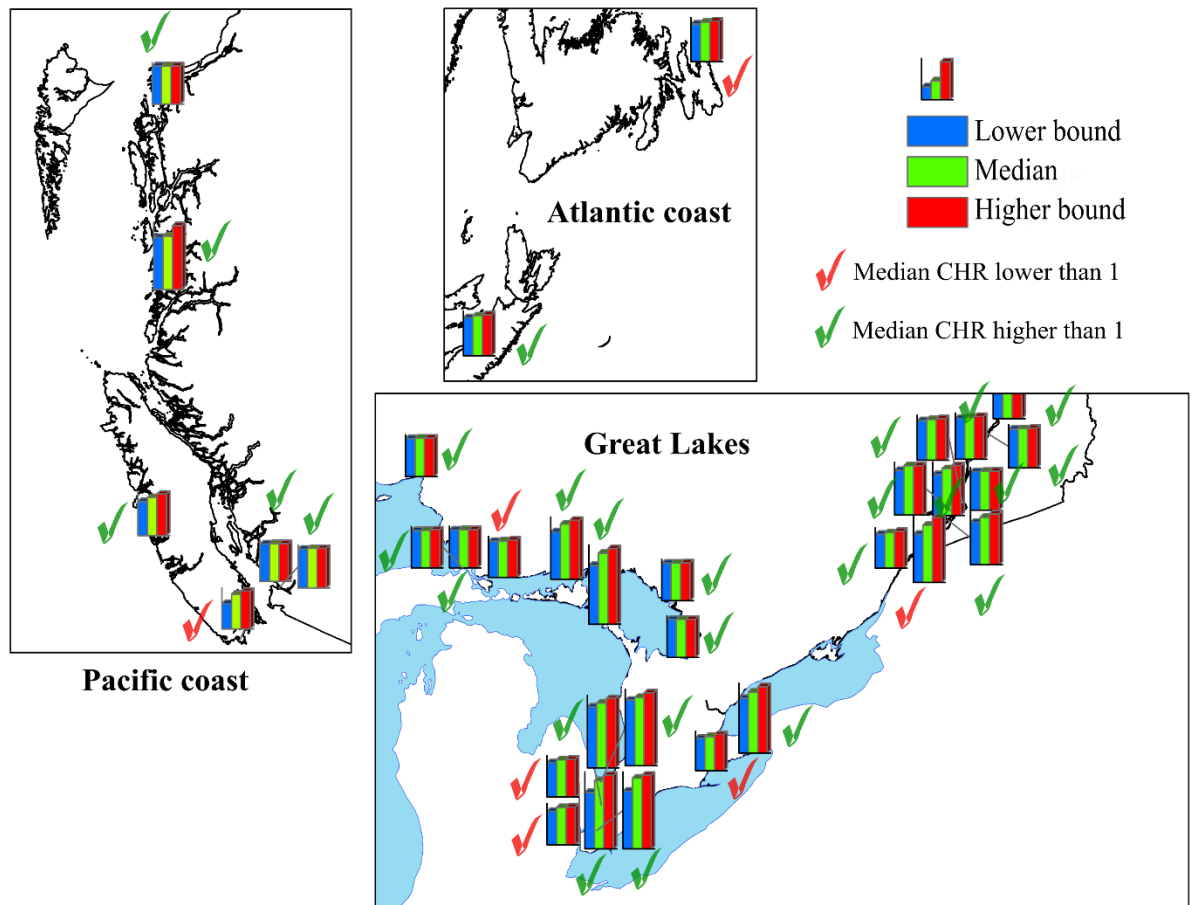
Figure 2.4) The CHR index values corresponding to the (TWL$_{e\_0.95}$, Q) event across the Pacific, Great Lakes, and Atlantic coasts.

2.4.6. Conditional RP

In a bivariate analysis, the conditional RP refers to the return period of a flood event associated with the occurrence of a second flood driver. The conditional RPs are assessed considering the dependencies between the paired drivers and are compared to estimates based on the independence assumption. The results suggest that provided two drivers have a positive interrelationship, the conditional RP would decline. Considering the (Q$_{e\_0.95}$, TWL) compound event (Figure 2.5), the conditional RP is smaller than the unconditional one at locations # 3, 4, 6, 8 (the Pacific), and 18 locations at the GL due to positive interdependencies between the two drivers. This decreased RP is more

considerable in areas 2 (Middle Pacific) 9, 23, 24, 25, 27, 28, 33, 36 at the (GL). Figure 2.5 also highlights the median RPs and the corresponding uncertainties across locations. The conditional RPs corresponding to (Pr$_{e\_0.95}$, S) show similar behavior but at fewer locations, as shown in Figure S2. 6. The results of other scenarios are provided in Figures S2.7 to S2.12. These results are consistent with the ones based on the CHR index.
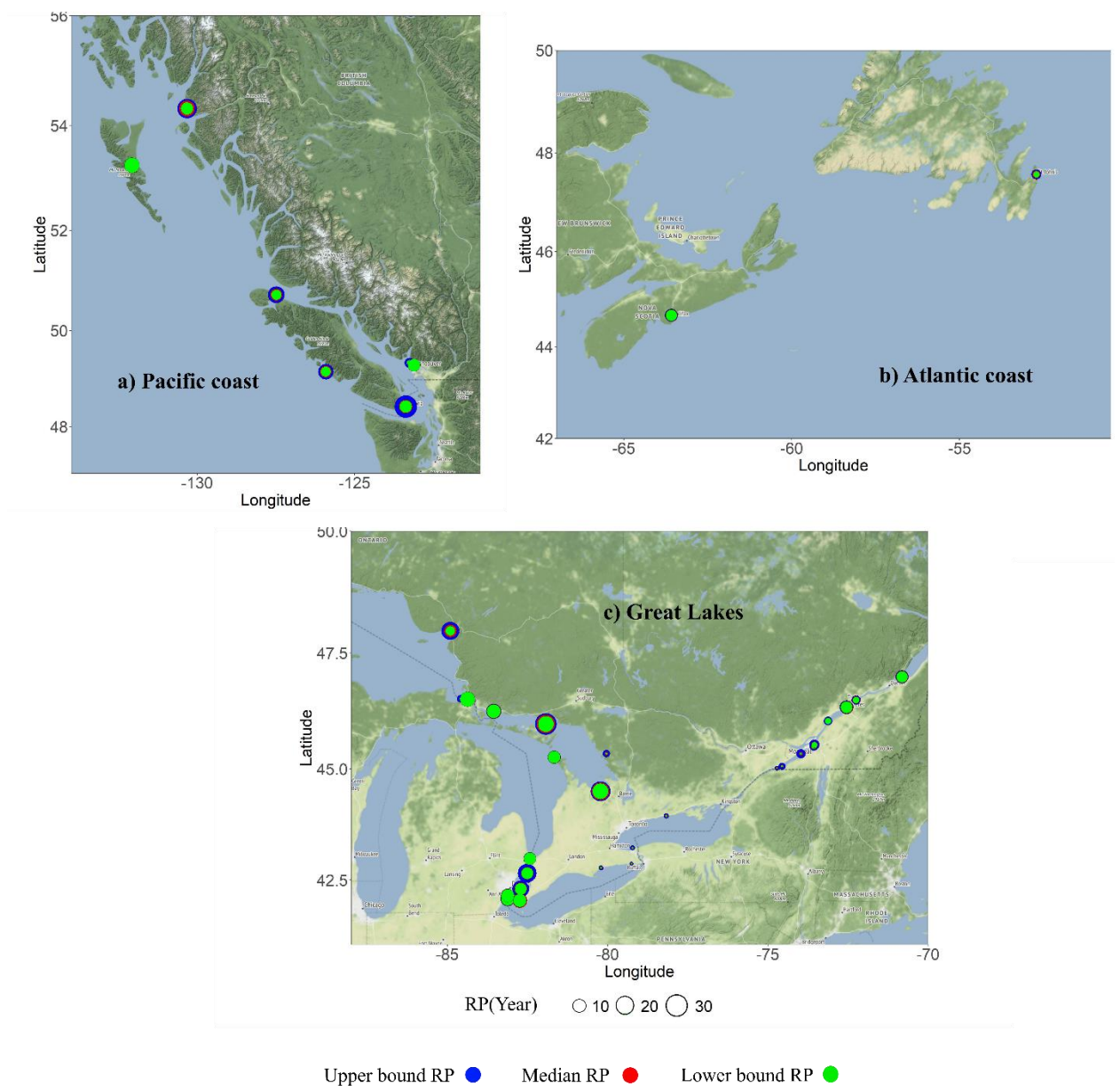
Figure 2.5) The conditional RPs and associated uncertainties for different locations considering the (Q$_{e\_0.95}$, TWL) bivariate compound event.

Figure 2.6 identifies the locations with higher flooding risks concerning all the bivariate scenarios according to the AND JRP results and the CHR index. The results indicate that most locations across Canada's coasts are at risk of compound flooding with a combination of at least two flooding mechanisms. The JRPs based on the AND scenario are lower than the ones estimated based on the independence assumption considering at least 4 bivariate compound events in 31 out of 41 locations. The following locations can be affected by the majority of the bivariate events (six out of eight combinations) including 4, 5, and 8 on the south Pacific and 15-18 and 24 south of Lake Huron, 20, 26 at Lake Erie, and 30, 36 at the Lake Ontario highlighting the importance of characterizing the interdependence structure of the corresponding flood mechanisms in these areas. However, the Atlantic area especially the south Atlantic is more susceptible to surge dominant bivariate events. In other words, there is a higher probability of the co-occurrence of the extreme S and TWL with Pr than in other scenarios. The impact of tropical cyclones on this area can explain the simultaneous occurrence of these two drivers (at least 4 tropical storms per year for most years between 1899 and 1996) in this area (Hart and Evans, 2001).
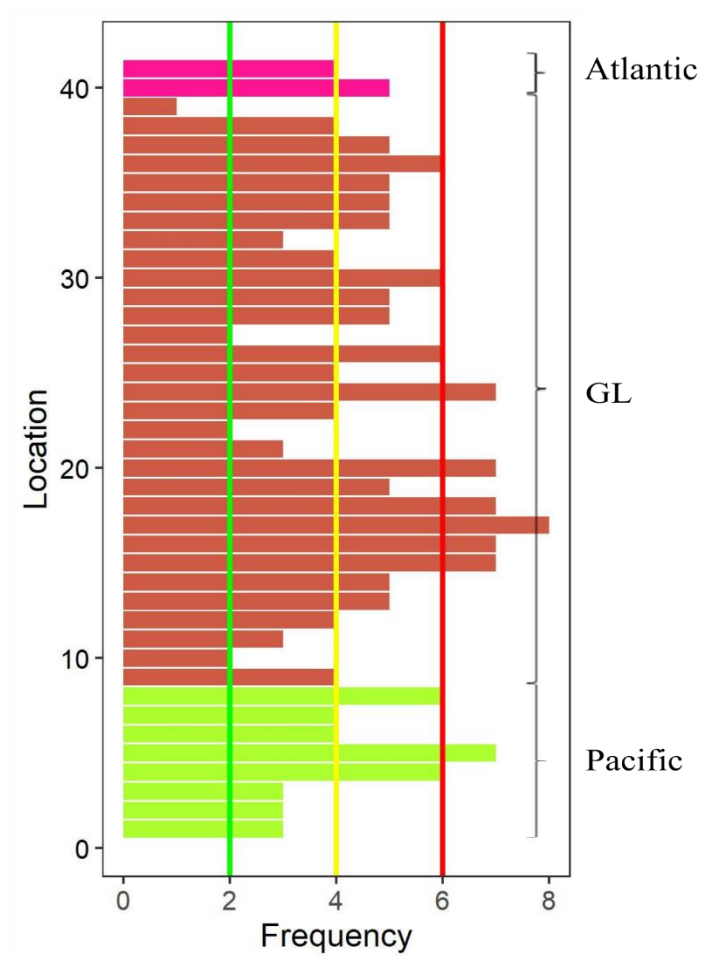
Figure 2.6) Number of bivariate events (out of eight) that can potentially affect the coastal location due to positive interrelationships between the corresponding flood driving mechanisms; locations with larger frequency are at higher risks of compound flooding

2.4.7. Failure Probability (FP) and bivariate hydrologic risk

RP provides information about the average recurrence time of an event (here flood hazard), however, for engineering purposes, such an event should be tied to the designed infrastructure. Here the bivariate hydrologic risks of (TWL$_{e\_0.95}$, Pr) and (Pr$_{e\_0.95}$, TWL) are quantified using the failure probability (FP), which refers to the possibility of a flood event occurring at least once during a given project lifetime (Xu et al., 2019a). The FPs

associated with univariate 10- and 100-year events and project lifetimes of 1 to 100 years are estimated for all the locations and hazard scenarios and are compared with the compounding FPs under dependence and independence OR scenarios. For the sake of brevity, we present the results for locations 5 (Tofino at south Pacific), 22 (Tobermory at Lake Huron), and 41 (St. John's at North Atlantic) (Figure 2.7). The FP increases with an increase in the lifetime and for 10-year events as compared to 100-year events, as expected. For example, considering a service time of 50 years for the St. John's site, FP is 0.38 for the 100-year event which increases to over 0.9 when RP is 10 years. Further, the univariate scenario underestimates the FP compared to the OR scenario as shown for the (Pre_0.95, TWL) event. Besides, the unrealistic independence OR FPs cause an overestimation of the flood hazard. Considering the service time of 50 years and 100-year RP for St. John's site (which has been affected by ~40 extratropical cyclones from 1979 to 2005 (Milrad et al., 2009)), the univariate analysis provides an FP of 0.38 while based on the OR scenario it increases to 0.67 meaning that there is a 76% increase in the FP as both flooding mechanisms and their interactions are considered. Besides, the FP of the independence scenario is 0.69 which signifies the overestimation of the FP when the interaction between the drivers is ignored. These results are in line with previous studies conducted over other coastal areas (e.g., Moftakhari et al., 2017 and Xu et al., 2019). In addition, Tofino can experience the joint event of TWL and Pr which can be exacerbated considering the impacts of climate change (Ebbwater Consulting Inc. 2019). There are also reports regarding flooding because of the temporary increase in the water level at Lake Huron (Dababneh et al., 2016). The scenario (TWL$_{e\_0.95}$, Pr) shows similar behavior from the viewpoint of bivariate hydrologic risk analysis (Figure S2. 13). The FP results associated with 100-year RP of other types of joint events approve the results by (Pr$_{e\_0.95}$, TWL) and (TWL$_{e\_0.95}$, Pr) scenarios for location #41 (Figure S2. 14).
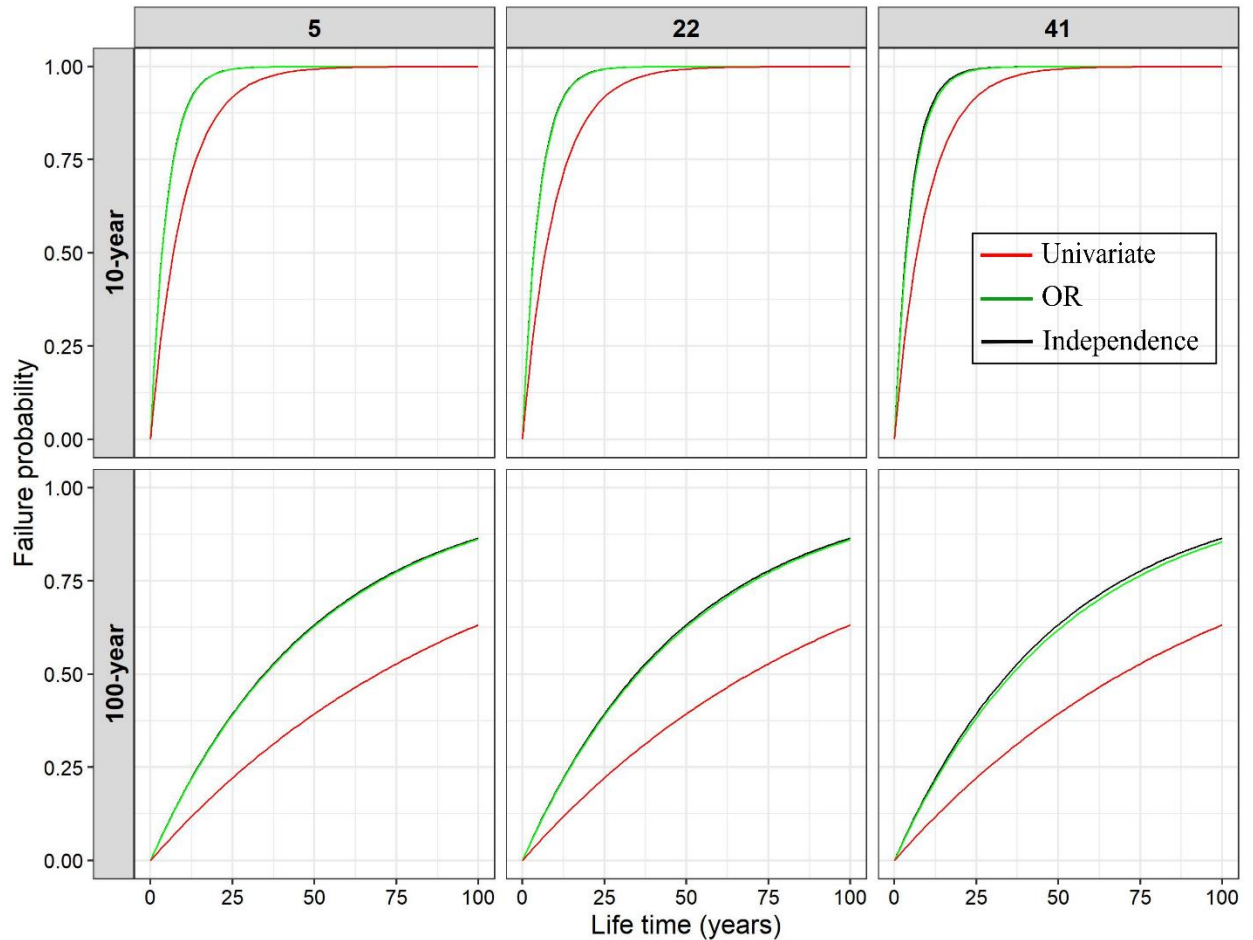
Figure 2.7) The estimated FPs corresponding to the (Pr$_{e\_0.95}$, TWL) bivariate event for locations 5 (Tofino at south Pacific), 22 (Tobermory at Lake Huron), and 41 (St. John's at North Atlantic) under the OR scenario.

Further, we analyze the bivariate hydrologic risks corresponding to (Pr$_{e\_0.95}$, TWL) for location #40 (in Halifax, Nova Scotia) and suggest the optimum design levels for both drivers considering the corresponding interdependencies, and compare them with those estimated by the univariate analyses. This site has also already been damaged by the extratropical cyclones in Canada. Hurricane Juan affecting this area is recognized as the most serious threat to Halifax, which caused over \$200 million in damages to Nova Scotia (Fogarty, 2003). The results show that bivariate hydrologic risk increases with an increase in the project lifetime and reduces with an increase in the RP (Figure 2.8).

Considering the 100- year event of TWL, the bivariate hydrologic risk decreases quickly if the design precipitation is more than ~85mm (~100 mm) corresponding to 10 (50)-year lifetimes and it drops to less than 0.12 (10-year) and 0.25 (100-year) lifetimes when the design precipitation is higher than 160 mm and then decreases slowly. This indicates the rainfall should be designed at least higher than 85 mm because the probabilities of failure of the designed infrastructures lower than this threshold are high and the corresponding design may not be safe. Besides, design levels higher than 160 mm causes superfluous expenses for managers. Therefore, the optimum design for Pr is between 85 and slightly higher than 160 mm. Besides, the bivariate hydrologic risk is at the highest level until the TWL reaches 1.8m (1.9m) for lifetimes of 10(50) years with respect to 100- years Pr. Then it drops and reaches below 0.2 for both RPs when TWL is close to 2.2. This indicates that the best design regarding TWL to both addresses the security issue and avoid overestimation designs is between 1.8m and 2.2m. These estimated design values help engineers to avoid under- or over-estimation of the corresponding risks and protection designs (Figure 2.8).
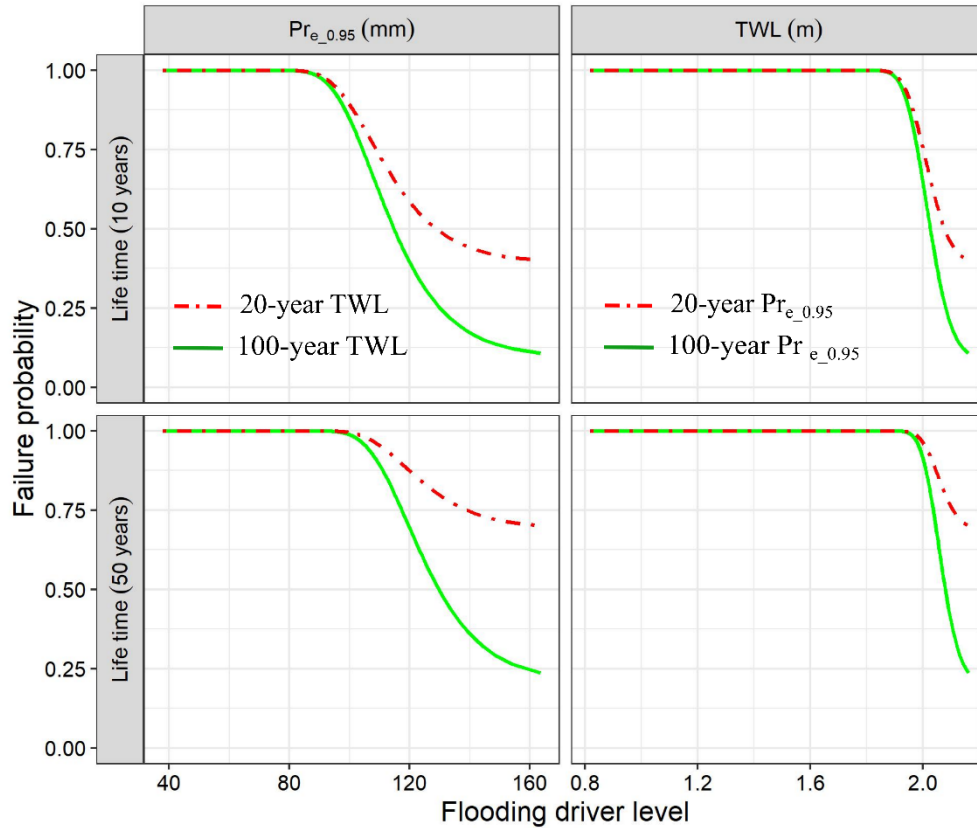
Figure 2.8) The bivariate hydrologic risks corresponding to lifetimes of 10 and 50 years at location 40 with the change of Pr$_{e\_0.95}$ at 100 and 10-year designed TWL. And with the change of TWL at 100 and 10-year designed Pr$_{e\_0.95}$.The green and red dotted colors show the 100 and 20 years RPs, respectively.

2.5. Conclusions

In this study, we investigate eight major bivariate compound flood drivers considering precipitation, streamflow, total water level, and skew surge across Canada's coastal areas. In each bivariate joint event, the extreme events corresponding to a flooding mechanism are extracted based on the POT approach and paired with the maximum values of the second mechanism within one day, before and after, the extreme events. A preliminary dependence analysis is performed for all paired events using Kendall's Tau correlation metric. Next, a suite of copula models is considered to represent the dependence

structures for all scenarios at all locations across the Pacific, Atlantic, and Great Lakes coasts. GPD distributions are fitted to the POT data and for the second driver, the best-fitted distribution is selected among ten univariate parametric distributions. The uncertainties corresponding to the copula and marginal parameters are estimated based on the Bayesian inference approach.

In this study, the frequency analysis of compound flooding for eight bivariate events is conducted and the corresponding joint return periods, failure probabilities, compound hazard ratios, and bivariate hydrologic risks are determined across coastal areas. The results, based on the AND scenario and CHR suggest that the ($Pr_{e\_0.95}$, TWL) bivariate compound event is dominant compared to other joint events affecting ~80% of the locations studied across Canada's coasts. This is followed by ($S_{e\_0.95}$, Pr) with ~70% and ($TWL_{e\_0.95}$, Pr) with ~63% of locations being at risk of such compound flood events, respectively. These dependencies can considerably affect the flood design estimation. For example, the positive interrelationships between Pr/TWL and Pr/S at location 41 on the north Atlantic coast where the St. John's city is located results in a significant drop in the estimated joint return periods of ~58 and 34 years for the ($Pr_{e\_0.95}$, TWL) and ($Pr_{e\_0.95}$, S) bivariate events, respectively in comparison to when assuming independence between the flooding drivers. The CHR index as a measure of the change in the streamflow level conditional on the water level shows values above unity for 35 locations (85% of all locations) regarding scenario ($Pr_{e\_0.95}$, TWL) indicating that with a fixed return period, the tidal-affected estuaries/rivers at these locations have a higher streamflow level when considering the effects of sea level than not considering these effect. Therefore, it avoids the underestimation of the streamflow level designs at these locations. The number of locations with this condition regarding several scenarios of 2 and 4 is 40 and 3. Some of the coastal areas in the southern Pacific and the GL are at risk of compound flooding associated with multiple combinations of flood mechanisms. For example, location 5 at Victoria Island where Tofino city is located can be affected by all bivariate events except ($Pr_{e\_0.95}$, S).

The bivariate hydrologic risk of three locations representing the three study areas is performed using the failure probability which reflects the flood risk level during the

40

entire project lifetime. The failure probability increases with an increase in the lifetime of the hydraulic facilities and decreases for milder flood events, as expected. The corresponding measure is investigated for multiple scenarios suggesting that for three sites, the failure probabilities of the designed infrastructures during their service time are underestimated with univariate analysis. Besides, the true FPs are obtained with respect to considering the interdependency between the Pr and TWL flooding drivers specifically at the northern Atlantic site. In addition, the bivariate hydrologic risk is applied to determine the optimum design levels of $Pr_{e\_0.95}$ and TWL at Halifax, south Atlantic. The determined levels can increase the security of the designed infrastructures as it considers the minimum design level, besides the estimated maximum level avoids the extra design expenses. The analyses conducted in this study highlight the importance of considering the interrelationships between drivers of flooding across Canada's coasts with distinct characteristics, which is in line with previous studies in other regions around the world. Further, the results indicate spatial variations in bivariate scenarios and their impacts across coastal regions. Therefore, for reliable flood risk management, multiple compound flood scenarios need to be investigated rather than relying on a single compound event. Besides, other flood-generating mechanisms such as snowmelt and rain-on-snow events can initiate or exacerbate compound flooding. In this study, the influence of these drivers is represented by changes in extreme flows in addition to the precipitation events. These analyses can lead to more robust flood risk analyses and the design of sustainable infrastructure systems across the coastal areas as it gives the policy-makers the correct probabilities regarding the flooding events.

Acknowledgment

References

Ai, P., Yuan, D., Xiong, C., 2018. Copula-based joint probability analysis of compound floods from rainstorm and typhoon surge: A case study of Jiangsu coastal areas, China. *Sustainability*, 10(7): 2232.

Akaike, H., 1974. A new look at the statistical model identification. *IEEE transactions on automatic control*, 19(6): 716-723.

Bevacqua, E. et al., 2019a. Higher probability of compound flooding from precipitation and storm surge in Europe under anthropogenic climate change. *Science advances*, 5(9): eaaw5531.

Bevacqua, E. et al., 2019b. Higher probability of compound flooding from precipitation and storm surge in Europe under anthropogenic climate change. *Science advances*, 5(9): eaaw5531.

Bevacqua, E., Vousdoukas, M.I., Shepherd, T.G., Vrac, M., 2020a. Brief communication: The role of using precipitation or river discharge data when assessing global coastal compound flooding. *Natural Hazards and Earth System Sciences*, 20(6): 1765-1782.

Bevacqua, E. et al., 2020b. More meteorological events that drive compound coastal flooding are projected under climate change. *Communications earth & environment*, 1(1): 1-11.

Biron, P.M. et al., 1999. The effects of antecedent moisture conditions on the relationship of hydrology to hydrochemistry in a small forested watershed. *Hydrological Processes*, 13(11): 1541-1555.

Bush, E., Lemmen, D., 2019. Canada's changing climate report. Government of Canada. Ottawa: Government of Canada. Retrieved from http://www. Changing climate.

Camus, P. et al., 2021. Regional analysis of multivariate compound coastal flooding potential around Europe and environs: sensitivity analysis and spatial patterns. *Natural Hazards and Earth System Sciences*, 21(7).

Canada, E., 1995. The state of Canada's climate: Monitoring variability and change.

Chakravarty, I.M., Roy, J., Laha, R.G., 1967. Handbook of methods of applied statistics.

Couasnon, A. et al., 2019. Measuring compound flood potential from river discharge and storm surge extremes at the global scale and its implications for flood hazard.

Couasnon, A. et al., 2020. Measuring compound flood potential from river discharge and storm surge extremes at the global scale. *Natural Hazards and Earth System* Sciences, 20(2): 489-504.

Couture, N., Manson, G., 2016. CanCoast: a tool for helping to assess climate vulnerability. *Natural Resources Canada*. Geological Survey of Canada.

Dababneh, A.J., Oskamp, J.A., Edwards, T., 2016. Probabilistic Storm Surge Hazard Assessment for a Site on Lake Huron. *International Journal of Offshore and Polar Engineering*, 26(04): 401-407.

Dutton, A. et al., 2015. Sea-level rise due to polar ice-sheet mass loss during past warm periods. *science*, 349(6244).

Eilander, D. et al., 2020. The effect of surge on riverine flood hazard and impact in deltas globally.

Fang, J. et al., 2020. Compound flood potential from storm surge and heavy precipitation in coastal China. *Hydrology and Earth System Sciences Discussions*: 1-24.

Fogarty, C., 2003. Hurricane Juan storm summary. Canadian Hurricane Centre.

Ganguli, P., Merz, B., 2019. Trends in Compound Flooding in Northwestern Europe During 1901–2014. *Geophysical Research Letters*, 46(19): 10810-10820.

Genest, C., Favre, A.-C., 2007. Everything you always wanted to know about copula modeling but were afraid to ask. *Journal of hydrologic engineering*, 12(4): 347-368.

Genest, C., Quessy, J.F., Rémillard, B., 2006. Goodness-of-fit procedures for copula models based on the probability integral transformation. *Scandinavian Journal of Statistics*, 33(2): 337-366.

Genest, C., Rivest, L.-P., 1993. Statistical inference procedures for bivariate Archimedean copulas. *Journal of the American statistical Association*, 88(423): 1034-1043.

Geweke, J., 1991. Evaluating the accuracy of sampling-based approaches to the calculation of posterior moments, 196. Federal Reserve Bank of Minneapolis, Research Department Minneapolis, MN.

Hallegatte, S., Green, C., Nicholls, R.J., Corfee-Morlot, J., 2013. Future flood losses in major coastal cities. *Nature climate change*, 3(9): 802-806.

Hart, R.E., Evans, J.L., 2001. A climatology of the extratropical transition of Atlantic tropical cyclones. *Journal of Climate*, 14(4): 546-564.

Hastings, W.K., 1970. Monte Carlo sampling methods using Markov chains and their applications.

Jalili Pirani, F., Najafi, M., 2020. Recent trends in individual and multivariate compound flood drivers in Canada's coasts. *Water Resources Research*, 56(8): e2020WR027785.

Jane, R., Cadavid, L., Obeysekera, J., Wahl, T., 2020. Multivariate statistical modelling of the drivers of compound flood events in south Florida. *Natural Hazards and Earth System Sciences*, 20(10): 2681-2699.

Jang, J.-H., Chang, T.-H., 2022. Flood risk estimation under the compound influence of rainfall and tide. *Journal of Hydrology*: 127446.

Kew, S., Selten, F., Lenderink, G., Hazeleger, W., 2013. The simultaneous occurrence of surge and discharge extremes for the Rhine delta. *Natural hazards and earth system sciences*, 13(8): 2017-2029.

Lane, D., Clarke, C.M., Forbes, D.L., Watson, P., 2013. The gathering storm: managing adaptation to environmental change in coastal communities and small islands. *Sustainability science*, 8(3): 469-489.

Lemmen, D.S., 2016. Canada's marine coasts in a changing climate. Government of Canada= Gouvernement du Canada.

Lian, J., Xu, K., Ma, C., 2013. Joint impact of rainfall and tidal level on flood risk in a coastal city with a complex river network: a case study of Fuzhou City, China. *Hydrology and Earth System Sciences*, 17(2): 679.

Liu, Z. et al., 2018. A framework for exploring joint effects of conditional factors on compound floods. *Water Resources Research*, 54(4): 2681-2696.

Lu, W., Tang, L., Yang, D., Wu, H., Liu, Z., 2022. Compounding Effects of Fluvial Flooding and Storm Tides on Coastal Flooding Risk in the Coastal-Estuarine Region of Southeastern China. *Atmosphere*, 13(2): 238.

Macrae, M., English, M., Schiff, S., Stone, M., 2010. Influence of antecedent hydrologic conditions on patterns of hydrochemical export from a first-order agricultural watershed in Southern Ontario, Canada. *Journal of Hydrology*, 389(1-2): 101-110.

McElreath, R., 2018. Statistical rethinking: A Bayesian course with examples in R and Stan. Chapman and Hall/CRC.

Mekis, É., Vincent, L.A.J.A.-O., 2011. An overview of the second generation adjusted daily precipitation dataset for trend analysis in Canada. 49(2): 163-177.

Milrad, S.M., Atallah, E.H., Gyakum, J.R., 2009. Dynamical and precipitation structures of poleward-moving tropical cyclones in eastern Canada, 1979–2005. *Monthly weather review*, 137(3): 836-851.

Moftakhari, H.R., Salvadori, G., AghaKouchak, A., Sanders, B.F., Matthew, R.A., 2017. Compounding effects of sea level rise and fluvial flooding. *Proceedings of the National Academy of Sciences*, 114(37): 9785-9790.

Mokrech, M. et al., 2007. The development of an integrated coastal simulator for supporting long term coastal management, Coastal management: Proceedings of the two-day international conference organised by the Institution of Civil Engineers and held in Cardiff on 31 October–1 November 2007. Thomas Telford Publishing, pp. 203-217.

Nandanwar, S.S., 2022. Lake Huron Shoreline Analysis.

Paprotny, D., Vousdoukas, M.I., Morales-Nápoles, O., Jonkman, S.N., Feyen, L., 2020. Pan-European hydrodynamic models and their ability to identify compound floods. *Natural Hazards*: 1-25.

Ranson, M. et al., 2014. Tropical and extratropical cyclone damages under climate change. *Climatic change*, 127(2): 227-241.

Rodolfo, K.S., Siringan, F.P., 2006. Global sea-level rise is recognised, but flooding from anthropogenic land subsidence is ignored around northern Manila Bay, Philippines. *Disasters*, 30(1): 118-139.

Salvadori, G., De Michele, C., 2004. Frequency analysis via copulas: Theoretical aspects and applications to hydrological events. *Water resources research*, 40(12).

Salvadori, G., De Michele, C., 2010. Multivariate multiparameter extreme value models and return periods: A copula approach. *Water resources research*, 46(10).

Salvadori, G., De Michele, C., Kottegoda, N.T., Rosso, R., 2007. Extremes in nature: an approach using copulas, 56. *Springer Science & Business Media*.

Salvadori, G., Durante, F., De Michele, C., Bernardi, M., Petrella, L., 2016. A multivariate copula-based framework for dealing with hazard scenarios and failure probabilities. *Water Resources Research*, 52(5): 3701-3721.

Santos, V.M. et al., 2020. Multivariate statistical modelling of extreme coastal water levels and the effect of climate variability: a case study in the Netherlands. *Hydrology and Earth System Sciences Discussions*: 1-25.

Schepsmeier, U. et al., 2015. Package 'VineCopula'. R package version, 2(5).

Shiau, J., 2006. Fitting drought duration and severity with two-dimensional copulas. *Water resources management*, 20(5): 795-815.

Smith, M. S. (2011). Bayesian approaches to copula modelling. *arXiv preprint* arXiv:1112.4204.

Svensson, C., Jones, D.A., 2002. Dependence between extreme sea surge, river flow and precipitation in eastern Britain. International Journal of Climatology: *A Journal of the Royal Meteorological Society*, 22(10): 1149-1168.

Wahl, T., Jain, S., Bender, J., Meyers, S.D., Luther, M.E., 2015. Increasing risk of compound flooding from storm surge and rainfall for major US cities. *Nature Climate Change*, 5(12): 1093-1097.

Wang, W., Wells, M.T., 2000. Model selection and semiparametric inference for bivariate failure-time data. *Journal of the American Statistical Association*, 95(449): 62-72.

Ward, P.J. et al., 2018. Dependence between high sea-level and high river discharge increases flood hazard in global deltas and estuaries. *Environmental Research* Letters, 13(8): 084012.

Wu, W. et al., 2018. Mapping dependence between extreme rainfall and storm surge. *Journal of Geophysical Research:* Oceans, 123(4): 2461-2474.

Xu, H., Xu, K., Lian, J., Ma, C., 2019a. Compound effects of rainfall and storm tides on coastal flooding risk. *Stochastic Environmental Research and Risk Assessment*, 33(7): 1249-1261.

Xu, P. et al., 2019b. Time-varying copula and design life level-based nonstationary risk analysis of extreme rainfall events. *Hydrology and Earth System Sciences Discussions*: 1-59.

Zhang, Y., Najafi, M.R., 2020. Probabilistic Numerical Modeling of Compound Flooding Caused by Tropical Storm Matthew Over a Data-Scarce Coastal Environment. *Water Resources Research*, 56(10): e2020WR028565.

Zhang, Y.J. et al., 2020. Simulating compound flooding events in a hurricane. *Ocean Dynamics*, 70(5): 621-640.

Chapter 3

3. Tri-variate analysis of compound flood risks across Canada's Atlantic, Pacific, and Great Lakes coastal areas

3.1. Introduction

Flooding, as the most common natural hazard in the world (Kundzewicz et al., 2014), has affected more than two billion people and caused approximately USD 656 billion of damage between 1998 and 2017 (AghaKouchak et al., 2020; Wallemacq, 2018). From 1980 to 2019, flood events accounted for 41% of all the 17300 weather-related events, 28% of 890,000 lives lost, 27% of USD 4,000 billion economic losses, and 10% of USD 1,300 billion insured losses worldwide (Golnaraghi et al., 2020a). The frequency of flood events has been increasing from 1960 to 2013, globally (Tanoue et al., 2016). Similarly, the magnitude of flooding shows increases in some regions around the world (Do et al. 2020). Around 0.8-1.1 million people experience flooding and its devastating socio-economic consequences each year (Muis et al., 2016a), especially the coastal communities. The population of the low-lying coastal areas was approximately 625 million in 2000, which is anticipated to reach 949 million by the 2030s and 1.4 billion by 2060s (Neumann et al., 2015), indicating larger exposure to different types of flood hazards in these regions in the future. Therefore, it is critical to understand and predict the mechanisms that drive flooding, including intense rainfall, high seawater levels, and river overflows, as well as their interactions, and interrelationships to develop effective flood mitigation and adaptation strategies.

Conventional approaches to flood hazard assessment are based on the assumption that the drivers of flooding are independent of one another. However, recent studies show strong evidence for the interactions between drivers of floods, especially in coastal areas around the world (Eilander et al., 2020; Hendry et al., 2019; Moftakhari et al., 2017; Nasr et al., 2021; Robins et al., 2021; Wahl et al., 2015; Ward et al., 2018). Different

mechanisms can trigger flood events simultaneously or successively, leading to an extreme impact even if the contributing drivers are not extreme (Masson-Delmotte et al., 2021). The physical and socioeconomic consequences of such compound events can be much more drastic compared to the ones associated with the individual drivers (Ward et al., 2018; Zscheischler et al., 2018). Therefore, analyzing different flood types (e.g. fluvial, pluvial, and coastal) in isolation can result in an underestimation of flood risks.

In coastal areas, compound flooding can be associated with low-pressure systems like tropical cyclones that generate strong winds and subsequently storm surges and high waves, along with heavy rainfall and possible river overflows (Couasnon et al., 2019; Paprotny et al., 2018; Svensson and Jones, 2002). Examples of such events include Hurricane Katrina (2005) affecting south Florida (Johnson, 2006), Hurricane Harvey (2017) in southeast Texas (Frame et al., 2020), both with at least $125 billion in damage, and recent hurricanes of Elsa, and Henri (Eckstein et al., 2021) with $1.2 billion and $550 million in damage respectively. Previous studies have analyzed compound flood events at global (Eilander et al., 2020; Ward et al., 2018), continental (Ganguli and Merz, 2019; Paprotny et al., 2020), national (Ghanbari et al., 2021; Jalili Pirani and Najafi, 2020) and regional scales (Valle-Levinson et al., 2020; van Berchum et al., 2020) using statistical and process-based approaches (Hao et al., 2018). These analyses include characterizing the statistical interrelationships between drivers of flooding based on Bayesian networks (Couasnon et al., 2018; Sebastian et al., 2017), copula theory (Bevacqua et al., 2017; Gori et al., 2020; Moftakhari et al., 2017; Paprotny et al., 2018; Xu et al., 2014), bivariate extreme value distributions (Zheng et al., 2014), correlation and linear regression (Robins et al., 2021), bivariate logistic threshold-excess model (Zheng et al., 2013) among others. Besides, recent studies have assessed the compound flood impacts and risks through process-based modeling and a hybrid statistical-dynamical framework (Ganguli and Merz, 2019; Ganguli et al., 2020; Najafi et al., 2021; Wang et al., 2021; Zhang and Najafi, 2020).

The theory of copula, introduced to the hydrologic community by De Michele and Salvadori (2003), is commonly applied for the multivariate analysis of flood events as it can represent a wide range of dependence structures between hydroclimatic variables. It

is a flexible approach for the frequency analysis of compound events that allows for characterizing the individual drivers with the most appropriate distribution functions. The corresponding hazards can be assessed under different scenarios according to the geographic location or the criteria considered for the design, planning, and management of infrastructure systems or coastal communities (1) either of the flood mechanisms is extreme and can affect the study region, for example, the occurrence of an intense rainfall event or storm surge (OR scenario), (2) all the drivers are extremes (AND scenario), and (3) the joint exceedance probability of the drivers is above a certain threshold (Kendall scenario). Using copula models, Ward et al. (2018) studied the global dependencies between high river discharge rates and sea levels and showed their significant role in the estimated design levels. Bevacqua et al. (2020) reported an overall 30% increase in the joint probability of extreme meteorological tides and inland precipitation under a high emission scenario along the global coasts by 2100 compared to the present conditions. Ganguly and Merz (2019) showed that for half of the studied locations in northwestern Europe the river discharge rates conditioned on extreme coastal water levels are higher than the unconditioned rates. Further, Paprotny et al. (2020) found strong dependencies in surge–precipitation and surge–discharge pairs along the northwestern coasts of Europe. Similar analyses have been conducted on the joint occurrence of storm surge and precipitation across coastal zones of China (Fang et al., 2020), Australia (Wu et al., 2018), storm surge, and river discharge in Britain (Robins et al., 2021), storm surge/sea levels and river discharge over the US coasts (Welch, 2020), among others.

Many studies on compound flooding have focused on the bivariate structure of the driving mechanisms, however, the range of dependencies between multiple factors that can contribute to regional/global flooding is less understood. Liu et al. (2018) investigated the joint occurrence of precipitation and surface runoff in Texas, with the El Nino-Southern Oscillation and rising temperatures as the underlying conditions using vine copula (also known as pair-copula). Santos et al. (2020) conducted bivariate and trivariate extreme analyses to study the return periods (RPs) of inland water levels as a function of storm surge, tide, and precipitation in the Netherland. Jane et al. (2020) characterized the dependencies between rainfall, sea level, and groundwater level for

49

coastal areas of Miami-Dade County in southeastern Florida. They found that vine copulas could better represent the dependencies between the drivers compared to the standard high-dimensional copulas, which consider homogeneity in the type of dependence between each pair of variables and do not account for the conditional dependence between the variables (Aas and Berg, 2009). Vine copula constructs the multidimensional copula without assuming conditional independence (Aas et al., 2009).

Communities and infrastructure systems in Canada's coastal areas, across the Atlantic, Pacific, and the Great Lakes, are at risk of flooding caused by extreme precipitation, river overflows, storm surges, and tides (Bush and Lemmen, 2019a). Some examples include Hurricane Juan which hit eastern Canada and Nova Scotia resulting in an economic loss of $200 million in September 2003, Hurricane Dorian in eastern Canada (September 2019) with $78.9 million in damage, and Hurricane Teddy affecting Nova Scotia in September 2020. Most previous analyses have been focused on the bivariate structure of compound flooding events (e.g., sea level and streamflow or sea level and precipitation). In this study, we analyze multiple drivers of flooding (sea level, precipitation, and streamflow) their interdependencies, and the corresponding joint and conditional return periods across Canada's coasts, for the first time, based on vine copulas. Instead of relying on a limited number of Archimedean (asymmetric) or elliptical (symmetric) copula functions (Beersma and Buishand, 2004; Rana et al., 2017; Shiau, 2006), we consider a comprehensive set of copulas to better represent the extreme dependencies. Bayes theorem is applied to estimate the parameters of the marginal distributions and the copula functions and characterize the uncertainties associated with different hazard scenarios, including AND, OR, and Kendall (dos Santos Silva and Lopes, 2008; Min and Czado, 2011; Pitt et al., 2006; Sarhadi et al., 2016; Smith, 2011). Further, we assess the return levels of flow discharge rates conditioned on precipitation and downstream seawater levels and compare them with the unconditional scenario. We also estimate the Failure Probabilities (FPs), i.e., the possibility of a flood event occurring at least once in a given project's lifetime (Xu et al., 2019), corresponding to different hazard scenarios. Besides, for the first time, we provide the trivariate Kendall RP/FP analysis through a

sampling technique. Finally, we suggest the optimum design levels of the three drivers considering the corresponding interdependencies.

The remainder of this paper is as follows. Section 2 describes the study area and data. The copula and Bayes approaches are presented in Section 3 followed by the discussion of results in Section 4 and the concluding remarks in Section 5.

3.2. Study area and data

Canada has the longest coastline (approximately 230,000 km) worldwide settling over seven million people. We assess compound flooding across its three main domains of the Pacific, Atlantic, and the Great Lakes coasts (Figure 3.1) by investigating the interactions between Precipitation (Pr; daily time scale), Streamflow (Q; daily), and Total Water Level at the coastal zones (TWL; hourly). The corresponding data at each location are selected for 1960 to 2015 according to the following criteria: each year having more than 20 percent missing data is removed for each tidal gauge, followed by removing gauges with more than 20 percent missing data over the entire period. Precipitation and streamflow gauges that lie within a radius of 0.5° (almost 55 km) from each tidal gauge are identified followed by the application of the first two selection steps. In addition to the physical distance of streamflow gauges, flow routes are tracked to make sure they are directed towards the oceans/lakes (Ward et al., 2018). At all locations, extreme sea levels are represented by the maximum hourly TWL at each 24-hour interval.
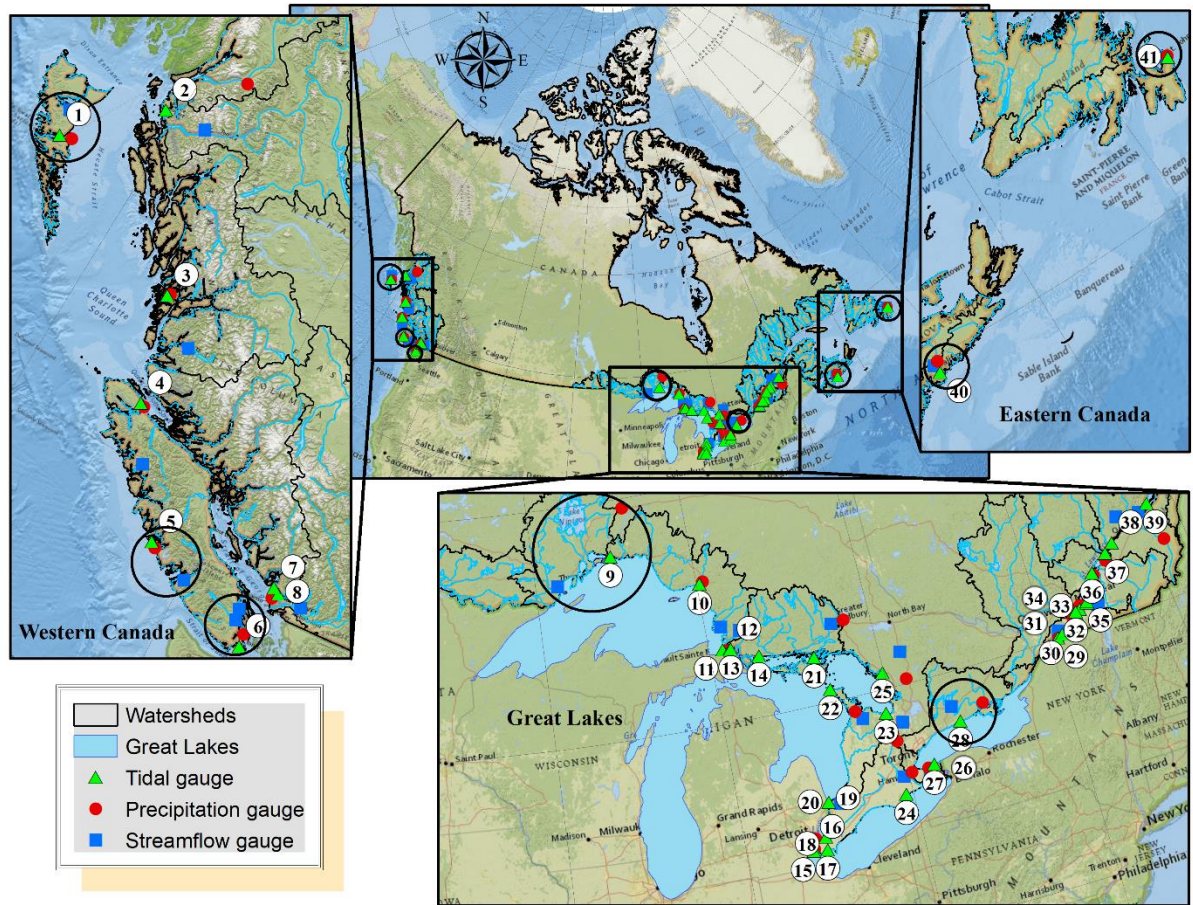
Figure 3.1) The study area and the locations of precipitation, streamflow, and tidal gauges across the Atlantic, Pacific, and the Great Lakes coasts. Circles show examples of three gauges that are grouped together for multivariate analysis.

In cases where several precipitation or streamflow gauges exist within the specified radius, the closest and most downstream ones are selected, respectively. If no hydroclimatic gauges exist within this distance, the radius is increased to a maximum of 100 km to identify at least one precipitation and one streamflow gauge (Wu et al., 2018). The choice of distance is to ensure that gauge data are representative of the homogeneous hydroclimatic conditions of their locations (Ward et al., 2018). 41 locations having more than 80 percent overlap between TWL, precipitation, and streamflow data records are retained.

3.3. Methodology

The simultaneous occurrence of multiple drivers of flooding, including extreme Pr, TWL, and/or Q, is relatively rare however the corresponding impacts can be catastrophic (Fang et al., 2020; Wahl et al., 2015). Such disasters can be associated with hurricanes striking coastal areas, especially in small, impervious, round-shape watersheds with a rapid hydrologic response. Besides, coastal flooding due to extreme waves and storm surges superimposed on high tides can be exacerbated by moderate or even low rainfall events. Furthermore, above-normal sea levels can block the river system drainage, which combined with high precipitation rates can lead to severe flood impacts in coastal zones. Similarly, simultaneous extreme discharge rates and low/moderate Pr and TWLs can lead to compound flood events threatening coastal communities and infrastructure.

In this study, we analyze compound flooding caused by extreme precipitation events and maximum TWL and Q within ± 1 day of the corresponding event. Extreme events are commonly identified based on the annual maxima of the data records or exceedances above high thresholds (Bezak et al., 2014; Dodangeh et al., 2019; Villarini et al., 2011). We consider the Peaks Over Threshold (POT) approach such that the ($Pr_e\_0.95$, TWL1, Q1) scenario represents the joint occurrence of extreme precipitation events exceeding the 95th percentile, and TWL1/Q1 which represents the maximum total water levels and flow discharge rates within a 1-day window of precipitation extreme events, respectively. To remove temporal dependencies in extreme precipitation events, only the peaks of 3-day intervals are retained.

The overall procedure for compound flood analysis is summarized in a flowchart (Figure 3.2) and illustrated in the following sections.
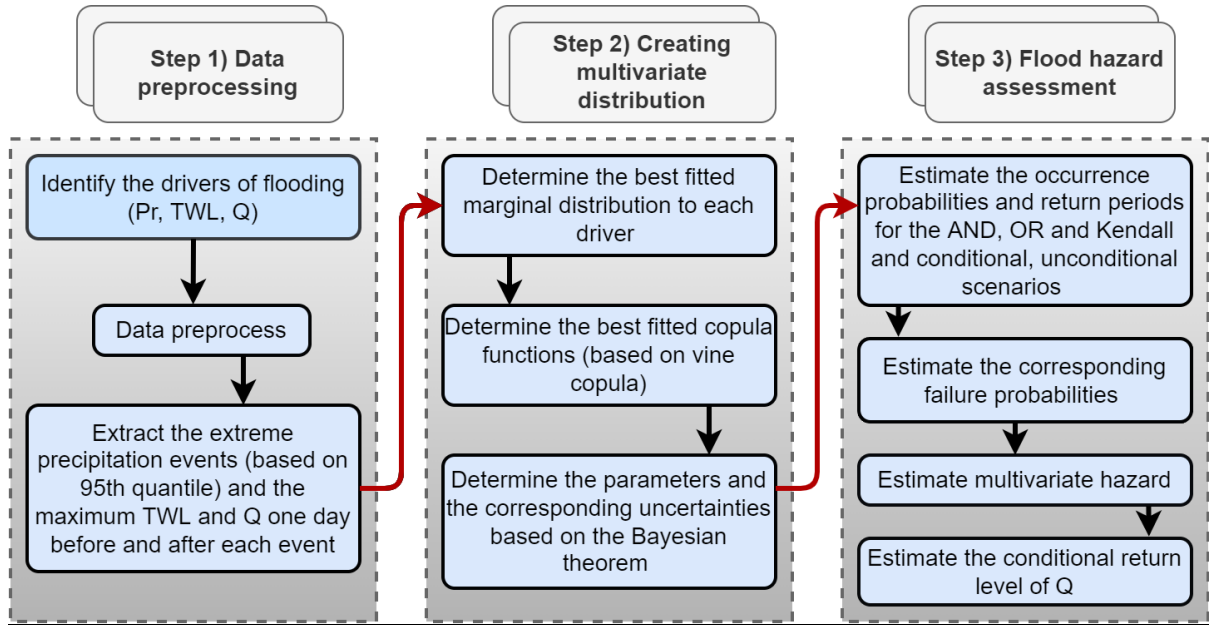
Figure 3.2) Statistical analysis of compound flooding; Pr, TWL, and Q denote precipitation, total water level, and streamflow, respectively.

3.3.1. Copula

The joint variability of the three drivers of flooding across Canada's coasts is characterized based on copula (Joe, 1997; Nelson, 1998). Copula functions (Sklar, 1959) can represent the multivariate behavior of random variables and characterize the corresponding dependence structure (linear, non-linear, tail dependence) (Genest and Favre, 2007). According to Sklar's theorem, if $X_1 \, X_2 \, ….. \, X_n$ are n continuous random variables, there exists a unique copula C on $(0,1)^d$ that can describe the corresponding joint Cumulative Distribution Function (CDF) (Liu et al., 2018):

$$F(X_1, \ldots, X_n) = C(F_1(X_1|\theta_1), F_2(X_2|\theta_2), \ldots, F_n(X_n|\theta_n)|\theta_c), \tag{3.1}$$

where d is the dimension, $F(X_1,…, X_n)$ is the joint CDF of $X_1, X_2 ….. X_n$, C is the copula function with the dependence parameter θ_c, $F_1(X_1|\theta_1), F_2(X_2|\theta_2) … F_n(X_n|\theta_n)$ are the marginal distributions with parameters θ_1 to θ_n, respectively. The practical implication of Sklar's theorem is that modeling the marginal distributions can be

54

conveniently separated from the dependence modeling using copula (Brechmann and Schepsmeier, 2013). The corresponding joint probability density function is(Liu et al., 2018):

$$f(X_1, \ldots, X_n) = (\prod_{i=1}^{n} f_i(X_i)) \times c(F_1(X_1|\theta_1), F_2(X_2|\theta_2), \ldots, F_n(X_n|\theta_n)|\theta_c), \qquad (3.2)$$

where c is the copula density function.

Initial analysis of the dependencies is performed using the nonparametric Kendall's Tau correlation metric, which measures the degree of association between two variables considering a significance level of 0.05:

$$\tau = \sqrt{\frac{9n(n-1)}{2(2n+5)}} |\tau_n|, \qquad (3.3)$$

τ is the test statistic, which follows the standard normal distribution, τ_n is the Kendall correlation, and the p-value is $2p(Z > \tau)$.

3.3.2. Vine Copula

We consider the vine copula, introduced by Joe et al. (1996) and further developed by Bedford and Cooke (2001, 2002), for the multivariate analysis of compound flooding. Vine copula can determine the different dependence structures between multiple variables and is not bound by parameter restrictions when the number of variables increases (Aas and Berg, 2009; Jane et al., 2020; Liu et al., 2018).

Vine copula creates $n - dimensional$ multivariate distributions using a cascade of n(n-1)/2 bivariate or conditional bivariate copulas that are independent of each other. The so-called pair-copulas are flexible in characterizing the dependence structure of multiple variables including the tail dependencies and asymmetries. Bedford and Cooke (2001, 2002) proposed a systemized procedure called regular vine, with two special subclasses of the canonical (C-vine) and drawable vines (D-vine), to decompose a multivariate probability in the form of a nested set of trees. Based on C-vine, in each tree, all the

pairwise dependencies with respect to a root node are modeled. In other words, all mutual dependencies are for the same variable in each tree (from the first to the last tree) (Figure S3.1-a). Based on D-vine, all mutual dependencies in each tree are determined in sequence (Figure S3.1-b). Figure 3 shows a four-dimensional structure of both models consisting of 3 trees with T$_j$, j= 1, 2, 3, and 5-j and 4-j nodes and edges in each tree, respectively. And each edge is related to a pair-copula. The edges of tree j become nodes for the next tree (j+1) and this continues until the last tree. In the 3-D case, there is no difference between C- or D-vine approaches except for the ordering of variables (Gräler et al., 2013).

Considering the three drivers of TWL, Pr, and Q, first, the pair-copulas (TWL, Pr) and (Pr, Q) are created at tree 1 and then the conditional copula (TWL, Q| Pr) is determined at tree 2, according to C-vine (Figure 3.3).
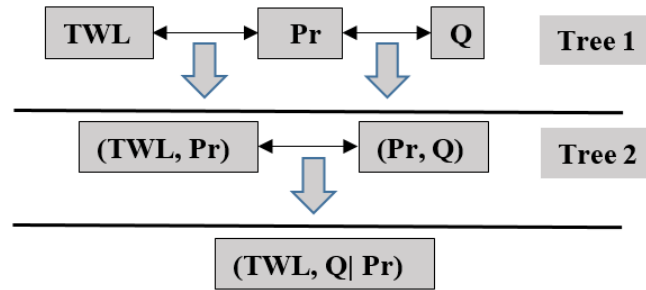
Figure 3.3) Three-dimensional C-vine copula considering three drivers of flooding (TWL, Pr, and Q).

The n-dimensional density function of the C-vine copula is expressed as follows (Brechmann and Schepsmeier, 2013; Czado, 2010):

$$f(X_1,\ldots,X_n) = \prod_{k=1}^{n} f_k(X_k) \times$$

$$\prod_{i=1}^{n-1} \prod_{j=1}^{n-i} c_{i,i+j|1:(i-1)}(F(X_i|X_1,\ldots,X_{i-1}), F(X_{i+j}|X_1,\ldots,X_{i-1})), \tag{3.4}$$

where $f(X_1,\ldots,X_n)$ is the joint probability density function of n random variables, $f(X_k)$, $k = 1,\ldots,n$, denotes the marginal probability densities, and $c_{i,i+j|1:(i-1)}$ represents the

bivariate copula densities with parameter(s) $\theta_{i,i+j|1:(i-1)}$. According to Equation 4, the three-dimensional probability density of the C-vine copula model is expressed as:

$$
\begin{aligned}
f(Pr, TWL, Q) = f(Pr) \times f(TWL) \times f(Q) \qquad &\text{(marginals)} \\
\times\, c_{Pr,TWL}(F(Pr), F(TWL)|\theta_{c(pr,twl)}) \times c_{Pr,Q}(F(Pr), F(Q)|\theta_{c(pr,q)}) \qquad &\text{(unconditional pairs)} \\
\times\, c_{TWL,Q|Pr}(F(TWL|Pr), F(Q|Pr)|\theta_{c(twl,q)}) \qquad &\text{(conditional pair)}
\end{aligned}
$$

,   (3.5)

where $f(Pr, TWL, Q)$ is the joint probability density of Pr, TWL, and Q; $f(Pr), f(TWL), f(Q)$ are the corresponding marginal distributions; $c_{Pr,TWL}$, $c_{Pr,Q}$ and $c_{TWL,Q|Pr}$ are the copula functions that characterize the dependencies between *Pr* and *TWL*, *Pr* and *Q*, and *TWL* and *Q* conditioned on *Pr*, respectively. $\theta_{c(pr,twl)}$, $\theta_{c(pr,q)}$ and $\theta_{c(twl,q)}$ are the corresponding copula parameters associated with (Pr, TWL), (Pr, Q), and (TWL, Q), respectively. The parameters of the marginal distributions θ_m are estimated using the maximum likelihood method. The best-fitted distributions of Q and TWL are selected among Normal, Lognormal, Gamma, Gumbel, Exponential, Generalized Extreme Value (GEV), Generalized Pareto Distribution (GPD), Weibull, Logistic, and Cauchy distributions (Table S2.2) based on the Akaike Information Criterion (AIC) (Akaike, 1974). AIC is defined as:

$$
AIC = 2k - 2\ln(L), \qquad (3.6)
$$

where k is the number of parameters and L represents the maximum value of the likelihood function for the model. The Kolmogorov-Smirnov (KS) goodness-of-fit test is also applied to verify the best-fitted distribution considering a significance level of 0.05 (Chakravarty et al., 1967). Extreme precipitation events are represented by the Generalized Pareto Distribution (GPD) with parameters $\theta_m = (\mu, \sigma, \xi)$.

The (un)conditional one- or two-parameter (θ_c) copulas (Schepsmeier et al., 2015) are selected from 41 functions including Gaussian, Student t, Frank, Joe, Clayton, Gumbel, BB1, BB6, BB7, BB8, Tawn type 1, and Tawn type 2 along with their rotational variants (90, 180, and 360 degrees) (Table S2.3). The best-fitted copula function is selected based on AIC. Besides, a goodness-of-fit test proposed by Genest et al. (2006) is applied to

evaluate the selected model, considering that AIC would select one model with the best relative score even if all models are "wrong" (Burnham et al., 2010; Singh et al., 2020). Genest et al. (2006) introduced two variants (S_n, T_n) of the Cramér–von Mises statistic, building on the previous studies by Genest Sand Rivest (1993) and Wang and Wells (2000):

$$S_n = \int_0^1 |(K_n(w)|^2 k_{\theta_n}(w) dw, \tag{3.7}$$

$$T_n = \sup_{0 \le w \le 1} |K_n(w)|, \tag{3.8}$$

where $\mathbb{K}_n(w) = \sqrt{n}\{K_n(w) - K_{\theta_n}(w)\}$. K_n is the empirical cumulative distribution of the data and K_{θ_n} refers to the theoretical cumulative distribution of samples taken from the fitted copula and k_{θ_n} is the corresponding density. Unlike the previous method of Genest Sand Rivest (1993) and Wang and Wells (2000) which can just be used for Archimedean copulas, the S_n and T_n statistics are not limited to any type of copula. Besides, Genest et al. (2006) discuss that comparing raw values of S_n and T_n could be just as misleading as Cramér–von Mises statistic in model selection in some cases. Therefore, they proposed a bootstrap method to calculate the p-values of S_n and T_n statistics under the null hypothesis H0 : $C_\theta \in \mathcal{C}_\theta$ here C_θ is the underlying empirical copula and $\mathcal{C}_\theta$ is the selected parametric family of the copula. A large number of independent samples ($N = 1000$) of size n are generated from, $\mathcal{C}_\theta$ and the corresponding values of S_n^* and T_n^* are computed to obtain the distribution of the statistics. The p-value are obtained as follows: For T_n, the p-value is computed in a similar way

$$P - value = \frac{1}{N} \sum_{k=1}^{N} 1(S_{n,k}^* > S_n), \tag{3.9}$$

S_n is the statistic value for the original data and $S_{n,k}^*$ is the statistic value for the kth bootstrap sample.

The parameters of the marginal distributions and the copula functions, corresponding to (Pr, TWL), (Pr, Q), and (Q, TWL|Pr), is inferred based on the Bayesian approach, and the uncertainties in return periods (RPs) and return levels are quantified. Considering n

bivariate observations of $(twl_1, q_1),..., (twl_n, q_n)$ representing the driving mechanisms, the joint posterior distribution of the parameters is estimated by (Smith, 2011):

$$p(\theta_c, \theta_m | (twl_1, q_1), (twl_2, q_2), \ldots, (twl_n, q_n)) \propto$$
$$p(\theta_m) \cdot p(\theta_c) \cdot \prod_{i=1}^{n} c(twl, q_i | \theta_c) \cdot f(twl_i | \theta_m) \cdot f(q_i | \theta_m), \qquad (3.10)$$

where $f(\theta_c, \theta_m | (twl_1, q_1), (twl_2, q_2), \ldots, (twl_n, q_n))$ is the joint posterior density function of the copula and marginal parameters (i.e. θ_c, θ_m), $TWL(twl_1, twl_2, \ldots, twl_n)$ and $Q(q_1, q_2, \ldots, q_n)$ are data records, $p(\theta_m)$ and $p(\theta_c)$ are the (uninformative) prior distributions of θ_c, θ_m, respectively, $c(twl_i, q_i | \theta_c)$ is the copula density function of twl and q, $f(twl_i)$, and $f(q_i)$ are the marginal densities of twl and q, respectively.

The parameters are estimated through Markov Chain Monte Carlo (MCMC) sampling based on the Metropolis-Hastings approach (Hastings, 1970), considering a chain size of 10000 iterations and a burn-in period of 1000. The convergence diagnosis is based on Geweke (1991) in which the mean of the first 10% of the chain is compared against the mean of the second half of the chain, which is assumed to have a stationary distribution t. If the chain converges, the two means are equal and Geweke's statistic has an asymptotically standard normal distribution (the test statistic falls between -1.96 to 1.96 of the Z distribution).

3.4. Hazard analysis

3.4.1. Estimating the Joint Return Period (JRP)

Assessing the hazard associated with individual and compound flood events is critical for water resources planning and management. We estimate the JRPs of multiple flood drivers considering OR (at least one driver exceeds a threshold), AND (all drivers are above specific thresholds), and Kendall (the joint probabilities exceed defined thresholds) scenarios (Salvadori and De Michele, 2004; Salvadori et al., 2007; Shiau, 2006). Considering *pr*, *q*, and *twl* as levels beyond which pluvial, fluvial, or coastal flooding can

occur, respectively, the exceedance probability and the corresponding return period of the OR scenario are estimated by:

$$P_{OR} = P\big((Pr > pr) \cup (Q > q) \cup (TWL > twl)\big) = 1 -$$
$$C(F_{Pr}(pr|\theta_{mp}), F_Q(q|\theta_{mq}), F_{TWL}(twl|\theta_{mtwl})|\theta_c), \tag{3.11}$$

$$JRP_{OR} = \frac{\mu}{P_{OR}}, \tag{3.12}$$

where P_{OR} is the probability that at least one of the drivers exceeds the specified threshold (either pr, q, or twl). θ_{mpr}, θ_{mq} and θ_{mtwl} are the set of parameters corresponding to the marginal distributions of Pr, Q, and TWL, respectively. C is the joint cumulative probability of the three drivers of flooding obtained by integrating Equation (5). θ_c is the set of parameters corresponding to the pair-copulas $C_{Pr,TWL}(F(Pr), F(TWL))$, $C_{Pr,Q}(F(Pr), F(Q))$, or $C_{TWL,Q|Pr}(F(TWL|Pr), F(Q|Pr))$, and μ is the average interarrival time between the flood events (in an annual time scale), which is obtained through summing the sequential time intervals between the events divided by 365*(n-1) and n is the number of events.

The worst-case scenario constitutes the simultaneous occurrence of multiple extreme events (i.e. joint occurrence of heavy precipitation, high river flows, and high water levels) that can lead to more severe hazard conditions. This joint probability (AND) and the corresponding JRP are obtained by:

$$P_{AND} = P\big((Pr > pr) \cap (Q > q) \cap (TWL > twl)\big) = 1 - F_{Pr}(pr|\theta_{mp}) - F_Q(q|\theta_{mq}) - F_{TWL}(twl|\theta_{mtwl})$$

$$+ C_{Pr,TWL}\big(F(Pr), F(TWL)|\theta_{c(pr,twl)}\big) + C_{Pr,Q}\big(F(Pr), F(Q)|\theta_{c(pr,q)}\big) +$$
$$C_{TWL,Q|Pr}\big(F(TWL|Pr), F(Q|Pr)|\theta_{c(twl,q)}\big) - C(F_{Pr}(pr|\theta_{mp}), F_Q(q|\theta_{mq}), F_{TWL}(twl|\theta_{mtwl})|\theta_c), \tag{3.13}$$

$$JRP_{AND} = \frac{\mu}{P_{AND}}, \tag{3.14}$$

where P_{AND} is the AND probability of the three drivers exceeding their corresponding thresholds (pr, q, or twl). $F_{Pr}(pr|\theta_{mp})$, $F_Q(q|\theta_{mq})$, and $F_{TWL}(twl|\theta_{mtwl})$ are the marginal probabilities of Pr, Q, and TWL given their set of parameters θ_{mpr}, θ_{mq},

and θ_{mtwl},

respectively. $C_{Pr,TWL}(F(Pr), F(TWL)|\theta_{c(pr,twl)})$, $C_{Pr,Q}(F(Pr), F(Q)|\theta_{c(f,q)})$, and $C_{TWL,Q|Pr}(F(TWL|Pr), F(Q|Pr)|\theta_{c(twl,q)})$ are the bivariate unconditional or conditional copula functions given the corresponding set of parameters θ_c. In this study, the JRPs of both scenarios (AND, OR) are estimated at all locations considering an exceedance probability of 0.01 and compared with the ones associated with the traditional approach (i.e. assuming independence between the drivers of flooding) and with the univariate RP of the individual drivers.

Previous studies (e.g. Salvadori et al. (2011, 2016) and Xu et al. (2019)) suggest that the OR and AND scenarios might not identify all the dangerous regions in the probability space that can result in under- or over-estimations of the engineering designs. Salvadori and De Michele, (2010) proposed Kendall's approach, which is based on the Kendall distribution function. However, the Kendall scenario does not have a direct physical/structural interpretation and can be used for preliminary hazard assessments (Salvadori et al., 2016). Accordingly, the probability space is divided into three zones, a critical probability layer p (a line in the 2D and a surface in the 3D probability space), a dangerous region denoted as S_p^d (d denotes dangerous region) that includes all the events with the joint probabilities more than p, a safe region denoted as S_p^s (s denotes safe region) including the events with joint probabilities less than p (Salvadori et al., 2016). The JRP of the dangerous region is defined as

$$JRP_{Kendall} = \frac{\mu}{P[C(F_{Pr}(pr|\theta_{mp}), F_Q(q|\theta_{mq}), F_{TWL}(twl|\theta_{mtwl})|\theta_c) > p]} = \frac{\mu}{1 - K_c(p)}, \quad (3.15)$$

where $K_c(p) = P[C(F_{Pr}(pr|\theta_{mp}), F_Q(q|\theta_{mq}), F_{TWL}(twl|\theta_{mtwl})|\theta_c) \le p]$. Estimation of $K_c(p)$ for trivariate analysis of compound flood drivers can be complex. In this study, we resample Pr, Q, and TWL n times using the generated joint probability distribution and assess the corresponding joint probabilities. And the critical layer is obtained considering the 0.01 exceedances for marginals. And the number of events out of n with

probabilities lower than the critical layer is divided by the sample size (n) to derive $K_c(p)$.

3.4.2. Compound Hazard Ratio (CHR)

Ganguli et al. (2019) proposed the CHR index to characterize the interactions between different drivers and their effects on the return level estimates of compound events. This index is the ratio between the conditional T-year flow discharge rate considering the annual maximum TWL as the covariate and the unconditional T-year discharge. In other words, the index is calculated by dividing the return level of streamflow conditional on annual max TWL by its univariate (unconditional) return level. We extend this index for trivariate analysis of compound flooding and estimate the ratio of conditional and unconditional streamflow. The probability of T-year Q given Pr and TWL, denoted as Q'_T, is obtained according to Gonzalez-Lopez et al. (2019):

$$P(Q \leq q | Pr \leq pr, TWL \leq twl) = \frac{P(Q \leq q, Pr \leq pr, TWL \leq twl)}{P(Pr \leq pr, TWL \leq twl)} = \frac{C(F_Q(q|\theta_{mq}), F_{Pr}(pr|\theta_{mpr}), F_{TWL}(twl|\theta_{mtwl})|\theta_c)}{C(F_{Pr}(pr|\theta_{mq}), F_{TWL}(twl|\theta_{mtwl})|\theta_c)},$$

(3.16)

The CHR index is (Ganguli et al., 2019):

$$CHR = \frac{Q'_T}{Q_T} = \frac{C^{-1}_{Q|(Pr=pr, TWL=twl)} \left[1 - \frac{\mu}{T_{Q|(Pr,TWL)}(q|pr,twl)} \right]}{F_Q^{-1} \left[1 - \frac{\mu}{T_Q(q)} \right]},$$

(3.17)

Q'_T and Q_T are the conditional and unconditional return levels of Q. In this study, the levels of p for the three drivers correspond to a return period of 100 years. $C^{-1}_{Q|(Pr=pr, TWL=twl)}$ and F_Q^{-1} are the inverse quantile transformations of copula-based and marginal distributions, respectively. $T_Q(q)$ is the T-year unconditional RP of streamflow $T_Q(q) = \frac{\mu}{1 - F_Q(q|\theta_{mq})}$, and the conditional RP of streamflow $T_{Q|(Pr,TWL)}(q|pr, twl)$ is calculated as:

$$T_{Q|(Pr,TWL)}(q|pr,twl) = \frac{\mu}{1- P(Q \leq q|Pr \leq pr, TWL \leq twl)}, \tag{3.18}$$

3.4.3. Failure Probability

The hydrologic risk is assessed based on the Failure Probability (FP), which refers to the probability of a flood event that occurs at least once during a given project lifetime (Xu et al., 2019). The failure probability is obtained from:

$$FP = 1 - \prod_{i=1}^{N} F(Pr_i, Q_i, TWL_i), \tag{3.19}$$

F represents the non-exceedance probability and N is the number of events during the project lifetime (D) which is inversely related to the average interarrival time between the events (μ):

$$N = \frac{D}{\mu}, \tag{3.20}$$

In this study, we assess Failure Probabilities corresponding to the AND, OR, Kendall, independence, and univariate scenarios for return periods of 100 and 10 years and lifetimes ranging from 1 to 50 years. Further, the trivariate hydrologic risk for each driver considering the 100-year RP of the other two drivers was quantified.

According to Equation 19, in the OR scenario:

$$FP_{OR} = 1 - \prod_{i=1}^{N} C(F_{Pr_i}(pr|\theta_{mp}), F_{Q_i}(q|\theta_{mq}), F_{TWL_i}(twl|\theta_{mtwl})|\theta_c), \tag{3.21}$$

In the AND scenario:

$$FP_{AND} = 1 - \prod_{i=1}^{N}(F_{Pr_i}(pr|\theta_{mp}) + F_{Q_i}(q|\theta_{mq}) + F_{TWL_i}(twl|\theta_{mtwl})$$

$$+ C_{Pr,TWL}(F(Pr), F(TWL)|\theta_{c(pr,twl)}) - C_{Pr,Q}(F(Pr), F(Q)|\theta_{c(pr,q)}) -$$
$$C_{TWL,Q|Pr}(F(TWL|Pr), F(Q|Pr)|\theta_{c(twl,q)})$$

$$+C(F_{Pr}(pr|\theta_{mpr}), F_Q(q|\theta_{mq}), F_{TWL}(twl|\theta_{mtwl})|\theta_c)), \qquad (3.22)$$

And, in the Kendall scenario:

$$FP_{Kendall} = 1 - \prod_{i=1}^{N} K_c^i(p), \qquad (3.23)$$

3.5. Results and discussion

3.5.1. Marginal distributions and pair-copula functions

The best-fitted distribution representing each driver of flooding at each location is selected from ten parametric distributions based on the AIC criterion. Further, the KS goodness of fit test is applied to verify the selected distributions, which are shown in Table S3.1 along with the corresponding AIC and p-values. In most locations, the river discharge rates (Q) are represented by GPD and exponential distributions, and the total water levels (TWL) by GPD and Weibull distributions. As discussed in Section 3, extreme precipitation amounts follow GPD at all locations.

The pair-copulas, of the C-vine model, are selected from 41 copula functions based on AIC at each location. According to Equation 5, three pair-copulas (two unconditional and one conditional) are determined to assess the corresponding compound flood hazards (Table S3.2). The results show that overall, the majority of the joint variations follow the Frank copula function. The analyses of the bivariate dependencies based on Kendall's tau show that the dependencies between (Pr, TWL) are mostly positive and significant across all locations, especially the Atlantic and Pacific coasts. Pr and Q show positive dependencies in fewer locations compared with (Pr, TWL), especially in the Great Lakes and Pacific regions. Moreover, the joint (Q, TWL) event indicates positive dependencies over both coasts and mostly eastern GL. The number of locations out of 41 with significant dependencies for (Pr, TWL), (Pr, Q), (Q, TWL) is 31 (7 at the Pacific, 22 at the Great Lakes, and 2 at the Atlantic area), 32 (4 at Pacific coast, 27 at Great Lakes, and 1 at Atlantic coast), and 33 (7 at Pacific coast, 24 at Great Lakes and 2 at Atlantic coast),

respectively (Table S3.3, Figure 4). Besides, there are 13 locations mainly at the Pacific and GL area where the three joints show positive dependencies. However, more sites with positive dependencies are found in three regions regarding the bivariate events of (Pr, TWL) and (Q, TWL). The dependencies between Pr/TWL are stronger (from 0.4 at the Pacific to 0.02 at the GL) than Pr/Q and Q/TWL in the majority of the locations across the three domains (Figure S3.2). This can be partly associated with the occurrence of seiche events combined with intense rainfall in the coastal areas at the GL and the extratropical cyclones striking the coasts, especially the Atlantic. Besides, extreme flows depend on several basin characteristics. For example, steep basins with a quick hydrological response, high mean elevation, compacted soil, and impermeable bedrocks are found on the west coast (Eatom & Moore, 2010), which can lead to a higher compound flooding hazard associated with Q/TWL.
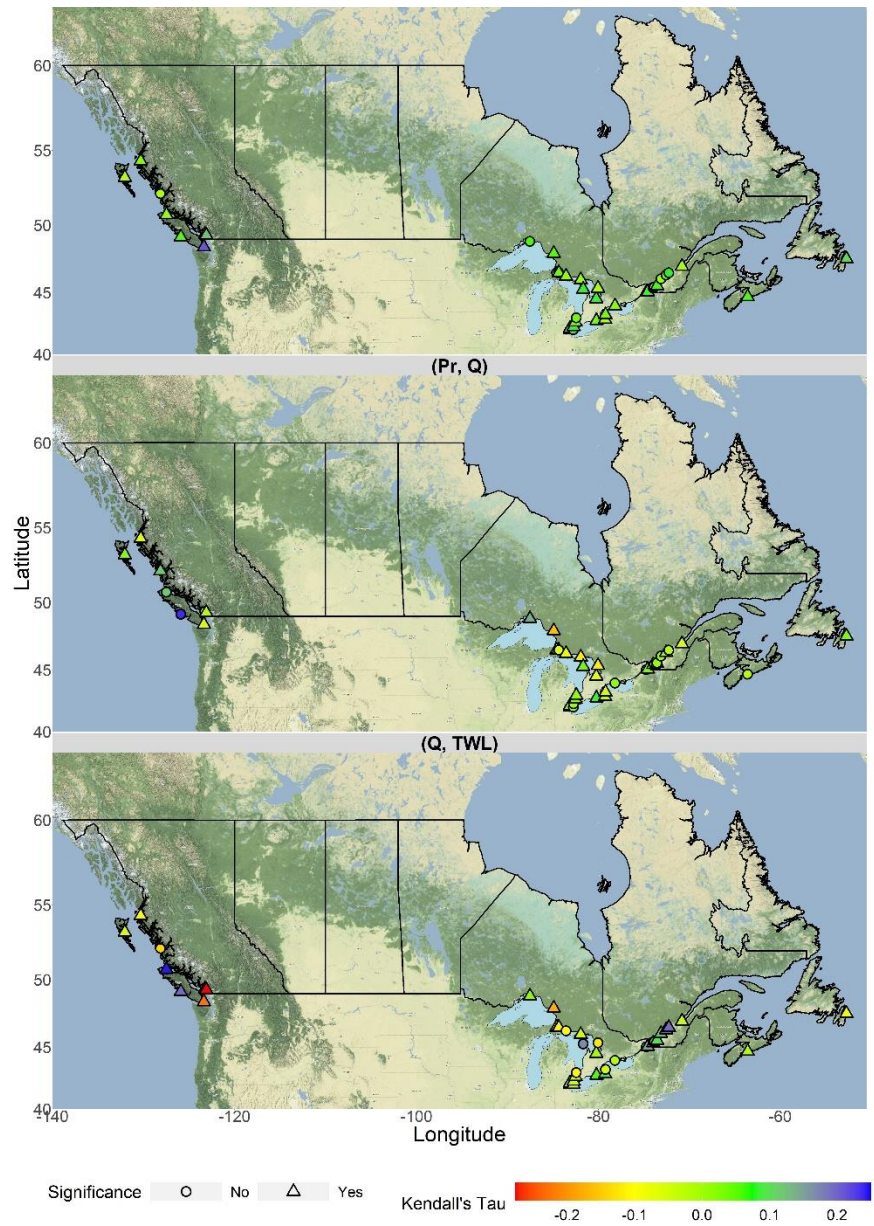
Figure 3.4) Kendall's Tau and its significance corresponding to (Pr, TWL), (Pr, Q), and (Q, TWL) at 41 locations across Canada.

3.5.2. Compound flood hazard analysis

3.5.2.1. Joint return periods of compound flood drivers

The trivariate JRPs corresponding to the AND, OR, and Kendall scenarios are determined based on the selected marginal distributions and pair-copula functions that form the multivariate joint distributions. Results are compared with the JRPs estimated assuming that the drivers are independent to investigate the extent of under- or over-estimations of the associated hazards. At each location, the trivariate joint distribution is developed considering both conditional and unconditional pair-copulas. In trivariate analysis, the estimated JRPs are affected by the interdependencies between (Pr, Q), (Q, TWL), and (Pr, TWL).

Figure 3.5 shows the estimated RPs of (Pr, Q, and TWL) for univariate, independent, and OR scenarios at 41 locations across Canada's coasts considering an exceedance probability of 0.01. The median OR-JRPs and the range of the uncertainties vary from 1.1 to 3.5 years and 0.08 to 17.5 years, respectively between all the locations. The independence OR-JRP varies from 2.8 to 3.2 years, and the univariate RPs range from 5.7 years on the Atlantic coast to 6.6 years on the Pacific coast. Overall, the estimated RPs corresponding to the univariate scenario is larger than those associated with the OR and independence scenarios. The independence and OR scenarios show larger differences at locations 24 to 29, in the Great Lakes region. The slight variations in independence and univariate cases at different locations are associated with changes in interarrival times due to different lengths of the time series. The lower bounds of the JPRs are lower than the ones based on the independence assumption, across all locations.

These differences highlight the importance of assessing multiple drivers of flooding and their interrelationships rather than studying each driver in isolation, to avoid underestimation/overestimation of the corresponding flood hazards, especially at the Great Lakes and the Atlantic coasts.
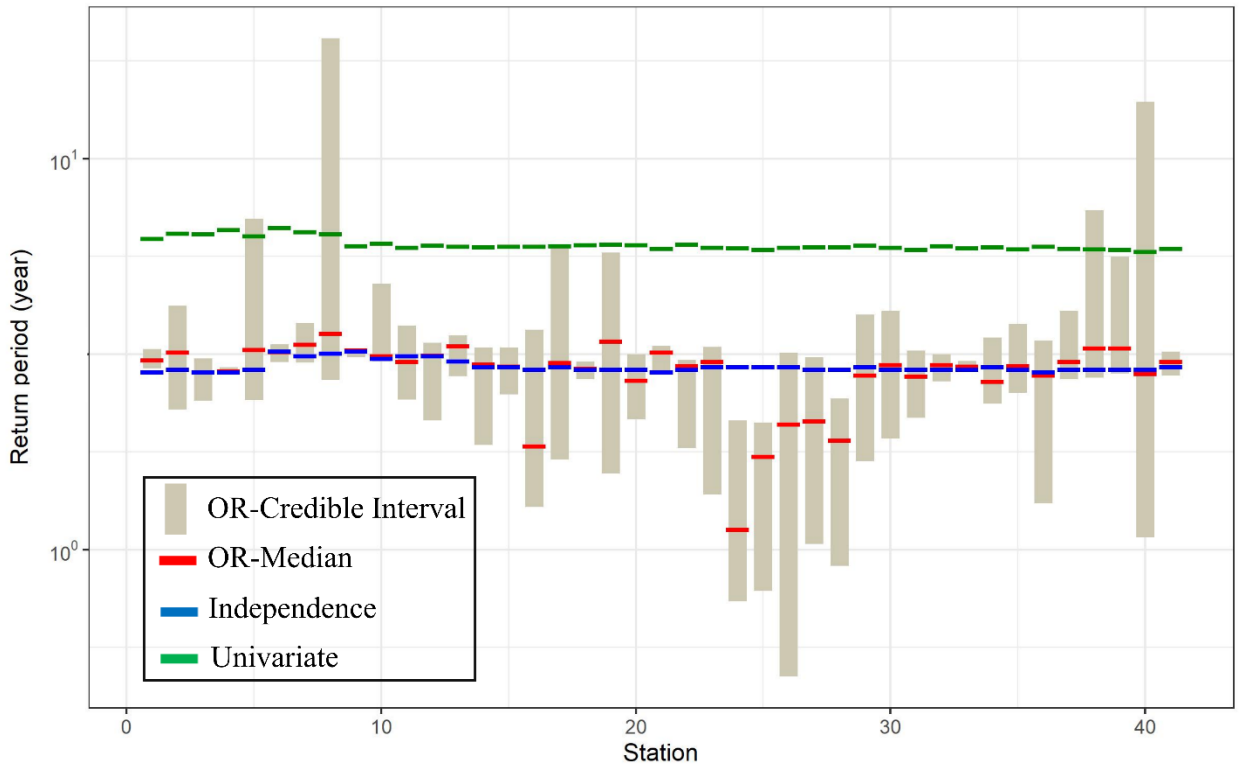
Figure 3.5) The estimated return periods of Pr, Q, and TWL based on univariate, independence, and OR scenarios at 41 locations across Canada's coasts.

The effects of positive interrelationships between the drivers on the AND-JRPs are shown in Figure 3.6. In assessing this scenario, we focus on the locations where at least two out of three dependencies between the drivers are positive because if the overall dependency between the flooding drivers is negative, then, there is a rare chance of their joint occurrences. The results are compared with univariate and independent scenarios at 21 locations. JRP increase by 2% to over 15% indicating possible overestimations of compound flood hazards associated with the three drivers, in the unrealistic independence scenario, when the dependencies are negative.

The median AND-JRPs vary from 16 to 202 years between different locations which in comparison with the independence scenario changing from 58297 to 63879 years are remarkably lower. The range of uncertainty varies from 13 (in the Great Lakes region) to 555 years (Pacific region). The large range of uncertainty for the AND scenario is partly associated with sensitivities to the dependencies between multiple variables and the

lengths of the data records. The lower quantiles in the AND-JRP are associated with higher dependencies between the drivers. The AND scenario also indicates that not considering the dependencies between the drivers can lead to underestimations of the flooding hazard (Figure 3.6).

It should also be mentioned that at locations 9, 12, 18 at the GL and 40 at the Atlantic area, the higher quantile JRP exceeds the independence JRP because the range of parameters for at least one pair-copula includes both negative and positive dependencies.
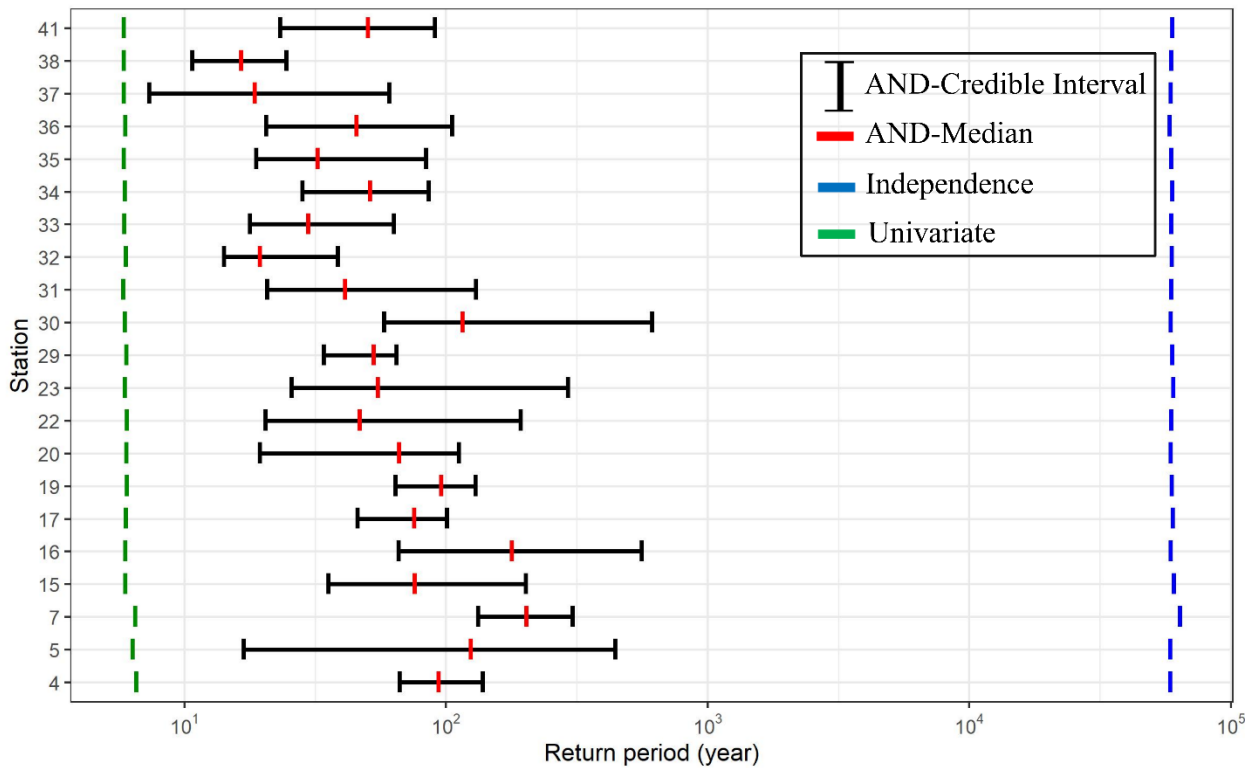
Figure 3.6) The estimated return periods of Pr, Q, and TWL based on univariate, independence, and AND scenarios at 21 locations across Canada's coasts.

The 100-year return period of Q under the independence condition is compared with its conditional RP considering the dependencies between the drivers. This RP is more than 100 years for 25 locations. Considering the median RP values, the maximum value is 140 years (related to higher dependency between the drivers) at location number 4 (Atlantic

region) and the lowest is 89 years (related to lower dependency between the drivers) at location 24 (GL) (Figure 3.7). The range of the uncertainty varies from 0.4 years to more than 54 years both at the Great Lakes. These results highlight that the univariate analyses, that do not consider the interrelationships between the drivers, can lead to either under- or over-estimations of the flood hazards undermining the sustainable, long-lasting, and cost-effective engineering designs in these areas. Moreover, these results would be useful for building regulations and guidelines, educating people to be prepared for these types of joint events, and emergency preparedness to protect lives, and reduce damages.
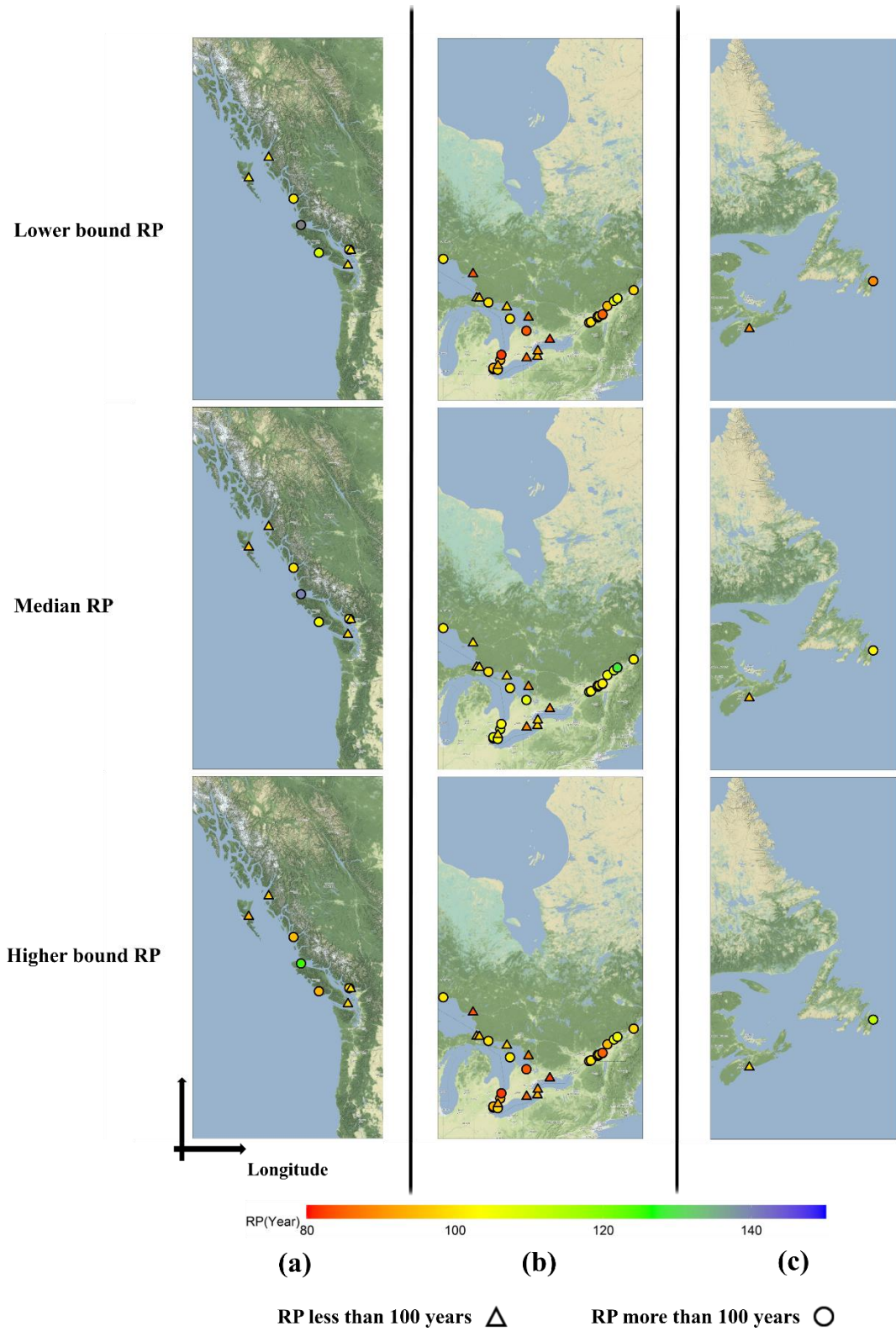
Figure 3.7) The return periods of Q and the corresponding uncertainties conditional on Pr and TWL for different locations across the three regions. a) the Pacific coast

b) the Great Lakes and c) the Atlantic coast. The points with RPs of more and less than 100 years are shown by circles and triangles, respectively.

The results of the Kendall JRP are shown in Figure 3.8, which fall between the OR and AND JRPs consistent with previous studies (e.g. Xu et al., (2019)). The same is almost true for both upper and lower bounds of JRPs. Overall, the estimated minimum and maximum values are 7 (at the Great Lakes) and 662 years (Atlantic region), respectively, and the uncertainties range from 9 to 502 years across all locations. The overall comparison of the three regions shows the JRPs for the Great Lakes are lower than those of the two coastal regions, and for the Atlantic region lower than the Pacific region. Similar to the AND scenario, with an increase in the strength of the positive dependency between the drivers, the JRP decreases and vice versa. For example, if the joint events of (TWL, Pr) and (Pr, Q) show moderate positive dependencies while the (TWL, Q) event has a high negative dependency at a location, the AND and Kendall JRPs may increase. This behavior is observed at some locations such as 4 and 5 (Pacific coast), 17, 20, 22, and 29 to 38 (Great Lakes), and 41 (at Atlantic coast).
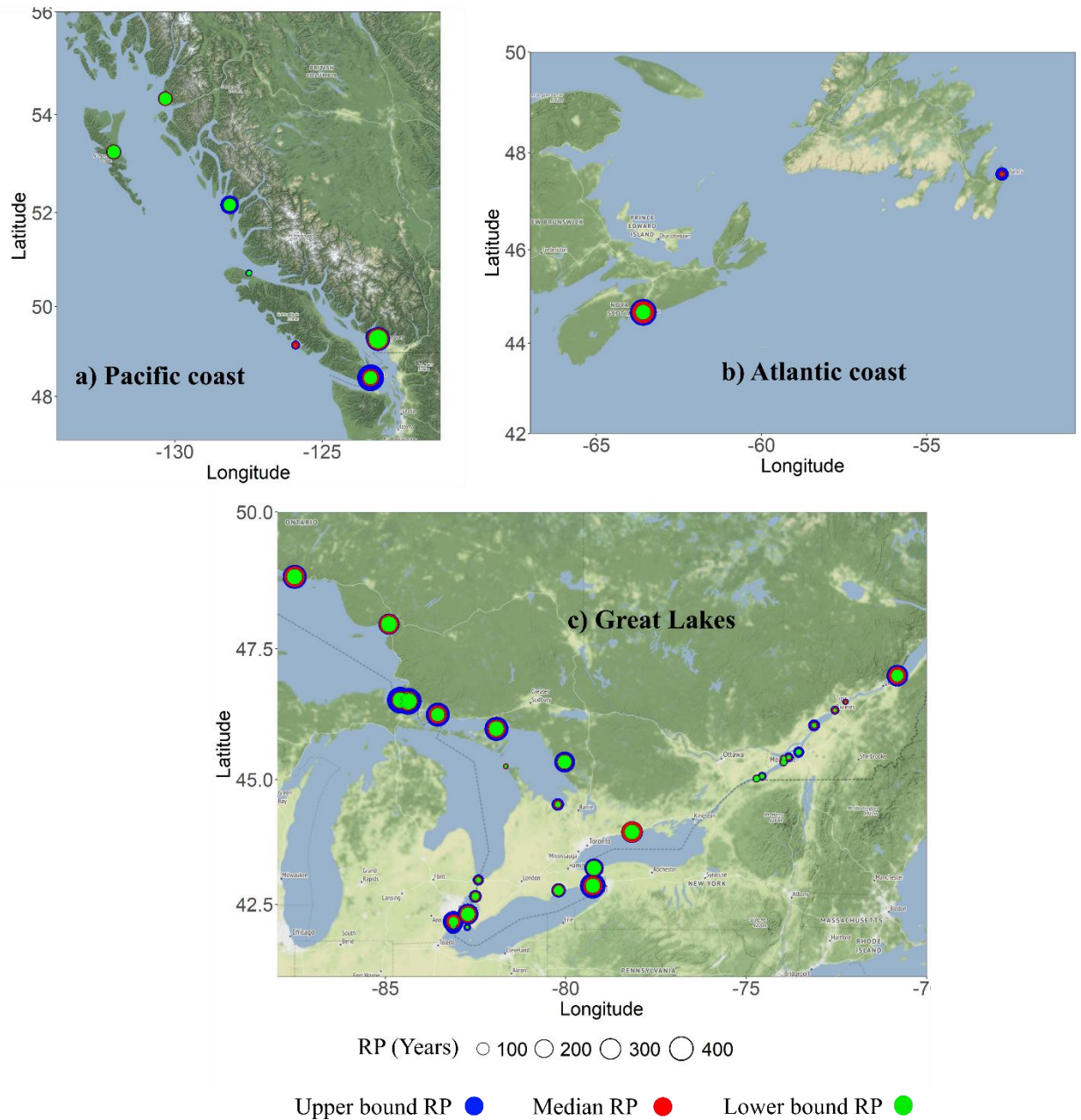
Figure 3.8) The estimated Kendall JRP and its uncertainty (lower and higher bounds of JRP) at different locations across three regions.

The results of the CHR index for 100-year streamflow events at 41 locations across Canada's coasts are shown in Figure 3.9. At 23 locations, the median index exceeds one which indicates that fluvial flood hazard is amplified by other mechanisms such as extreme sea levels in the study area. These sites are highlighted in Table S3.1.
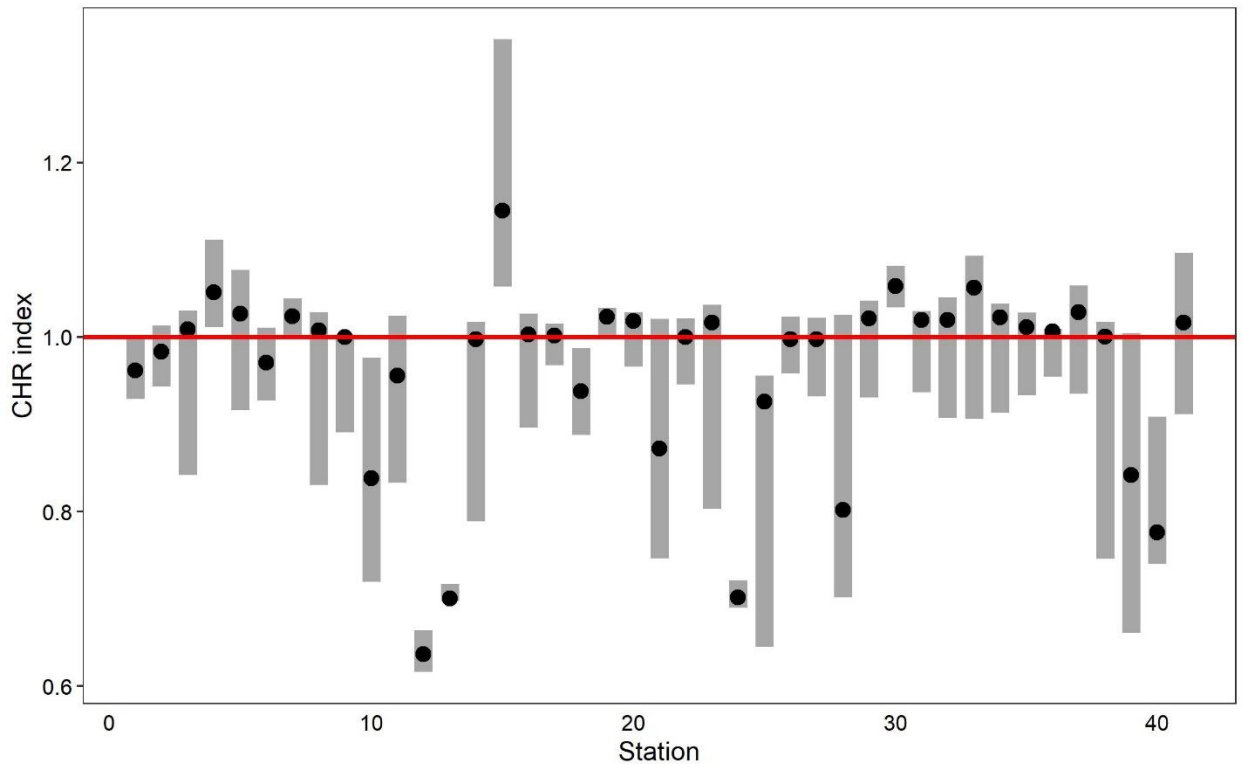
Figure 3.9) The CHR index and the related uncertainty estimated for Q|TWL, Pr at different locations.

3.5.3. Failure Probability

We estimate the FPs corresponding to 100 and 10-year events for different hazard scenarios including OR, AND, and Kendall, and characterize their uncertainties. These FPs are compared with the estimated FPs corresponding to the independent, univariate, and conditional scenarios. Analyses are conducted at all locations however, for the sake of brevity, we present the results for location 41 on the Atlantic coast. As expected, an increase in the JRP reduces the chances of the concurrent and univariate occurrence of multiple flood events and the corresponding FP values (Figure 3.10). These are true for three OR, AND, and Kendall scenarios, their lower quantile, and upper quantile FP

values as well. Considering both RPs, the univariate and conditional univariate FP is lower than the FP of the trivariate OR scenario. This highlights the importance of analyzing the combination of multiple flood hazards at a location to avoid underestimation of the corresponding hazards. This is also evident in the univariate analysis as the conditional scenario has higher FP than the univariate scenario. Besides, under the OR scenario, the FP can be overestimated based on the independence scenario, which is consistent with studies in other areas (Moftakhari et al. (2017) and Xu et al. (2019)). It should also be mentioned that under all scenarios, the FP rises with increases in the project lifetime.
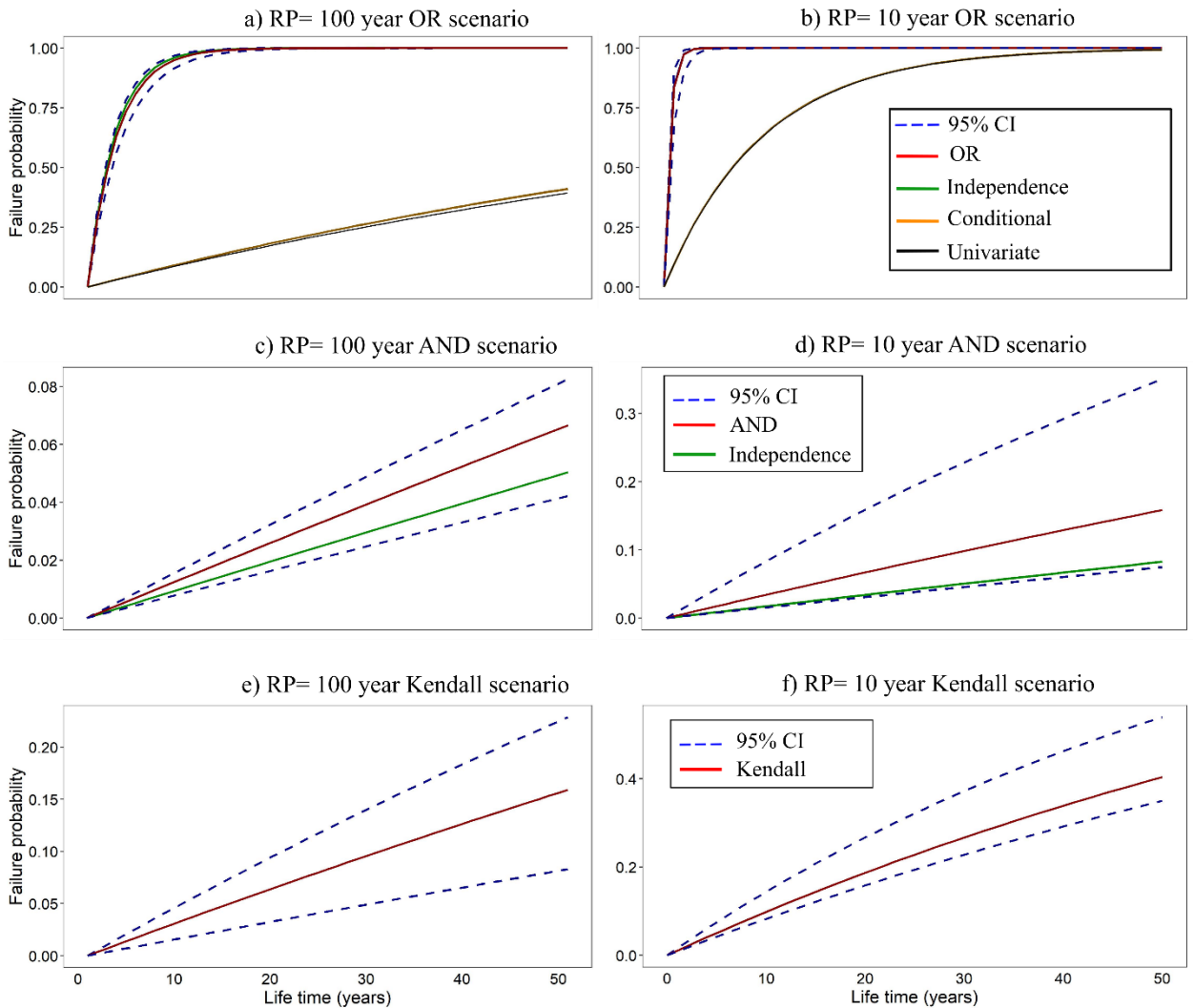
Figure 3.10) The failure probability (FP) values corresponding to a,b) OR, univariate and conditional, c,d) AND, e,f) Kendall scenarios for 10 and 100-year events.

The trivariate hydrologic risks (determined based on FPs) of different levels of each driver with a 100-year recurrence interval of the other two drivers are obtained for all the locations for project lifetimes of 100, 50, 20, and 5 years. Figure 3.11 compares different scenarios for location #41 on the Atlantic coast. Accordingly, considering the median FP, the trivariate hydrologic risk is constant as long as the design rainfall is less than 80, 100, 115, and 125 mm, respectively for service times of 5, 20, 50, and 100 years and then it decreases sharply, considering 100-year Q and TWL. These values are 18, 24, 28, and 31 m^3/s for design Q with 100-year Pr and TWL and 2.2, 2.4, 2.5, and 2.6 m for design TWL, with 100-year Q and Pr events. Considering the 100-year lifetime, the hydrologic risk approaches zero when the precipitation design level exceeds 170 mm and this avoids over-design leading to extra expenses. Therefore, the design rainfall in this location should be between 80 and 170 mm considering the security point of view. These design values should be between 20 to 50 m^3 for Q and between 2.2 and 2.7 m for TWL. These results are important for the robust management of the coastal areas as they provide reliable hazard assessments for the engineers and the policymakers to avoid underestimation (which causes the failure of the design) or overestimation (which causes the surplus expenses) of the engineering safety levels in these areas.
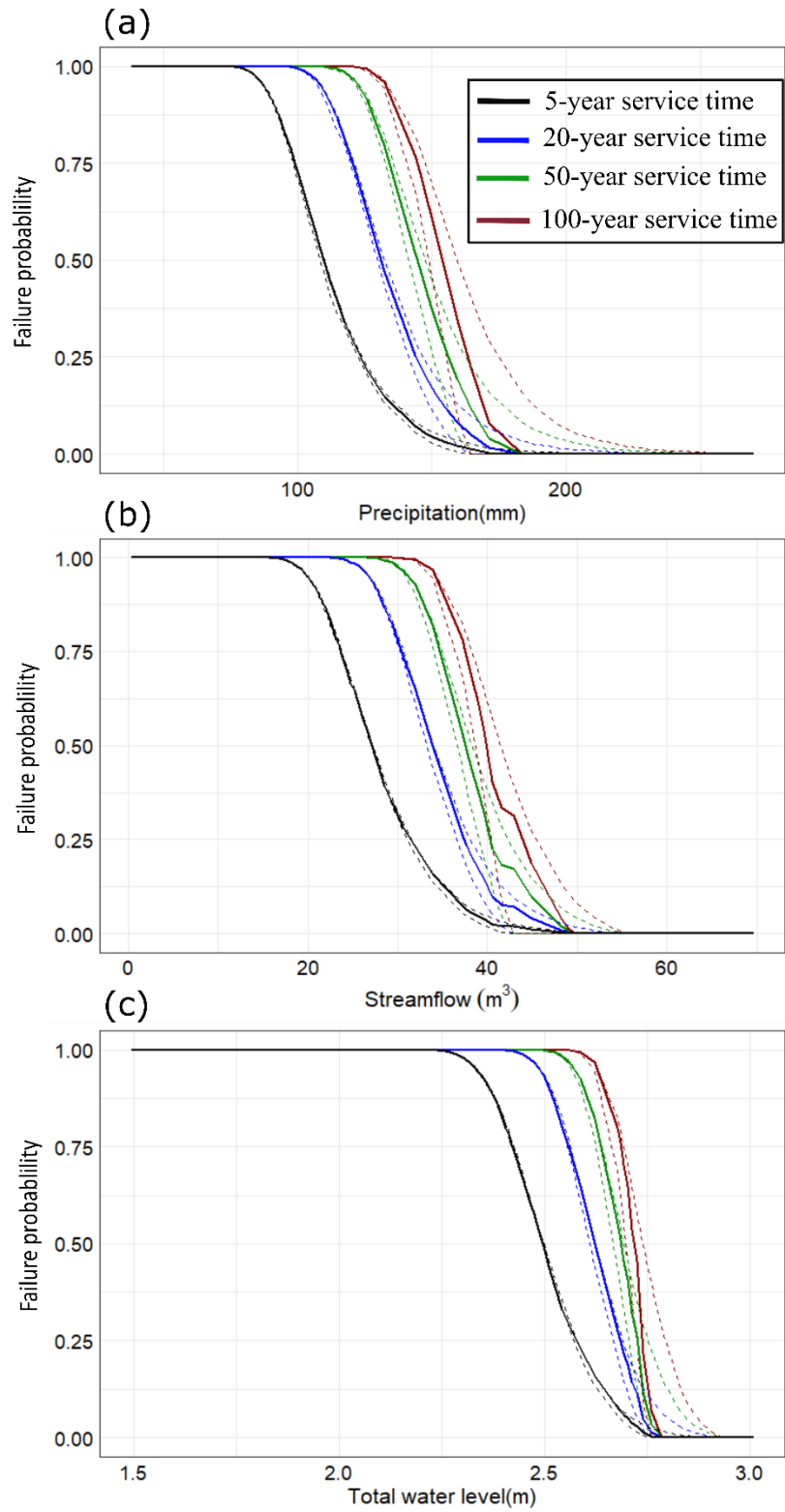
Figure 3.11) The trivariate hydrologic risk under different project lifetimes for each driver considering the 100-year event of the other two drivers: a) Pr, b) Q, and c) TWL.

The obtained results indicate that the conventional approach for flood hazard estimation, as currently adopted by most agencies, can lead to an underestimation of the corresponding risks across Canada's coastal areas in particular the Atlantic. More robust design levels are obtained by considering all the flooding mechanisms and the corresponding interrelationships. The trivariate approach proposed in this study can be applied for such analyses and other interrelated hazards

3.6. Conclusions

This study analyzes the compound flood hazard hazards across Canada's coasts considering the interrelationships between three main drivers of flooding including precipitation, total water level, and streamflow. We focus on extreme precipitation events and the corresponding high flows and total water levels within a 1-day time lag. After preprocessing the data, 41 locations distributed across three regions of the Pacific, Great Lake, and Atlantic coasts are selected for the analysis of compound flooding by developing the corresponding trivariate joint distributions.

The best-fitted marginal distribution for each variable at each location is selected from ten continuous univariate distributions. Further, according to the C-vine algorithm, the best-fitted conditional and unconditional bivariate copulas among 40 different copula functions are selected using AIC to represent the dependencies between drivers of flooding. All parameters and the corresponding uncertainties are estimated through the Bayesian approach.

Further, the joint (OR, AND, Kendall) and conditional RPs and the corresponding uncertainties are quantified in this study. The return periods of individual drivers of flooding are compared with those estimated based on the joint and conditional scenarios. The results indicate positive interactions between at least two flooding drivers at 21

locations across three regions mainly at the Atlantic coast. Besides, the dependency between the TWL and Pr is higher than in the other two scenarios, especially at the Atlantic coast. Results also highlight the underestimations of the corresponding hazards when drivers are investigated in isolation. Overall, 23 locations, across Canada's coasts, show positive dependencies between different drivers of flooding resulting in CHR values above unity.

The univariate analysis underestimates the failure probability of compound flood events. For example at location 41, in the Atlantic, the FP is underestimated by almost 70% when the interrelationships between drivers of flooding are not considered considering a design lifetime of 50 years. Besides, the FP corresponding to the unrealistic independence scenario results in under- or over-estimations of FP compared to AND/OR scenarios. Considering the 100-year project lifetime, the trivariate hydrologic risk decreases sharply when the design Pr is larger than 80 mm, and approaches zero with a design level of 170 mm, suggesting a design rainfall magnitude of 80 mm to 170 mm for this location. The estimated design values of Q and TWL are between 20 to 50 m^3/s and between 2.2 and 2.8 m, respectively. The trivariate analysis conducted in the study can lead to more robust assessments of the flooding hazards over the Canadian coastal zones. Further, it provides critical information for the sustainable design and planning of communities and infrastructure systems. Similar analyses can be conducted over other coastal areas.

Acknowledgment

Vincent, 2011). The VineCopula package (Schepsmeier et al., 2015) available in R
programming software is applied to construct the pair copulas.

References

Aas, K., Berg, D., 2009. Models for construction of multivariate dependence–a
    comparison study. *The European Journal of Finance*, 15(7-8): 639-659.

Aas, K., Czado, C., Frigessi, A., Bakken, H., 2009. Pair-copula constructions of multiple
    dependence. *Insurance: Mathematics and economics*, 44(2): 182-198.

AghaKouchak, A. et al., 2020. Climate Extremes and Compound Hazards in a Warming
    World. *Annual Review of Earth and Planetary Sciences,* 48.

Akaike, H., 1974. A new look at the statistical model identification. *IEEE transactions on
    automatic control*, 19(6): 716-723.

Beersma, J.J., Buishand, T.A., 2004. Joint probability of precipitation and discharge
    deficits in the Netherlands. *Water resources research*, 40(12).

Bevacqua, E., Maraun, D., Hobæk Haff, I., Widmann, M., Vrac, M., 2017. Multivariate
    statistical modelling of compound events via pair-copula constructions: analysis
    of floods in Ravenna (Italy). *Hydrology and Earth System Sciences*, 21(6): 2701-
    2723.

Bevacqua, E. et al., 2020a. Global projections of compound coastal meteorological
    extremes.

Bevacqua, E., Vousdoukas, M.I., Shepherd, T.G., Vrac, M., 2020b. Brief communication:
    The role of using precipitation or river discharge data when assessing global
    coastal compound flooding. *Natural Hazards and Earth System Sciences*, 20(6):
    1765-1782.

Bezak, N., Brilly, M., Šraj, M., 2014. Comparison between the peaks-over-threshold
    method and the annual maximum method for flood frequency analysis.
    Hydrological Sciences Journal, 59(5): 959-977.

Brechmann, E., Schepsmeier, U., 2013. Cdvine: Modeling dependence with c-and d-vine
    copulas in r. *Journal of statistical software*, 52(3): 1-27.

Burnham, K., Anderson, D., Huyvaert, K., 2010. AICc model selection in ecological and behavioural science: some background, observations and comparisons. *Behav Ecol Sociobiol*. doi, 10.

Bush, E., Lemmen, D., 2019. Canada's changing climate report. Government of Canada. Ottawa: Government of Canada. Retrieved from http://www. *changing climate. ca ....*

Chakravarty, I.M., Roy, J., Laha, R.G., 1967. Handbook of methods of applied statistics.

Couasnon, A. et al., 2019. Measuring compound flood potential from river discharge and storm surge extremes at the global scale and its implications for flood hazard.

Couasnon, A., Sebastian, A., Morales-Nápoles, O., 2018. A copula-based Bayesian network for modeling compound flood hazard from riverine and coastal interactions at the catchment scale: An application to the Houston Ship Channel, Texas. Water, 10(9): 1190.

Czado, C., 2010. Pair-copula constructions of multivariate copulas, Copula theory and its applications. Springer, pp. 93-109.

De Michele, C., Salvadori, G., 2003. A generalized Pareto intensity-duration model of storm rainfall exploiting 2-copulas. *Journal of Geophysical Research: Atmospheres*, 108(D2).

Do, H.X. et al., 2020. Historical and future changes in global flood magnitude–evidence from a model–observation investigation. *Hydrology and Earth System Sciences*, 24(3): 1543-1564.

Dodangeh, E., Shahedi, K., Solaimani, K., Shiau, J.-T., Abraham, J., 2019. Data-based bivariate uncertainty assessment of extreme rainfall-runoff using copulas: comparison between annual maximum series (AMS) and peaks over threshold (POT). *Environmental monitoring and assessment*, 191(2): 67.

dos Santos Silva, R., Lopes, H.F., 2008. Copula, marginal distributions and model selection: a Bayesian note. *Statistics and Computing*, 18(3): 313-320.

Eckstein, D., Künzel, V., Schäfer, L., 2021. Global Climate Risk Index 2021. Who Suffers Most from Extreme Weather Events: 2000-2019.

Eilander, D. et al., 2020. The effect of surge on riverine flood hazard and impact in deltas globally.

Fang, J. et al., 2020. Compound flood potential from storm surge and heavy precipitation in coastal China. *Hydrology and Earth System Sciences Discussions:* 1-24.

Frame, D.J., Wehner, M.F., Noy, I., Rosier, S.M., 2020. The economic costs of Hurricane Harvey attributable to climate change. *Climatic Change*, 160(2): 271-281.

Ganguli, P., Merz, B., 2019. Trends in Compound Flooding in Northwestern Europe During 1901–2014. *Geophysical Research Letters*, 46(19): 10810-10820.

Ganguli, P., Paprotny, D., Hasan, M., Güntner, A., Merz, B., 2020. Projected changes in compound flood hazard from riverine and coastal floods in northwestern Europe. *Earth's Future*, 8(11): e2020EF001752.

Genest, C., Favre, A.-C., 2007. Everything you always wanted to know about copula modeling but were afraid to ask. *Journal of hydrologic engineering*, 12(4): 347-368.

Genest, C., Quessy, J.F., Rémillard, B., 2006. Goodness-of-fit procedures for copula models based on the probability integral transformation. *Scandinavian Journal of Statistics*, 33(2): 337-366.

Ghanbari, M., Arabi, M., Kao, S.C., Obeysekera, J., Sweet, W., 2021. Climate Change and Changes in Compound Coastal-Riverine *Flooding Hazard Along the US Coasts*. Earth's Future: e2021EF002055.

Golnaraghi, M., Surminski, S., Mehryar, S., Kousky, C., Roezer, V., 2020. *Building Flood Resilience in a Changing Climate*.

González-López, V.A., Piovesana, M.C., Romano, N., 2019. Tail conditional probabilities to predict academic performance. 4open, 2: 18.

Gori, A., Lin, N., Xi, D., 2020. Tropical cyclone compound flood hazard assessment: from investigating dependence to quantifying impacts. *Earth and Space Science* Open Archive ESSOAr.

Hao, Z., Singh, V., Hao, F., 2018. Compound extremes in hydroclimatology: a review. *Water*, 10(6): 718.

Hendry, A. et al., 2019. Assessing the characteristics and drivers of compound flooding events around the UK coast. *Hydrology and Earth System Sciences*, 23: 3117-3139.

Jalili Pirani, F., Najafi, M., 2020. Recent trends in individual and multivariate compound flood drivers in Canada's coasts. *Water Resources Research*, 56(8): e2020WR027785.

Jane, R., Cadavid, L., Obeysekera, J., Wahl, T., 2020. Multivariate statistical modelling of the drivers of compound flood events in south Florida. *Natural Hazards and Earth System Sciences*, 20(10): 2681-2699.

Joe, H., 1996. Families of m-variate distributions with given margins and m (m-1)/2 bivariate dependence parameters. Lecture Notes-Monograph Series: 120-141.

Joe, H., 1997. Multivariate models and multivariate dependence concepts. CRC Press.

Johnson, D.L., 2006. Service assessment: Hurricane Katrina, August 23–31, 2005. Silver Spring, MD: US Department of Commerce, National Ocean ic and Atmospheric Administration, & National Weather Service.

Kundzewicz, Z.W. et al., 2014. Flood risk and climate change: global and regional perspectives. *Hydrological Sciences Journal*, 59(1): 1-28.

Lavell, A. et al., 2012. Managing the risks of extreme events and disasters to advance climate change adaptation. A Special Report of Working Groups I and II of the Intergovernmental Panel on Climate Change (IPCC): 25-64.

Liu, Z. et al., 2018. A framework for exploring joint effects of conditional factors on compound floods. *Water Resources Research*, 54(4): 2681-2696.

Marcos, M. et al., 2019. Increased extreme coastal water levels due to the combined action of storm surges and wind waves. *Geophysical Research Letters*, 46(8): 4356-4364.

Masson-Delmotte, V. et al., 2021. Climate Change 2021: The Physical Science Basis. Contribution of Working Group I to the Sixth Assessment Report of the Intergovernmental Panel on Climate Change. IPCC: Geneva, Switzerland.

Mekis, É., Vincent, L.A.J.A.-O., 2011. An overview of the second generation adjusted daily precipitation dataset for trend analysis in Canada. 49(2): 163-177.

Min, A., Czado, C., 2011. Bayesian model selection for D-vine pair-copula constructions. *Canadian Journal of Statistics*, 39(2): 239-258.

Moftakhari, H.R., Salvadori, G., AghaKouchak, A., Sanders, B.F., Matthew, R.A., 2017. Compounding effects of sea level rise and fluvial flooding. *Proceedings of the National Academy of Sciences*, 114(37): 9785-9790.

Muis, S., Verlaan, M., Winsemius, H.C., Aerts, J.C., Ward, P.J., 2016. A global reanalysis of storm surges and extreme sea levels. *Nature communications*, 7(1): 1-12.

Najafi, M.R., Zhang, Y., Martyn, N., 2021. A flood risk assessment framework for interdependent infrastructure systems in coastal environments. *Sustainable Cities and Society*, 64: 102516.

Nasr, A.A., Wahl, T., Rashid, M.M., Camus, P., Haigh, I.D., 2021. Assessing the dependence structure between oceanographic, fluvial, and pluvial flooding drivers along the United States coastline. *Hydrology and Earth System Sciences Discussions*: 1-31.

Nelson, R., 1998. An Introduction to Copulas, 1999. Lecture notes in statistics.

Neumann, B., Vafeidis, A.T., Zimmermann, J., Nicholls, R.J., 2015. Future coastal population growth and exposure to sea-level rise and coastal flooding-a global assessment. PloS one, 10(3): e0118571.

Paprotny, D., Vousdoukas, M.I., Morales-Nápoles, O., Jonkman, S.N., Feyen, L., 2018. Compound flood potential in Europe. *Hydrol. Earth Syst. Sci*. Discuss, 2018: 1-34.

Paprotny, D., Vousdoukas, M.I., Morales-Nápoles, O., Jonkman, S.N., Feyen, L., 2020. Pan-European hydrodynamic models and their ability to identify compound floods. *Natural Hazards*: 1-25.

Petroliagkis, T.I., 2018. Estimations of statistical dependence as joint return period modulator of compound events–Part 1: Storm surge and wave height. Natural Hazards and Earth System Sciences, 18(7): 1937-1955.

Pitt, M., Chan, D., Kohn, R., 2006. Efficient Bayesian inference for Gaussian copula regression models. *Biometrika*, 93(3): 537-554.

Rana, A., Moradkhani, H., Qin, Y., 2017. Understanding the joint behavior of temperature and precipitation for climate change impact studies. Theoretical and Applied Climatology, 129(1): 321-339.

Robins, P.E. et al., 2021. Compound flooding: Dependence at sub-daily scales between extreme storm surge and fluvial flow. *Frontiers in Built Environment*: 116.

Salvadori, G., De Michele, C., 2004. Frequency analysis via copulas: Theoretical aspects and applications to hydrological events. *Water resources research*, 40(12).

Salvadori, G., De Michele, C., 2010. Multivariate multiparameter extreme value models and return periods: A copula approach. *Water resources research*, 46(10).

Salvadori, G., De Michele, C., Kottegoda, N.T., Rosso, R., 2007. Extremes in nature: an approach using copulas, 56. Springer Science & Business Media.

Salvadori, G., Durante, F., De Michele, C., Bernardi, M., Petrella, L., 2016. A multivariate copula-based framework for dealing with hazard scenarios and failure probabilities. *Water Resources Research*, 52(5): 3701-3721.

Salvadori, G., Michele, C.D., Durante, F., 2011. On the return period and design in a multivariate framework. *Hydrology and Earth System Sciences*, 15(11): 3293-3305.

Santos, V.M. et al., 2020. Multivariate statistical modelling of extreme coastal water levels and the effect of climate variability: a case study in the Netherlands. *Hydrology and Earth System Sciences Discussions*: 1-25.

Sarhadi, A., Burn, D.H., Concepcion Ausin, M., Wiper, M.P., 2016. Time-varying nonstationary multivariate risk analysis using a dynamic Bayesian copula. *Water Resources Research*, 52(3): 2327-2349.

Schepsmeier, U. et al., 2015. Package 'VineCopula'. R package version, 2(5).

Sebastian, A., Dupuits, E., Morales-Nápoles, O., 2017. Applying a Bayesian network based on Gaussian copulas to model the hydraulic boundary conditions for hurricane flood risk analysis in a coastal watershed. *Coastal Engineering*, 125: 42-50.

Shiau, J., 2006. Fitting drought duration and severity with two-dimensional copulas. *Water resources management*, 20(5): 795-815.

Singh, H., Pirani, F.J., Najafi, M.R., 2020. Characterizing the temperature and precipitation covariability over Canada. *Theoretical and Applied Climatology*, 139(3): 1543-1558.

Sklar, M., 1959. Fonctions de repartition an dimensions et leurs marges. Publ. inst. statist. univ. Paris, 8: 229-231.

Smith, M.S., 2011. Bayesian approaches to copula modelling. *arXiv preprint* arXiv:1112.4204.

Svensson, C., Jones, D.A., 2002. Dependence between extreme sea surge, river flow and precipitation in eastern Britain. International Journal of Climatology: *A Journal of the Royal Meteorological Society*, 22(10): 1149-1168.

Tanoue, M., Hirabayashi, Y., Ikeuchi, H., 2016. Global-scale river flood vulnerability in the last 50 years. *Scientific reports*, 6(1): 1-9.

Valle-Levinson, A., Olabarrieta, M., Heilman, L., 2020. Compound flooding in Houston-Galveston Bay during Hurricane Harvey. *Science of The Total Environment*, 747: 141272.

van Berchum, E.C., van Ledden, M., Timmermans, J.S., Kwakkel, J.H., Jonkman, S.N., 2020. Rapid flood risk screening model for compound flood events in Beira, Mozambique. *Natural Hazards and Earth System Sciences*, 20(10): 2633-2646.

Villarini, G., Smith, J.A., Ntelekos, A.A., Schwarz, U., 2011. Annual maximum and peaks-over-threshold analyses of daily rainfall accumulations for Austria. Journal of Geophysical Research: *Atmospheres*, 116(D5).

Wahl, T., Jain, S., Bender, J., Meyers, S.D., Luther, M.E., 2015. Increasing risk of compound flooding from storm surge and rainfall for major US cities. *Nature Climate Change*, 5(12): 1093-1097.

Wallemacq, P., 2018. Economic losses, poverty & disasters: 1998-2017. Centre for Research on the Epidemiology of Disasters, CRED.

Wang, S., Najafi, M.R., Cannon, A.J., Khan, A.A., 2021. Uncertainties in Riverine and Coastal Flood Impacts under Climate Change. *Water*, 13(13): 1774.

Ward, P.J. et al., 2018. Dependence between high sea-level and high river discharge increases flood hazard in global deltas and estuaries. *Environmental Research Letters*, 13(8): 084012.

Welch, E.D., 2020. The Occurrence of Compound Events in Rhode Island and Their Associated Damage Costs, University of Massachusetts Boston.

Wu, W. et al., 2018. Mapping dependence between extreme rainfall and storm surge. *Journal of Geophysical Research*: Oceans, 123(4): 2461-2474.

Xu, K., Ma, C., Lian, J., Bin, L., 2014. Joint probability analysis of extreme precipitation and storm tide in a coastal city under changing environment. PLoS One, 9(10): e109341.

Zhang, Y., Najafi, M.R., 2020. Probabilistic numerical modeling of compound flooding caused by Tropical Storm Matthew over a data-scarce coastal environment. *Water Resources Research*, 56(10): e2020WR028565.

Zheng, F., Westra, S., Leonard, M., Sisson, S.A., 2014. Modeling dependence between extreme rainfall and storm surge to estimate coastal flooding risk. *Water Resources Research*, 50(3): 2050-2071.

Zheng, F., Westra, S., Sisson, S.A., 2013. Quantifying the dependence between extreme rainfall and storm surge in the coastal zone. *Journal of hydrology*, 505: 172-187.

Zscheischler, J. et al., 2018. Future climate risk from compound events. *Nature Climate Change*, 8(6): 469-477.

Chapter 4

4. Trends in Individual and Multivariate Compound Flood Drivers in Canada's Coasts

4.1. Introduction

Flooding is the most common natural disaster in the world causing 215,000 fatalities and $1 trillion of damage between 1980-2016 (Re, 2017). About 0.8-1.1 million people experience flooding each year, which is commonly followed by devastating socioeconomic consequences (Muis et al., 2016b). After the Fort McMurray wildfires in 2016, flood events ranked second among the costliest natural disasters in Canadian history (Landis et al., 2018). Coastal environments are particularly susceptible to flooding caused by hydrometeorological (e.g. rainfall, runoff), and coastal (e.g. storm surges, tides) processes. According to the Intergovernmental Panel on Climate Change (IPCC, 2012), the simultaneous or successive occurrence of such events can lead to compound flooding with significant coastal impacts.

Wind stress and to a lesser extent falling atmospheric pressure are the main drivers of storm surges, which can penetrate the river system and cause excessive flooding in the low-lying coastal zones. Storm surge arrivals might coincide with high tides, caused by the gravitational attraction of the moon and the sun on the earth, resulting in more intense coastal flooding. Low-pressure systems like tropical cyclones commonly result in the co-occurrence of storm surges, heavy rainfall, and possible river overflow that can lead to compound flooding (Couasnon et al., 2019; Paprotny et al., 2018; Sarhadi et al., 2018; Svensson and Jones, 2002; Wu et al., 2018). Such effects can be exacerbated by antecedent conditions (Verhoest et al., 2010). For example, Hurricane Igor in 2010 resulted in excessive rainfall, swollen rivers, storm surge, and wave heights, with peaks up to 2.5m, which impacted 97 communities and caused at least $100 million in damages to public infrastructure in Newfoundland, Canada. Zscheischler et al. (2018) discussed several examples of such compound events and their hydroclimatic and coastal drivers.

There has been a growing interest in the study of compound flood events in recent years at regional and global scales. In this regard, the copula is widely used as an effective statistical approach to characterize the dependence structure of compound events (Paprotny et al., 2018; Ward et al., 2018). In a recent study, Jane et al. (2020) used copulas and a conditional threshold exceedance model to characterize the dependence structure of multiple food drivers. Bevacqua et al. (2017) applied pair-copula to model the dependency between sea level and streamflow and the corresponding meteorological drivers. They showed that ignoring the estimated dependence between sea and river levels may lead to an underestimation of flood risk. Hao et al. (2018) compared several statistical methods including empirical, multivariate distribution, indicator approach, quantile regression, and a Markov Chain model to characterize compound extremes. Ward et al. (2018) studied the dependency between high river discharge and sea level using copula over the globe and demonstrated its significant role in the estimated exceedances of both design discharge and design sea level. Considering that the duration of each event might take over a day, they assessed the dependencies for time lags of one to five days. Eilander et al. (2020) recently assessed the joint influence of riverine and coastal drivers of flooding in deltas worldwide using the CaMa-Flood model. They showed that ignoring storm surge can result in significant underestimations of the flood depths. Couasnon et al. (2019) studied daily river discharge and storm surge to identify the hotspots of compound flooding using copulas. In a study by Hendry et al. (2019), the joint occurrence of storm surge and fluvial flooding was assessed along the UK coast. They analyzed the frequency of compound events and showed the spatial variability of dependencies between flood drivers based on Kendall's Tau. Wu et al. (2018) investigated the dependence between observed and modeled storm surge and rainfall over the Australian coastline and found good agreements between the two sets of dependencies. Papronty et al. (2018) studied the probability of joint occurrence of storm surges, rainfall, river flows, and waves over Europe using different datasets including ground-based observations, ERA-Interim reanalysis, and a regional climate model, and carried out a statistical analysis based on copulas. They found regional differences in the dependence structures and the resulting joint probabilities of different compound flood drivers. Serafin et al. (2019) highlighted that understanding the dominant,

spatially varying drivers of flooding events will help coastal communities better understand their risks.

Temporal variations of individual processes that contribute to compound flooding can change their dependence structure and the corresponding joint behavior. This can lead to increases in the frequency and severity of compound flood hazards in coastal regions. Understanding the nonstationary behavior of individual flood hazards has progressed significantly (Altava-Ortiz et al., 2011; Chingombe et al., 2005; Clement and Thas, 2009; Gan, 1998; Modarres and Sarhadi, 2009; Zhang et al., 2001), However, only a few studies have performed quantitative assessments of the joint occurrence of different types of flooding (Moftakhari et al., 2017; Sarhadi et al., 2016; Wahl et al., 2015) while such studies over Canada are lacking. The resultant flood risk is often significantly underestimated with severe consequences (Bevacqua et al., 2019b; Xu et al., 2019a; Zscheischler et al., 2018).

Only a few studies have investigated the nonstationarity of the dependence structure between multiple flood drivers (Ganguli and Merz, 2019). Wahl et al. (2015) studied changes in the joint occurrence of storm surge and rainfall over some locations around the U.S coastline due to increases in the corresponding dependencies. In addition, recent studies have assessed the impacts of climate change on compound flooding in different regions around the world (Pasquier et al., 2019; Wu and Leonard, 2019). Khanal et al. (2019) found a higher probability of storm surge and extreme river discharge co-occurrence than the random chance for different time lags. Moftakhari et al. (2017) quantified the increase in failure probabilities in 2030 and 2050 resulting from joint seal level rise and fluvial flooding.

The nonstationarity of hydroclimatic and coastal variables can be due to their monotonic trends, shifts, step changes, and periodic behavior (Machiwal and Jha, 2012). These spatial and temporal variabilities are partly associated with internal variability and in several cases with anthropogenic climate and land-use change effects (Miao et al., 2011; Milly et al., 2008). To understand nonstationary hazards, univariate trend analysis approaches are commonly used, including descriptive methods based on smoothing such as a moving average window to reduce the random variation and reveal the underlying

trends, non-parametric approaches, and time series methods that model the serial correlations explicitly (Clement and Thas, 2009). The univariate Mann-Kendall test (MK) is a widely used non-parametric approach to detect monotonic trends (Cavadias, 1994). Contrary to the parametric regression approach, MK is not limited to normally distributed and linear data and is robust to outliers (Lettenmaier, 1988a). However, the variance of the MK test statistic is inflated by serial correlation, which would cause the type I error and an incorrect rejection of the null hypothesis (Von Storch, 1999).

The univariate trends of hydroclimatic variables have been investigated extensively (Abdulkareem and Sulaiman, 2016; Khalili et al., 2013; Shadmani et al., 2012; Sonali and Kumar, 2013). However, only a few studies have assessed multivariate trends of water quality parameters (Hirsch and Slack, 1984b; Lettenmaier, 1988b; Loftis et al., 1991a; Loftis et al., 1991b; Thas et al., 1998; Van Belle and Hughes, 1984), and flood characteristics (Chebana et al., 2013; Kang et al., 2019; Ye et al., 2015). Further, while univariate autocorrelation effects in the data are commonly considered using pre-whitening, trend-free pre-whitening, variance correction, and block bootstrap sampling techniques (Önöz and Bayazit, 2012), multivariate autocorrelation is rarely addressed. Chebana et al. (2013) analyzed the univariate and joint trends of the flood peak, volume, and duration using MK, Covariance Inversion Test (CIT), Covariance Sum Test (CST), and Covariance Eigenvalue Test (CET) by considering the correlations between flood characteristics. Modarres (2018) studied the trends in dust storm frequency and its covariation with climatic variables. He found that the two methods of CIT and CET show more significant trends compared to CST.

In this study, we analyze the nonstationarity of individual and compound flood hazards in Canadian coastal zones based on univariate and multivariate trend approaches. To the knowledge of the authors, this study is the first of its kind to study the trends of multiple drivers that can contribute to compound flooding. This includes characterizing the dynamic relationships between Precipitation (P), streamflow (Q), skew surge (S), and Total Water Level (TWL) over the Atlantic, Pacific, and the Great Lakes coastal regions. A new non-parametric approach based on the inverse cumulative density function (CDF) of each contributing variable is proposed to characterize the joint trends of multiple drivers of

flooding. It addresses the limitations of current multivariate trend methods including the sensitivity to sample size and outliers, and allows for the regional analysis of potential compound flooding (hereafter called compound flooding for sake of brevity). Additionally, the univariate block bootstrap sampling technique (Modarres, 2018) is generalized to account for the effects of autocorrelation in the data and eliminate its impacts on the detection of multivariate trends.

The remainder of this paper is as follows. In Section 2, the study area and data are presented. Section 3 discusses the univariate and multivariate trend methods and the proposed compound flood trend index. Section 4 presents the results followed by the discussion and conclusions in Sections 5 and 6.

4.2. Study area and data

As the second-largest country with the longest coastline (approximately 230,000 km) in the world, Canada (Figure 4.1) has a vast array of climate regimes due to its extensive geographical features, presence of oceans to the east, west, and north, and the Great Lakes to the south. Regions to the north experience polar and sub-Arctic climates, eastern provinces have a temperate climate and the southwestern areas experience hot and humid summer continental climates (Peel et al., 2007). Western and northwestern parts of Canada have experienced the highest mean annual warming rates (> 1.7 °C) from 1948 to 2016 particularly over the winter and spring while its eastern parts had the lowest rates (< 0.5 °C) (Bush and Lemmen, 2019b). The magnitude and frequency of extreme sea levels are projected to increase in the future at a higher rate compared to the global mean along with parts of the Atlantic and Pacific coasts (Bush and Lemmen, 2019b).
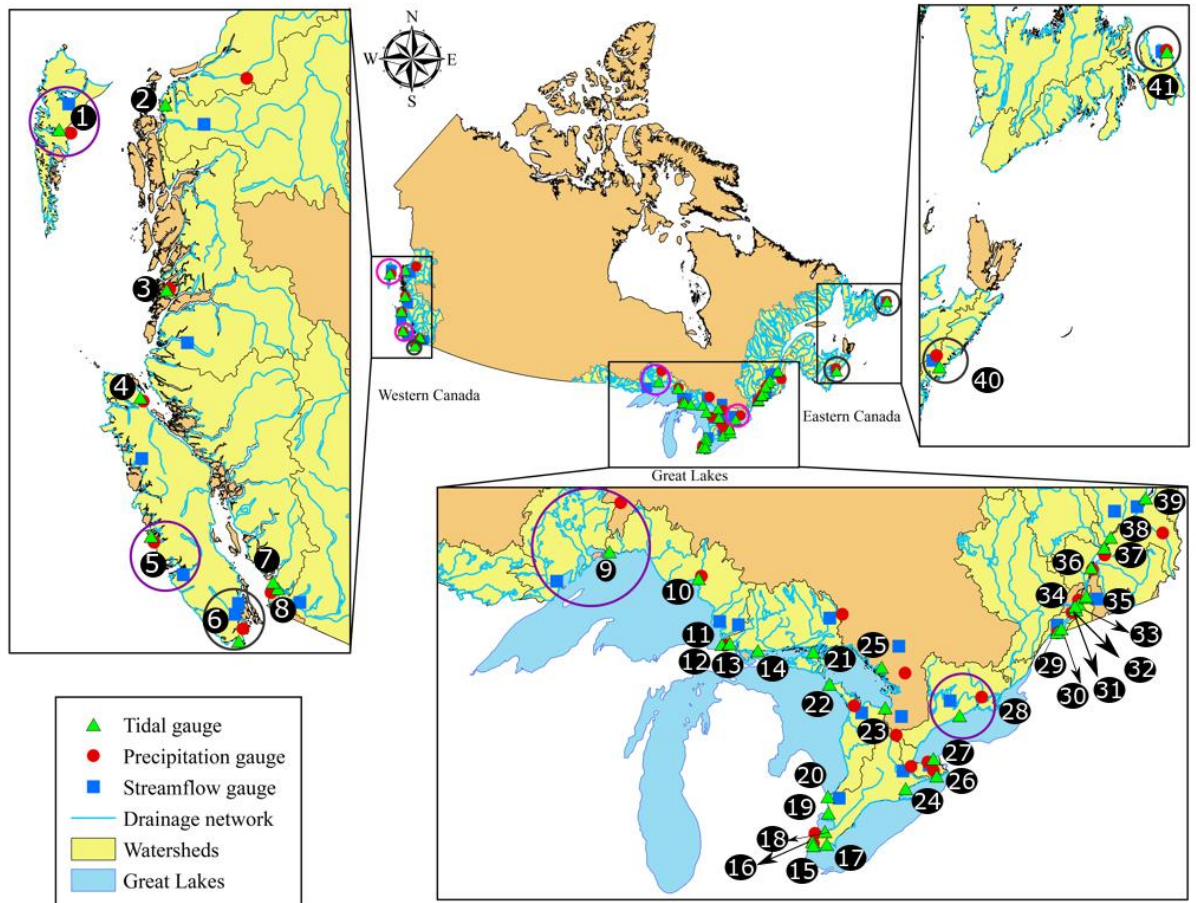
Figure 4.1) The study area showing precipitation, streamflow, and tidal gauges across Canada's coasts (Atlantic, Pacific, Great Lakes). Circles show examples of three gauges that are matched together.

Over seven million people living on the Canadian coasts are at risk of flooding caused by extreme precipitation, river overflows, storm surges, and tides (Bush and Lemmen, 2019a). The compounding effects of multiple drivers of flooding in these regions can lead to catastrophes, however quantitative trend assessments of the joint occurrences of compounding flood hazards are lacking. Therefore, in this study, the individual and multivariate trends of precipitation (P), streamflow (Q), skew surge (S), and total water level (T), which play major roles in compound flooding, are analyzed for the Canadian

coastal zones. The sources and resolution of these four flood drivers are summarized in Table S2.1

4.2.1. Total water level, storm surge, and skew surge

Records of Total water level at hourly resolution are available from tidal gauges located across Canadian coasts. Using this data we analyze the characteristics of maximum 24-hour T at each site. To identify and extract its constituents (including tides and storm surges), the secular trends of T are removed followed by harmonic analysis using the U_Tide package (Codiga, 2011). To remove seasonality from tidal records in the Great Lakes, we subtract every 30 days of T from its average. Storm surges are estimated, at an hourly timescale, by taking the difference between detrended Ts and the predicted tides. However, previous studies have shown that storm surge does not provide a reliable representation of coastal flooding because of harmonic prediction or timing errors and non-linear interactions, which can artificially bias the surge (Mawdsley and Haigh, 2016; Williams et al., 2016). Therefore, the concept of the skew surge is proposed as an alternative more reliable measure of meteorological contribution to coastal flooding (Eilander et al., 2020; Haigh et al., 2016; Williams et al., 2016). Skew surge represents the difference between the maximum observed water level and the maximum predicted tidal level regardless of their timing during the tidal cycle. For every 24 hours, the peak of T within 6 hours before and after the corresponding tide's peak is identified and the skew surge is estimated as the difference between the two peaks (Figure S4.1) (Mawdsley and Haigh, 2016). In cases where tidal patterns at both Atlantic and Pacific coasts are semiduneral (i.e. with two peaks in a day), the one with the highest peak is selected as it can increase the chances of coastal flooding. This process is repeated for all existing tidal gauges across the Canadian coastline.

4.2.2. Selection of stations and data preprocessing

Analysis of compound flood trends over the Canadian coastal zones is performed for the period of 1960 to 2015. There are over 1000 tidal gauges available, however many of them

are inactive or have large missing data. Data records are selected according to the following filtering criteria:

(5) Each year having more than 20 percent of missing data is removed for each tidal gauge.

(6) Tidal gauges with more than 20 percent of missing data over the entire period are removed, which leads to about 61 remaining gauges.

(7) Precipitation and streamflow gauges that lie within a radius of 0.5° (about 55 km) from each tidal gauge are identified followed by the application of steps 1&2 on each record. In addition to the physical distance of streamflow gauges, flow routes are tracked to make sure they are directed towards the tidal gauge (Ward et al., 2018). In cases where several precipitation or streamflow gauges exist within the specified radius, the closest and most downstream ones are selected. If no hydroclimatic gauges exist within this distance (including gauges 2, 3, 19, 15, and 17 in Figure 4.1), the radius is increased to 100 km to identify at least one precipitation and one streamflow gauge (Wu et al., 2018). The choice of the distance is to ensure that gauges are representative of the homogeneous hydro-climatic conditions of their locations (Ward et al., 2018).

(8) Only the locations that have more than 80 percent overlap between T, skew surge, precipitation, and streamflow data records are retained.

Fourty one coastal locations (2 on the Atlantic Coast, 7 in the Pacific, and 32 on the Great Lakes) are selected after assessing the data (Figure 4.1). All locations include one tidal gauge; however, precipitation and streamflow data could be matched with two different tidal gauges because of physical proximity (resulting in 27 and 25 selected stations, respectively). Besides, to analyze the coincidence of multiple drivers of flooding the three data records are temporally matched. Following Ward et al. (2018) we shift the streamflow data for five hydrometric stations that are located > 55 km upstream of the coast. We use the Kirpich equation to estimate the corresponding time lag (Mata-Lima et al., 2007):

$$T_c = KL^{0.770}S^{-0.385} , \tag{4.1}$$

where T_c is the time of concentration, K is a unit conversion coefficient and K=0.0195 in SI units, L is the channel flow length in feet or meters as dictated by K and S is the

dimensionless main-channel slope. The range of T_C for these five gauges ranges between 18 to 36 hours. We further applied the Pickering method and noticed minor differences in the estimated time lags.

4.3. Methodology

4.3.1. Univariate trend analysis

We use the non-parametric Mann-Kendall test to study monotonic trends of the individual variables at each location.

Given a data record of size n, the MK test statistic is calculated using (Kendall, 1975; Mann, 1945):

To account for the effects of autocorrelation, we apply the Block Bootstrap Sampling (BBS) approach (Politis, 2003; Svensson et al., 2005).

$$S = \sum_{i=1}^{n-1} \sum_{j=i+1}^{n} sgn(x_j - x_i)$$

$$,$$ (4.2)

where sgn(.) is the sign function

$$sgn(x) = \begin{cases} 1 & ; x > 0 \\ 0 & ; x = 0 \\ -1 & ; x < 0 \end{cases}$$ (4.3)

x represents the variable (Q, T, P, S), i and j are temporal indices that correspond to daily data series (for daily trend analyses), annual max series (for the analyses of annual maxima), or peaks over the selected thresholds

Under the Null hypothesis (H_0) of no monotonic trend, the test statistic (S) follows a normal distribution with the approximate variance of:

$$Var(S) = n(n-1)(2n+5)/18,$$ (4.4)

Bootstrapping is based on resampling the data points with replacement to generate new data series with the same length as the original data. This process is repeated many times (1000 iterations in this study) to generate a large set of trend-free data. If the test statistic of the original data record lies in the tail of the distribution of test statistics corresponding to the resampled series, the trend is considered to be significant (Svensson et al., 2005). This is because any existing trend would be eliminated due to resampling, and the derived distribution is that of the test statistic for trend-free data. In BBS, instead of removing the autocorrelation from the data (similar to pre-whitening), the effects of autocorrelation on the distribution of the test statistic are considered.

In BBS, the entire data record is divided into non-overlapping blocks with a fixed length such that data points are approximately independent between each block. Bootstrapping is then performed in blocks to replicate the data autocorrelation (Önöz and Bayazit, 2012). Block lengths are determined based on the number of contiguous significant autocorrelation (Khaliq et al., 2009) corresponding to each variable (a 5% significance level is considered in this study). Since the autocorrelation functions for our data (e.g. Figure S4.3) show clear patterns of seasonality in data, to preserve this periodic structure we use the seasonal block bootstrap approach, proposed by Politis, (2003). In this approach, the block length is always an integer multiple of the period length (one year) (Dudek, 2018; Dudek et al., 2014). Consequently, the selected block lengths are 1 year (corresponding to precipitation and streamflow), 7 years (Total water level; Pacific coast), 10 years (T; Atlantic coast), 1 year (T; Great Lakes), and 2 to 40 days (skew surge, which does not show periodic behavior). Figure S4.2 shows an example of a streamflow data series before and after resampling for location #40.

4.3.2. Multivariate correlation and trend analysis

In addition to the univariate trend analysis, we use the extended MK test to analyze the multivariate trends of compound flooding. Considering d variables, the univariate trend of each data record is first estimated using MK and a vector S_{multi}, which includes the corresponding test statistics for variables $1, 2, 3, ... d$ is generated as (Lettenmaier,1988):

$$S_{multi} = (S_1, S_2, \ldots S_d)', \tag{4.5}$$

S_{multi} follows a d-dimensional normal distribution with a mean of zero and a covariance matrix $C_M = (c_{u,v})_{u,v=1,\ldots,d}$, with $c_{u,v} = cov(S_u, S_v)$. For each pair of data records (u,v), the covariance ($c_{u,v}$) is estimated by:

$$\hat{c}_{u,v} = \frac{t_{u,v} + r_{u,v}}{3} \quad \text{for } u \neq v, \tag{4.6}$$

Where

$$t_{u,v} = \sum_{1 \leq i < j \leq n} sgn((x_j^{(u)} - x_i^{(u)})(x_j^{(v)} - x_i^{(v)})), \tag{4.7}$$

$$r_{u,v} = \sum_{i,j,k=1}^{n} sgn((x_k^{(u)} - x_j^{(u)})(x_k^{(v)} - x_i^{(v)})), \tag{4.8}$$

t and *r* represent Kendall's test and Spearman's rho statistics.

We apply the Covariance Inversion Test (CIT), Covariance Sum Test (CST), and Covariance Eigenvalue Test (CET) to study the multivariate trends of compound flood drivers based on the covariance structure of multiple data records. More details about these three methods are provided in Chabena et al., (2013). In CIT, proposed by Dietz and Killeen (1981), the test statistic (D) is asymptotically $\chi^2(q)$ - distributed:

$$D = S'_{multi} C_M^{-1} S_{multi}, \tag{4.9}$$

where C_M^{-1} is the inverse of the covariance matrix and q is the rank of the matrix $1 \leq q \leq d$

 In CST (Hirsch and Slack, 1984a) the test statistic is defined as:

$$H = 1'S_{multi} = \sum_{u=1}^{d} S_{multi}^{(u)}, \tag{4.10}$$

with $1 = (1,\ldots,1) \in R^d$. Under the null hypothesis, the H statistic is asymptotically normally distributed with $E(H) = 0$ and variance:

$$var(H) = \sum_{u=1}^{d} var(S_{multi}^{(u)}) + 2\sum_{v=1,u=1}^{d,v-1} c_{u,v} \,, \tag{4.11}$$

The test statistic in CET (Lettenmaier,1988) is:

$$L = S'_{multi} S_{multi} = \sum_{u=1}^{d} (S_{multi}^{(u)})^2 \,, \tag{4.12}$$

L statistic is $\sigma^2 \chi^2(q)$(normal)- distributed under the null hypothesis where q is the rank of the covariance matrix as in (5).

If the value of the statistics (D, H, L) is more than the critical threshold determined based on the related distribution quantiles, the null hypothesis (i.e. no multivariate trend) is rejected.

Using these non-parametric trend approaches we assess the univariate, bivariate, and multivariate trends of the drivers of compound flooding on the Canadian coasts. Besides, the overall significance level is controlled and false trend detection can be avoided (Chebana et al., 2013). However, some drawbacks are noticeable in these multivariate trend approaches. The power of CIT decreases with decreasing sample size. CST was proposed to solve this issue, however, it has lower power if the univariate MK test statistics have different signs. Additionally, although the CET approach avoids CIT's matrix inversion, it is very conservative concerning type I error. To address these limitations, we propose a flexible metric, called Probability Summation (PS), to analyze multivariate trends of the drivers of compound flooding.

Further, we extend the BBS approach to the multivariate analysis of compound flooding. First, BBS is applied over each data record (i.e. each variable at each location) similar to the univariate analysis. Next, the shuffled records are matched and the four non-parametric trend tests are performed. This process is repeated 1000 times, and the multivariate trend is compared with the test statistic distribution of the shuffled data.

In addition to the joint trends of multiple flood drivers, we study the corresponding dependencies that represent their simultaneous occurrences (Figure S4.4). Kendall's Tau correlation coefficient is used to measure the significant ordinal association between two different drivers at a 0.05 significance level from 1960 to 2015. Kendall's Tau test is a non-

parametric hypothesis test for statistical dependence based on the Tau coefficient. The corresponding associations are investigated for both daily and extreme scenarios. This allows us to identify locations where flood drivers have positive correlations, indicating risks of compound flooding, and show increasing joint trends, suggesting increases in the corresponding risks.

4.3.3. Probability Summation index

We propose the Probability Summation (PS) index as a relatively simple and flexible metric to study the multivariate trends of compound flood drivers. PS transforms each variable to its probability space (ranging between 0 and 1). The probabilities are then aggregated leading to a single time series. The equation is as follows.

$$PS(t) = \sum_{i=1}^{d} F_{X_i^t}(x), \tag{4.13}$$

where $PS(t)$ is the summation of the transformed values of each element of d drivers with length n (i.e. t = 1, 2, 3, ... n), X represents the drivers including precipitation, streamflow, T, and skew surge that change in time (t), and $F_X(x) = P(X \leq x)$ is the corresponding cumulative probability.

Based on historical extreme events or expert knowledge, the extreme values of more than a specific quantile (threshold) can be extracted. In this study, $Q_{0.99}$, $Q_{0.975,}$ and $Q_{0.95}$ are considered as the thresholds. The univariate MK test is then applied over the joint time series to assess the overall trend of the drivers of compound flooding.

The PS index does not require estimating the (inverse) covariance matrix between different variables. It also allows for the analysis of various compound flood scenarios: 1) when all flood drivers are extremes, 2) only one is extreme, for example, low or moderate streamflow coinciding with extreme T leading to compound flooding, 3) none are extremes, however, their cumulative impacts result in an extreme event. In this study, we aggregate the transformed data records through summation (no weights applied). In other words, the PS approach, as proposed and applied in this study, assumes each of the drivers is equally responsible for compound flooding. The regional analysis is performed by taking

the spatial average of the records corresponding to each variable before applying PS and the other multivariate trend tests. However, this index has the flexibility to combine data records spatially, in the probability space, for regional analysis of compound flooding. Further, one can increase the significance of different drivers by assigning weights to the variables in the probability space, before aggregation. This index can also be used to analyze the temporal changes of compound flooding with specific aggregated levels (in the probability space) based on historical events or defined thresholds.

4.3.4. Trend scenarios

A suite of scenarios (Figure 2.2) is investigated to evaluate the univariate and multivariate trends of variables that contribute to compound flooding on the Canadian coasts. This includes analyzing the trends of daily data records, extremes including the annual maxima and peaks over the threshold, and overall regional trends.

- Daily trend analyses include changes in daily data records from 1960 to 2015. We study the univariate trends of daily streamflow (Q_d), Total Water Level (T_d), Precipitation (P_d), and skew surge (S_d) using the MK test, as well as the corresponding bivariate and trivariate trends including (Q_d, T_d), (Q_d, S_d), (T_d, P_d), (P_d, S_d) and (Q_d, T_d, P_d) using CIT, CST and CET.

- Extreme trend analyses include the individual and multivariate changes of the annual maximum values of each variable, Q_{e_am}, T_{e_am}, P_{e_am}, and S_{e_am}, and the corresponding peaks over the 0.95 and 0.99 quantiles. To remove the temporal dependencies in the latter, only the peaks of 3-day intervals are retained. The Peaks over Threshold (POT) approach allows for the analysis of the frequency of extremes besides their magnitudes. The multivariate analysis of extremes is performed based on PS besides CIT, CST, and CET. In the PS approach, the transformed value for each variable at each day varies between zero and one. We selected the 99th percentile of the aggregated values of both bivariate and trivariate scenarios as the threshold, to study the trends of the extremes. Analyses are also performed for other thresholds ($Q_{0.95}$ and $Q_{0.975}$). As mentioned before, this index can be applied for the analysis of other scenarios as well.

- To study the successive occurrence of multiple events, which can subsequently cause compound flooding, we analyze the bivariate and trivariate trends of Q, T, P, and S considering a time lag of one day between each variable (Moftakhari et al., 2017). For example, in the $(Q_{e\_0.99}, T_1)$ scenario, extreme daily flow events (e.g. flows larger than the 0.99 quantiles) and the maximum T values one day before or after the event is retained (including the event's day of occurrence). Similarly, in the $(T_{e\_0.99}, Q_1)$ scenario the relationships between extremes of T and the maximum values of Q within one day before and after these extremes are taken. This analysis is performed for other scenarios of $(Q_{e\_0.99}, S_1)$, $(S_{e\_0.99}, Q_1)$, $(T_{e\_0.99}, P_1)$, $(P_{e\_0.99}, T_1)$, $(P_{e\_0.99}, S_1)$, $(S_{e\_0.99}, P_1)$ as well as $(Q_{e\_0.99}, T_1, P_1)$, $(T_{e\_0.99}, Q_1, P_1)$ and $(P_{e\_0.99}, Q_1, T_1)$. As discussed before, in addition to the analysis of joint trends, we characterize the dependencies between different drivers based on Kendall's τ correlation coefficient. This is performed for the daily and extreme scenarios mentioned above.

- To understand the overall trends of variables that contribute to compound flooding in the three Canadian coastal areas (Atlantic, Pacific, and Great Lakes), regional trend analysis is performed on spatially averaged data records corresponding to each region. In the PS approach, at first, the spatial mean of each variable for each day has been calculated, and then it has been transformed into the corresponding probability domain. Multivariate trend tests are then applied similar to the at-site trend analyses using the four methods of CIT, CST, CET, and PS.

  To illustrate the procedure, we implement the above steps for a bivariate scenario for site #40: 1) the univariate time series of the four variables are plotted in Figure S4.5. BBS is applied to account for the autocorrelation effects in the data (Figure S4.2), 2) the covariance matrix between the four variables and the corresponding test statistics of CIT, CST, and CET are calculated for (Q_d, T_d) (Tables S4.1 and S4.2), 3) The test statistics corresponding to the CIT, CET, CST and PS methods are calculated for the $(T_{e\_0.99}, Q)$ scenario (Table S4.2). All flood drivers except P have shown increasing trends. CIT, CST, and CET detect a significant increasing trend in the (T_d, Q_d) scenario. The PS index detects an increasing trend for the $(T_{e\_0.99}, Q_1)$ scenario.
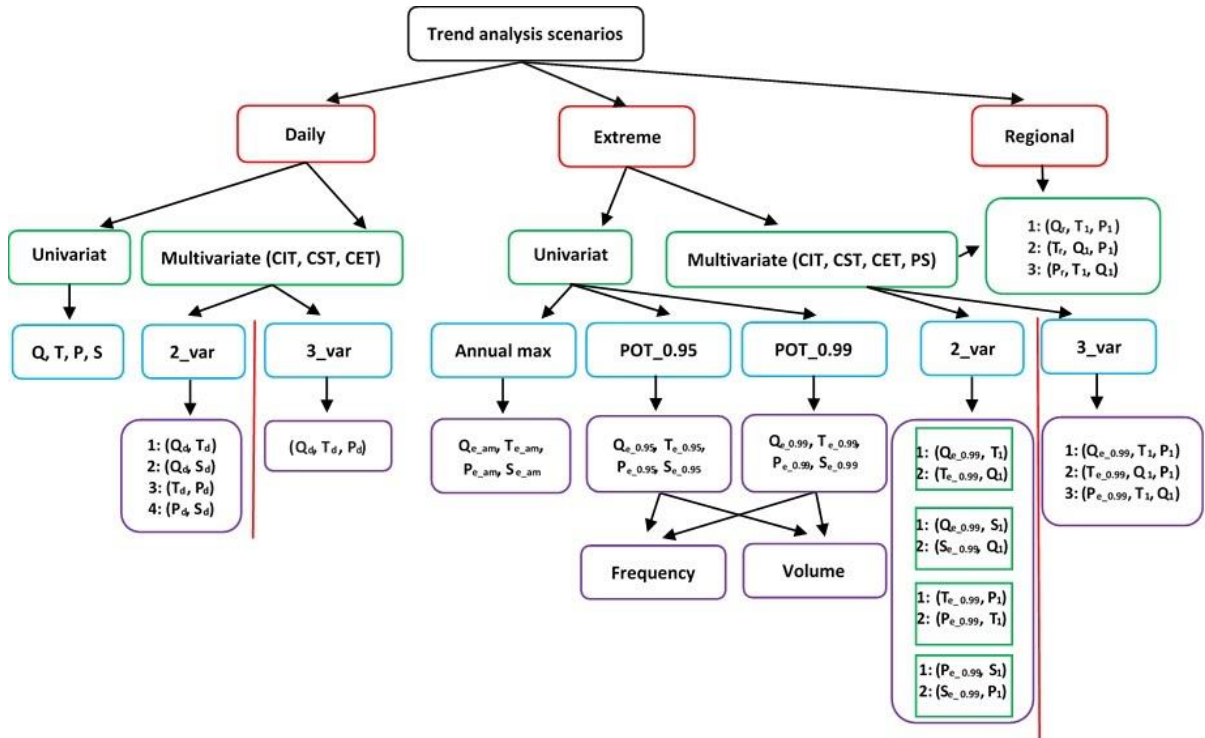
Figure 4.2) The univariate and multivariate trend scenarios based on Streamflow (Q), Total water level (T), Precipitation (P), and Skew surge (S). Letters accompanied by "1" in multivariate extreme scenarios indicate that the corresponding variable(s) (e.g. T1 in (e.g. T1 in (Qe_0.99, T1)) are selected within one day before or after the selected extreme variable (e.g. Qe_0.99 in (Qe_0.99, T1)). Qe_0.99 indicates all the extreme values above the 99th percentile.

4.4. Results

4.4.1. Trends of daily hydrological and coastal variables

2.4.1.1. Univariate trends

Overall, streamflow gauges on the Atlantic coast show statistically significant increasing trends, and the ones on the Great Lakes and the Pacific coasts have a combination of increasing, decreasing, and no significant trends (Figure 4.3). The total water level has increasing trends over the Atlantic coast, and a mix of increases, decreases, and no significant trends on the Pacific coast. Decreases in the Great Lakes' total water levels are

consistent with the results of (Shlozberg et al., 2014) for the study period of 1997-8 to 2012-3. Precipitation data records show decreases in parts of the Great Lakes, increases in parts of the Pacific, and no significant trends over the Atlantic coast, which are consistent with previous findings such as (Akinremi et al., 1999). Skew surge heights are increasing on the Atlantic coasts while increases and decreases are seen over the Great Lakes and the Pacific coasts (Figure 4.3). Locations that have experienced increasing trends in over three variables (total water level, streamflow, and skew surge) are shown by black circles in Figure 4.3, which include the Atlantic regions (including the Cities of St John's and Halifax) and southern parts of the Vancouver Island in the Pacific (e.g. the City of Victoria). Table S4.3 presents the rates of change of the four variables over the study period.
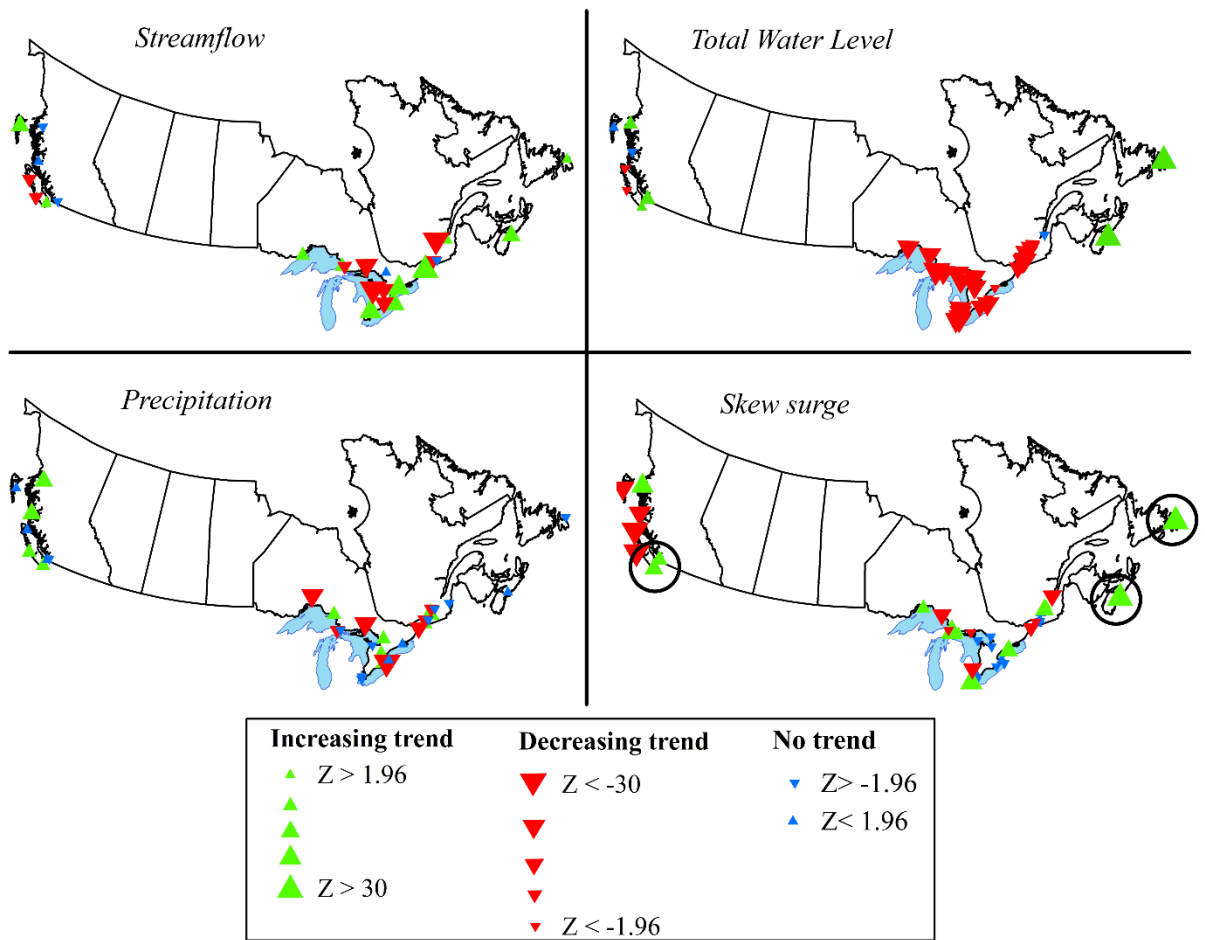
Figure 4.3) The univariate MK trend test results and Z values of the standard normal distribution corresponding to four variables (Q, T, P, and S) over coastal zones of the Atlantic, Pacific, and the Great Lakes. The upward and downward triangles indicate statistically significant increasing and decreasing trends, respectively. The blue solid dots represent no significant trends. The size of the triangles is proportional to the magnitudes of the trends from 1960 to 2015.

2.4.1.2. Multivariate trends

Overall, according to the CIT and CET statistics 25 locations, out of 41, show increasing trends of flow and skew surge (Q_d, S_d), 14 indicate decreases and 2 have no significant trends (6 based on CST) (Figure S4.6). Daily flows and total water levels (Q_d, T_d) show joint temporal changes that are consistent with those of (Q_d, S_d) over the Atlantic and Pacific coasts. However, the majority of stations show decreasing trends in the Great Lakes contrary to the (Q_d, S_d) behavior in this region. Overall, 28 locations show decreasing trends of (Q_d, T_d), 10 locations show increases and 1 station has no statistically significant trend (2 based on CST).

Bivariate trend analyses of daily flows and skew surges (Q_d, S_d) show increases in their joint occurrences over the Atlantic coast consistent with their univariate trends. Decreases over the Pacific coast except for a few locations close to the north and south of Vancouver Island are detected. More locations have experienced increasing trends over the Great Lakes regions than decreases (Figure 4.4). Spatial variations of the precipitation and skew surge (P_d, S_d) bivariate daily trends are similar to those of (Q_d, S_d). Fewer stations (20 locations) show increases, 11 decreases and 10 (17 based on CST) have no significant trends. Bivariate trends of precipitation and total water levels (T_d, P_d) show decreasing trends in almost all locations on the Great Lakes coasts. Overall, 32, 7, and 2 stations show increasing, decreasing and no significant trends, respectively.

Analyses of the joint trends suggest that most locations are expected to experience compound flooding due to joint occurrences of (Q_d, S_d) and (P_d, S_d), especially over the

Great Lakes and the Atlantic coasts. CST, with an additive test statistic (Equation 9), shows fewer locations with significant joint trends compared to the other two methods, because of the different signs of univariate trend statistics as discussed by Lettenmaier (1988). The results indicate that precipitation and skew surge have both positive correlations and increasing joint trends at sites 2, 3, 7, 8 (Pacific coast), 40, and 41 (Atlantic coast) and 9, 10, 11, 12, 13, 14, 15, 24, 25 and 28 (Great Lakes) based on CIT and CET. With a slight difference at the Great Lakes, the results of CST are similar to CIT and CET. Regrading skew surge and streamflow locations 2, 7, and 8 at the Pacific coast, locations 11, 12, 18, 19, 26-31 at the Great Lakes, and site 40 at the Atlantic coast have also a positive correlation with increasing joint trend based on CIT and CET. The Results of CST are only slightly different. This points to potential risks of compound flooding which have been increasing over time at the corresponding locations. The correlation coefficients of the four bivariate daily scenarios at each location and the corresponding significance levels are shown in Figure S4.7.
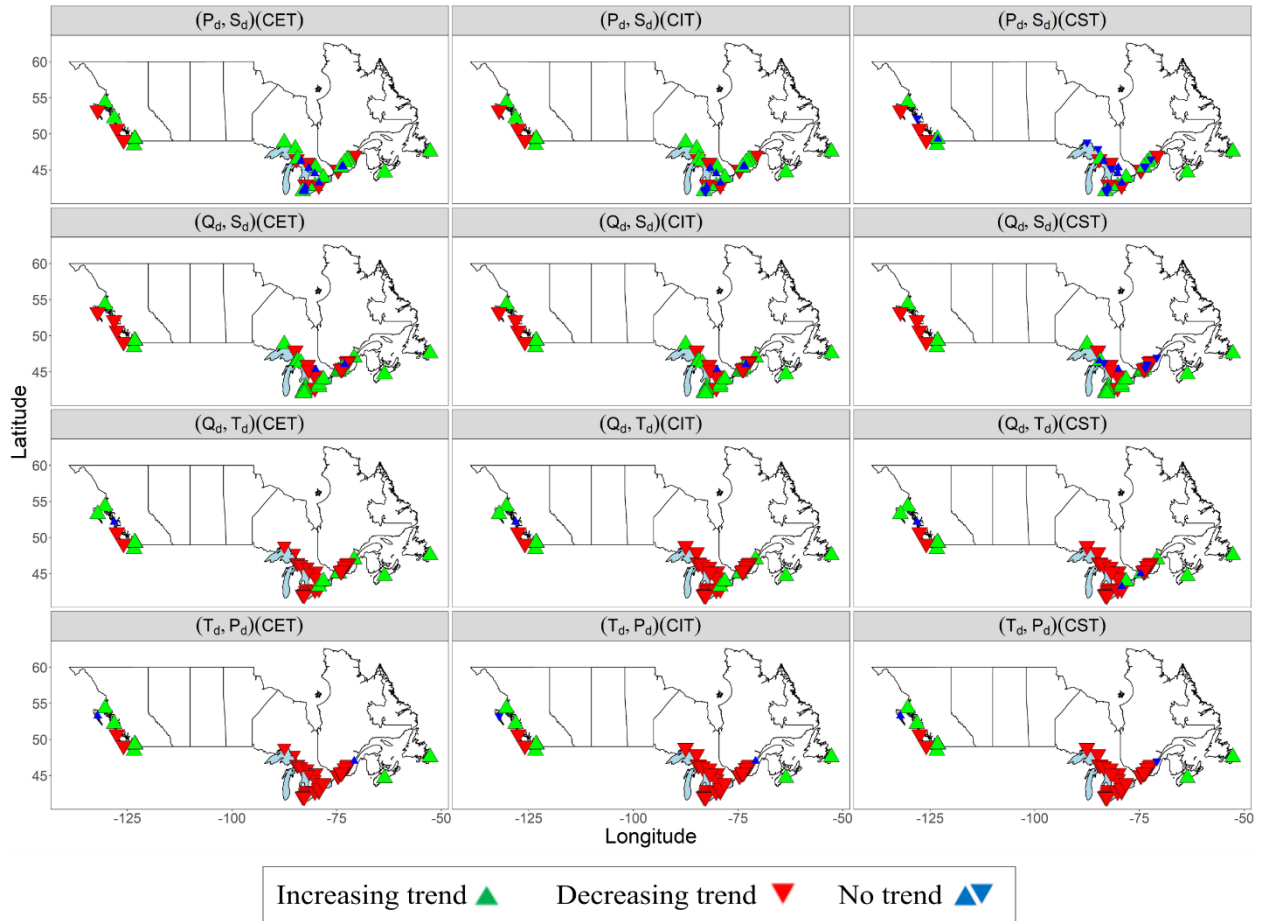
Figure 4.4) The spatial variations of (Qd, Sd), (Qd, Td), (Pd, Sd), and (Td, Pd) bivariate trends based on CIT, CST, and CET. The sizes of symbols represent the magnitudes of the trends.

The trivariate trend analysis of (Q_d, T_d, P_d) shows increases in the Atlantic coast and increases in the north and south parts of the Pacific coast. Almost all locations (more than 20 stations; except for a few locations in Lake Erie and Lake Ontario) show decreasing trivariate trends over the Great Lakes (Figure 4.5). These results are consistent with those of (Q_d, T_d), and (T_d, P_d). The results for the (Q_d, P_d, S_d) scenario are shown in Figure S4.8 (Supplementary materials).
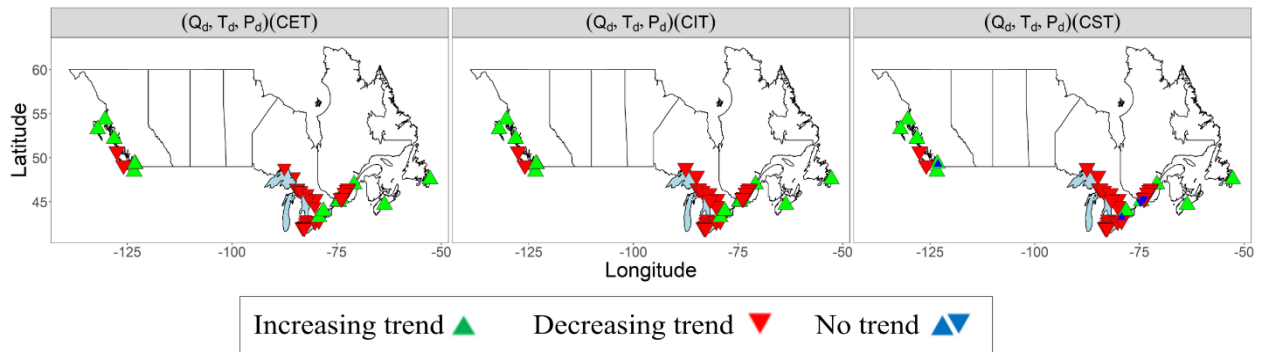
Figure 4.5) Trivariate daily trends of streamflow, precipitation, and total water level over the Atlantic, Pacific, and the Great Lakes coasts. The size of the triangles is proportional to the magnitude of the trends.

4.4.2. Trends of extreme hydrological and coastal variables

4.4.2.1. Univariate trends of the magnitude of extremes

Univariate trends of the annual maximum, $Q_{0.95}$ (95th percentile) and $Q_{0.99}$ (99th percentile) of streamflow, precipitation, skew surge, and total water levels for 41 locations across Canada's coasts (Atlantic, Pacific, and the Great Lakes) are shown in Figure 2.6. While the majority of the streamflow station records show no significant trends (over 35 locations), a few stations on the Atlantic and (northern) Pacific coasts show increases consistent with their univariate daily trends and with previous findings for different periods (Burn et al., 2010; Zhang et al., 2001). Precipitation extremes show no significant trends over the Great Lakes (more than 28 locations) and the Pacific coast except for a few stations based on $Q_{0.99}$ and the annual maxima, respectively. The Atlantic coast shows an increasing trend based on $Q_{0.95}$, which is consistent with *Canada's Changing Climate Report* (2019) and Shephard et al. (2018). Water levels of the Great Lakes show decreasing trends in more than 20 locations according to the annual maximum; however, it shows increases based on $Q_{0.95}$ and $Q_{0.99}$. Water levels corresponding to the $Q_{0.95}$ and $Q_{0.99}$ thresholds do not show significant trends over the Atlantic and Pacific coasts. Similarly, the majority of tidal stations show no significant trends for the skew surge (35 locations), however, increasing trends are detected in the Atlantic and Pacific regions (north and south based on $Q_{0.95}$ and

Q_{0.99}, respectively). The increasing trends of total water level on a daily basis over both the Atlantic and some of Pacific coastal areas are not detected for extreme levels, while, precipitation extremes have increased in several regions. Table S4.4 shows the rates of change of the annual maximum series for the four drivers.
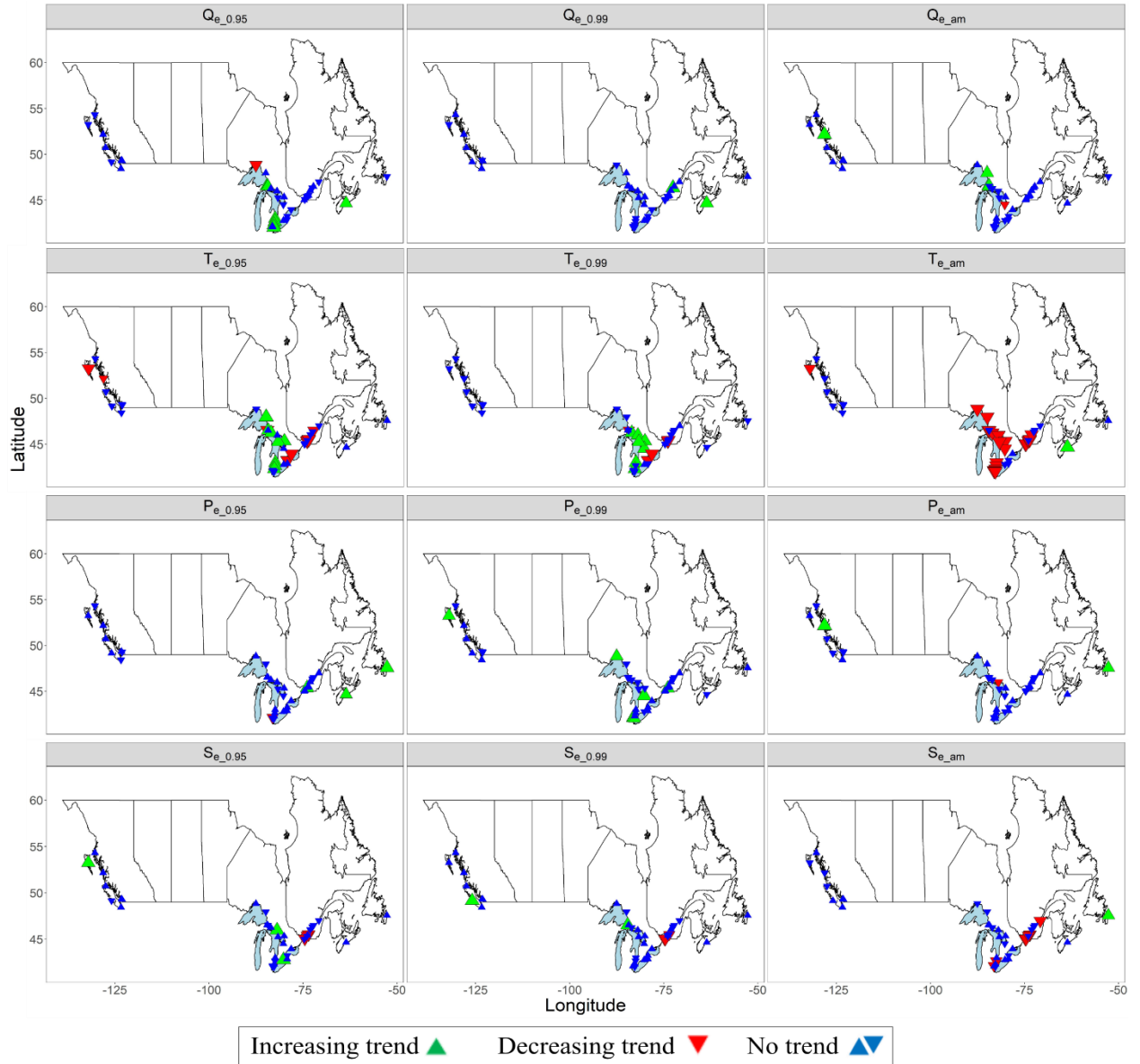
Figure 4.6) Univariate trends of the magnitude of extreme streamflow, precipitation, total water level, and skew surge for 41 locations. Columns show the trends based on the annual maximum, Q0.95, and Q0.99 of the four variables. The size of the triangles is proportional to the magnitude of the trends.

4.4.2.2. Univariate trends of the frequency of extremes

The frequency of extremes is assessed by counting the number of days in each year when the values corresponding to Q, P, T, and S are larger than the $Q_{0.95}$ and $Q_{0.99}$ thresholds (Figure 4.7). Overall, the frequency of extreme streamflow did not change significantly over the study period. However, results show increasing trends of high extreme values (above $Q_{0.99}$) over several locations on the Great Lakes. The Atlantic coasts have experienced increases in the number of extreme total water levels (similar to their magnitudes) while most locations over the Great Lakes experienced decreasing trends (more than 20 for $Q_{0.95}$ and over 17 for $Q_{0.99}$). The frequencies of extreme precipitation events in the Canadian coastal zones do not show significant trends except for the Atlantic where increasing trends are detected, consistent with Menendez and Woodworth (2010). Trends in the Atlantic coasts might indicate increases in the number of tropical cyclones. Similarly, a majority of the studied tidal gauges do not show trends in the skew surge frequency across the coastline except for the Atlantic (based on both $Q_{0.95}$ and $Q_{0.99}$).

The east coasts show increasing skew surge trends while regions on the west coasts and the Great Lakes did not generally possess significant trends.

Increasing trend ▲   Decreasing trend ▼   No trend ▲▼
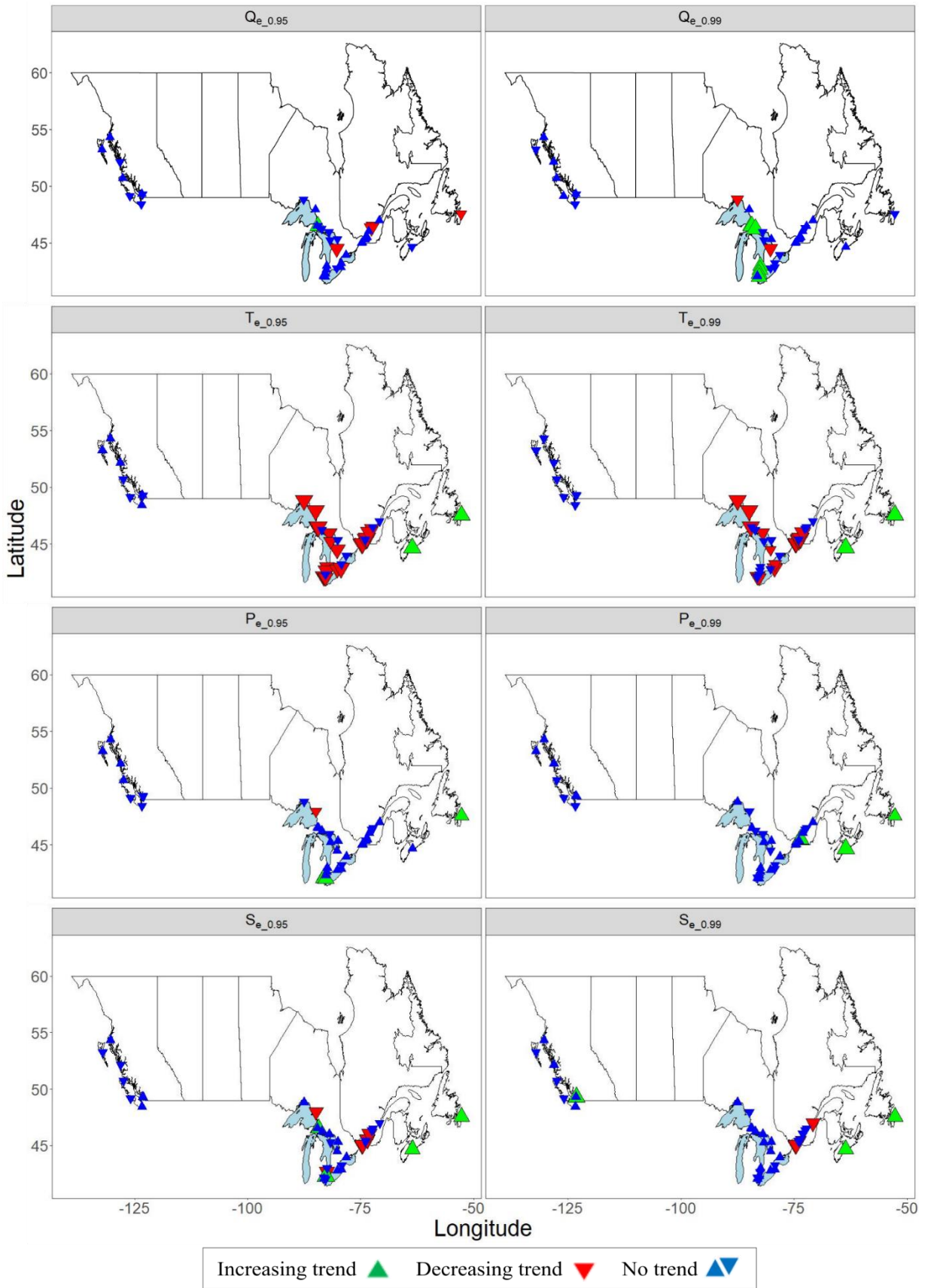
Figure 4.7) The univariate trends of the frequency of extreme streamflow, precipitation, total water level, and skew surge for 41 locations. Columns show the trends based on Q0.95 and Q0.99 values of the four variables. The size of the triangles is proportional to the magnitude of the trends.

4.4.2.3. Bivariate trends of extremes

Trends of bivariate extremes that can cause compound coastal flooding are assessed using CIT, CST, CET, and PS (Table 4.1). Figure 4.8 shows spatially varying trends of the $(Q_{e\_0.99}, T_1)$ and $(T_{e\_0.99}, Q_1)$ scenarios (other scenarios are presented in the Supplementary Information). CET, CIT, and CST show no bivariate trends over the Pacific coast in both scenarios (with insignificant correlations except for 2 sites based on the scenario $(T_{e\_0.99}, Q_1)$). Increasing trends of $(Q_{e\_0.99}, T_1)$ are detected over the Atlantic coast but no significant correlations exist between the two variables. Over the Great Lakes, except for some locations with no trends, several locations show increasing trends for both $(Q_{e\_0.99}, T_1)$ and $(T_{e\_0.99}, Q_1)$ based on CIT, CET, and CST. Locations 14 to 24 (except 17 and 18) also show positive significant correlations. Locations with no significant trends based on these methods show decreasing trends based on PS. The range of $Q_{0.99}$ of the aggregated transformed values is between 1.88 to 1.92 for different gauges.

Table 4.1) The number of locations with increasing, decreasing, and no significant bivariate trend for different scenarios

Scenario	CIT			CST			CET			PS		
	▲	▼	▲▼	▲	▼	▲▼	▲	▼	▲▼	▲	▼	▲▼
Q,T1	**28**	0	13	**28**	0	13	**23**	4	14	10	11	**20**
T,Q1	20	0	21	20	0	**21**	9	6	**26**	11	13	**17**
Q,S1	9	1	**31**	9	1	**31**	8	7	**26**	5	8	**28**
S,Q1	9	2	**30**	10	2	**29**	11	2	**28**	2	10	**29**
T,P1	14	0	**27**	15	0	**26**	6	7	28	11	5	**25**
P,T1	**29**	0	12	**28**	0	13	**18**	5	18	2	10	**29**
P,S1	10	1	**30**	10	1	**30**	9	0	**32**	6	1	**34**
S,P1	6	4	**31**	6	4	**31**	5	4	**32**	2	1	**38**

Increasing trend ▲   Decreasing trend ▼   No trend ▲▼

Figure 4.8) The bivariate trends of two extreme scenarios of (Qe_0.99, T1) (Q values above the Q0.99 threshold and maximum T values within one day before or after) and (Te_0.99, Q1) for 41 locations using CIT, CST, CET, and PS. The size of the triangles is proportional to the magnitude of the trends.

As mentioned before, the proposed index has the flexibility to assess the joint trends of compound flood drivers for different levels of magnitude. We analyze the trends of such compound extremes based on $Q_{0.99}$, $Q_{0.975,}$ and $Q_{0.95}$ of the joint variability of ($T_{e\_0.99}$, Q_1) using this metric. The results are shown for site #40 on the Atlantic coast (Figure S4.9). Increasing trends are detected for this location based on the PS index while the other approaches (i.e. CIT, CET, and CST) reveal no trends. Figures S4.10 and S4.11 show the spatial variations of the joint trends based on PS for (Q_e, T_1) and (T_e, Q_1) scenarios, and the corresponding bivariate correlations, respectively.

The results of CIT, CST, and CET are consistent in representing the two scenarios of ($Q_{e\_0.99}$, S_1) and ($S_{e\_0.99}$, Q_1), (between 26 to 30 locations have no significant trends). The Atlantic coast shows increases in ($Q_{e\_0.99}$, S_1), but not ($S_{e\_0.99}$, Q_1), however, the correlation is not significant indicating less risk of flooding. At the Great Lakes, only site# 24 has both increasing joint trends of ($S_{e\_0.99}$, Q_1) based on CIT and CST and positive correlation. Between 2 to 5 gauges on the Great Lakes have increasing trends in ($Q_{e\_0.99}$, S_1), however, the correlations are not significant. Similarly, 1-2 gauges on the Pacific coast have increasing trends, but there is no significant positive correlation. The bivariate trends and the correlation coefficients along with their corresponding significance levels of these two bivariate scenarios are presented in Figures S4.12 and S4.13, respectively. The information related to other bivariate scenarios is in supplementary materials (Figures S4.14 to S4.19).

4.4.2.4. Tri-variate trends of extremes

Spatial distributions of trivariate trends of ($Q_{e\_0.99}$, T_1, P_1) (i.e. $Q > Q_{0.99}$), ($T_{e\_0.99}$, Q_1, P_1) and ($P_{e\_0.99}$, Q_1, T_1) are shown in Figure 2.9. Similar to the bivariate scenarios, there are generally no significant trivariate trends over the Pacific coast. Significant increasing and decreasing trends are detected over the Atlantic coast for ($Q_{e\_0.99}$, T_1, P_1) (based on CIT, CET, and PS) as well as increases in ($P_{e\_0.99}$, Q_1, T_1) (based on the four methods),

respectively. Figure S4.20 also illustrates the trend of PS values for different gauges concerning $Q_{0.95}$ and $Q_{0.975}$ in this scenario.

Following Jaiswal et al. (2015) and Rahmani et al. (2015), we performed a change point detection analysis of the data in univariate daily and extreme scenarios besides investigating the overall trends. No more than a few gauges (sites 7, 12, 18, and 24) indicated change points in their data records.
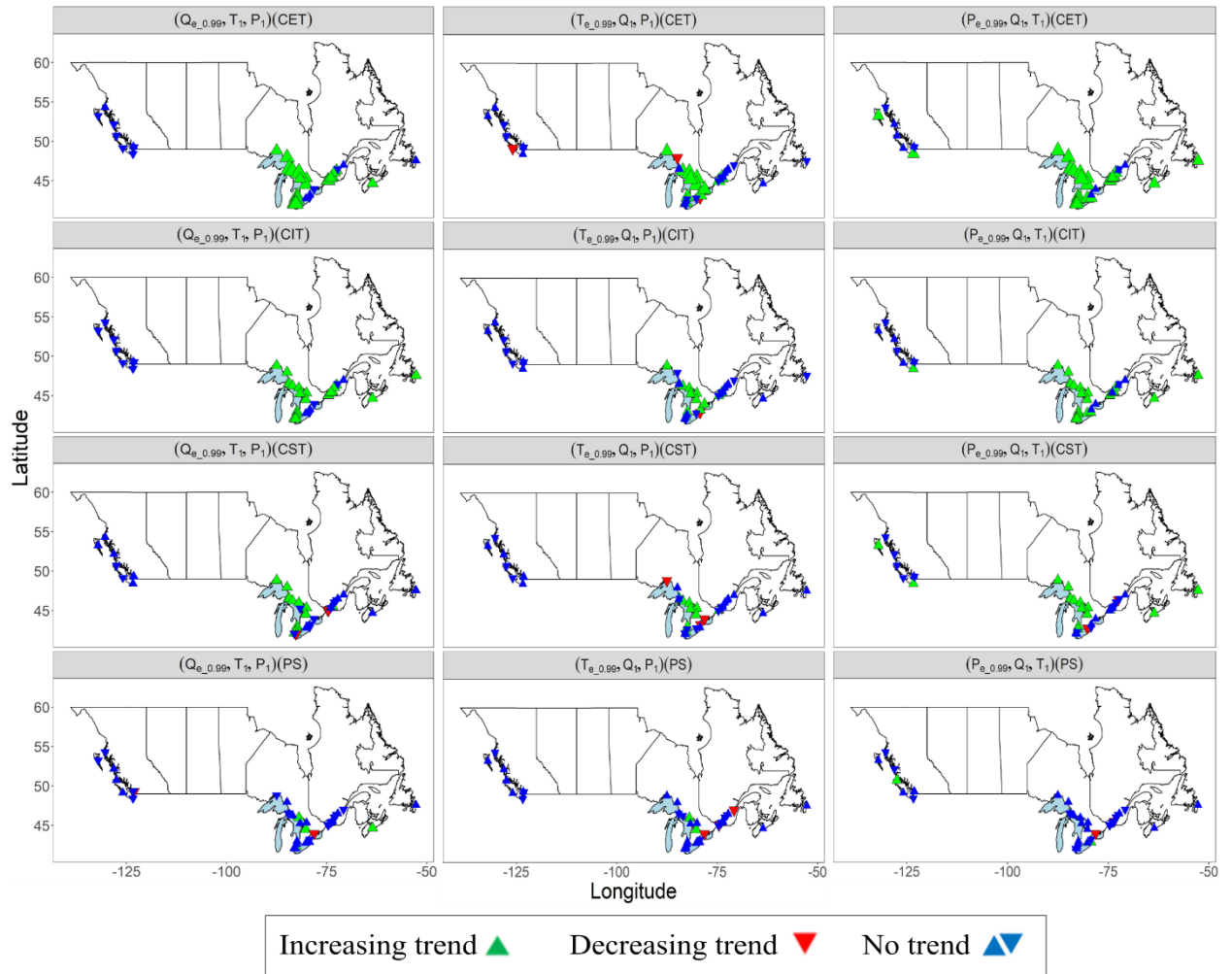
Figure 4.9) The extreme trend analysis for trivariate scenarios (Q, T, P) using four metrics of CIT, CST, CET, and PS. The threshold for extremes is Q0.99. The size of the triangles is proportional to the magnitude of the trends.

4.4.3. Regional trends of the extremes

The results of regional extreme trend analysis indicate that ($Q_{e\_0.99}$, T_1, P_1) does not show significant trends over most areas except for the Pacific coast, which shows increases based on CIT and CET. Regarding ($T_{e\_0.99}$, Q_1, P_1), the CIT, CST, and CET methods show an increasing trend on the Atlantic coast and CST indicates decreases over the Pacific. Otherwise, on the Pacific and the Great Lakes, there are no significant trivariate ($T_{e\_0.99}$, Q_1, P_1) trends. CST detected an increasing trend in ($P_{e\_0.99}$, Q_1, T_1) over the Pacific and CET showed no trends over the Atlantic coast (Figure S4.21).

4.5. Discussion

This study provides a comprehensive analysis of the individual trends of hydroclimatic and coastal variables at the Canadian coasts and extends the analyses to multivariate scenarios. Variations in streamflow trends over Canada's coasts, such as increases in eastern Canada, can be attributed to changes in the snowpack/snowmelt magnitude and timing over the region (Najafi et al., 2017; Najafi et al., 2016), changes in rain-on-snow events, among others due to climate change, water usage and land-use change (Bush and Lemmen, 2019b). Results of daily precipitation trends are consistent with previous findings such as (Akinremi et al., 1999).

The three coastal areas that are analyzed in this study have distinct characteristics. Total water levels on the Atlantic and Pacific coasts are associated with the mean sea level of the oceans, storm surges, and tides, while the Great Lakes' water levels are mainly governed by mean levels, and inflows from the surrounding watersheds and storm surges. Skew surge changes in the Great Lakes are mainly dependent on squall lines and seiches (Danard et al., 2003; Pugh and Woodworth, 2014). In addition, increasing trends of daily skew surges over the Atlantic coast are mainly due to changes in the tropical cyclones' intensities, track, and size (Bush and Lemmen, 2019b). With fewer tropical cyclone occurrences, this is also partly true for the Pacific coast (Bromirski et al., 2017).

According to Bush and Lemmen (2019), evaporation in the Great Lakes is increasing while runoff is decreasing, resulting in overall decreases in the Great Lakes' daily water levels.

In addition, Kuo et al. (2008) reported land uplifts in Lake Superior, Lake Huron, Lake Ontario, and the upper part of Lake Michigan and Lake Erie and subsidence in the lower part of Lake Michigan and Lake Erie. These changes can result in decreases or increases in total water levels as discussed in the previous section. The increasing water levels observed over the Atlantic coasts can be attributed to the thermal expansion and glacier melts due to climate change, and land subsidences (Karegar et al., 2016). Our analyses are also consistent with previous studies that showed the average relative sea levels have increased at Prince Rupert, Victoria, and Vancouver, and have declined at Tofino (White et al., 2016).

The analyses show that the individual and joint drivers of compound flooding have nonstationary behavior over Canada's coasts. Previous studies have found nonstationarity in the dependencies between such variables. Wahl et al. (2015) studied changes in the dependencies between historical storm surge and precipitation events over the U.S coasts and identified regions that are at higher risk of flooding. Bevacqua et al. (2019) and Moftakhari et al. (2017) studied changes in the bivariate behavior (dependence) of storm surge/precipitation and fluvial flooding/sea level using historical and projected data, respectively. Building on such previous studies, we characterized the dependencies between multiple drivers and analyzed the corresponding joint trends over all locations. The combination of the two metrics allowed us to identify regions on the Pacific coast (sites 2, 3, and 8) and on the Atlantic coast (locations 40 and 41) that show positive correlations of the skew surge and precipitation and have increasing daily joint trends, therefore facing increasing risks of compound flooding (joint skew surge and pluvial flooding). This situation is also true for locations at the Great Lakes coasts such as 14, 24, 17, and 18 in Figure 4.8 for scenarios ($Q_{e\_0.99}$, T). Ward et al. (2018) found significant dependence between high discharge and skew surge and total sea-level for some locations at the western U.S which is consistent with our results. Regarding scenario ($S_{e\_0.99}$, Q), the results are consistent with those of Couasnon et al. (2019) who found no significant correlations. This consistency is true for scenario ($Q_{e\_0.99}$, S) except at the Atlantic coast where we detected a significant correlation. Regarding scenario ($P_{e\_0.99}$, Q1, T1), all three drivers have increasing joint trends at the Atlantic coast. This indicates relatively high

flood risks in this region. The results highlight that current policies for managing and mitigating flood risks in these coastal areas based on individual drivers should be updated and new strategies considering multidriver scenarios should be adopted.

We propose a simple and flexible index (i.e. PS) to study compound flooding and its temporal characteristics. The corresponding results of the joint trends are consistent with the ones obtained from CIT, CET, and CST. The advantage of PS is that different flood drivers can be weighted based on historical events and expert knowledge to determine which variables have more significant impacts. The metric can also be extended to pool data from neighboring stations for regional analyses.

4.6. Conclusions

The univariate and multivariate historical trends of four variables that contribute to compound flooding in Canadian coastal zones are studied. This includes multiple scenarios of daily, extreme, and regionally aggregated streamflow, precipitation, total water level, and skew surge over the western (Pacific) and eastern (Atlantic) coasts, and the Great Lakes regions.

The univariate analysis of daily data records shows both positive and negative trends, however, all variables except for precipitation, show increases over the Atlantic coast. The multivariate trend analysis indicates strong associations between drivers of compound flooding in Canada's coasts. Overall, results show negative joint trends over the Great Lakes and increases in the Atlantic coast. Trends of univariate extremes are not as strong as the ones related to daily values. However, they all show increases in the frequency and intensity of individual extreme events over the Atlantic coast. The bivariate daily scenarios highlight increasing compound flood risks over the Great Lakes, Pacific, and Atlantic coasts due to a combination of streamflow, precipitation, and total water level extremes. The sites at the Atlantic coast and a few locations at the Pacific coast show both increasing joint trends of precipitation and skew surge and positive correlations. This indicates high risks of compound flooding that have been increasing historically. The Atlantic coast also shows increasing trends in trivariate extremes.

Overall, the three non-parametric methods of CIT, CST, and CET show consistent results. CST detects slightly fewer significant trends compared to the other methods. It is shown that the CST power is decreased if the individual variables have different directions (Lettenmaier, 1988a), therefore, CET and CIT are relatively stronger metrics to detect multivariate trends (Modarres, 2018). The results of the proposed PS metric are consistent with the other three methods. PS is not sensitive to the effects of outliers and the sample size and can be easily modified to increase the weights of individual flood drivers and pool data from different locations. Therefore, the proposed index is a simple, flexible, and robust approach to study compound flooding.

The univariate and multivariate trend analysis of compound flood drivers can provide a more in-depth understanding of the corresponding nonstationarities. This will lead to the development of more accurate and robust models to predict compound flooding in coastal zones.

Acknowledgment

References

Abdulkareem, J.H., Sulaiman, W.N.A., 2016. TREND ANALYSIS OF PRECIPITATION DATA IN FLOOD SOURCE AREAS OF KELANTAN RIVER BASIN. *Jurnal Teknologi*, 78(9-4).

Akinremi, O., McGinn, S., Cutforth, H., 1999. Precipitation trends on the Canadian prairies. *Journal of Climate*, 12(10): 2996-3003.

Altava-Ortiz, V., Llasat, M.C., Ferrari, E., Atencia, A., Sirangelo, B., 2011. Monthly rainfall changes in Central and Western Mediterranean basins, at the end of the 20th and beginning of the 21st centuries. *International Journal of Climatology*, 31(13): 1943-1958.

Bevacqua, E., Maraun, D., Hobæk Haff, I., Widmann, M., Vrac, M., 2017. Multivariate statistical modelling of compound events via pair-copula constructions: analysis of floods in Ravenna (Italy). *Hydrology and Earth System Sciences*, 21(6): 2701-2723.

Bevacqua, E. et al., 2019. Higher probability of compound flooding from precipitation and storm surge in Europe under anthropogenic climate change. *Science advances*, 5(9): eaaw5531.

Bromirski, P.D., Flick, R.E., Miller, A.J., 2017. Storm surge along the P acific coast of N orth A merica. *Journal of Geophysical Research*: Oceans, 122(1): 441-457.

Burn, D.H., Sharif, M., Zhang, K., 2010. Detection of trends in hydrological extremes for Canadian watersheds. *Hydrological processes*, 24(13): 1781-1790.

Bush, E., Lemmen, D., 2019a. Canada's changing climate report. Government of Canada. Ottawa: Government of Canada. Retrieved from http://www. *Changing climate*. ca ….

Bush, E., Lemmen, D.S., 2019b. Canada's Changing Climate Report. Government of Canada= Gouvernement du Canada.

Cavadias, G., 1994. Detection and modeling of the impact of climatic change on river flows, *Engineering Risk in Natural Resources Management*. Springer, pp. 207-218.

Chebana, F., Ouarda, T.B., Duong, T.C., 2013. Testing for multivariate trends in hydrologic frequency analysis. *Journal of hydrology*, 486: 519-530.

Chingombe, W., Gutierrez, J., Pedzisai, E., Siziba, E., 2005. A Study of Hydrological Trends and Variability of Upper Mazowe Catchment, Zimbabwe. *Journal of Sustainable Development in Africa*, 7(1): 1-17.

Clement, L., Thas, O., 2009. Nonparametric trend detection in river monitoring network data: a spatio-temporal approach. Environmetrics: *The official journal of the International Environmetrics Society*, 20(3): 283-297.

Codiga, D.L., 2011. Unified tidal analysis and prediction using the UTide Matlab functions. Graduate School of Oceanography, University of Rhode Island Narragansett, RI.

Couasnon, A. et al., 2019. Measuring compound flood potential from river discharge and storm surge extremes at the global scale and its implications for flood hazard.

Danard, M., Munro, A., Murty, T., 2003. Storm surge hazard in Canada. *Natural Hazards*, 28(2-3): 407-434.

Dietz, E.J., Killeen, T.J., 1981. A nonparametric multivariate test for monotone trend with pharmaceutical applications. *Journal of the American Statistical Association*, 76(373): 169-174.

Dudek, A.E., 2018. Block bootstrap for periodic characteristics of periodically correlated time series. *Journal of Nonparametric Statistics*, 30(1): 87-124.

Dudek, A.E., Leśkow, J., Paparoditis, E., Politis, D.N., 2014. A generalized block bootstrap for seasonal time series. *Journal of Time Series Analysis*, 35(2): 89-114.

Eilander, D. et al., 2020. The effect of surge on riverine flood hazard and impact in deltas globally.

Fraser, J., Smith, R., 2002. Indicators of climate change for British Columbia. Ministry of Water, *Land and Air Protection*, Victoria.

Gan, T.Y., 1998. Hydroclimatic trends and possible climatic warming in the Canadian Prairies. *Water resources research*, 34(11): 3009-3015.

Ganguli, P., Merz, B., 2019. Trends in Compound Flooding in Northwestern Europe During 1901–2014. *Geophysical Research Letters*, 46(19): 10810-10820.

Haigh, I.D. et al., 2016. Spatial and temporal analysis of extreme sea level and storm surge events around the coastline of the UK. *Scientific data*, 3(1): 1-14.

Hao, Z., Singh, V., Hao, F., 2018. Compound extremes in hydroclimatology: *a review. Water*, 10(6): 718.

Hendry, A. et al., 2019. Assessing the characteristics and drivers of compound flooding events around the UK coast. *Hydrology and Earth System Sciences*, 23: 3117-3139.

Hirsch, R.M., Slack, J.R., 1984a. A nonparametric trend test for seasonal data with serial dependence. *Water Resources Research*, 20(6): 727-732.

Hirsch, R.M., Slack, J.R.J.W.R.R., 1984b. A nonparametric trend test for seasonal data with serial dependence. 20(6): 727-732.

Jaiswal, R., Lohani, A., Tiwari, H., 2015. Statistical analysis for change detection and trend assessment in climatological parameters. *Environmental Processes*, 2(4): 729-749.

Kang, L., Jiang, S., Hu, X., Li, C., 2019. Evaluation of Return Period and Risk in Bivariate Non-Stationary Flood Frequency Analysis. *Water*, 11(1): 79.

Karegar, M.A., Dixon, T.H., Engelhart, S.E., 2016. Subsidence along the Atlantic Coast of North America: Insights from GPS and late Holocene relative sea level data. *Geophysical Research Letters*, 43(7): 3126-3133.

Kendall, M. (1975). Rank correlation methods, book series, Charles Griffin. In: Oxford University Press, USA, London.

Khalili, K., Ahmadi, F., Dinpashoh, Y., Fard, A.F., 2013. Determination of climate changes on stream flow process in the West of Lake Urmia with used to trend and stationarity analysis. *International journal of Advanced Biological and Biomedical Research*, 1(10): 1220-1235.

Khaliq, M., Ouarda, T., Gachon, P., Sushama, L., St-Hilaire, A., 2009. Identification of hydrological trends in the presence of serial and cross correlations: A review of selected methods and their application to annual flow regimes of Canadian rivers. *Journal of Hydrology*, 368(1-4): 117-130.

Khanal, S., Ridder, N., Terink, W., Hurk, B.v.d., 2019. Storm surge and extreme river discharge: A compound event analysis using ensemble impact modelling. *Frontiers in Earth Science*, 7: 224.

Kuo, C.-Y., Shum, C., Braun, A., Cheng, K.-C., Yi, Y., 2008. Vertical motion determined using satellite altimetry and tide gauges. Terr. Atmos.

Landis, M.S. et al., 2018. The impact of the 2016 Fort McMurray Horse River wildfire on ambient air pollution levels in the Athabasca Oil Sands Region, Alberta, Canada. *Science of the Total Environment*, 618: 1665-1676.

Lavell, A. et al., 2012. Managing the risks of extreme events and disasters to advance climate change adaptation. A Special Report of Working Groups I and II of the *Intergovernmental Panel on Climate Change* (IPCC): 25-64.

Lettenmaier, D.P., 1988a. MULTIVARIATE NONPARAMETRIC TESTS FOR TREND IN WATER QUALITY 1. JAWRA *Journal of the American Water Resources Association*, 24(3): 505-512.

Lettenmaier, D.P.J.J.J.o.t.A.W.R.A., 1988b. MULTIVARIATE NONPARAMETRIC TESTS FOR TREND IN WATER QUALITY 1. 24(3): 505-512.

Loftis, J.C., Taylor, C.H., Chapman, P.L.J.W.R.R., 1991a. *Multivariate tests for trend in water quality*. 27(7): 1419-1429.

Loftis, J.C., Taylor, C.H., Newell, A.D., Chapman, P.L.J.J.J.o.t.A.W.R.A., 1991b. MULTIVARIATE TREND TESTING OF LAKE WATER QUALITY 1. 27(3): 461-473.

Machiwal, D., Jha, M.K., 2012. Hydrologic time series analysis: theory and practice. Springer Science & Business Media.

Mann, H. B. (1945). Nonparametric tests against trend. Econometrica*: Journal of the econometric society*, 245-259.

Mata-Lima, H. et al., 2007. Comportamento hidrológico de bacias hidrográficas: integração de métodos e aplicação a um estudo de caso. *Rem: Revista Escola de Minas*, 60(3): 525-536.

Mawdsley, R.J., Haigh, I.D., 2016. Spatial and temporal variability and long-term trends in skew surges globally. *Frontiers in Marine Science*, 3: 29.

Menéndez, M., Woodworth, P.L., 2010. Changes in extreme high water levels based on a quasi-global tide-gauge data set. *Journal of Geophysical Research: Oceans*, 115(C10).

Miao, C., Ni, J., Borthwick, A.G., Yang, L., 2011. A preliminary estimate of human and natural contributions to the changes in water discharge and sediment load in the Yellow River. *Global and Planetary Change*, 76(3-4): 196-205.

Milly, P.C. et al., 2008. Stationarity is dead: Whither water management? *Science*, 319(5863): 573-574.

Modarres, R., 2018. Bivariate trend assessment of dust storm frequency in relation to climate drivers. *Natural Hazards and Earth System Sciences Discussions:* 1-24. DOI:10.5194/nhess-2018-302

Modarres, R., Sarhadi, A., 2009. Rainfall trends analysis of Iran in the last half of the twentieth century. *Journal of Geophysical Research: Atmospheres*, 114(D3).

Moftakhari, H.R., Salvadori, G., AghaKouchak, A., Sanders, B.F., Matthew, R.A., 2017. Compounding effects of sea level rise and fluvial flooding. *Proceedings of the National Academy of Sciences,* 114(37): 9785-9790.

Muis, S., Verlaan, M., Winsemius, H.C., Aerts, J.C., Ward, P.J., 2016. A global reanalysis of storm surges and extreme sea levels. *Nature communications*, 7: 11969.

Najafi, M.R., Zwiers, F., Gillett, N., 2017. Attribution of the observed spring snowpack decline in British Columbia to anthropogenic climate change. *Journal of Climate*, 30(11): 4113-4130.

Najafi, M.R., Zwiers, F.W., Gillett, N.P., 2016. Attribution of the spring snow cover extent decline in the Northern Hemisphere, Eurasia and North America to anthropogenic influence. *Climatic Change*, 136(3-4): 571-586.

Önöz, B., Bayazit, M., 2012. Block bootstrap for Mann–Kendall trend test of serially dependent data. *Hydrological Processes*, 26(23): 3552-3560.

Paprotny, D., Vousdoukas, M.I., Morales-Nápoles, O., Jonkman, S.N., Feyen, L., 2018. Compound flood potential in Europe. *Hydrol. Earth Syst.* Sci. Discuss, 2018: 1-34.

Pasquier, U., He, Y., Hooton, S., Goulden, M., Hiscock, K.M., 2019. An integrated 1D–2D hydraulic modelling approach to assess the sensitivity of a coastal region to compound flooding hazard under climate change. *Natural Hazards*, 98(3): 915-937.

Peel, M.C., Finlayson, B.L., McMahon, T.A.J.H., discussions, e.s.s., 2007. Updated world map of the Köppen-Geiger climate classification. 4(2): 439-473.

Politis, D.N., 2003. The impact of bootstrap methods on time series analysis. *Statistical Science:* 219-230.

Pugh, D., Woodworth, P., 2014. Sea-level science: understanding tides, surges, tsunamis and mean sea-level changes. Cambridge University Press.

Rahmani, V., Hutchinson, S.L., Harrington Jr, J.A., Hutchinson, J.S., Anandhi, A., 2015. Analysis of temporal and spatial distribution and change-points for annual precipitation in Kansas, USA. *International Journal of Climatology*, 35(13): 3879-3887.

Re, M., 2017. NatCatSERVICE Database (Munich: Munich Reinsurance Company, *Geo Risks Research*).

Sarhadi, A., Ausín, M.C., Wiper, M.P., Touma, D., Diffenbaugh, N.S., 2018. Multidimensional risk in a nonstationary climate: Joint probability of increasingly severe warm and dry conditions. *Science advances*, 4(11): eaau3487.

Sarhadi, A., Burn, D.H., Concepcion Ausin, M., Wiper, M.P., 2016. Time-varying nonstationary multivariate risk analysis using a dynamic Bayesian copula. *Water Resources Research*, 52(3): 2327-2349.

Seneviratne, S.I. et al., 2012. Changes in climate extremes and their impacts on the natural physical environment, Managing the risks of extreme events and disasters to advance climate change adaptation: *Special report of the Intergovernmental Panel on Climate Change.* Cambridge University Press, pp. 109-230.

Serafin, K.A., Ruggiero, P., Parker, K., 2019. What's streamflow got to do with it? A probabilistic simulation of the competing oceanographic and fluvial processes driving extreme along-river water levels. *Natural Hazards and Earth System Sciences*, 19.

Shadmani, M., Marofi, S., Roknian, M., 2012. Trend analysis in reference evapotranspiration using Mann-Kendall and Spearman's Rho tests in arid regions of Iran. *Water resources management*, 26(1): 211-224.

Shlozberg, R., Dorling, R., Spiro, P., 2014. Low water blues: An economic impact assessment of future low water levels in the great lakes and st. lawrence river. Mowat Centre.

Sonali, P., Kumar, D.N., 2013. Review of trend detection methods and their application to detect temperature changes in India. *Journal of Hydrology*, 476: 212-227.

Svensson, C., Jones, D.A., 2002. Dependence between extreme sea surge, river flow and precipitation in eastern Britain. International Journal of Climatology: *A Journal of the Royal Meteorological Society*, 22(10): 1149-1168.

Svensson, C., Kundzewicz, W.Z., Maurer, T., 2005. Trend detection in river flow series: 2. Flood and low-flow index series/Détection de tendance dans des séries de débit fluvial: 2. Séries d'indices de crue et d'étiage. *Hydrological Sciences Journal*, 50(5).

Thas, O., Vooren, L.V., Ottoy, J.-P.J.J.o.t.A.W.R.A., 1998. NONPARAMETRIC TEST PERFORMANCE FOR TRENDS IN WATER QUALITY WITH SAMPLING DESIGN APPLICATIONS 1. 34(2): 347-357.

Van Belle, G., Hughes, J.P.J.W.r.r., 1984. Nonparametric tests for trend in water quality. 20(1): 127-136.

Verhoest, N.E. et al., 2010. Are stochastic point rainfall models able to preserve extreme flood statistics? *Hydrological processes*, 24(23): 3439-3445.

Von Storch, H., 1999. Misuses of statistical analysis in climate research, Analysis of climate variability. Springer, pp. 11-26.

Wahl, T., Jain, S., Bender, J., Meyers, S.D., Luther, M.E., 2015. Increasing risk of compound flooding from storm surge and rainfall for major US cities. *Nature Climate Change*, 5(12): 1093-1097.

Ward, P.J. et al., 2018. Dependence between high sea-level and high river discharge increases flood hazard in global deltas and estuaries. *Environmental Research Letters*, 13(8): 084012.

White, T., Wolf, J., Anslow, F., Werner, A., Creative, R., 2016. Indicators of climate change for British Columbia. 2016 update. *British Columbia Ministry of Environment*, Victoria, BC.

Williams, J., Horsburgh, K.J., Williams, J.A., Proctor, R.N., 2016. Tide and skew surge independence: New insights for flood risk. *Geophysical Research Letters*, 43(12): 6410-6417.

Wu, W., Leonard, M., 2019. Impact of ENSO on dependence between extreme rainfall and storm surge. *Environmental Research Letters*, 14(12): 124043.

Wu, W. et al., 2018. Mapping dependence between extreme rainfall and storm surge. *Journal of Geophysical Research:* Oceans, 123(4): 2461-2474.

Xu, H., Xu, K., Lian, J., Ma, C., 2019. Compound effects of rainfall and storm tides on coastal flooding risk. *Stochastic Environmental Research and Risk Assessment*, 33(7): 1249-1261.

Ye, L., Zhou, J., Zeng, X., Tayyab, M., 2015. Hydrological Mann-Kendal multivariate trends analysis in the Upper Yangtze River basin. *Journal of Geoscience and Environment Protection*, 3(10): 34.

Zhang, X., Harvey, K.D., Hogg, W., Yuzyk, T.R., 2001. Trends in Canadian streamflow. *Water Resources Research*, 37(4): 987-998.

Zheng, F., Westra, S., Leonard, M., Sisson, S.A., 2014. Modeling dependence between extreme rainfall and storm surge to estimate coastal flooding risk. *Water Resources Research*, 50(3): 2050-2071.

Zscheischler, J. et al., 2018. Future climate risk from compound events. *Nature Climate Change*, 8(6): 469-477.

Chapter 5

5. Nonstationary frequency analysis of compound flooding across coastal environments

5.1. Introduction

Flooding is the most common natural hazard causing an estimated annual damage of around US$50 billion worldwide (Wilhelm et al., 2022). In Canada, the associated impacts on the communities and assets have been increasing in many regions, such as along most of the Atlantic and Pacific coasts and the Beaufort coast in the Arctic, in part due to increases in the frequency and intensity of floods and also high exposure of people, property and infrastructure to flooding events (Bush and Lemmen, 2019a; Golnaraghi et al., 2020b; Sánchez-Almodóvar et al., 2022). In Canada, the most severe flood events have occurred in recent decades (Golnaraghi et al., 2020b).

There is strong evidence for relative sea-level rise across coastal areas that can lead to an increase in the frequency and magnitude of storm-surge flooding (Lemmen, 2016). The global mean sea level has increased from 2.2 ± 0.3 mm yr^{-1} in 1993 to 3.3 ± 0.3 mm yr^{-1} in 2014 (Chen et al., 2017). Moreover, existing records of Atlantic tropical storms or hurricanes (from 1878 to the present) show a pronounced upward trend (Alimonti et al., 2022). Previous studies have shown an increase in the number of tropical storms, that can lead to coastal compound flooding, particularly in the number of major hurricanes (categories 3, 4, and 5) in the Atlantic region since 1995 (Sugi et al., 2002). Glenn, 2022 and Howarth et al., 2019 found increases in the intensity and frequency of the storms and hurricanes in the US (Glenn, 2022; Howarth et al., 2019). The past and future changes in flood, stronger precipitation, and greater river runoff can be partly explained by global warming (Blöschl et al., 2020; Dore, 2005; Jonkman and Kelman, 2005; Liang, 2022; Trenberth, 2011; Xia et al., 2022). The projections suggest that the frequency and magnitude of floods will increase in many parts of the world over the decades to come (IPCC, 2018; (Glenn, 2022). Long-term changes in sea level are expected in a changing climate, due to increases in ocean temperature, melting of glaciers, tectonic movements

of the Earth, changes in ocean circulation, accumulation of sediments, and other factors (Change, 2018). The hydrological regimes are also affected by climate change. The historical and future changes in flood mechanisms are commonly represented by non-stationary approaches to quantify the statistical properties of hydroclimatic variables (Xiong et al., 2018) in different forms of monotonic trend, step change, jump, and periodicity (Machiwal and Jha, 2012).

Recent compound flood events, associated with the successive occurrence of two or more flood mechanisms, have caused catastrophes in several coastal regions. Such events can occur at a higher rate in the future considering the potential impacts of climate change on drivers of flooding and their interrelationships. Therefore, it is critical to develop nonstationary compound flood assessment approaches for the engineering design and planning of infrastructure.

Sarhadi et al (2016) using the nonstationary copula model obtained different joint return periods (JRPs) of drought duration and severity under the climate change scenarios for the years 2015 and 2100. Singh et al (2021) have found nonstationary JRPs of warm-wet and warm dry events between1950 between and 2100. Zhou et al., (2022) applied a full non-stationarity model (both marginal and the copula parameter) to see the change in the JRP of the annual maximum streamflow of two hydrometric gauges in China and they highlighted the more reliability of their applied method for the design flood than the stationary scenario. Regarding the CF, Ghanbari et al (2021) applied the same approach to study the CF over the US coastal zones, they referred to the decrease in the AND return period (RP) of sea level and streamflow from 2020 to 2050. In a study by Bevacqua et al, (2019), the probability of CF from precipitation and storm surges in the Baltic Sea is projected to increase. Ganguli and Merz (2019) have referred to the time-varying behavior of the dependence structure between coastal water level and peak flow and compound flood magnitudes and frequency in northwestern Europe. Using the same approach, Whal et al., (2015) studied the change in the dependence structure between storm surge and rainfall over the US coastal areas.

Moftakhari et el., (2017) also studied the CF over the US and quantified the change in the failure probabilities (OR scenario) of sea level and fluvial flooding between 2030 to 2050 under the effect of sea-level rise forced by different climate scenarios. In a study by Erik et al (2015), the effects of climate change on riverine and sea-level flooding types were assessed. They referred that 100-year flood event is becoming more frequent concerning the climate change effects (Čepienė et al., 2022). Furthermore, studies are focusing on the seasonality of compound flooding of sea level and precipitation (Couasnon et al., 2022; Duy et al., 2017).

The coastal regions of Canada are at risk of compound flooding caused by multiple flood mechanisms. The Atlantic region has been affected by ~40 extratropical cyclones from 1979 to 2005 (Milrad et al., 2009) including hurricanes Juan (2003) and Igor (2010) that caused intense rainfall and high sea level with 200 $ million in damages (Almeida et al., 2019). The flooding drivers (precipitation, streamflow, and seal level) and their joint occurrences show time-varying behavior over the Canadian coastal regions (Jalili Pirani and Najafi, 2020).

This study proposes a nonstationary trivariate statistical approach to study compound flooding and characterize the temporal variability in the contributing flooding drivers and their interdependencies in these regions, which can be applied to other coastal environments. The dependence structure between three major flooding drivers (Precipitation, streamflow, and total water level) at different locations is first analyzed using copula functions, followed by assessing the nonstationary marginal distributions and the interdependences based on linear and nonlinear functions of the corresponding statistical parameters. The time-varying return periods are estimated for engineering design and planning (Li et al., 2020; Zhou et al., 2022).

In the remainder of the paper, the study area and data are described in Section 2. The proposed approach is discussed in Section 3, followed by the results and conclusions in Sections 4 and 5, respectively.

5.2. Study area and data

Extending from 43°N to 83°N latitude and from 53°W to 141°W Longitude, Canada has the longest coastline (approximately 230,000 km) worldwide. Sea level rise flooding and the increase in its intensity and frequency have been reported in different Canadian regions, especially the Atlantic part (Bush and Lemmen, 2019a) (Figure 5.1). Besides, the east, west, and some parts of Northern Canada have experienced increases in extreme precipitation events (Bush and Lemmen, 2019a). Continued warming and associated reductions in snow cover, shrinking mountain glaciers, and accelerated permafrost thaw are expected to continue to drive changes in the seasonality of streamflow. This includes increased winter flows, earlier spring freshets, and reduced summer flows, besides shifts from snowmelt-dominated regimes toward rainfall-dominated ones. Annual streamflow is projected to increase in some areas (mainly northern regions), and decline in others (southern interior regions). Thawing permafrost can cause future changes in many northern Canadian lakes, including rapid drainage. The frequency and intensity of future streamflow-driven flooding are uncertain, because of the complexity of factors involved. Projected increases in extreme precipitation are expected to increase the potential for future urban flooding. However, it is uncertain how projected higher temperatures and reductions in snow cover will combine to affect the frequency and magnitude of future snowmelt-related flooding. Lower surface water levels of lakes and wetlands are expected, especially toward the end of this century, under higher emission scenarios (see Chapter 3, Section 3.2), due to higher temperatures and increased evaporation.
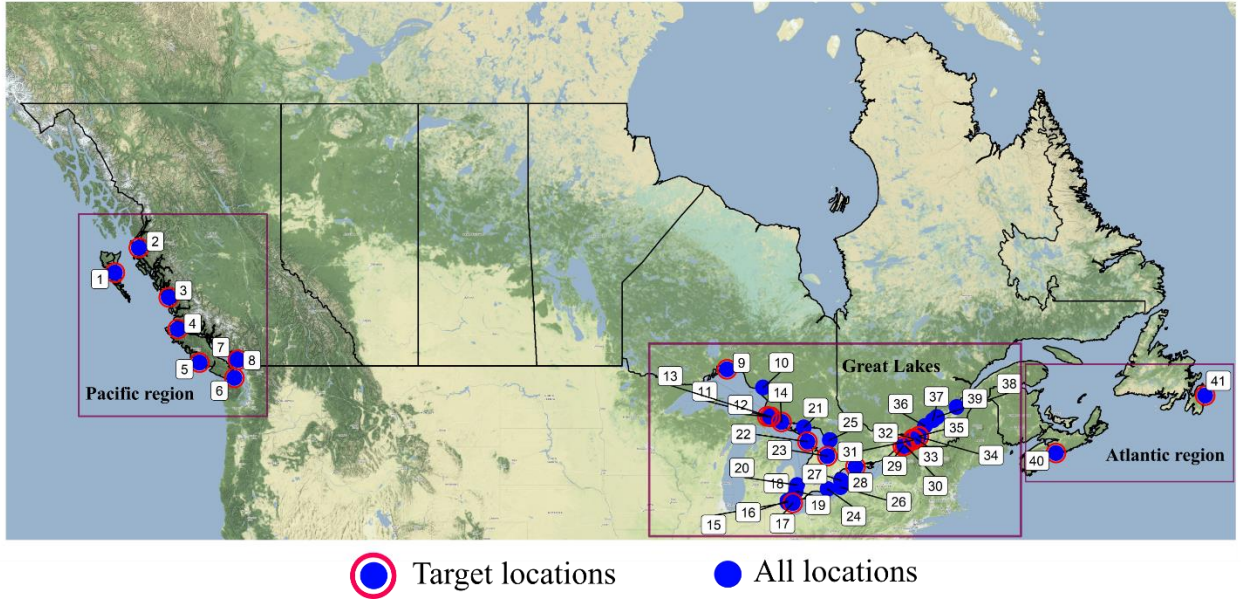
Figure 5. 1) Study area and 41 study sites located in the Pacific, Atlantic, and Great Lakes regions.

The potential flooding drivers considered in this study include precipitation (Pr), streamflow (Q), and maximum total water level (TWL) at each 24-hour interval for 1960 to 2015. At each location, the selected data records have less than 20 percent missing values in each year and the entire period. Besides, there is a minimum of 80 percent overlap between the paired data. Accordingly, 41 locations distributed across the three regions of the Pacific/Atlantic coasts and the Great Lakes (GL) are selected for further analysis. The physical distance between tidal, hydrometric, and meteorological gauges is considered as 50 km, consistent with previous studies. Besides, the flow path is tracked to make sure it reaches the closest tidal gauge (Ward et al., 2018).

5.3. Methodology

Spatial and temporal interactions between moderate or extreme flood hazards (including pluvial, fluvial, and coastal) can lead to compound flooding in coastal regions.

Accordingly, different scenarios can be developed based on the extracted extreme events (Ghanbari et al., 2021; Zheng et al., 2014). In this study, extreme Pr events larger than the 95th percentile, as the threshold, are extracted and analyzed using the Peak over Threshold (POT) method (Bezak et al., 2014; Dodangeh et al., 2019; Villarini et al., 2011). Maximum TWL and Q events within ± 1 day of the corresponding extreme precipitation events are then selected and paired for compound flood analysis (Moftakhari et al., 2017; Wahl et al., 2015; Ward et al., 2018). The temporal dependencies in extreme Pr events are removed by considering the peak values in every 3-day window. The interdependencies between the drivers are then assessed and the potential for (non)stationary compound flood events is investigated.

5.3.1. Extreme value distributions of flood mechanisms

The POT-derived precipitation events are represented by the Generalized Pareto distribution (GPD), and the best-fitted distribution for TWL/Q, at each location, is selected among Gamma, Normal, Lognormal, Cauchy, Weibull, Logistic, Gumbel, and Exponential distributions using the AIC criterion and the KS test (Table S2.2). The nonstationary process of flooding drivers is represented by both linear and nonlinear time-variant location parameters of the marginal distributions (Sarhadi et al., 2016; Zhou et al., 2022). Accordingly, different forms of constant, linear, and quadratic models are assumed for the location parameter of the distribution, for each variable at every location, using the Generalized Linear Model (GLM) method to determine the corresponding nonstationary behavior. The location parameter can show both increases or decreases over time. Under the normal distribution, we can write (Sarhadi et al., 2016).

$$\mu_t = a \quad \text{Constant,} \tag{5.1}$$

$$\mu_t = a + bt \quad \text{Linear,} \tag{5.2}$$

$$\mu_t = a + bt + ct^2 \quad \text{Quadratic,} \tag{5.3}$$

where μ is the location parameter, t is time and a, b and c are the set of model parameters ($\beta_m = (a, b, c)$). The best model has the lowest AIC value.

Considering that the parameter has a positive domain in the Weibull, Gamma, and Exponential distributions (Table S2.2) it is modeled using a log link function that allows for both positive/negative values regardless of the parameter range of the distribution (Sarhadi et al., 2016).

$$\log(\mu_t) = a \quad \text{Constant,} \tag{5.4}$$

$$\log(\mu_t) = a + bt \quad \text{Linear,} \tag{5.5}$$

$$\log(\mu_t) = a + bt + ct^2 \quad \text{Quadratic,} \tag{5.6}$$

5.3.2. Vine Copula

Copula functions (Nelson, 1998) are used to create the multivariate distribution of the three drivers at each location. Copulas have the flexibility to describe any type of dependence (linear and non-linear and tail dependence) between the drivers (Joe, 1997). The joint Probability Distribution Function (PDF) (Liu et al., 2018) of the three drivers is determined using Equation 7:

$$f(\text{Pr}, \text{TWL}, Q) = f_{\text{Pr}}(\text{Pr}|\theta_{\text{pr}}) \times f_{\text{TWL}}(\text{TWL}|\theta_{\text{twl}}) \times f_Q(Q|\theta_q) \times$$
$$c(F_{\text{Pr}}(\text{Pr}|\theta_{\text{pr}}), F_{\text{TWL}}(\text{TWL}|\theta_{\text{twl}}), F_Q(Q|\theta_q)|\phi_c), \tag{5.7}$$

where c is the copula function with the dependence parameter ϕ_c, $f(\text{Pr}, \text{TWL}, Q)$ is the joint PDF, $f_{\text{Pr}}(\text{Pr}|\theta_{\text{pr}}), f_{\text{TWL}}(\text{TWL}|\theta_{\text{twl}}), f_Q(Q|\theta_q)$ are the marginal distributions of three drivers with the corresponding parameters $\theta_{\text{pr}}, \theta_{\text{twl}}$ and θ_q, respectively.

In this study, we consider vine copula to assess the dependence structure between multiple drivers of compound flooding (Aas and Berg, 2009; Jane et al., 2020). Vine copula decomposes an n-dimensional multivariate distribution into a cascade of n(n-1)/2 bivariate or conditional bivariate copulas, that are independent of each other, in the form of a nested set of trees. The structure of the canonical vine (C-vine) for three drivers is

shown in figure 5.2 and the corresponding PDF is presented in Equation 8 (Brechmann and Schepsmeier, 2013; Czado, 2010):
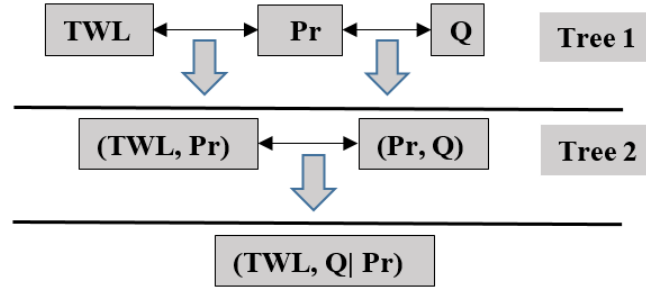
Figure 5. 2) The cascading unconditional and conditional bivariate copulas of TWL, Pr, and Q using a three-dimensional C-vine copula.

$$
\begin{aligned}
f(Pr, TWL, Q) &= f_{Pr}(Pr|\theta_{pr}) \times f_{TWL}(TWL|\theta_{twl}) \times f_Q(Q|\theta_q) && \text{(marginals)} \\
&\times c_{Pr,TWL}(F(Pr), F(TWL)|\varphi_{c(pr,twl)}) \times c_{Pr,Q}(F(Pr), F(Q)|\varphi_{c(pr,q)}) && \text{(unconditional pair)} \\
&\times c_{TWL,Q|Pr}(F(TWL|Pr), F(Q|Pr)|\varphi_{c(twl,q)}) && \text{(conditional pair)}
\end{aligned}
$$

(5.8)

where $c_{Pr,TWL}$, $c_{Pr,Q}$ and $c_{TWL,Q|Pr}$ are the copula functions fitted to the joint events of (Pr, TWL), (Pr, Q), and (TWL, Q conditioned on Pr) with the dependence parameters of $\varphi_{c(pr,twl)}$, $\varphi_{c(pr,q)}$ and $\varphi_{c(twl,q)}$, respectively.

The (un)conditional one- or two-parameter (θ_c) copulas (Schepsmeier et al., 2015) are selected based on the AIC metric among 41 copula functions including Gaussian, Student t, Frank, Joe, Clayton, Gumbel, BB1, BB6, BB7, BB8, Tawn type 1, and Tawn type 2 along with their rotational variants (90, 180, and 360 degrees) (Table S2.3). This is followed by a goodness-of-fit test proposed by Genest et al. (2006) to test the significance of the selected models.

5.3.3. Dynamic Vine Copula models

Previous studies have shown that the dependence structure between drivers of flooding can change in time partly because of the nonstationarity of the hydroclimate system (Sarhadi et al., 2016; Wahl et al., 2015; Zhou et al., 2022). Here, we consider both constant and

temporally varying dependence parameters of the selected copula functions using two linear and quadratic models. The corresponding parameters are characterized by log and logit link functions for copulas with parameter ranges above 0 (e.g., Clayton) and above 1 (e.g., Gumbel), respectively. Table 5.1 presents the link functions suitable for each copula when the parameter is considered constant, and Tables S5.1 and S5.2 show the linear and quadratic models. The dependence between the drivers is characterized using Kendall's Tau, in one-parameter copula functions, and then Tau is converted to the copula parameter (Sarhadi et al., 2016; Wen et al., 2019). However, in some other copula types, there is not a closed form for such conversion and therefore, their parameters are directly represented by the time-varying link functions. As an example, the dependence parameter of the Gumbel copula is modeled using the logit function as follows.

$$\text{Log}(\frac{\tau_t}{1-\tau_t}) = a \quad \text{Constant,} \tag{5.9}$$

$$\text{Log}(\frac{\tau_t}{1-\tau_t}) = a + bt \quad \text{Linear,} \tag{5.10}$$

$$\text{Log}(\frac{\tau_t}{1-\tau_t}) = a + bt + ct^2 \quad \text{Quadratic,} \tag{5.11}$$

τ is Kendall's Tau and t is time. Therefore, the set of parameters for the dependence parameter is $\beta_c = (a, b, c)$.

Table 5. 1) The link functions developed for different copulas considering stationary framework. a is the distribution/copula parameter when the model is constant.

Link function	Copula families for the first parameter	Copula families for the second parameter
$\tau_t = \dfrac{1}{1 + e^{-a}}$	3, 4, 6, 13, 14, 16	10, 120, 104, 114, 124, 134, 204, 214, 224, 234
$\tau_t = 2 \times \left(\dfrac{1}{1 + e^{-a}} - 0.5\right)$	1, 2, 5	
$\phi_t = 2.01 + \left(100 \times \left(\dfrac{1}{1 + e^{-a}}\right)\right)$		2
$\tau_t = \dfrac{1}{1 + e^{-tau}} - 1$	23, 24, 26, 33, 34, 36	30, 40
$\phi_t = 0.01 + \left(100 \times \left(\dfrac{1}{1 + e^{-a}}\right)\right)$	7, 17	9, 19
$\phi_t = 1.01 + \left(100 \times \left(\dfrac{1}{1 + e^{-a}}\right)\right)$	8, 9, 10, 18, 19, 20, 104, 114, 204, 214	7, 8, 17, 18
$\phi_t = -0.01 - \left(100 \times \left(\dfrac{1}{1 + e^{-a}}\right)\right)$	27, 37	29, 39
$\phi_t = -1.01 + \left(100 \times \left(\dfrac{1}{1 + e^{-a}}\right)\right)$	28, 29, 30, 38, 39, 40, 124, 134, 224, 234	27, 28, 37, 38

The best-fitted (non)stationary marginal are inserted in Equation 8 and the full model is created for each location. Each model has six parameters (either stationary or dynamic), three dependence parameters corresponding to three copulas, and three location parameters related to three marginal distributions. Different combinations of three models for six parameters are possible as shown in Table 5.2. For example, at location #41, the Pr and TWL are nonstationary while Q is stationary. Further, the dependence parameters

of the (Pr, TWL) and (Pr, Q) pairs change linearly and polynomially with time, respectively, while, the dependence parameter associated with (Q, Pr) is constant. In this study, the effect of the dependency on join probability is higher than the marginal as the trend rate of the marginal is not so remarkable. Therefore, between the dependency and the driver, dependency is our priority in selecting the locations for further analysis. For example, if at a location, two of the dependencies are increasing while two of the marginal are decreasing, the location is selected for further flood hazard analysis. In table 5.2, the sites having the conditions with the green tick mark are our focus.

Table 5. 2) Different model (constant and time-varying) combinations of three dependencies and three drivers. 1/3, 2/3, and 3/3 imply one-third, two-third, and all of the either marginal or dependence parameters.

Location par / Copula par	1/3 ▲ / 2/3 ▼	1/3 ▬ / 2/3 ▲	1/3 ▬ / 2/3 ▼	1/3 ▬, 1/3 ▲, 1/3 ▼	2/3 ▼ / 1/3 ▲	3/3 ▬	3/3 ▲	3/3 ▼	1/3 ▲ / 2/3 ▬	1/3 ▼ / 2/3 ▬
1/3 ▲ 2/3 ▼	✗	✓	✗	✗	✗	✗	✓	✗	✗	✗
1/3 ▬ 2/3 ▲	✓	✓	✓	✓	✓	✓	✓	✗	✓	✓
1/3 ▬ 2/3 ▼	✗	✗	✗	✗	✗	✗	✓	✗	✗	✗
1/3 ▬ 1/3 ▲ 1/3 ▼	✗	✓	✗	✓	✗	✗	✓	✗	✓	✗
2/3 ▼ 1/3 ▲	✗	✓	✗	✗	✗	✗	✓	✗	✗	✗
3/3 ▬	✗	✓	✗	✓	✗	✗	✓	✗	✓	✗
3/3 ▲	✓	✓	✓	✓	✓	✓	✓	✓	✓	✓
3/3 ▼	✗	✗	✗	✗	✗	✗	✗	✗	✗	✗
1/3 ▲ 2/3 ▬	✓	✓	✗	✓	✗	✓	✓	✗	✓	✓
1/3 ▼ 2/3 ▬	✗	✓	✗	✗	✗	✗	✓	✗	✗	✗

Regarding dependency, the time-varying behavior should be on increasing towards the positive side (even if the correlation is negative at the beginning) with respect to at least 1/3 of the dependence parameters. The locations that have positive dependency but diminish with time are also considered for flood hazard analysis. We do this because it

might be the locations with the negative dependency between the drivers which are increasing positively but still with less positiveness than the locations with positive dependency and decreasing over time.

The model parameters and their corresponding uncertainties are estimated using the Bayesian approach (McElreach, 2018). In this technique, which operates based on the Bayes theorem, the knowledge brought by the prior distribution is integrated with the observations to generate the joint posterior distribution of the corresponding parameters. There are different approaches for searching and sampling the joint posterior distribution. We apply The Markov Chain Monte Carlo (MCMC) method of the Metropolis-Hastings algorithm (Hastings, 1970). Here, the MCMC chain has 10000 samples with the first 5000 samples discarded to mitigate the effect of initial samplings and to acquire the full convergence. The convergence of the chain is tested using the Geweke test (1991). For the sake of brevity, we avoid presenting these results. As an example, the joint posterior probability density function (pdf) of the three drivers is obtained as follows.

$$f\left(\phi_c, \theta_m \big| (twl_1, pr_1, q_1), (twl_2, pr_2, q_2), \ldots, (twl_n, pr_n, q_n)\right) \propto$$

$$p(\theta_m) . p(\phi_c) . \prod_{i=1}^{n} c(twl_i, pr_i, q_i | \phi_c) . f(twl_i | \theta_m) . f(pr_i | \theta_m) . f(q_i | \theta_m) \qquad (5.12)$$

where $f(\phi_c, \theta_m | (twl_1, pr_1, q_1), (twl_2, pr_2, q_2), \ldots, (twl_n, pr_n, q_n))$ is the joint posterior density function of ϕ_c, θ_m, which are the parameter sets of copula and marginals, respectively. $p(\theta_m), p(\phi_c)$ are the prior distributions of θ_m, ϕ_c, and $c(twl_i, pr_i | \phi_c)$ is the copula density of TWL, Pr and Q. $f(twl_i | \theta_m), f(pr_i | \theta_m)$ and $f(q_i | \theta_m)$ represent the marginal densities of TWL, Pr and Q, respectively. As we don't have any external source of information about the parameters, here we consider uninformative prior distributions for all the parameters.

5.3.4. Model selection

The best-fitted constant, linear, and quadratic model, for each variable in each location, is selected according to the Widely Applicable Information Criterion (WAIC) criterion.

WAIC is one type of information theory that does not have the restrictions of AIC metric including flat prior distributions, multivariate posterior Gaussian distributions, and great sample size when applying the Bayes theorem (McElreath, 2018). WAIC is defined as follows.

$$\text{WAIC} = -2(\text{lppd} - \text{pwaic}), \tag{5.13}$$

$$\text{lppd} = \sum_{i=1}^{N} \log \text{Prob}(y_i), \tag{5.14}$$

$$\text{pwaic} = \sum_{i=1}^{N} V(y_i), \tag{5.15}$$

$\text{Prob}(y_i)$ is the average likelihood of observation *i* given different samples from the posterior distribution, $V(y_i)$ is the variance in log-likelihood for observation *i,* log-pointwise-predictive-density (lppd) is the total across observations of the logarithm of the average likelihood of each observation and pwaic is the effective number of parameters.

5.3.5. Nonstationary Joint Return Period (JRP)

Estimating the recurrence interval of (individual and compound) extreme events is important for water resources planning and management. Depending on the past flooding events, the design levels can be obtained when each of the drivers is extreme (OR JRP) or when the extremes of all drivers occur simultaneously (AND JRP) (Salvadori and De Michele, 2004; Salvadori et al., 2007; Shiau, 2006). In this study, we quantify the nonstationary JRPs corresponding to these multivariate scenarios at each location for 1960 to 2015. The time-varying OR exceedance probabilities and the corresponding JRPs considering pr, q, and twl exceeding their respective thresholds (here 0.01) are obtained as follows:

$$P_t\big((Pr > pr) \cup (Q > q) \cup (TWL > twl)\big) = 1 -$$
$$C(F_{Pr}(pr|\theta_p), F_Q(q|\theta_q), F_{TWL}(twl|\theta_{twl})|\phi_c^t), \tag{5.16}$$

$$JRP_t = \frac{\mu}{P_t},$$ (5.17)

where P_t is the time-varying OR exceedance probability. θ_{pr}, θ_q and θ_{twl} are the parameter set of the three drivers. C is the joint cumulative probability of the three drivers. ϕ_c^t is the set of parameters corresponding to the pair-copulas $C_{Pr,TWL}(F(Pr), F(TWL))$, $C_{Pr,Q}(F(Pr), F(Q))$, or $C_{TWL,Q|Pr}(F(TWL|Pr), F(Q|Pr))$, and μ is the average inter-arrival time between the flood events (in an annual time scale). It should be mentioned that we also explored the non-stationarity of the μ using the Man-Kendall test and we did not find any significant trend at all locations.

The AND exceedance probability and the associated JRPs are obtained as follows.

$$P_t\big((Pr > pr) \cap (Q > q) \cap (TWL > twl)\big)$$
$$= 1 - F_{Pr}(pr|\theta_p) - F_Q(q|\theta_q) - F_{TWL}(twl|\theta_{twl})$$

$$+ C_{Pr,TWL}^t\big(F(Pr), F(TWL)\big|\phi_{C(pr,twl)}^t\big) + C_{Pr,Q}^t\big(F(Pr), F(Q)\big|\phi_{C(pr,q)}^t\big) +$$
$$C_{TWL,Q|Pr}^t\big(F(TWL|Pr), F(Q|Pr)\big|\phi_{C(twl,q)}^t\big) -$$
$$C_t(F_{Pr}(pr|\theta_{mp}), F_Q(q|\theta_{mq}), F_{TWL}(twl|\theta_{mtwl})|\phi_C^t),$$ (5.18)

$$JRP_t = \frac{\mu}{P_t},$$ (5.19)

where P_t is the AND exceedance probability of the three drivers exceeding their corresponding thresholds. $F_{Pr}(pr|\theta_p)$, $F_Q(q|\theta_q)$, and $F_{TWL}(twl|\theta_{twl})$ are the marginal distributions of Pr, Q, and TWL given their set of parameters θ_{pr}, θ_q, and θ_{twl}, respectively. $C_{Pr,TWL}^t(F(Pr), F(TWL)|\phi_{C(pr,twl)}^t)$, $C_{Pr,Q}^t(F(Pr), F(Q)|\phi_{C(pr,q)}^t)$, and $C_{TWL,Q|Pr}^t(F(TWL|Pr), F(Q|Pr)|\phi_{C(twl,q)}^t)$ are the bivariate unconditional or conditional copula functions given the corresponding set of parameters ϕ_C^t.

In this study, JRPs and their time variation are compared with the unrealistic independence and univariate scenarios.

5.3.6. Compound Hazard Ratio (CHR)

The interconnection between the drivers can influence the joint probability of the drivers and the corresponding return levels of flood events. Ganguli et al (2019) proposed the CHR index, which is the ratio of the T-year discharge level conditional on the extreme coastal water level (CWL) to the unconditional T-year discharge. To extend this index for multivariate analysis of compound floods, the probability of T-year Q given Pr and TWL is estimated (Gonzalez-Lopez et al., 2019):

$$P_t(Q \le q | Pr \le pr, TWL \le twl) = \frac{P_t(Q \le q, Pr \le pr, TWL \le twl)}{P_t(Pr \le pr, TWL \le twl)} = \frac{C_t(F_Q(q|\theta_q), F_{Pr}(pr|\theta_{pr}), F_{TWL}(twl|\theta_{twl})|\phi_C^t)}{C_t(F_{Pr}(pr|\theta_q), F_{TWL}(twl|\theta_{twl})|\phi_C^t)} \quad (5.20)$$

The nonstationary CHR index is defined as follows:

$$CHR_t = \frac{Q'_t}{Q_t} = \frac{C_{Q_t|(Pr \le pr, TWL \le twl)}^{-1}\left[1 - \frac{\mu}{T_{Q_t|(Pr,TWL)}(q|pr,twl)}\right]}{F_{Q_t}^{-1}\left[1 - \frac{\mu}{T_{Q_t}(q)}\right]}, \quad (5.21)$$

Q'_t and Q_t are the conditional and unconditional return levels of Q at time t. $C_{Q_t|(Pr=pr,TWL=twl)}^{-1}$ and F_Q^{-1} are the inverse quantile transformations of copula functions and marginal distributions at time t, respectively. $T_{Q_t}(q)$ is the T-year unconditional RP of streamflow $T_{Q_t}(q) = \frac{\mu}{1 - F_{Q_t}(q|\theta_q)}$, and the conditional RP of streamflow $T_{Q_t|(Pr,TWL)}(q|pr,twl)$ is defined as:

$$T_{Q_t|(Pr,TWL)}(q|pr,twl) = \frac{\mu}{1 - P_t(Q_t \le q|Pr \le pr, TWL \le twl)}, \quad (5.22)$$

the levels of *p* for the three drivers correspond to a return period of 100 years.

5.3.7. Failure Probability (FP)

Failure probability represents the probability of a flood event happening at least once in a given project lifetime, which can provide a better understanding of the potential impacts

of flooding for engineering design (Xu et al., 2019a). The hydrologic failure of infrastructure increases with time at a fixed rate in stationary conditions, however, under the nonstationary environment, this rate is variant with time. Here, we quantify such changes in the OR FPs corresponding to 100 and 10-year RPs and lifetimes ranging from 1 to 50 years for location # 41 and compare them with univariate and OR stationary dependence scenarios. The nonstationary FP is calculated as follows (Ghanbari et al, 2021).

$$FP_{OR} = 1 - \prod_{i=1}^{N} C_t(F_{Pr_i}(pr|\theta_c^t), F_{Q_i}(q|\theta_c^t), F_{TWL_i}(twl|\theta_c^t)|\phi_c^t), \tag{5.23}$$

N is the number of events during the project lifetime (D) which in the case of annual max data, it is equal to the project lifetime; however, in the case of the POT approach, it is the ratio of D over μ (average interarrival time between the events):

$$N = \frac{D}{\mu}, \tag{5.24}$$

5.4. Results and discussion

5.4.1. Marginal distributions

Table S5.3 presents the selected marginal distribution at each location according to the AIC metric and the KS test. Aside from extreme Pr data represented by GPD, for TWL and Q, GPD/exponential and GPD/Weibull are the best-fitted distributions, respectively.

The results of the Mann-Kendall test indicate that Pr has a significant trend at only 5 locations: 31, 32 at the GL and 40, 41 at the Atlantic region with an increasing trend, and site 16 at the GL with a decreasing trend. Besides, Q has an increasing trend at 9 locations mainly at the GL while TWL is rising over the Atlantic region and at one location in the Pacific, and 27 spots present a diminishing behavior regarding this driver (Table S5.4). Overall, there are 13 locations where at least one of the drivers has an increasing trend (6, 7 at the Pacific, 15, 24, 26, 27, 29, 30, 31, 32, 39 at the GL, and 40,

41 at the Atlantic region). The AIC results of fitting three generalized linear models to each driver at each location indicate that at only two locations (#1 at Atlantic and 39 at GL), all three drivers are stationary. Nonstationary TWL and Q events are best represented by the quadratic model, especially at the GL while Pr is mostly stationary across all locations except at the Atlantic region (Table S5.5). It should be noted these results are without any significance check.

5.4.2. Dependence analysis

Kendall's tau dependence analysis indicates more locations with significant positive dependence between Pr and TWL (at all three regions particularly in both coastal regions) than TWL and Q and, Pr and Q (mostly in the GL and Pacific areas) (Table S5.6). Moreover, the average interdependencies between Pr/TWL and Q/TWL are stronger than Pr/Q at the majority of the locations, especially the Atlantic domain. Due to the occurrence of the extra-tropical cyclones in the Atlantic region and the seiche events along with intense Pr in the GL area, the interdependencies between Pr/TWL are higher than Pr/Q and Q/TWL Besides, extreme flows depend on several basin characteristics. The higher dependency between TWL and Q on the Pacific region can be associated with the hydrological responses in mountainous regions.

The copula functions selected based on AIC and genest significance test at each location are shown in Table S5.7. Frank copula is the prevalent function at most locations. Out of the 41 locations investigated in this study, about half (19 locations) are represented by time-invariant dependence parameters. At 8, 10, and 7 locations, the dependence parameter of (Pr, TWL), (Pr, Q), and (Q, TWL) events are represented by time-varying functions (either linear or polynomial), respectively (Table S5.8). The nonstationary dependencies between (Pr, Q) and (Pr, TWL) are more pronounced across the Atlantic coast. This can be associated with the increase in the frequency of hurricanes in this region since 1970 (Bush and Lemmen, 2019a). Over the Great Lakes (GL) area, nonstationary interactions between (Q, Pr) and (Q, TWL) are found. The variations in the TWL in this area are mostly associated with the seiche events and the inflow and outflow from the Lakes. Besides, increases in the extent of the streamflow in some spots over the

GL region (Jalili Pirani and Najafi, 2020) result in more co-occurrence with TWL and Pr. Across the Pacific region, the joint (Q, TWL) events are nonstationary at some locations, which can be due to the existence of the basins with rapid hydrological response in this area.

Considering the selected (non)stationary marginal distributions and dependence parameters based on the AIC and WAIC values, respectively, 23 locations (6 on the Pacific coast, 2 on the Atlantic coast, and 16 on the GL) show potential increases in the hydrologic risks associated with compound flooding.

5.4.3. Time-varying Joint Return Period (JRP)

The nonstationary trivariate OR and AND JRPs and their corresponding uncertainties are quantified for 23 locations considering an exceedance probability of 0.01 for the marginals. To show the temporal variations in the corresponding JRPs, we present the results for the years 1960 and 2015. Figure 5.3 presents the JRP results for the OR scenario. The average Independence OR JRP across all locations is lower than the corresponding average under the dependence scenario and both are less than their corresponding univariate RPs. Under the OR scenario condition, the lowest (1.12 years) and the highest (3.33 years) JRPs occur in GL (location 24) and the Pacific areas (location 7), respectively. The range of uncertainty also varies from 0.08 to 12.8 years (locations 4 in the Pacific and 40 in the Atlantic region), respectively. In most locations due to an increase in the dependency between the drivers, the JRPs increase from 1960 to 2015. The highest rise is in location 41 in the Atlantic region (8.2 years), which is associated with an increase in the tail dependency between the drivers. At locations 6, 7, 15, 24, 29, 30, and 32 the JRPs do not change with time as the dependence parameters are constant; however, at least one of the drivers shows increases over time. Table 5.3 shows the Pr return levels and their uncertainties associated with 0.01 exceedance for the years 1960 to 2015. While most locations experience no change, the Pr return levels show

increases at locations 40 and 41. The corresponding levels for TWL and Q are provided in Tables S5.9 and S.10.
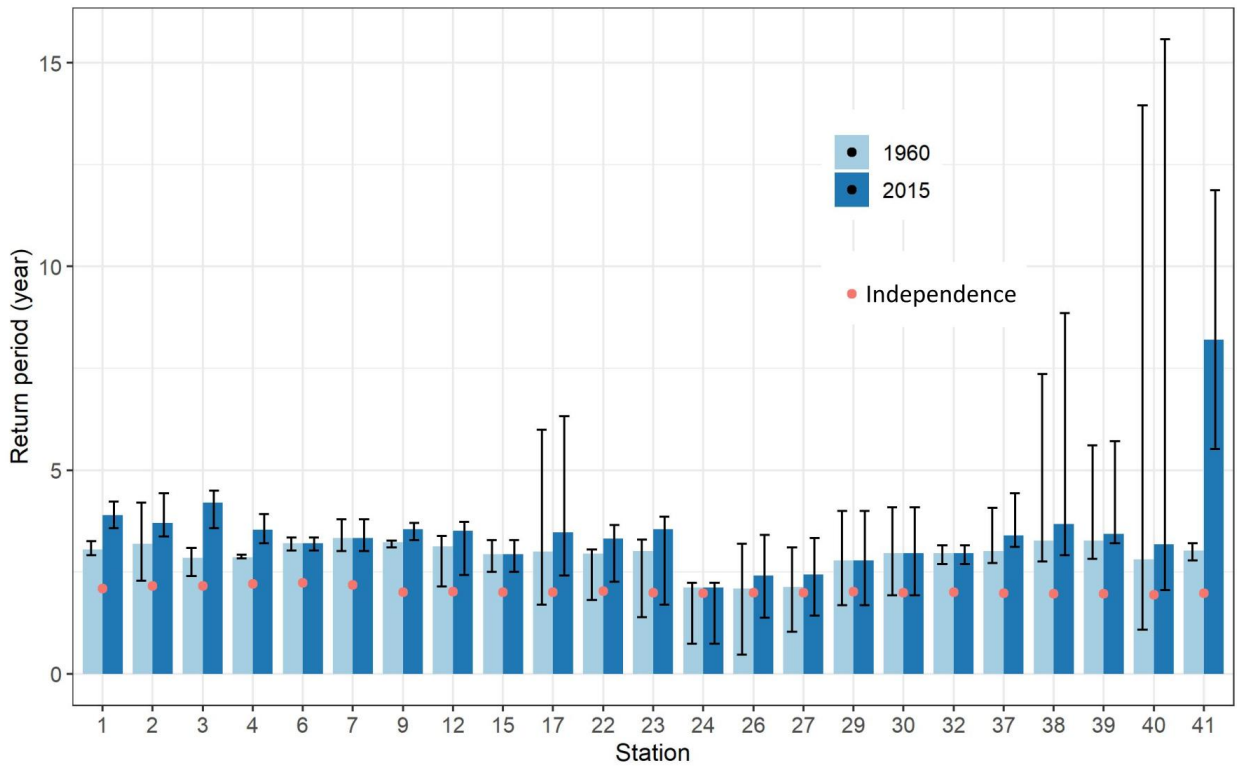
Figure 5. 3) The nonstationary OR JRPs (for 1960 and 2015) and the corresponding 95 percentile uncertainty ranges. The results associated with the unrealistic independence assumption are shown by red circles.

Table 5. 3) The nonstationary Pr return levels and the corresponding uncertainties estimated for 1960 and 2015 at 24 locations.

	Pr-lower bound		Pr-median		Pr-higher bound	
Location	1960	2015	1960	2015	1960	2015
1	64.08	64.08	66.11	66.11	68.13	68.13
2	65.10	65.10	67.72	67.72	70.35	70.35
3	59.65	59.65	62.04	62.04	64.43	64.43
4	60.90	60.90	63.30	63.30	65.69	65.69
6	55.01	55.01	56.89	56.89	58.77	58.77
7	56.47	56.47	58.65	58.65	60.83	60.83
9	54.30	54.30	56.33	56.33	58.36	58.36
12	72.42	72.42	74.90	74.90	77.39	77.39
15	72.69	72.69	75.17	75.17	77.66	77.66
17	56.43	56.43	58.55	58.55	60.68	60.68
22	53.56	53.56	55.50	55.50	57.44	57.44
23	52.65	52.65	54.37	54.37	56.09	56.09
24	54.20	54.20	55.55	55.55	56.89	56.89
26	50.76	50.76	53.27	53.27	55.77	55.77
27	69.80	69.80	72.29	72.29	74.78	74.78
29	92.95	92.95	96.42	96.42	99.88	99.88
30	89.74	89.74	94.20	94.20	98.65	98.65
32	56.77	58.74	59.17	61.23	61.56	62.78
36	63.35	63.35	65.22	65.22	67.09	67.09
37	54.98	54.98	56.94	56.94	58.90	58.90
38	53.97	53.97	55.89	55.89	57.80	57.80
39	76.11	76.11	78.34	78.34	80.56	80.56
40	79.91	84.58	83.18	88.85	86.44	93.12
41	85.76	90.01	90.08	93.33	94.39	98.64

The AND JRPs are also affected by changes in the drivers and the corresponding interactions. The stationary AND JRPs vary from 16.48 years at location 38 to 314.73 years at location 39 both at the GL area which is considerably lower compared to the ones estimated based on the unrealistic independence assumption. Similar to the OR scenario, there is no change in the AND JRP at locations 6, 7, 15, 24, 29, 30, and 32; however, given the exceedance of 0.01, the return levels of the three drivers increase for these locations. For other sites, the JRPs decrease in time at all locations with the highest decrease at location 41 (31 years at St Jones city- Atlantic region) and the lowest at location number 38 (two years decrease), indicating a higher risk of compound flooding in these regions. The lower quantiles in the AND-JRP are associated with higher

dependencies between the drivers. These results indicate that it is critical to consider both the dependencies between drivers of flooding and their non stationarities for robust flood risk assessments in the future (Figure 5.4).
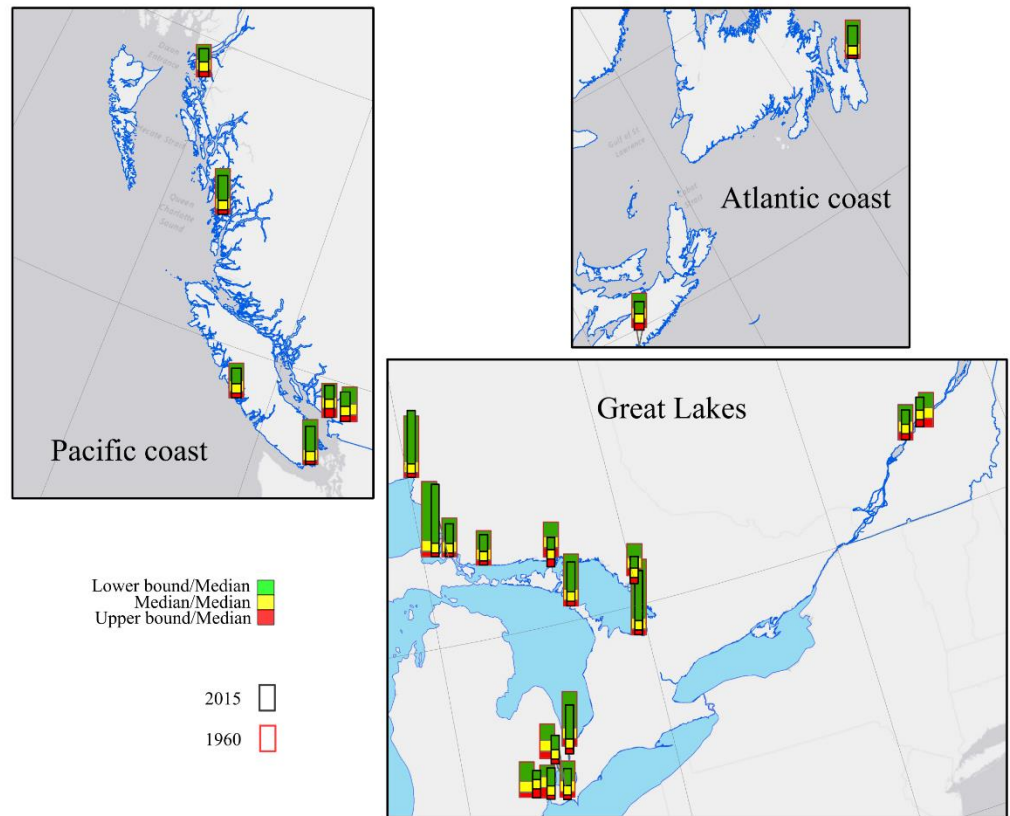
Location	1	2	3	4	6	7	9	12	15	17	22	23	24	26	27	29	30	32	37	38	39	40	41
1960	216	122	72	93	226	203	158	250	76	76	47	55	54	98	217	53	115	28	19	16	315	76	50
2015	205	112	47	85	226	203	135	232	76	66	32	45	54	83	204	53	115	28	15	14	306	65	19

Figure 5. 4) The AND JRPs and the corresponding uncertainties estimated for the years 1960 and 2015. The table shows the median JRPs for the two years.

148

5.4.4. Time-varying Compound Hazard Ratio (CHR) index

The results of the CHR index are presented in Figure 5.5 showing that the interconnections between the drivers affect the return levels of the three drivers. For example, the return levels of 100-year Q given Pr and TWL are different from those of unconditional/univariate 100-year Q levels at 23 locations with a CHR higher than 1 distributed over the three regions. Moreover, at all the locations an increase in the dependency between the drivers results in an increase in the CHR index. The percentage changes from 1960 to 2015, shown in Figure 5, have the lowest and the highest range of …. are at locations 12, and 17 (both at the GL).
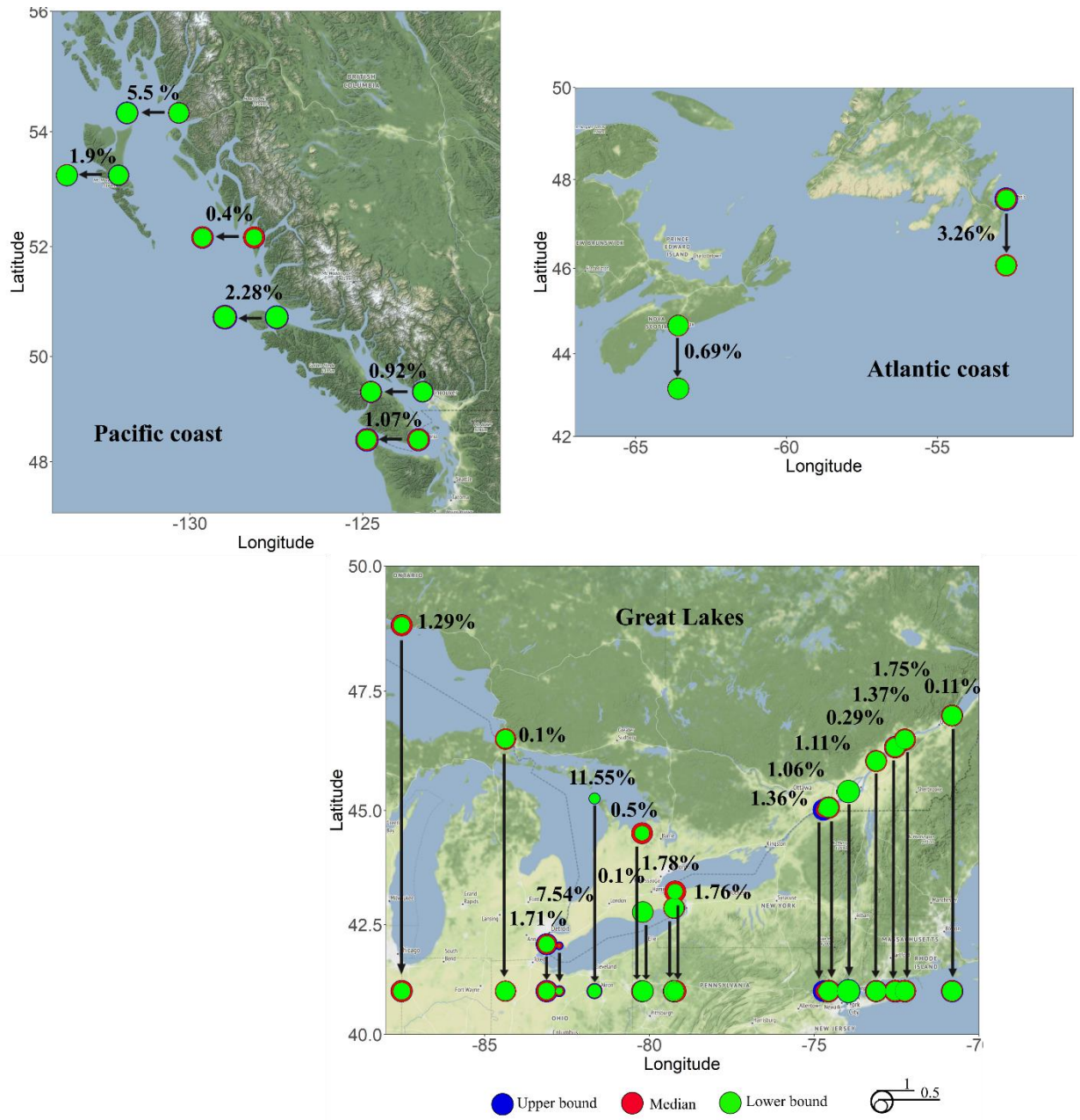
Figure 5. 5) The CHR index values (median and uncertainty), for 24 sites. The percent changes from 1960 to 2015 are shown by arrows. The length of the arrows is not scaled based on the percent change values.

5.4.5. Nonstationary Failure Probability (FP)

The time-varying FPs corresponding to 100 and 10-year events are calculated for the OR scenario and the corresponding uncertainty ranges are quantified at different locations. The results are compared with the estimated FPs corresponding to the stationary OR and three univariate drivers. In this section, the results are shown for location (#41) with the strongest nonstationary behavior among other locations (Figure 5.6). As expected, with increases in the lifetime, the FPs increase for both bivariate and univariate cases. The bivariate FPs are higher than those of univariate FPs for the three drivers of total water level, precipitation and flow rate. Considering the RP of 100 years for TWL, Q, and Pr, the FPs of TWL is higher than the other two drivers as it has a higher increase rate from 1960 to 2015. Besides, the estimated FPs are higher under the non-stationarity scenario compared to the stationarity condition. This highlights two main points. Firstly, flooding risk considering the compound of multiple drivers avoids the risk underestimation. Secondly, under the OR scenario, the FP is overestimated based on the independence scenario, which is consistent with studies in other areas (Moftakhari et al. (2017) and Xu et al. (2019)). In other words, not considering the dependency between the drivers cause underestimation of the FPs for both RPs. And finally, the time-varying dependence FPs show possible underestimations of risks of the nonstationary behavior of compound flood events are not accounted for.
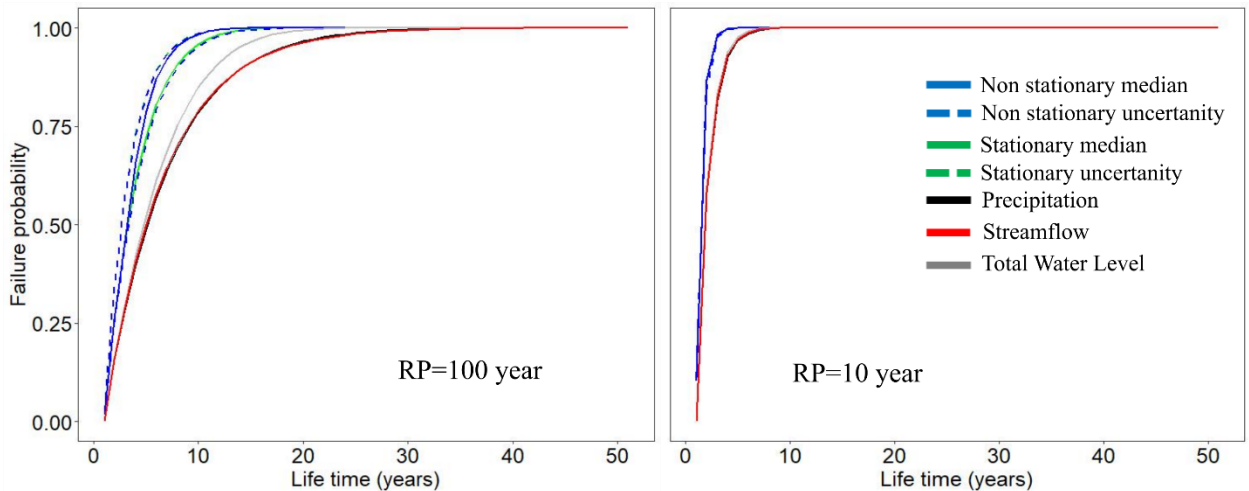
Figure 5. 6) The (non)stationary OR and univariate FPs for 100 and 10-year events regarding location #41.

5.5. Discussion and Conclusion

In this study, we investigate the hydrologic risk of compound flooding under a nonstationary framework across the Canadian coastal areas. The analysis is performed in over 41 locations along three major coastal regions including the Pacific, the Great Lakes, and the Atlantic coasts for 1960 to 2015 for 41 coastal locations. Using the POT approach, the extreme Pr data are extracted and paired with maximum TWL and Q within a time window of 1-day. The best-fitted univariate distributions are selected for each of the three drivers based on the AIC metric. Constant (time-invariant), linear and quadratic models (i.e., generalized linear model) are evaluated to represent the mean of marginal distributions. The interdependencies between the flooding drivers are investigated using the C-Vine Copula approach. Further, time (in)variant models are considered for the (first) parameter of the copula functions to investigate the associated nonstationarities and their influence on the estimated return levels/periods. The best-fitted copula model and the corresponding link function are selected according to the WAIC metric for each location. The parameters of marginal distributions and dependencies and the corresponding uncertainty ranges are estimated using the Bayesian approach. The hydrologic risk of compound flooding is analyzed using the OR, AND joint return periods, the CHR index, and failure probabilities.

Results show that the non-stationarity of the individual flood hazards and the corresponding dependencies can lead to potential increases in the risk of compound flooding at over half of the locations analyzed in this study. The results of the OR JRPs indicate that at most locations, the JRP is lower than the univariate RP, as expected. Further, the estimated nonstationary JRPs show increases from the year 1960 to 2015. The AND scenario shows similar behavior, however, the corresponding values are more sensitive to the dependencies between the drivers, and therefore, there are more pronounced differences between the AND JRPs and the ones based on the unrealistic

interdependence assumption. In addition, there is a decrease in the JRPs with time especially on the Atlantic coast as the number of weather systems has increased in this area since 1970 resulting in more compound events of Pr, Q, and TWL.

Consistently, the nonstationary CHR index results suggest increases in the return levels of conditional Q at the majority of locations over time. Moreover, the FP results for location #41 show how bivariate FPs are higher than those of the univariate FPs and especially when the FPs increase with time.

The results of this research provide more robust estimates of nonstationary compound flood risks across Canada's coasts that help different stakeholders including coastal engineers and planners to update their design estimates and develop effective technical and non-technical flood mitigation and resilience measures for upstream reservoirs, flood barriers, dykes (technical measures), and building regulations and guidelines, educating people to be prepared for these type of joint events, emergency preparedness to protect lives and reduce damages (non-technical measures).

References

Aas, K., Berg, D., Models for construction of multivariate dependence–a comparison study, *The European Journal of Finance* **15**(2009), pp. 639-659.

Alimonti, G., Mariani, L., Prodi, F., Ricci, R.A., A critical assessment of extreme events trends in times of global warming, *The European Physical Journal Plus* **137**(2022), pp. 1-20.

Almeida, L.S., Goerlandt, F., Pelot, R., Effects of major hurricanes in Atlantic Canada from 2003 to 2018. *Risk Analysis Based on Data and Crisis Response Beyond Knowledge*, CRC Press (2019), pp. 390-396.

Bezak, N., Brilly, M., Šraj, M., Comparison between the peaks-over-threshold method and the annual maximum method for flood frequency analysis, *Hydrological Sciences Journal* **59**(2014), pp. 959-977.

Blöschl, G. *et al.*, Current European flood-rich period exceptional compared with past 500 years, *Nature* **583**(2020), pp. 560-566.

Brechmann, E., Schepsmeier, U., Cdvine: Modeling dependence with c-and d-vine copulas in r, *Journal of statistical software* **52**(2013), pp. 1-27.

Bush, E., Lemmen, D., Canada's changing climate report. Government of Canada. Ottawa: Government of Canada. Retrieved from http://www. changing climate. ca … (2019).

Čepienė, E., Dailidytė, L., Stonevičius, E., Dailidienė, I., Sea level rise impact on compound coastal river flood risk in Klaipėda city (Baltic Coast, Lithuania), *Water* **14**(2022), p. 414.

Change, I.P.o.C., *Global warming of 1.5° C: an IPCC special report on the impacts of global warming of 1.5° C above pre-industrial levels and related global greenhouse gas emission pathways, in the context of strengthening the global response to the threat of climate change, sustainable development, and efforts to eradicate poverty*. Intergovernmental Panel on Climate Change (2018).

Chen, X. *et al.*, The increasing rate of global mean sea-level rise during 1993–2014, *Nature Climate Change* **7**(2017), pp. 492-495.

Couasnon, A. *et al.*, A flood risk framework capturing the seasonality of and dependence between rainfall and sea levels–an application to Ho Chi Minh City, Vietnam, *Water Resources Research*(2022), p. e2021WR030002.

Czado, C., Pair-copula constructions of multivariate copulas. *Copula theory and its applications*, Springer (2010), pp. 93-109.

Dodangeh, E., Shahedi, K., Solaimani, K., Shiau, J.-T., Abraham, J., Data-based bivariate uncertainty assessment of extreme rainfall-runoff using copulas: comparison between annual maximum series (AMS) and peaks over threshold (POT), *Environmental monitoring and assessment* **191**(2019), p. 67.

Dore, M.H., Climate change and changes in global precipitation patterns: what do we know?, *Environment international* **31**(2005), pp. 1167-1181.

Duy, P.N., Chapman, L., Tight, M., Linh, P.N., Thuong, L.V., Increasing vulnerability to floods in new development areas: evidence from Ho Chi Minh City, *International Journal of Climate Change Strategies and Management*(2017).

Genest, C., Quessy, J.F., Rémillard, B., Goodness-of-fit procedures for copula models based on the probability integral transformation, *Scandinavian Journal of Statistics* **33**(2006), pp. 337-366.

Ghanbari, M., Arabi, M., Kao, S.C., Obeysekera, J., Sweet, W., Climate Change and Changes in Compound Coastal-Riverine Flooding Hazard Along the US Coasts, *Earth's Future*(2021), p. e2021EF002055.

Glenn, E., On a New Framework for Detecting, Classifying, and Forecasting Floods for Large-Scale Flood Risk Analysis. The City College of New York (2022).

Golnaraghi, M., Thistlethwaite, J., Henstra, D., Stewart, C., Flood Risk Management in Canada: Building flood resilience in a changing climate, *Retrieved February* **4**(2020), p. 2021.

González-López, V.A., Piovesana, M.C., Romano, N., Tail conditional probabilities to predict academic performance, *4open* **2**(2019), p. 18.

Howarth, M.E., Thorncroft, C.D., Bosart, L.F., Changes in extreme precipitation in the northeast United States: 1979–2014, *Journal of Hydrometeorology* **20**(2019), pp. 673-689.

Jalili Pirani, F., Najafi, M., Recent trends in individual and multivariate compound flood drivers in Canada's coasts, *Water Resources Research* **56**(2020), p. e2020WR027785.

Jane, R., Cadavid, L., Obeysekera, J., Wahl, T., Multivariate statistical modelling of the drivers of compound flood events in south Florida, *Natural Hazards and Earth System Sciences* **20**(2020), pp. 2681-2699.

Joe, H., *Multivariate models and multivariate dependence concepts*. CRC Press (1997).
Jonkman, S.N., Kelman, I., An analysis of the causes and circumstances of flood disaster deaths, *Disasters* **29**(2005), pp. 75-97.

Lemmen, D.S., *Canada's marine coasts in a changing climate*. Government of Canada= Gouvernement du Canada (2016).

Li, S. *et al.*, Estimating the design flood under the influence of check dams by removing nonstationarity from the flood peak discharge series, *Hydrology Research* **51**(2020), pp. 1261-1273.

Liang, X.-Z., Extreme rainfall slows the global economy. Nature Publishing Group (2022).

Liu, Z. et al., 2018. A framework for exploring joint effects of conditional factors on compound floods. *Water Resources Research*, 54(4): 2681-2696.

Machiwal, D., Jha, M.K., *Hydrologic time series analysis: theory and practice*. Springer Science & Business Media (2012).

Mahmoudi MH, Najafi MR, Singh H, Schnorbus M. Spatial and temporal changes in climate extremes over northwestern North America: the influence of internal climate variability and external forcing. Climatic Change. 2021 Mar;165(1):1-9.

McElreath, R., *Statistical rethinking: A Bayesian course with examples in R and Stan*. Chapman and Hall/CRC (2018).

Milrad, S.M., Atallah, E.H., Gyakum, J.R., Dynamical and precipitation structures of poleward-moving tropical cyclones in eastern Canada, 1979–2005, *Monthly weather review* **137**(2009), pp. 836-851.

Moftakhari, H.R., Salvadori, G., AghaKouchak, A., Sanders, B.F., Matthew, R.A., Compounding effects of sea level rise and fluvial flooding, *Proceedings of the National Academy of Sciences* **114**(2017), pp. 9785-9790.

Nelson, R., An Introduction to Copulas, 1999, *Lecture notes in statistics*(1998).
Salvadori, G., De Michele, C., Frequency analysis via copulas: Theoretical aspects and applications to hydrological events, *Water resources research* **40**(2004).

Salvadori, G., De Michele, C., Kottegoda, N.T., Rosso, R., *Extremes in nature: an approach using copulas*. Springer Science & Business Media (2007).

Sánchez-Almodóvar, E., Olcina-Cantos, J., Martí-Talavera, J., Adaptation Strategies for Flooding Risk from Rainfall Events in Southeast Spain: Case Studies from the Bajo Segura, Alicante, *Water* **14**(2022), p. 146.

Sarhadi, A., Burn, D.H., Concepcion Ausin, M., Wiper, M.P., Time-varying nonstationary multivariate risk analysis using a dynamic Bayesian copula, *Water Resources Research* **52**(2016), pp. 2327-2349.

Schepsmeier, U. *et al.*, Package 'VineCopula', *R package version* **2**(2015).

Shiau, J., Fitting drought duration and severity with two-dimensional copulas, *Water resources management* **20**(2006), pp. 795-815.

Heterogeneous snowpack response and snow drought occurrence across river basins of northwestern North America under 1.0° C to 4.0° C global warming

Singh, H., Najafi, M.R., Cannon, A.J., Characterizing non-stationary compound extreme events in a changing climate based on large-ensemble climate simulations, *Climate Dynamics* **56**(2021), pp. 1389-1405.

Singh H, Pirani FJ, Najafi MR. Characterizing the temperature and precipitation covariability over Canada. *Theoretical and Applied Climatology*. 2020 Feb;139(3):1543-58.

Singh H, Najafi MR. Evaluation of gridded climate datasets over Canada using univariate and bivariate approaches: Implications for hydrological modelling. *Journal of Hydrology*. 2020 May 1;584:124673.

Singh H, Najafi MR, Cannon A. Evaluation and joint projection of temperature and precipitation extremes across Canada based on hierarchical Bayesian modelling and large ensembles of regional climate simulations. *Weather and Climate Extremes*. 2022 Jun 1;36:100443.

Sugi, M., Noda, A., Sato, N., Influence of the global warming on tropical cyclone climatology: An experiment with the JMA global model, *Journal of the Meteorological Society of Japan. Ser. II* **80**(2002), pp. 249-272.

Trenberth, K.E., Changes in precipitation with climate change, *Climate research* **47**(2011), pp. 123-138.

Villarini, G., Smith, J.A., Ntelekos, A.A., Schwarz, U., Annual maximum and peaks-over-threshold analyses of daily rainfall accumulations for Austria, *Journal of Geophysical Research: Atmospheres* **116**(2011).

Wahl, T., Jain, S., Bender, J., Meyers, S.D., Luther, M.E., Increasing risk of compound flooding from storm surge and rainfall for major US cities, *Nature Climate Change* **5**(2015), pp. 1093-1097.

Wang S, Najafi MR, Cannon AJ, Khan AA. Uncertainties in Riverine and Coastal Flood Impacts under Climate Change. *Water*. 2021 Jan;13(13):1774.

Ward, P.J. *et al.*, Dependence between high sea-level and high river discharge increases flood hazard in global deltas and estuaries, *Environmental Research Letters* **13**(2018), p. 084012.

Wen, T., Jiang, C., Xu, X., Nonstationary analysis for bivariate distribution of flood variables in the Ganjiang River using time-varying copula, *Water* **11**(2019), p. 746.

Wilhelm, B. *et al.*, Impact of warmer climate periods on flood hazard in the European Alps, *Nature geoscience* **15**(2022), pp. 118-123.

Xia, J., Yang, X.-y., Liu, J., Wang, M., Li, J., Dominant change pattern of extreme precipitation and its potential causes in Shandong Province, China, *Scientific Reports* **12**(2022), pp. 1-15.

Xiong, B., Xiong, L., Chen, J., Xu, C.-Y., Li, L., Multiple causes of nonstationarity in the Weihe annual low-flow series, *Hydrology and Earth System Sciences* **22**(2018), pp. 1525-1542.

Xu, H., Xu, K., Lian, J., Ma, C., Compound effects of rainfall and storm tides on coastal flooding risk, *Stochastic Environmental Research and Risk Assessment* **33**(2019), pp. 1249-1261.

Zhang Y, Najafi MR. Probabilistic numerical modeling of compound flooding caused by Tropical Storm Matthew over a data-scarce coastal environment. *Water Resources Research*. 2020 Oct;56(10):e2020WR028565.

Zheng, F., Westra, S., Leonard, M., Sisson, S.A., Modeling dependence between extreme rainfall and storm surge to estimate coastal flooding risk, *Water Resources Research* **50**(2014), pp. 2050-2071.

Zhou, Y. et al., Probabilistic interval estimation of design floods under non-stationary conditions by an integrated approach, *Hydrology Research* 53(2022), pp. 259-278.

Chapter 6

6.1. Conclusion

Canadian coastal regions are prone to compound flooding events, which is the co-occurrence of multiple flooding sources including pluvial, fluvial, and sea level forces. Analyzing each of these drivers in isolation can lead to the underestimation of the flooding risk in these areas. Therefore, in our research, initially, we investigate the compound flooding risk over the Canadian coastal regions in a bivariate case. To this end, at first, we identify eight bivariate scenarios of four flooding drivers (total water level, streamflow, precipitation, and skew surge) in the way that the extreme values (higher than quantile 0.95) of one driver are matched with the corresponding maximum values of the second driver within a time window of 1-day. The dependence structure between the drivers of each scenario is also captured using the copula. Following producing the joint distribution of each scenario at each location, the associated parameters are estimated using the Bayes theorem. Then, compound flood hazard analyses are performed using the return period, failure probability, and CHR index concepts. This step helped us to mark the spots with a higher compound flooding potential with regard to most of the bivariate events. Similar to the bivariate methodology, in our second step, we apply the C-Vine copula approach to account for the joint behavior of total water level, precipitation, and streamflow. RP, FP, and CHR index techniques are also employed here to quantify the univariate and multivariate flooding risks. Further, we explored how the daily and extreme magnitudes and the frequency of each flooding driver change with time using the Mann-Kendall trend test. Besides, the bivariate/trivariate trends were assessed using the CIT, CST, and CET and PS index at each site. Due to the effects of climate change, flooding drivers and, also the interdependencies between them might show a time-varying behavior. This causes the drivers to have a nonstationary joint probability, subsequently. Considering the tri-variate case study, to capture such non-stationarities, we fit three constant, linear, and polynomial models to both marginal locations and the interdependency between them. In case of the existence of any non-stationarity in the joint probability of the drivers, we

accounted for time-dependent joint return periods and failure probabilities at each location. The obtained results of this study highlight that the real picture of flooding over the Canadian coastal areas is acquired concerning multiple flooding drivers and also the interconnection between them. Moreover, the nonstationarity in the flooding sources and the respected dependencies would lead to a time-varying flooding hazard. This gives the policy-makers open views to suggest more correct, robust, and long-lasting design levels and resilience strategies such as upstream reservoirs, flood barriers, dykes, building regulations, and guidelines, educating people to be prepared for these types of joint events, emergency preparedness to protect lives, and reduce damages. The proposed approach in this study is not only extendable to other coastal regions across the world, but is also applicable to other studies working with multiple variables.

6.2. Summary of findings

- In a bivariate analysis, the highest dependence is found between $TWL_{e\_0.95}$ and Pr followed by the bivariate events of $(S_{e\_0.95}, Pr)$, $(Pr_{e\_0.95}, S)$, $(Pr_{e\_0.95}, TWL)$, $(Q_{e\_0.95}, S)$, $(Q_{e\_0.95}, TWL)$, $(S_{e\_0.95}, Q)$ and $(TWL_{e\_0.95}, Q)$.

- The results of the bivariate JRPs are similar to those of the tri-variate JRPs. The OR and AND JRPs increase and decrease, respectively with an enhancement in the dependency between the drivers. However, the results highlight the importance of S over both coasts and the TWL in the GL region.

- According to the bivariate AND JRP results and the CHR index. The results indicate that most locations across Canada's coasts are at risk of compound flooding with a combination of at least two flooding mechanisms.

- Due to the positive interaction between the drivers, at the majority of the locations, the tri-variate OR JRPs are higher than the independence JRPs and lower than the univariate RP. This is vice versa for the AND scenario as at 23 locations the JRP under the dependence condition is far lower than the independence one.

160

- The stationary CHR index results also indicate that at locations with positive dependency between the drivers, the return levels of Q conditioning on the TWL and Pr are higher than unconditional Q.

- The failure probabilities go up with the increase in the project lifetime considering all the hazard scenarios (univariate, multivariate… etc). However, the multivariate FPs are higher for the dependence condition in comparison with the independence and the univariate options. Moreover, the 10-year-related FPs are higher than 100-year FPs.

- The daily univariate trend results indicate a mixture of increasing, decreasing, and no trend for four drivers over the three main regions. All variables, except for Pr, show an increasing trend over the Atlantic coast. The daily TWL also decreases in the GL area.

- For the majority of the locations mainly in the Atlantic region, the joint trend of daily Q/S, Q/TWL, and Q/S is increasing. However, TWL/Pr mostly indicate increasing behavior over the GL area.

- The frequency of extremes higher than a quantile shows a raising trend over some spots at three regions more remarkable at the Atlantic region regarding TWL, Pr and S. However, mainly the extreme magnitudes of Pr show increasing behavior on the Atlantic area.

- More locations show a positive significant dependency between TWL and Pr than (TWL, Q) and (Pr, Q). Moreover, the joints of (Pr, TWL) and (Q, TWL) present stronger interconnections than (Pr, Q).

- Due to the change in the interconnection between the drivers, the OR and AND JRPs raise and diminish, respectively from 1960 to 2015 for 16 locations, more highlighted for the Atlantic coast. At 7 locations, although the dependency is time-constant, the return levels of at least one of the drivers are accretionary with time.

- The nonstationary tri-variate FPs are higher than tri-variate FPs under the stationary conditions and also the univariate FPs.

6.3. Recommendations for future work

The current research tried to assess the flooding hazard over the Canadian coastal regions both in the univariate and multivariate scenarios. The following recommendations are suggested for future work:

- Considering the effects of climate change, such analysis can be extended for the assessment of compound flood event projections.

- In this study, we considered the monotonic trends of the drivers and the interdependencies between them. The flooding analysis can be assessed considering other types of non-stationarities including jump and step change as well.

- The obtained results (univariate and multivariate) of this study can be used as input to the hydrodynamic models to assess the flood impacts associated with individual and compound flood events.

- The risk analysis of the flooding in the coastal regions can be obtained by combining these results with exposure and vulnerability data.
- Other flooding drivers such as groundwater flooding can also be incorporated into the compound flooding analysis similar to other flooding divers in this study over the Canadian regions or elsewhere.
- The missing values in some locations can be filled out using different statistical approaches. However, in case of existing considerable missing values in the data, the satellite data can be considered as an option for compound flooding analysis.

Note: The related R-script of this study is provided in the below link and the package will also be provided soon for the users.

"https://github.com/fjalilip?tab=repositories".

Appendix A: List of supplementary Tables and Figures

Supplementary Table 2. 1) Four variables that contribute to compound flooding in Canada's coastal zones

Variable	Source	Resolution
Total Water Level (TWL)	Tidal gauge records, Fisheries and Oceans Canada (https://tides.gc.ca/eng/data)	Hourly
Skew surge	Extracted from TWL using the U_Tide package (Codiga, 2011)	Daily
Streamflow	Water Survey of Canada (https://www.canada.ca/en/environment-climate-change/services/water-overview/quantity/monitoring/survey.html)	Daily
Precipitation	Adjusted and Homogenized Canadian Climate Data (AHCCD) (Mekis and Vincent, 2011)	Daily

Supplementary Table 2. 2) The marginal distributions and the corresponding parameters

Distribution	First parameter range	Second parameter range	Third parameter range
Generalized Pareto Distribution (GPD)	μ (Location), $(-\infty, +\infty)$	σ (Scale) > 0	ξ (Shape), $(-\infty, +\infty)$
Generalized Extreme Value distribution (GEV)	μ (Location), $(-\infty, +\infty)$	σ (Scale) > 0	ξ (Shape), $(-\infty, +\infty)$
Gamma	α (Shape) > 0	β (Rate) > 0	-
Gumbel	μ (Location), $(-\infty, +\infty)$	β (Scale) > 0	-
Cauchy	χ_0 (Location), $(-\infty, +\infty)$	γ (Scale) > 0	-
Logistic	μ (Location), $(-\infty, +\infty)$	S (Scale) > 0	-
Weibull	λ (Scale) >0	K (Shape) > 0	-
Normal	μ (Location), $(-\infty, +\infty)$	σ (Scale) > 0	-
Lognormal	μ (Location), $(-\infty, +\infty)$	σ (Scale) > 0	-
Exponential	λ (Rate) > 0	-	-

Supplementary Table 2. 3) The Copula functions, the corresponding family codes, and the range of parameters

Copula family	Symbol	family	First parameter range	Second parameter range
Independence	C0	0		-
Gaussian	C1	1	(-1, 1)	-
Student t	C2	2	(-1, 1)	[2, Inf)
(Survival) Clayton	C3, C4	3, 13	(0, Inf)	-
Rotated Clayton (90 and 270 degrees)	C5, C6	23, 33	(-Inf, 0)	-
(Survival) Gumbel	C7, C8	4, 14	(1, Inf)	-
Rotated Gumbel (90 and 270 degrees)	C9, C10	24, 34	(-Inf, -1]	-
Frank	C11	5	R \ {0}	-
(Survival) Joe	C12, C13	6, 16	(1, Inf)	-
Rotated Joe (90 and 270 degrees)	C14, C15	26, 36	(-Inf, -1)	-
(Survival) Clayton-Gumbel (BB1)	C16, C17	7, 17	(0, Inf)	[1, Inf)
Rotated Clayton-Gumbel (90 and 270 degrees)	C18, C19	27, 37	(-Inf, 0)	(-Inf, -1]
(Survival) Joe-Gumbel (BB6)	C20, C21	8, 18	[1 , Inf)	[1, Inf)
Rotated Joe-Gumbel (90 and 270 degrees)	C22, C23	28, 38	(-Inf, -1]	(-Inf, -1]
(Survival) Joe-Clayton (BB7)	C24, C25	9, 19	[1, Inf)	(0, Inf)
Rotated Joe-Clayton (90 and 270 degrees)	C26, C27	29, 39	(-Inf, -1]	(-Inf, 0)
(Survival) Joe-Frank (BB8)	C29, C30	10, 20	[1, Inf)	(0, 1]
Rotated Joe-Frank (90 and 270 degrees)	C31, C32	30, 40	(-Inf, -1]	[-1, 0)
(Survival) Tawn type 1	C33, C34	104, 114	[1, Inf)	[0, 1]
Rotated Tawn type 1(90 and 270 degrees)	C35, C36	124, 134	(-Inf, -1]	[0, 1]
(Survival) Tawn type 2	C37, C38	204, 214	[1, Inf)	[0, 1]
Rotated Tawn type 2 (90 and 270 degrees)	C39, C40	224, 234	(-Inf, -1]	[0, 1]

Supplementary Table 2. 4) The best-fitted copula functions to the bivariate (Pr$_{e\_0.95}$, TWL) and (Pr$_{e\_0.95}$, S) events at each location.

Location	(Pr$_{e\_0.95}$, TWL)			(Pr$_{e\_0.95}$, S)		
	Copula family	AIC	P-value	Copula family	AIC	P-value
1	24	1.22	0.60	1	-18.51	0.16
2	104	-6.51	0.72	0	0	0.81
3	124	-1.49	0.88	33	-3.17	0.67
4	214	0.60	0.32	0	0	0.75
5	3	-0.97	0.97	0	0	0.94
6	5	-28.70	0.35	5	-31.49	0.78
7	114	-9.38	0.49	5	-4.99	0.51
8	114	-12.36	0.61	5	-7.84	0.78
9	0	0	0.89	104	-4.51	0.52
10	4	-1.49	0.76	36	-2.35	0.22
11	114	-1.75	0.31	5	-1.31	0.28
12	114	-2.99	0.41	5	-0.93	0.30
13	1	0.68	0.30	1	-1.52	0.07
14	0	0	0.85	0	0	0.65
15	5	-8.71	0.72	10	-1.21	0.12
16	5	-12.10	0.70	10	-0.44	0.06
17	5	-7.48	0.92	14	-4.02	0.14
18	114	-8.52	0.21	1	-25.79	0.51
19	114	0.51	0.47	5	-8.40	0.96
20	1	0.82	0.75	5	-2.48	0.45
21	16	0.82	0.73	5	0.22	0.68
22	204	-4.91	0.39	134	-1.33	0.37
23	1	-5.17	0.41	0	0	0.92
24	1	0.38	0.38	0	0	0.85
25	234	-0.68	0.60	134	-0.59	0.33
26	134	-8.43	0.62	0	0	0.75
27	3	-2.15	0.35	0	0	0.71
28	214	-1.95	0.26	5	-3.23	0.47
29	204	-1.57	0.45	1	-8.82	0.35
30	204	-7.77	0.28	1	-18.42	0.08
31	13	1.36	0.46	13	-10.62	0.48
32	134	0.00	0.92	6	-1.51	0.39
33	104	-3.74	0.17	1	-17.69	0.47
34	5	-1.20	0.37	1	-18.11	0.67
35	5	-0.51	0.39	1	-16.58	0.97
36	204	-1.48	0.42	5	-1.70	0.38
37	5	1.16	0.01	204	-1.08	0.08
38	5	-2.28	0.01	0	0	0.73
39	24	-0.10	0.30	0	0	0.89
40	5	-0.52	0.98	5	-0.51	0.65
41	13	-11.15	0.66	13	-21.99	0.89

Supplementary Table 2. 5) Similar to Table S2.4 but for ($Q_{e\_0.95}$, TWL) and ($Q_{e\_0.95}$, S) scenarios.

Location	($Q_{e\_0.95}$, TWL)			($Q_{e\_0.95}$, S)		
	Copula family	AIC	P-value	Copula family	AIC	P-value
1	0	0	0.62	0	0	0.70
2	224	-4.96	0.16	114	-0.27	0.84
3	6	-4.29	0.31	204	-11.95	0.34
4	0	0	0.92	3	-4.98	0.76
5	5	-8.66	0.30	1	-18.79	0.69
6	23	-5.67	0.21	36	-15.47	0.19
7	23	-0.53	0.19	36	-9.10	0.09
8	204	-1.77	0.44	114	-4.98	1.00
9	16	-7.67	0.41	36	-3.52	0.40
10	224	-14.18	0.75	5	-6.60	0.34
11	134	-1.71	0.68	36	-4.27	0.31
12	224	-12.74	0.46	224	-5.07	0.40
13	23	-4.61	0.24	0	0	0.72
14	23	-6.13	0.66	5	-6.49	0.14
15	6	-6.24	0.41	36	-4.30	0.20
16	6	-15.54	0.44	36	-0.58	0.24
17	6	-9.78	0.36	6	-8.74	0.15
18	6	-22.94	0.19	6	-2.62	0.25
19	13	-12.71	0.50	16	-1.48	0.40
20	6	-8.85	0.22	0	0	0.87
21	224	-6.56	0.83	224	-7.88	0.70
22	5	-4.60	0.57	0	0	0.37
23	224	-4.08	0.44	3	-5.98	0.43
24	13	-5.03	0.12	13	-6.01	0.82
25	36	-13.37	0.38	0	0	0.85
26	13	-1.61	0.30	6	-3.11	0.41
27	0	0	0.96	234	-3.90	0.52
28	0	0	0.62	34	-2.47	0.43
29	10	-16.02	0.11	10	-15.85	0.79
30	10	-23.42	0.37	1	-11.07	0.89
31	104	-0.93	0.33	36	-19.37	0.33
32	1	-12.21	0.45	1	-14.77	0.15
33	5	-4.35	0.72	1	-6.51	0.08
34	1	-11.76	0.62	1	-14.33	0.23
35	5	-8.82	0.11	1	-15.51	0.12
36	5	-8.17	0.05	1	-12.59	0.09
37	5	-16.76	0.00	5	-5.63	0.40
38	5	-14.27	0.01	5	-6.95	0.73
39	0	0	0.93	224	-4.95	0.89
40	124	-1.21	0.39	204	-2.79	0.94
41	134	-1.75	0.52	124	-2.39	0.61

Supplementary Table 2. 6) Similar to Table S2.4 but for (TWL$_{e\_0.95}$, Q) and (TWL$_{e\_0.95}$, Pr) scenarios.

Location	(TWL$_{e\_0.95}$, Q)			(TWL$_{e\_0.95}$, Pr)		
	Copula family	AIC	P-value	Copula family	AIC	P-value
1	33	-12.66	0.86	10	-43.32	0.14
2	134	-9.07	0.04	14	-0.12	0.25
3	5	-19.24	0.3	20	-12.04	0.27
4	114	-65.71	0.05	5	-27.16	0.4
5	114	-34.63	0.18	1	-8.6	0.74
6	5	-5.3	0.59	20	-39.62	0.87
7	224	-23.78	0.35	1	-20.83	0.81
8	224	-17.48	0.24	1	-15.3	0.46
9	33	-18.11	0	0	0	0.56
10	224	-4.49	0.16	0	0	0.64
11	16	-8.34	0.33	1	-0.92	0
12	26	-0.4	0.2	1	-2.94	0.04
13	224	-2.2	0.23	16	0.46	0.15
14	16	-10.25	0	14	-2.91	0.38
15	6	-7.23	0.27	10	-15.93	0.26
16	3	-2.51	0	13	-6.61	0.39
17	6	-5.63	0.13	5	-3.01	0.01
18	0	0	0.52	204	-5.22	0.09
19	104	0.61	0.19	36	-0.92	0.1
20	26	0.7	0.17	114	-0.77	0.9
21	224	-0.7	0.05	16	-2.13	0.09
22	224	-2.49	0	0	0	0.79
23	224	-4.78	0.01	0	0	0.77
24	204	-14.57	0.73	204	-7.7	0.83
25	114	-16.75	0.74	114	0.32	0.5
26	1	-29.1	0.1	114	-17.99	0.62
27	0	0	0.76	0	0	0.97
28	224	0.73	0.09	0	0	0.81
29	134	-14.48	0.31	4	-0.95	0
30	1	-13.23	0.18	0	0	95
31	0	0	0.83	33	-0.07	0.09
32	0	0	0.75	0	0	0.78
33	104	-2.14	0.74	26	-2.35	0.06
34	124	-1.47	0.01	0	0	0.86
35	0	0	0.91	0	0	0.88
36	4	-0.04	0.88	5	1.47	0.3
37	26	-2.78	0.44	5	-3.39	0.79
38	0	0	0.68	0	0	1
39	23	-7.34	0.98	214	-2.4	0.63
40	0	0	0.83	1	-13.34	0.11
41	23	-4.14	0.33	3	-2.27	0.24

Supplementary Table 2. 7) Similar to Table S2.4 but for $(S_{e\_0.95}, Q)$ and $(S_{e\_0.95}, Pr)$ scenarios

Location	$(S_{e\_0.95}, Q)$			$(S_{e\_0.95}, Pr)$		
	Copula family	AIC	P-value	Copula family	AIC	P-value
1	224	-8.66	0.74	1	-36.52	0.00
2	134	-2.88	0.72	0	0	0.77
3	30	-12.97	0.30	33	0.47	0.89
4	5	-67.38	0.90	5	-15.14	0.98
5	5	-45.64	0.00	3	-17.94	0.07
6	5	-6.00	0.00	13	-13.83	0.00
7	5	-5.07	0.02	3	-4.78	0.56
8	1	-6.02	0.39	1	-2.59	0.96
9	114	-2.85	0.38	1	-11.26	0.16
10	0	0	0.68	1	-17.40	0.29
11	0	0	0.95	13	-14.10	0.53
12	0	0	0.88	1	-19.13	0.08
13	214	-5.99	0.15	204	-19.80	0.01
14	16	-3.87	0.05	13	-9.65	0.71
15	1	-7.39	0.39	5	-24.72	0.06
16	5	-18.00	0.96	1	-33.90	0.02
17	114	-20.30	0.49	5	-28.36	0.05
18	3	-3.25	0.73	13	-14.31	0.00
19	5	-5.27	0.62	5	1.48	0.11
20	5	-8.60	0.01	5	-2.78	0.00
21	114	-8.81	0.10	204	-14.22	0.04
22	5	0.57	0.31	204	-10.25	0.00
23	114	-7.12	0.07	5	-5.25	0.80
24	17	-20.75	0.05	204	-25.02	0.97
25	16	-1.62	0.66	1	-32.60	0.95
26	1	-44.71	0.01	114	-22.05	0.74
27	5	-24.31	0.09	0	0	0.73
28	10	-21.99	0.61	204	-3.50	0.49
29	23	-2.28	0.05	134	-9.45	0.92
30	14	-3.33	0.59	0	0	0.92
31	10	-25.96	0.00	0	0	0.95
32	134	-2.84	0.15	0	0	0.74
33	5	-0.99	0.06	0	0	0.88
34	5	-8.49	0.00	214	-1.62	0.47
35	134	-15.21	0.04	114	-5.13	0.45
36	124	-2.43	0.66	26	0.92	0.91
37	134	-5.69	0.66	5	-4.36	0.41
38	134	-4.85	0.37	5	0.99	0.12
39	1	-5.31	0.27	0	0	0.68
40	234	-0.93	0.48	204	-3.90	0.07
41	5	-5.95	0.00	4	-16.81	0.11

Supplementary Table 2. 8) The number of locations out of 8 (Pacific), 31 (GL) and 2 (Atlantic) passing the goodness of fit test with respect to each scenario.

Scenario	Region		
	Atlantic	GL	Pacific
$(Pr_{e\_0.95}, TWL)$	8	29	2
$(Pr_{e\_0.95}, S)$	8	31	2
$(Q_{e\_0.95}, TWL)$	8	29	2
$(Q_{e\_0.95}, S)$	8	30	2
$(TWL_{e\_0.95}, Pr)$	8	27	2
$(TWL_{e\_0.95}, Q)$	7	25	2
$(S_{e\_0.95}, Pr)$	6	25	2
$(S_{e\_0.95}, Q)$	5	26	1

Supplementary Table 3. 1) The selected marginal distributions for Pr, Q, and TWL at each location along with their AIC and KS test p-values. The stations where the fluvial flood is amplified are highlighted.

Station	Name	Distribution (Pr)	AIC (Pr)	KS p-value (Pr)	Distribution (Q)	AIC (Q)	KS p-value (Q)	Distribution (TWL)	AIC (TWL)	KS p-value (TWL)
1	Queen charlotte city	GPD	5503.62	0.02	GPD	182.33	0.00	Gamma	4333.34	0.05
2	Prince rupert	GPD	5238.61	0.03	Gumbel	-166.62	0.00	GPD	7728.43	0.00
3	**Bella bella**	GPD	4627.48	0.03	Normal	1095.58	0.04	GPD	7864.04	0.00
4	**Port hardy**	GPD	4475.93	0	GEV	1029.30	0.13	GPD	7929.93	0.00
5	**Tofino**	GPD	5070.43	0	Gumbel	1369.70	0.06	Logistic	10074.13	0.00
6	Victoria harbour	GPD	4710.81	0.01	Weibull	114.48	0.00	GPD	5672.24	0.00
7	**Point atkinson**	GPD	4820.84	0	GEV	229.33	0.05	GEV	10180.39	0.02
8	**Vancouver**	GPD	4435.98	0.02	GEV	164.84	0.01	GPD	8230.06	0.00
9	Rossport	GPD	5192.10	0	Cauchy	1041.26	0.00	Gamma	6312.51	0.01
10	Michipicoten	GPD	5398.56	0	Exponential	2962.52	0.00	GPD	6751.61	0.30
11	Gros cap	GPD	5383.14	0	GEV	706.46	0.17	GPD	8443.35	0.00
12	Sault ste marie	GPD	4412.80	0.04	GEV	1023.76	0.13	GPD	10324.52	0.00
13	Sault ste marie	GPD	4402.73	0	GEV	1160.24	0.18	GEV	2017.58	0.04
14	Thessalon	GPD	4360.03	0	Logistic	-22.18	0.02	Normal	10185.42	0.00
15	Bar_point	GPD	4879.51	0	GEV	-103.02	0.01	Weibull	3036.65	0.08
16	**Amherstburg**	GPD	4669.34	0	Normal	-260.82	0.03	Weibull	3147.14	0.04
17	**Kingsville**	GPD	4465.04	0	Logistic	-104.21	0.03	Weibull	2903.24	0.36
18	Belle river	GPD	4441.81	0.03	Cauchy	1265.54	0.00	GPD	2981.94	0.08
19	**Port lambton**	GPD	4421.76	0	Cauchy	1190.94	0.00	GPD	2956.70	0.02
20	**Point edward**	GPD	4993.34	0	Cauchy	1147.81	0.00	GEV	4137.62	0.04
21	Little current	GPD	4430.77	0	Cauchy	1126.49	0.00	GPD	5363.58	0.03
22	**Tobermory**	GPD	5131.90	0	GPD	1060.68	0.00	GEV	6238.63	0.39
23	**Collingwood**	GPD	5293.28	0	GPD	1112.50	0.00	GPD	2229.97	0.02
24	Port dover	GPD	5132.25	0.03	Cauchy	1074.73	0.00	Weibull	2225.61	0.04
25	Parry sound	GPD	5160.88	0	Exponential	1328.24	0.00	Weibull	2302.63	0.09
26	Port colborne	GPD	5273.40	0	GEV	448.91	0.11	Weibull	2527.03	0.12
27	Port weller	GPD	5162.88	0	Exponential	1464.63	0.00	Weibull	1904.00	0.04
28	cobourg	GPD	5432.84	0	Exponential	1706.30	0.00	Weibull	2067.15	0.13
29	**cornwall**	GPD	5548.74	0	Exponential	1667.09	0.00	Weibull	2126.93	0.01
30	**summerstown**	GPD	4506.43	0.03	Exponential	1545.39	0.00	GPD	3116.46	0.00
31	**pointe-des-cascades**	GPD	4756.21	0	Exponential	1748.39	0.00	GPD	5006.49	0.04
32	**sainte-anne-de-bellevue**	GPD	5013.82	0	Exponential	1055.73	0.00	GPD	5239.57	0.01
33	**pointe-claire**	GPD	5230.62	0.03	GPD	1146.67	0.00	Gamma	3775.56	0.00
34	**Montreal jetee**	GPD	5400.88	0.03	Exponential	1014.14	0.00	GEV	2326.27	0.08
35	**Mtl rue frontenac**	GPD	5304.60	0	Cauchy	-1383.51	0.00	GEV	2252.59	0.01
36	**Sorel**	GPD	4721.96	0	Weibull	648.83	0.16	GEV	2037.43	0.04
37	**Trois-rivières**	GPD	5201.40	0	Cauchy	1045.38	0.00	GPD	6375.99	0.00
38	**Batiscan**	GPD	5166.74	0.04	GEV	1661.58	0.07	GPD	6315.33	0.00
39	Saint-francois	GPD	4896.70	0	GEV	1525.74	0.04	GPD	5985.24	0.00
40	Halifax	GPD	4763.44	0	GEV	1311.09	0.00	GPD	5950.20	0.00
41	**St johns**	GPD	4579.59	0	Cauchy	1046.42	0.00	GPD	5657.46	0.00

Supplementary Table 3. 2) The pair-copulas at each location along with the best-fitted copula function, AIC values, and the corresponding p-values.

Station	Joint, copula family	AIC(Pr, TWL)	p-value (Pr, TWL)	Joint, copula family	AIC(Pr, Q)	p-value (Pr, Q)	Joint, copula family	AIC(Q, TWL)	p-value (Q, TWL)
1	(Pr, TWL), 5	-0.52	0.97	(Pr, Q|TWL), 4	0.73	0.85	(Q, TWL), 3	-6.88	0.46
2	(Pr, TWL), 13	-11.14	0.64	(Pr, Q|TWL), 134	-4.96	0.53	(Q, TWL), 134	-35.95	0.03
3	(Pr, TWL|Q), 24	-0.11	0.26	(Pr, Q), 124	-4.09	0.23	(Q, TWL), 134	-2.68	0.45
4	(Pr, TWL), 5	-2.27	0.01	(Pr, Q|TWL), 104	1.52	0.77	(Q, TWL), 6	-77.80	0.06
5	(Pr, TWL), 5	1.15	0.01	(Pr, Q|TWL), 214	-2.52	0.01	(Q, TWL), 6	-110.40	0
6	(Pr, TWL), 5	-28.70	0.35	(Pr, Q|TWL), 5	-22.7	0.25	(Q, TWL), 5	-33.71	0.12
7	(Pr, TWL), 214	-12.36	0.60	(Pr, Q|TWL), 224	-5.63	0.42	(Q, TWL), 5	-56.07	0
8	(Pr, TWL), 214	-9.38	0.51	(Pr, Q|TWL), 5	-1.31	0.87	(Q, TWL), 30	-50.65	0
9	(Pr, TWL|Q), 5	-3.28	0.15	(Pr, Q), 5	-7.54	0.98	(Q, TWL), 1	-44	0.76
10	(Pr, TWL|Q), 1	-19.91	0.98	(Pr, Q), 10	-39.25	0.03	(Q, TWL), 1	-26.59	0.56
11	(Pr, TWL|Q), 124	-1.65	0.82	(Pr, Q), 13	-10.43	0.87	(Q, TWL), 5	-12.16	0.27
12	(Pr, TWL|Q), 104	-7.08	0.69	(Pr, Q), 5	-1.01	0.96	(Q, TWL), 5	-3.71	0.53
13	(Pr, TWL), 134	1.22	0.6	(Pr, Q|TWL), 114	0.99	0.93	(Q, TWL|Pr), 5	-0.03	0.84
14	(Pr, TWL), 14	-1.00	0.91	(Pr, Q), 5	-11.56	0.22	(Q, TWL), 3	-7.53	0.1
15	(Pr, TWL|Q), 5	-12.24	0.4	(Pr, Q), 5	-18.52	0.57	(Q, TWL), 5	-21.5	0
16	(Pr, TWL|Q), 1	-8.99	0.22	(Pr, Q), 234	-7.54	0.53	(Q, TWL), 5	-14.6	0
17	(Pr, TWL|Q), 114	-5.37	0.16	(Pr, Q), 26	-2.37	0.46	(Q, TWL), 5	-15.75	0
18	(Pr, TWL|Q), 1	-0.42	0.19	(Pr, Q), 134	-7.56	0.04	(Q, TWL), 1	-7.61	0.54
19	(Pr, TWL|Q), 114	-0.95	0.23	(Pr, Q), 134	-8.15	0.01	(Q, TWL), 5	-6.1	0.29
20	(Pr, TWL|Q), 16	0.72	0.92	(Pr, Q), 124	-16.44	0.01	(Q, TWL), 134	-1.89	0.27
21	(Pr, TWL|Q), 6	1.00	0.61	(Pr, Q), 224	-13.72	0.36	(Q, TWL|Pr), 5	-8.32	0.27
22	(Pr, TWL), 1	-5.17	0.24	(Pr, Q), 24	-2.72	0.28	(Q, TWL), 134	0.54	0.78
23	(Pr, TWL), 104	-4.90	0.50	(Pr, Q|TWL), 204	-6.33	0.03	(Q, TWL), 1	-25.28	0.17
24	(Pr, TWL), 1	0.82	0.6	(Pr, Q|TWL), 13	-1.02	0.93	(Q, TWL), 234	-14.54	0
25	(Pr, TWL|Q), 5	1.60	0.54	(Pr, Q), 13	-2.93	0.78	(Q, TWL), 234	-0.27	0.49
26	(Pr, TWL), 114	-8.52	0.2	(Pr, Q|TWL), 5	-9.79	0.14	(Q, TWL), 13	-9.34	0.35
27	(Pr, TWL), 5	-12.10	0.72	(Pr, Q|TWL), 124	-1.89	0.10	(Q, TWL), 6	-7.47	0.36
28	(Pr, TWL), 5	-8.70	0.66	(Pr, Q|TWL), 6	-11.52	0.07	(Q, TWL), 5	-0.03	0.45
29	(Pr, TWL), 5	-7.47	0.93	(Pr, Q|TWL), 136	0.55	0.43	(Q, TWL), 234	-7.81	0.39
30	(Pr, TWL|Q), 104	-1.50	0.25	(Pr, Q) 13	-4.74	0.82	(Q, TWL), 6	-4.39	0.47
31	(Pr, TWL|Q), 134	-7.16	0.59	(Pr, Q), 33	0.40	0.47	(Q, TWL), 104	-16.32	0.58
32	(Pr, TWL|Q), 3	-2.25	0.62	(Pr, Q), 26	-14.5	0.12	(Q, TWL|Pr),23	-0.56	0
33	(Pr, TWL), 114	-1.95	0.25	(Pr, Q), 5	0.95	0.65	(Q, TWL), 13	1.94	0.09
34	(Pr, TWL), 104	-1.56	0.44	(Pr, Q|TWL), 5	-0.12	0.41	(Q, TWL), 204	-16.12	0.72
35	(Pr, TWL), 104	-7.76	0.25	(Pr, Q|TWL), 5	-1.56	0.59	(Q, TWL), 19	-32.11	0.11
36	(Pr, TWL|Q), 13	0.06	0.35	(Pr, Q), 5	0.83	0.44	(Q, TWL), 19	-29.69	0.39
37	(Pr, TWL), 204	-3.74	0.17	(Pr, Q|TWL), 214	-1.09	0.03	(Q, TWL), 204	-41.24	0.85
38	(Pr, TWL), 5	-1.19	0.38	(Pr, Q|TWL), 5	1.02	0.64	(Q, TWL), 204	-33.62	0.91
39	(Pr, TWL), 5	-0.51	0.39	(Pr, Q|TWL), 13	0.91	0.80	(Q, TWL), 204	-31.42	0.9
40	(Pr, TWL), 104	-1.48	0.43	(Pr, Q|TWL), 214	-4.17	0.72	(Q, TWL), 9	-35.64	0
41	(Pr, TWL|Q), 16	1.79	0.85	(Pr, Q), 5	0.55	0.34	(Q, TWL), 9	-65.33	0

Supplementary Table 3. 3) The pair-copulas at each location and the p-values corresponding to the dependence test.

173

Station	Joint	p-value (Pr, TWL)	Joint	p-value (Pr, Q)	Joint	p-value (Q, TWL)
1	(Pr, TWL)	0.03	(Pr, Q|TWL)	0.02	(Q, TWL)	0.0
2	(Pr, TWL)	0.00	(Pr, Q|TWL)	0.04	(Q, TWL)	0
3	(Pr, TWL|Q)	0.66	(Pr, Q)	0.01	(Q, TWL)	0.33
4	(Pr, TWL)	0.03	(Pr, Q|TWL)	0.21	(Q, TWL)	0
5	(Pr, TWL)	0.04	(Pr, Q|TWL)	0.17	(Q, TWL)	0
6	(Pr, TWL)	0	(Pr, Q|TWL)	0.01	(Q, TWL)	0
7	(Pr, TWL)	0	(Pr, Q|TWL)	0.05	(Q, TWL)	0
8	(Pr, TWL)	0	(Pr, Q|TWL)	0.04	(Q, TWL)	0
9	(Pr, TWL|Q)	0.87	(Pr, Q)	0	(Q, TWL)	0
10	(Pr, TWL|Q)	0.04	(Pr, Q)	0	(Q, TWL)	0
11	(Pr, TWL|Q)	0.71	(Pr, Q)	0	(Q, TWL)	0
12	(Pr, TWL|Q)	0.51	(Pr, Q)	0.03	(Q, TWL)	0.01
13	(Pr, TWL)	0.01	(Pr, Q|TWL)	0.06	(Q, TWL)	0.04
14	(Pr, TWL)	0	(Pr, Q)	0	(Q, TWL|Pr)	0.14
15	(Pr, TWL|Q)	0.03	(Pr, Q)	0	(Q, TWL)	0
16	(Pr, TWL|Q)	0.03	(Pr, Q)	0.04	(Q, TWL)	0
17	(Pr, TWL|Q)	0.18	(Pr, Q)	0.11	(Q, TWL)	0
18	(Pr,TWL|Q)	0.02	(Pr, Q)	0.05	(Q, TWL)	0
19	(Pr,TWL|Q)	0.04	(Pr, Q)	0.03	(Q, TWL)	0
20	(Pr, TWL|Q)	0.78	(Pr, Q)	0	(Q, TWL)	0.217
21	(Pr, TWL|Q)	0.02	(Pr, Q)	0	(Q, TWL)	0
22	(Pr, TWL)	0.01	(Pr, Q)	0	(Q, TWL|Pr)	0.06
23	(Pr, TWL)	0.02	(Pr, Q|TWL)	0	(Q, TWL)	0
24	(Pr, TWL)	0.02	(Pr, Q|TWL)	0	(Q, TWL)	0.03
25	(Pr, TWL|Q)	0.04	(Pr, Q)	0	(Q, TWL)	0.32
26	(Pr, TWL)	0.02	(Pr, Q|TWL)	0	(Q, TWL)	0.04
27	(Pr, TWL)	0	(Pr, Q|TWL)	0.02	(Q, TWL)	0.35
28	(Pr, TWL)	0	(Pr, Q|TWL)	0.38	(Q, TWL)	0.05
29	(Pr, TWL)	0	(Pr, Q|TWL)	0.21	(Q, TWL)	0.08
30	(Pr, TWL|Q)	0	(Pr, Q)	0.03	(Q, TWL)	0.03
31	(Pr, TWL|Q)	0.74	(Pr, Q)	0.05	(Q, TWL)	0.01
32	(Pr, TWL|Q)	0.38	(Pr, Q)	0.01	(Q, TWL)	0.23
33	(Pr, TWL)	0.61	(Pr, Q)	0.05	(Q, TWL|Pr)	0.69
34	(Pr, TWL)	0	(Pr, Q|TWL)	0.04	(Q, TWL)	0
35	(Pr, TWL)	0.01	(Pr, Q|TWL)	0.18	(Q, TWL)	0
36	(Pr, TWL|Q)	0.05	(Pr, Q)	0.07	(Q, TWL)	0
37	(Pr, TWL)	0.05	(Pr, Q|TWL)	0.02	(Q, TWL)	0
38	(Pr, TWL)	0.07	(Pr, Q|TWL)	0.64	(Q, TWL)	0
39	(Pr, TWL)	0.01	(Pr, Q|TWL)	0.04	(Q, TWL)	0
40	(Pr, TWL)	0.03	(Pr, Q|TWL)	0.13	(Q, TWL)	0
41	(Pr, TWL|Q)	0.02	(Pr, Q)	0.02	(Q, TWL)	0

Supplementary Table 4. 1) The covariance matrix between four variables obtained using equation 5 of the manuscript

	Q	T	P	S
Q	415085982598	56391347780	5396555294	30695552024
T	56391347780	415082382657	-4990354966	117862424112
P	5396555294	-4990354966	349302324753	-17785307195
S	30695552024	117862424112	-17785307196	415085342656

Supplementary Table 4. 2) The multivariate trend method, the trend statistics, the critical z/chi square values and trend type for the daily and extreme scenario of site# 40.

Scenario	Method	Test statistics	Trend type
Daily (T_d, Q_d)	CIT	2137.958	Increasing trend
	CET	87871090000	Increasing trend
	CST	-30578559	Increasing trend
Extreme ($T_{e\_0.99}$, Q)	CIT	4.33	No trend
	CET	163098	No trend
	CST	90	No trend
	PS	3.68	Increasing trend

Supplementary Table 4. 3) The decadal changes of the magnitude of the daily skew surge, streamflow, total water level and precipitation at each location.

Gauge number	Mean S (m)	Rate S (m)	Percent Change S (%)	Mean Q (m3)	Rate Q (m3)	Percent Change Q (%)	Mean T (m)	Rate T (m)	Percent Change T (%)	Mean P (m)	Rate P (m)	Percent Change P (%)
1	0.057	-0.008	-14.035	7.413	-0.028	-0.3777	6.306	0.001	0.0159	3.942	0.031	0.786
2	0.053	0.009	16.981	909.584	7.954	0.8745	6.186	0.016	0.2586	2.926	0.087	2.973
3	0.037	-0.007	-18.919	106.489	-0.029	-0.0272	4.503	-0.002	-0.0444	7.225	0.284	3.931
4	0.041	-0.011	-26.829	9.711	0.04	0.4119	4.557	-0.008	-0.1756	5.424	0.105	1.936
5	0.036	-0.017	-47.222	19.204	-0.664	-3.4576	3.378	-0.012	-0.3552	9.174	0.041	0.447
6	0.032	0.003	9.375	21.947	-0.024	-0.1094	2.646	0.004	0.1512	2.576	0.015	0.582
7	0.04	0.003	7.500	132.235	0.982	0.7426	4.461	0.007	0.1569	3.323	0.002	0.060
8	0.048	0.003	6.250	766.315	-0.534	-0.0697	4.477	0.006	0.1340	3.364	-0.01	-0.327
9	0.026	0.001	3.846	253.57	-4.328	-1.7068	0.199	-0.13	-65.3266	2.358	0.005	0.212
10	0.034	-0.002	-5.882	3.025	0.047	1.5537	0.223	-0.12	-54.2601	3.102	-0.11	-3.740
11	0.042	-0.001	-2.381	2.993	0.088	2.9402	0.247	-0.08	-32.3887	2.849	-0.002	-0.070
12	0.075	0.004	5.333	2.97	0.121	4.0741	0.309	-0.06	-19.7411	2.856	0.009	0.315
13	0.041	0.004	9.756	2.672	-0.046	-1.7216	0.595	-0.24	-41.6807	2.861	0.031	1.084
14	0.02	0.001	5.000	2.645	-0.063	-2.3819	0.567	-0.21	-37.2134	2.87	0.028	0.976
15	0.065	0.005	7.692	0.578	0.015	2.5952	0.939	-0.06	-7.3482	2.682	0.074	2.759
16	0.038	~0	~0.000	0.582	0.009	1.5464	0.875	-0.08	-9.8286	2.697	0.068	2.521
17	0.056	~0	~0.000	0.572	0.018	3.1469	0.917	-0.071	-7.7426	2.674	0.069	2.580
18	0.013	~0	~0.000	0.577	0.02	3.4662	0.817	-0.103	-12.6071	2.851	0.073	2.561
19	0.018	~0	~0.000	0.576	0.022	3.8194	0.813	-0.116	-14.2681	2.854	0.073	2.558
20	0.038	-0.002	-5.263	0.562	0.028	4.9822	0.659	-0.156	-23.6722	2.86	0.078	2.727
21	0.041	-0.001	-2.439	4.999	-0.197	-3.9408	0.589	-0.189	-32.0883	2.851	0.001	0.035
22	0.016	~0	~0.000	1.64	-0.14	-8.5366	0.516	-0.168	-32.5581	3.186	0.029	0.910
23	0.04	~0	~0.000	17.563	-0.738	-4.2020	0.559	-0.159	-28.4436	2.677	0.07	2.615
24	0.057	~0	~0.000	1.325	-0.025	-1.8868	0.947	-0.081	-8.5533	2.709	0.078	2.879
25	0.037	~0	~0.000	16.56	0.307	1.8539	0.6	-0.151	-25.1667	3.326	0.084	2.526
26	0.072	~0	~0.000	6.41	0.383	5.9750	0.988	-0.09	-9.1093	2.936	-0.003	-0.102
27	0.012	~0	~0.000	6.276	0.206	3.2823	0.663	-0.018	-2.7149	2.621	0.041	1.564
28	0.02	0.002	10.000	3.085	0.11	3.5656	0.653	-0.007	-1.0720	2.624	0.078	2.973
29	0.038	-0.002	-5.263	0.88	0.057	6.4773	0.63	-0.016	-2.5397	3.022	0.032	1.059
30	0.027	-0.001	-3.704	0.877	0.062	7.0696	0.525	~0	~0.0000	3.021	0.032	1.059
31	0.02	0.001	5.000	0.859	0.062	7.2177	0.987	-0.066	-6.6869	2.889	0.126	4.361
32	0.023	-0.003	-13.043	23.448	0.708	3.0194	0.786	-0.036	-4.5802	2.924	0.084	2.873
33	0.016	-0.001	-6.250	23.257	0.697	2.9969	1.061	-0.102	-9.6136	3.068	0.066	2.151
34	0.024	-0.001	-4.167	23.265	0.74	3.1807	1.142	-0.212	-18.5639	3.047	0.055	1.805
35	0.021	-0.001	-4.762	23.509	0.663	2.8202	1.075	-0.216	-20.0930	3.069	0.056	1.825
36	0.014	0.001	7.143	23.494	0.898	3.8223	1.19	-0.175	-14.7059	3.055	0.123	4.026
37	0.051	0.006	11.765	100.572	-4.649	-4.6226	1.374	-0.068	-4.9491	2.791	-0.004	-0.143
38	0.094	0.002	2.128	102.233	-5.557	-5.4356	1.907	-0.041	-2.1500	2.787	-0.025	-0.897
39	0.164	-0.011	-6.707	94.755	0.484	0.5108	5.453	0	~0.0000	2.851	0.057	1.999
40	0.051	0.028	54.902	6.836	0.12	1.7554	1.738	0.027	1.5535	4.332	0.152	3.509
41	0.049	0.032	65.306	80.599	-1.015	-1.2593	1.29	0.03	2.3256	5.066	0.138	2.724

Supplementary Table 4. 4) The decadal changes of the annual maximum skew surge, streamflow, total water level and precipitation at each location.

Gauge number	Mean S (m)	Rate S (m)	Percent Change S (%)	Mean Q (m3)	Rate Q (m3)	Percent Change Q (%)	Mean T (m)	Rate T (m)	Percent Change T (%)	Mean P (m)	Rate P (m)	Percent Change P (%)
1	0.67	-0.009	-1.343	23.482	-1.712	-7.291	7.646	-0.033	-0.432	47.682	1.613	3.383
2	0.61	0.008	1.311	988.341	0.678	0.069	7.581	-0.018	-0.237	52.107	-2.463	-4.727
3	0.564	-0.007	-1.241	117.221	2.553	2.178	5.599	-0.019	-0.339	83.008	3.427	4.129
4	0.508	-0.016	-3.150	60.868	8.359	13.733	5.612	-0.023	-0.410	73.821	-1.029	-1.394
5	0.601	0.01	1.664	75.215	2.679	3.562	4.292	-0.004	-0.093	125.16	-0.259	-0.207
6	0.542	0.003	0.554	64.337	-1.936	-3.009	3.372	-0.007	-0.208	50.945	2.381	4.674
7	0.632	0.004	0.633	138.793	17.447	12.571	5.275	-0.011	-0.209	50.307	-1.817	-3.612
8	0.624	0.019	3.045	988.479	0.822	0.083	5.3	-0.014	-0.264	50.165	-1.501	-2.992
9	0.169	-0.004	-2.367	470.63	56.003	11.900	0.477	-0.125	-26.205	44.461	-0.101	-0.227
10	0.281	-0.015	-5.338	9.712	0.06	0.618	0.568	-0.143	-25.176	55.318	1.103	1.994
11	0.391	0.02	5.115	9.724	0.069	0.710	0.676	-0.086	-12.722	46.482	-1.469	-3.160
12	0.571	0.029	5.079	9.731	0.068	0.699	0.896	-0.035	-3.906	46.018	-1.488	-3.234
13	0.307	0.015	4.886	9.601	-0.026	-0.271	0.946	-0.255	-26.956	46.642	-1.828	-3.919
14	0.212	-0.005	-2.358	9.638	-0.027	-0.280	0.829	-0.208	-25.090	47.595	-1.758	-3.694
15	0.56	-0.007	-1.250	8.389	-0.177	-2.110	1.467	-0.08	-5.453	57.071	1.629	2.854
16	0.417	-0.033	-7.914	8.413	-0.25	-2.972	1.319	-0.117	-8.870	58.53	0.33	0.564
17	0.476	-0.023	-4.832	8.38	-0.156	-1.862	1.397	-0.089	-6.371	56.948	1.494	2.623
18	0.289	0.011	3.806	8.538	0.029	0.340	1.168	-0.086	-7.363	53.76	0.266	0.495
19	0.358	-0.025	-6.983	8.517	0.023	0.270	1.194	-0.129	-10.804	53.123	0.478	0.900
20	0.376	0.007	1.862	8.491	0.057	0.671	1.048	-0.138	-13.168	53.44	0.39	0.730
21	0.398	0.005	1.256	11.783	0.139	1.180	0.992	-0.187	-18.851	48.028	-4.173	-8.689
22	0.223	0.005	2.242	10.708	1.634	15.260	0.794	-0.164	-20.655	50.116	-3.048	-6.082
23	0.44	-0.004	-0.909	71.596	-8.866	-12.383	0.963	-0.157	-16.303	47.439	-0.089	-0.188
24	0.918	0.053	5.773	8.907	-0.029	-0.326	1.8	-0.041	-2.278	47.221	-1.368	-2.897
25	0.468	0.01	2.137	15.864	2.341	14.757	1.062	-0.151	-14.218	47.286	1.18	2.495
26	1.272	0.014	1.101	40.15	-1.567	-3.903	2.136	-0.057	-2.669	50.544	2.179	4.311
27	0.226	-0.022	-9.735	40.655	-0.908	-2.233	1.111	-0.029	-2.610	47.328	-0.577	-1.219
28	0.206	0.003	1.456	12.815	-0.361	-2.817	1.055	-0.01	-0.948	49.158	1.028	2.091
29	0.356	-0.039	-10.955	8.447	-0.033	-0.391	1.027	-0.073	-7.108	51.943	-0.766	-1.475
30	0.244	-0.03	-12.295	8.435	-0.026	-0.308	0.761	-0.036	-4.731	51.768	-0.627	-1.211
31	0.502	-0.033	-6.574	8.432	-0.141	-1.672	1.744	-0.075	-4.300	51.166	1.102	2.154
32	0.759	-0.055	-7.246	87.156	1.575	1.807	2.105	-0.087	-4.133	52.815	-0.319	-0.604
33	0.508	-0.035	-6.890	85.93	1.838	2.139	1.848	-0.122	-6.602	50.32	0.004	0.008
34	1.012	-0.157	-15.514	86.014	1.84	2.139	2.797	-0.369	-13.193	49.853	-0.279	-0.560
35	0.92	-0.125	-13.587	85.603	2.031	2.373	2.651	-0.335	-12.637	50.53	-0.226	-0.447
36	0.901	-0.066	-7.325	85.028	2.482	2.919	2.734	-0.243	-8.888	55.384	0.237	0.428
37	1.071	-0.066	-6.162	205.518	31.304	15.232	3.077	-0.073	-2.372	48.416	-0.892	-1.842
38	1.052	-0.034	-3.232	198.714	21.767	10.954	3.409	-0.031	-0.909	47.961	-1.254	-2.615
39	1.428	-0.127	-8.894	116.828	20.265	17.346	6.942	-0.042	-0.605	57.678	0.367	0.636
40	0.605	0.028	4.628	9.899	0.009	0.091	2.415	0.025	1.035	74.289	2.143	2.885
41	0.578	0.038	6.574	98.857	0.123	0.124	1.962	0.019	0.968	69.593	5.625	8.083

Supplementary Table 5. 1) but for the nonstationary (linear) dependence parameter.

Link function	Copula families for the first parameter	Copula families for the second parameter
$\tau_t = \dfrac{1}{1 + e^{-(a+bt)}}$	3, 4, 6, 13, 14, 16	10, 120, 104, 114, 124, 134, 204, 214, 224, 234
$\tau_t = 2 \times \left(\dfrac{1}{1 + e^{-(a+bt)}} - 0.5\right)$	1, 2, 5	
$\phi_t = 2.01 + \left(100 \times \left(\dfrac{1}{1 + e^{-(a+bt)}}\right)\right)$		2
$\tau_t = \dfrac{1}{1 + e^{-(a+bt)}} - 1$	23, 24, 26, 33, 34, 36	30, 40
$\phi_t = 0.01 + \left(100 \times \left(\dfrac{1}{1 + e^{-(a+bt)}}\right)\right)$	7, 17	9, 19
$\phi_t = 1.01 + \left(100 \times \left(\dfrac{1}{1 + e^{-(a+bt)}}\right)\right)$	8, 9, 10, 18, 19, 20, 104, 114, 204, 214	7, 8, 17, 18
$\phi_t = -0.01 - \left(100 \times \left(\dfrac{1}{1 + e^{-(a+bt)}}\right)\right)$	27, 37	29, 39
$\phi_t = -1.01 + \left(100 \times \left(\dfrac{1}{1 + e^{-(a+bt)}}\right)\right)$	28, 29, 30, 38, 39, 40, 124, 134, 224, 234	27, 28, 37, 38

Supplementary Table 5. 2) Similar to table 5.1 but for the nonstationary (Quadratic) dependence parameter.

Link function	Copula families for the first parameter	Copula families for the second parameter
$\tau_t = \dfrac{1}{1 + e^{-(a+bt+ct^2)}}$	3, 4, 6, 13, 14, 16	10, 120, 104, 114, 124, 134, 204, 214, 224, 234
$\tau_t = 2 \times \left(\dfrac{1}{1 + e^{-(a+bt+ct^2)}} - 0.5\right)$	1, 2, 5	
$\phi_t = 2.01 + \left(100 \times \left(\dfrac{1}{1 + e^{-(a+bt+ct^2)}}\right)\right)$		2
$\tau_t = \dfrac{1}{1 + e^{-(a+bt+ct^2)}} - 1$	23, 24, 26, 33, 34, 36	30, 40
$\phi_t = 0.01 + \left(100 \times \left(\dfrac{1}{1 + e^{-(a+bt+ct^2)}}\right)\right)$	7, 17	9, 19
$\phi_t = 1.01 + \left(100 \times \left(\dfrac{1}{1 + e^{-(a+bt+ct^2)}}\right)\right)$	8, 9, 10, 18, 19, 20, 104, 114, 204, 214	7, 8, 17, 18
$\phi_t = -0.01 - \left(100 \times \left(\dfrac{1}{1 + e^{-(a+bt+ct^2)}}\right)\right)$	27, 37	29, 39
$\phi_t = -1.01 + \left(100 \times \left(\dfrac{1}{1 + e^{-(a+bt+ct^2)}}\right)\right)$	28, 29, 30, 38, 39, 40, 124, 134, 224, 234	27, 28, 37, 38

Supplementary Table 5. 3) The selected marginal distributions for Pr, Q, and TWL at each location along with their AIC and KS test p-values.

Station	Distribution (Pr)	AIC (Pr)	KS p-value (Pr)	Distribution (Q)	AIC (Q)	KS p-value (Q)	Distribution (TWL)	AIC (TWL)	KS p-value (TWL)
1	GPD	5503.62	0.02	GPD	182.33	0.00	Gamma	4333.34	0.05
2	GPD	5238.61	0.03	Gumbel	-166.62	0.00	GPD	7728.43	0.00
3	GPD	4627.48	0.03	Normal	1095.58	0.04	GPD	7864.04	0.00
4	GPD	4475.93	0	GEV	1029.30	0.13	GPD	7929.93	0.00
5	GPD	5070.43	0	Gumbel	1369.70	0.06	Logistic	10074.13	0.00
6	GPD	4710.81	0.01	Weibull	114.48	0.00	GPD	5672.24	0.00
7	GPD	4820.84	0	GEV	229.33	0.05	GEV	10180.39	0.02
8	GPD	4435.98	0.02	GEV	164.84	0.01	GPD	8230.06	0.00
9	GPD	5192.10	0	Cauchy	1041.26	0.00	Gamma	6312.51	0.01
10	GPD	5398.56	0	Exponential	2962.52	0.00	GPD	6751.61	0.30
11	GPD	5383.14	0	GEV	706.46	0.17	GPD	8443.35	0.00
12	GPD	4412.80	0.04	GEV	1023.76	0.13	GPD	10324.52	0.00
13	GPD	4402.73	0	GEV	1160.24	0.18	GEV	2017.58	0.04
14	GPD	4360.03	0	Logistic	-22.18	0.02	Normal	10185.42	0.00
15	GPD	4879.51	0	GEV	-103.02	0.01	Weibull	3036.65	0.08
16	GPD	4669.34	0	Normal	-260.82	0.03	Weibull	3147.14	0.04
17	GPD	4465.04	0	Logistic	-104.21	0.03	Weibull	2903.24	0.36
18	GPD	4441.81	0.03	Cauchy	1265.54	0.00	GPD	2981.94	0.08
19	GPD	4421.76	0	Cauchy	1190.94	0.00	GPD	2956.70	0.02
20	GPD	4993.34	0	Cauchy	1147.81	0.00	GEV	4137.62	0.04
21	GPD	4430.77	0	Cauchy	1126.49	0.00	GPD	5363.58	0.03
22	GPD	5131.90	0	GPD	1060.68	0.00	GEV	6238.63	0.39
23	GPD	5293.28	0	GPD	1112.50	0.00	GPD	2229.97	0.02
24	GPD	5132.25	0.03	Cauchy	1074.73	0.00	Weibull	2225.61	0.04
25	GPD	5160.88	0	Exponential	1328.24	0.00	Weibull	2302.63	0.09
26	GPD	5273.40	0	GEV	448.91	0.11	Weibull	2527.03	0.12
27	GPD	5162.88	0	Exponential	1464.63	0.00	Weibull	1904.00	0.04
28	GPD	5432.84	0	Exponential	1706.30	0.00	Weibull	2067.15	0.13
29	GPD	5548.74	0	Exponential	1667.09	0.00	Weibull	2126.93	0.01
30	GPD	4506.43	0.03	Exponential	1545.39	0.00	GPD	3116.46	0.00
31	GPD	4756.21	0	Exponential	1748.39	0.00	GPD	5006.49	0.04
32	GPD	5013.82	0	Exponential	1055.73	0.00	GPD	5239.57	0.01
33	GPD	5230.62	0.03	GPD	1146.67	0.00	Gamma	3775.56	0.00
34	GPD	5400.88	0.03	Exponential	1014.14	0.00	GEV	2326.27	0.08
35	GPD	5304.60	0	Cauchy	-1383.51	0.00	GEV	2252.59	0.01
36	GPD	4721.96	0	Weibull	648.83	0.16	GEV	2037.43	0.04
37	GPD	5201.40	0	Cauchy	1045.38	0.00	GPD	6375.99	0.00
38	GPD	5166.74	0.04	GEV	1661.58	0.07	GPD	6315.33	0.00
39	GPD	4896.70	0	GEV	1525.74	0.04	GPD	5985.24	0.00
40	GPD	4763.44	0	GEV	1311.09	0.00	GPD	5950.20	0.00
41	GPD	4579.59	0	Cauchy	1046.42	0.00	GPD	5657.46	0.00

Supplementary Table 5. 4) The estimated Mann-Kendall trend test Z statistics for three drivers at each location. Z values higher than 1.96 and lower than -1.96 indicate the significant increasing and decreasing trends, respectively.

Station	Pr	Q	TWL
1	1.57	1.83	0.19
2	-1.21	0.22	0.39
3	0.94	0.11	-1.56
4	0.77	0.00	-1.64
5	0.68	-0.22	-1.72
6	-0.33	2.89	-0.35
7	0.13	1.95	2.03
8	-0.03	-0.82	1.25
9	0.53	1.87	-18.19
10	-0.86	-0.40	-16.50
11	0.27	1.22	-12.61
12	0.44	1.56	-6.92
13	0.03	0.62	-19.20
14	0.20	0.16	-15.71
15	-1.38	2.51	-8.80
16	-2.51	1.66	-11.20
17	-1.71	1.82	-9.55
18	0.54	1.27	-13.43
19	0.77	1.46	-14.38
20	0.93	1.85	-16.43
21	0.21	-1.61	-16.80
22	-0.43	-0.25	-17.90
23	-1.75	-0.50	-17.45
24	0.78	4.41	-7.72
25	1.75	1.62	-12.51
26	0.66	3.44	-7.25
27	0.56	3s.43	-1.51
28	1.52	1.56	0.79
29	1.38	5.63	-4.79
30	1.42	6.25	-1.43
31	2.37	4.50	-7.13
32	2.34	0.30	-2.76
33	0.68	0.20	-9.72
34	0.28	0.16	-11.42
35	0.45	0.10	-10.74
36	1.22	0.96	-10.22
37	-0.92	-1.33	-4.66
38	-1.40	-1.54	-2.33
39	1.59	2.03	-0.38
40	2.68	1.16	6.07
41	2.03	0.63	5.89

Supplementary Table 5. 5) The best-selected models (stationary, linear and quadratic) for three flooding drivers according to their AIC values. The highlighted values in red indicate the selected model.

Location	Pr			TWL			Q		
	Stationary	Linear	Polynomial	Stationary	Linear	Polynomial	Stationary	Linear	Polynomial
1	**5006.2**	5006.4	5007.3	**1171.9**	1173.9	1175.5	**4360.2**	4362.1	4364.1
2	5229.7	5230.1	**5229.1**	**1034.2**	1035.8	1037.7	**10996.7**	10998.5	11000.3
3	**6178.0**	6179.1	6180.8	716.0	**714.9**	716.9	**9700.7**	9702.5	9703.5
4	**5873.5**	5875.4	5877.4	756.4	**755.4**	757.4	**6310.6**	6312.4	6314.4
5	**6063.2**	6064.8	6066.8	347.6	**345.7**	347.4	**7589.2**	7591.0	7592.0
6	**5428.5**	5430.5	5432.5	**-7.0**	-5.1	-4.7	6701.0	6701.3	**6694.6**
7	**5138.8**	5140.8	5142.4	179.6	**178.5**	179.3	9131.9	**9131.6**	9133.0
8	**5544.2**	5546.2	5547.7	**242.4**	243.2	243.5	11582.1	11583.1	**11578.7**
9	**5105.2**	5105.6	5107.0	-82.2	**-463.7**	-461.7	**10185.4**	10187.4	10187.8
10	**5673.1**	5675.0	5676.9	-97.5	-404.1	**-501.3**	**3032.9**	3034.8	3033.0
11	**5573.2**	5574.9	5576.4	-260.5	-437.2	**-533.7**	3108.1	3107.0	**3106.1***
12	**5303.0**	5304.9	5305.8	-115.1	-164.3	**-278.7**	2885.3	2881.7	**2878.9**
13	**5266.2**	5267.5	5269.2	874.8	429.8	**248.1**	**4168.1**	4169.2	4171.1
14	**5254.1**	5255.7	5257.5	812.5	489.7	**265.1**	4152.5	4154.3	**4155.8**
15	**6372.3**	6374.1	6373.7	249.9	170.7	**138.2**	1692.8	1691.8	**1690.3**
16	6029.3	6031.0	**6028.0**	286.2	152.6	**95.3**	1637.7	1638.6	**1637.6**
17	**6450.5**	6452.5	6452.0	318.2	228.8	**152.0**	1772.5	1772.9	**1771.7**
18	**6061.1**	6062.9	6062.1	460.5	257.7	**82.0**	1933.1	1934.6	**1931.6**
19	5901.3	5902.8	**5901.2**	403.0	159.8	**-4.2**	1922.7	1923.8	**1919.9**
20	**5898.4**	5899.7	5899.7	681.0	364.5	**172.3**	1854.1	1855.0	**1853.0**
21	**5761.2**	5762.8	5764.8	805.2	448.2	**215.8**	**5562.4**	5564.4	5564.6
22	**6131.1**	6131.8	6133.8	920.6	542.4	**359.9**	4915.7	**4915.1**	4913.9
23	**6037.0**	6037.9	6039.0	888.3	538.1	**300.2**	**7371.8**	7372.5	7374.1
24	**5202.2**	5204.2	5205.3	416.4	361.6	**223.5**	**4109.8**	4106.0	4106.7
25	**5219.7**	5220.4	5221.2	788.8	608.6	**272.4**	**5772.2**	5772.9	5772.4
26	**5561.7**	5563.3	5562.1	573.6	533.8	**472.6**	7085.4	7085.5	**7086.5**
27	**5871.1**	5873.0	5873.5	147.4	142.6	**140.9**	7515.5	7516.8	**7518.8**
28	6017.8	**6015.3**	6016.6	239.3	240.5	**213.5**	3830.3	3830.8	**3828.5***
29	6265.5	6266.4	**6265.3**	-638.9	-654.2	**-736.2**	4268.2	4265.4	**4263.7***
30	**6130.8**	6131.7	6131.3	-1603.0	-1601.6	**-1702.8**	4123.2	**4115.4***	4114.3
31	5448.8	**5444.7**	5446.1	648.8	603.0	**582.4**	3796.7	**3795.4**	3793.7
32	5302.2	**5300.2**	5300.8	919.3	**914.2**	915.5	6968.0	**6963.7**	6965.7
33	**5886.9**	5886.9	5888.2	748.7	**672.4**	672.8	7897.3	**7894.1**	7896.0
34	**5858.4**	5859.1	5860.2	1723.3	1590.8	**1590.2**	7833.1	**7829.9***	7830.8
35	**5563.7**	5564.3	5565.5	1586.8	1468.8	**1465.7**	**7443.4**	7439.8	7441.0
36	**5547.5**	5548.5	5549.4	1355.8	1261.8	**1251.5**	**7208.6**	7205.4	7206.2
37	**5896.1**	5897.5	5899.2	1500.8	1483.3	**1479.9**	10448.0	**10449.3***	10451.1

38	**5218.4**	5218.6	5220.6	1097.1	1094.0	**1093.7**	9195.5	9196.8	**9196.0***
39	**5740.4**	5741.6	5743.0	**1095.6**	1097.6	1099.5	**9238.1**	9238.0	9239.6
40	6228.8	**6225.7**	6227.5	-203.4	-241.0	**-242.5**	4324.4	4325.6	**4322.4***
41	5898.3	**5893.6**	5894.7	-237.5	**-269.0**	-267.2	**8749.1**	8750.3	8751.5

Supplementary Table 5. 6) The best-fitted copula functions at each location along with their corresponding AIC values, and the p-values.

Station	Joint, copula family	AIC(Pr, TWL)	p-value (Pr, TWL)	Joint, copula family	AIC(Pr, Q)	p-value (Pr, Q)	Joint, copula family	AIC(Q, TWL)	p-value (Q, TWL)
1	(Pr, TWL), 5	-0.52	0.97	(Pr, Q|TWL), 4	0.73	0.85	(Q, TWL), 3	-6.88	0.46
2	(Pr, TWL), 13	-11.14	0.64	(Pr, Q|TWL), 134	-4.96	0.53	(Q, TWL), 134	-35.95	0.03
3	(Pr, TWL|Q), 24	-0.11	0.26	(Pr, Q), 124	-4.09	0.23	(Q, TWL), 134	-2.68	0.45
4	(Pr, TWL), 5	-2.27	0.01	(Pr, Q|TWL), 104	1.52	0.77	(Q, TWL), 6	-77.80	0.06
5	(Pr, TWL), 5	1.15	0.01	(Pr, Q|TWL), 214	-2.52	0.01	(Q, TWL), 6	-110.40	0
6	(Pr, TWL), 5	-28.70	0.35	(Pr, Q|TWL), 5	-22.7	0.25	(Q, TWL), 5	-33.71	0.12
7	(Pr, TWL), 214	-12.36	0.60	(Pr, Q|TWL), 224	-5.63	0.42	(Q, TWL), 5	-56.07	0
8	(Pr, TWL), 214	-9.38	0.51	(Pr, Q|TWL), 5	-1.31	0.87	(Q, TWL), 30	-50.65	0
9	(Pr, TWL|Q), 5	-3.28	0.15	(Pr, Q), 5	-7.54	0.98	(Q, TWL), 1	-44	0.76
10	(Pr, TWL|Q), 1	-19.91	0.98	(Pr, Q), 10	-39.25	0.03	(Q, TWL), 1	-26.59	0.56
11	(Pr, TWL|Q), 124	-1.65	0.82	(Pr, Q), 13	-10.43	0.87	(Q, TWL), 5	-12.16	0.27
12	(Pr, TWL|Q), 104	-7.08	0.69	(Pr, Q), 5	-1.01	0.96	(Q, TWL), 5	-3.71	0.53
13	(Pr, TWL), 134	1.22	0.6	(Pr, Q|TWL), 114	0.99	0.93	(Q, TWL|Pr), 5	-0.03	0.84
14	(Pr, TWL), 14	-1.00	0.91	(Pr, Q), 5	-11.56	0.22	(Q, TWL), 3	-7.53	0.1
15	(Pr, TWL|Q), 5	-12.24	0.4	(Pr, Q), 5	-18.52	0.57	(Q, TWL), 5	-21.5	0
16	(Pr, TWL|Q), 1	-8.99	0.22	(Pr, Q), 234	-7.54	0.53	(Q, TWL), 5	-14.6	0
17	(Pr, TWL|Q), 114	-5.37	0.16	(Pr, Q), 26	-2.37	0.46	(Q, TWL), 5	-15.75	0
18	(Pr, TWL|Q), 1	-0.42	0.19	(Pr, Q), 134	-7.56	0.04	(Q, TWL), 1	-7.61	0.54
19	(Pr, TWL|Q), 114	-0.95	0.23	(Pr, Q), 134	-8.15	0.01	(Q, TWL), 5	-6.1	0.29
20	(Pr, TWL|Q), 16	0.72	0.92	(Pr, Q), 124	-16.44	0.01	(Q, TWL), 134	-1.89	0.27
21	(Pr, TWL|Q), 6	1.00	0.61	(Pr, Q), 224	-13.72	0.36	(Q, TWL|Pr), 5	-8.32	0.27
22	(Pr, TWL), 1	-5.17	0.24	(Pr, Q), 24	-2.72	0.28	(Q, TWL), 134	0.54	0.78
23	(Pr, TWL), 104	-4.90	0.50	(Pr, Q|TWL), 204	-6.33	0.03	(Q, TWL), 1	-25.28	0.17
24	(Pr, TWL), 1	0.82	0.6	(Pr, Q|TWL), 13	-1.02	0.93	(Q, TWL), 234	-14.54	0
25	(Pr, TWL|Q), 5	1.60	0.54	(Pr, Q), 13	-2.93	0.78	(Q, TWL), 234	-0.27	0.49
26	(Pr, TWL), 114	-8.52	0.2	(Pr, Q|TWL), 5	-9.79	0.14	(Q, TWL), 13	-9.34	0.35
27	(Pr, TWL), 5	-12.10	0.72	(Pr, Q|TWL), 124	-1.89	0.10	(Q, TWL), 6	-7.47	0.36
28	(Pr, TWL), 5	-8.70	0.66	(Pr, Q|TWL), 6	-11.52	0.07	(Q, TWL), 5	-0.03	0.45
29	(Pr, TWL), 5	-7.47	0.93	(Pr, Q|TWL), 136	0.55	0.43	(Q, TWL), 234	-7.81	0.39
30	(Pr, TWL|Q), 104	-1.50	0.25	(Pr, Q) 13	-4.74	0.82	(Q, TWL), 6	-4.39	0.47
31	(Pr, TWL|Q), 134	-7.16	0.59	(Pr, Q), 33	0.40	0.47	(Q, TWL), 104	-16.32	0.58
32	(Pr, TWL|Q), 3	-2.25	0.62	(Pr, Q), 26	-14.5	0.12	(Q, TWL|Pr),23	-0.56	0
33	(Pr, TWL), 114	-1.95	0.25	(Pr, Q), 5	0.95	0.65	(Q, TWL), 13	1.94	0.09
34	(Pr, TWL), 104	-1.56	0.44	(Pr, Q|TWL), 5	-0.12	0.41	(Q, TWL), 204	-16.12	0.72
35	(Pr, TWL), 104	-7.76	0.25	(Pr, Q|TWL), 5	-1.56	0.59	(Q, TWL), 19	-32.11	0.11
36	(Pr, TWL|Q), 13	0.06	0.35	(Pr, Q), 5	0.83	0.44	(Q, TWL), 19	-29.69	0.39
37	(Pr, TWL), 204	-3.74	0.17	(Pr, Q|TWL), 214	-1.09	0.03	(Q, TWL), 204	-41.24	0.85
38	(Pr, TWL), 5	-1.19	0.38	(Pr, Q|TWL), 5	1.02	0.64	(Q, TWL), 204	-33.62	0.91
39	(Pr, TWL), 5	-0.51	0.39	(Pr, Q|TWL), 13	0.91	0.80	(Q, TWL), 204	-31.42	0.9
40	(Pr, TWL), 104	-1.48	0.43	(Pr, Q|TWL), 214	-4.17	0.72	(Q, TWL), 9	-35.64	0
41	(Pr, TWL|Q), 16	1.79	0.85	(Pr, Q), 5	0.55	0.34	(Q, TWL), 9	-65.33	0

Supplementary Table 5. 7) The p-values associated with the dependence test of three joints at each site.

Station	Joint	Cor (Pr, TWL)	p-value (Pr, TWL)	Joint	Cor (Pr, Q)	p-value (Pr, Q)	Joint	Cor (Q, TWL)	p-value (Q, TWL)
1	(Pr, TWL)	-0.023	0.03	(Pr, Q|TWL)	0.018	0.02	(Q, TWL)	-0.055	0.0
2	(Pr, TWL)	0.025	0.00	(Pr, Q|TWL)	-0.067	0.04	(Q, TWL)	-0.094	0
3	(Pr, TWL|Q)	-0.014	0.66	(Pr, Q)	0.118	0.01	(Q, TWL)	-0.140	0.33
4	(Pr, TWL)	0.006	0.03	(Pr, Q|TWL)	0.116	0.21	(Q, TWL)	0.244	0
5	(Pr, TWL)	0.052	0.04	(Pr, Q|TWL)	0.236	0.17	(Q, TWL)	0.193	0
6	(Pr, TWL)	0.209	0	(Pr, Q|TWL)	-0.062	0.01	(Q, TWL)	-0.228	0
7	(Pr, TWL)	0.120	0	(Pr, Q|TWL)	0.024	0.05	(Q, TWL)	0.250	0
8	(Pr, TWL)	0.124	0	(Pr, Q|TWL)	-0.022	0.04	(Q, TWL)	-0.277	0
9	(Pr, TWL|Q)	0.059	0.87	(Pr, Q)	0.142	0	(Q, TWL)	0.013	0
10	(Pr, TWL|Q)	0.055	0.04	(Pr, Q)	-0.160	0	(Q, TWL)	-0.178	0
11	(Pr, TWL|Q)	0.057	0.71	(Pr, Q)	-0.075	0	(Q, TWL)	-0.143	0
12	(Pr, TWL|Q)	0.050	0.51	(Pr, Q)	-0.069	0.03	(Q, TWL)	-0.155	0.01
13	(Pr, TWL)	0.038	0.01	(Pr, Q|TWL)	-0.067	0.06	(Q, TWL)	-0.111	0.04
14	(Pr, TWL)	0.012	0	(Pr, Q)	-0.079	0	(Q, TWL|Pr)	-0.106	0.14
15	(Pr, TWL|Q)	0.116	0.03	(Pr, Q)	0.021	0	(Q, TWL)	-0.025	0
16	(Pr, TWL|Q)	0.138	0.03	(Pr, Q)	0.012	0.04	(Q, TWL)	-0.047	0
17	(Pr, TWL|Q)	0.109	0.18	(Pr, Q)	0.010	0.11	(Q, TWL)	-0.050	0
18	(Pr,TWL|Q)	0.081	0.02	(Pr, Q)	0.005	0.05	(Q, TWL)	-0.047	0
19	(Pr,TWL|Q)	0.030	0.04	(Pr, Q)	0.016	0.03	(Q, TWL)	-0.054	0
20	(Pr, TWL|Q)	0.037	0.78	(Pr, Q)	0.014	0	(Q, TWL)	-0.107	0.217
21	(Pr, TWL|Q)	0.011	0.02	(Pr, Q)	-0.119	0	(Q, TWL)	-0.046	0
22	(Pr, TWL)	0.080	0.01	(Pr, Q)	0.039	0	(Q, TWL|Pr)	0.168	0.06
23	(Pr, TWL)	0.083	0.02	(Pr, Q|TWL)	-0.071	0	(Q, TWL)	-0.003	0
24	(Pr, TWL)	0.038	0.02	(Pr, Q|TWL)	0.081	0	(Q, TWL)	0.058	0.03
25	(Pr, TWL|Q)	-0.018	0.04	(Pr, Q)	-0.114	0	(Q, TWL)	-0.122	0.32
26	(Pr, TWL)	-0.013	0.02	(Pr, Q|TWL)	-0.039	0	(Q, TWL)	0.097	0.04
27	(Pr, TWL)	0.032	0	(Pr, Q|TWL)	-0.057	0.02	(Q, TWL)	-0.049	0.35
28	(Pr, TWL)	0.019	0	(Pr, Q|TWL)	0.015	0.38	(Q, TWL)	-0.020	0.05
29	(Pr, TWL)	0.046	0	(Pr, Q|TWL)	0.041	0.21	(Q, TWL)	0.105	0.08
30	(Pr, TWL|Q)	0.084	0	(Pr, Q)	0.038	0.03	(Q, TWL)	0.151	0.03
31	(Pr, TWL|Q)	0.021	0.74	(Pr, Q)	0.041	0.05	(Q, TWL)	0.177	0.01
32	(Pr, TWL|Q)	-0.017	0.38	(Pr, Q)	0.046	0.01	(Q, TWL)	0.154	0.23
33	(Pr, TWL)	0.041	0.61	(Pr, Q)	0.017	0.05	(Q, TWL|Pr)	0.147	0.69
34	(Pr, TWL)	0.065	0	(Pr, Q|TWL)	0.016	0.04	(Q, TWL)	0.096	0
35	(Pr, TWL)	0.059	0.01	(Pr, Q|TWL)	0.007	0.18	(Q, TWL)	0.089	0
36	(Pr, TWL|Q)	0.007	0.05	(Pr, Q)	0.004	0.07	(Q, TWL)	0.122	0
37	(Pr, TWL)	0.033	0.05	(Pr, Q|TWL)	-0.015	0.02	(Q, TWL)	0.196	0
38	(Pr, TWL)	0.078	0.07	(Pr, Q|TWL)	-0.019	0.64	(Q, TWL)	0.193	0
39	(Pr, TWL)	-0.015	0.01	(Pr, Q|TWL)	-0.057	0.04	(Q, TWL)	-0.036	0
40	(Pr, TWL)	0.059	0.03	(Pr, Q|TWL)	-0.024	0.13	(Q, TWL)	-0.018	0
41	(Pr, TWL|Q)	0.102	0.02	(Pr, Q)	0.027	0.02	(Q, TWL)	-0.090	0

Supplementary Table 5. 8) The WAIC values corresponding to the three models (stationary, linear, and polynomial) for three pair copulas at each location.

Location	Joint1 (Pr, TWL)			Joint2 (Pr, Q)			Joint3 (Q, TWL)		
	Stationary	Linear	Polynomial	Stationary	Linear	Polynomial	Stationary	Linear	Polynomial
1	-1384.67	-1221.93	**-1395.62**	**-1386.51**	-1131.99	-1052.58	**-1386.51**	2241.77	9599.48
2	**-1342.75**	-195.05	-184.36	**-1347.30**	-183.09	-186.66	-1344.01	-583.47	**-1870.98**
3	**-1482.62**	-1325.23	-12232.54	**-1487.40**	-223.10	-249.40	-1460.42	**-1667.20**	-746.69
4	**-1430.73**	-216.73	-178.77	-858.98	**-1479.51**	-1462.23	**-1413.16**	-192.28	-204.06
5	**-1376.94**	-1213.45	-1246.54	**-1457.75**	-1330.86	-1340.47	**-1457.79**	-1298.92	-1300.25
6	**-1427.64**	-282.24	-265.95	**-1435.20**	-256.92	-264.14	**-1401.24**	-217.56	-222.31
7	**-1398.46**	6638.66	6598.68	**-1444.51**	-646.41	-634.00	**-1373.49**	-174.51	-171.33
8	**-1521.76**	-267.05	4644.09	**-1600.22**	-292.59	-331.74	**-1488.87**	-257.69	-1231.40
9	-1375.85	-1370.31	**-1379.50**	**-1380.23**	-164.24	-160.12	**-1368.57**	3113748.63	-617.07
10	**-1509.79**	-221.96	-238.26	**-1456.93**	-178.06	-209.26	**-1471.27**	-164.60	-172.00
11	**-1500.01**	817.42	-1488.74	6650.75	**-238.24**	-200.56	-1498.74	-965.36	**-1500.99**
12	**-1424.03**	-1325.32	-1397.89	**-1402.87**	-1080.12	-230.40	-1429.28	**-1468.97**	-794.84
13	-1421.67	**-2946.40**	-2095.96	**-1782.10**	-1413.76	-1418.15	**-1553.37**	-1419.55	-1419.42
14	-1410.71	**-2035.28**	-1570.84	**-1415.15**	-191.41	-212.34	**-1408.27**	-734.85	-972.52
15	**-1595.29**	-212.35	-199.68	**-1535.07**	5137.94	5356.80	**-1586.49**	118.07	169.87
16	**-1499.46**	-1067.35	-326.42	-1325.39	-260.71	**-1469.35**	**-1490.05**	25364.32	24025.25
17	**-1614.71**	-204.22	-177.76	**-1636.87**	-271.03	-238.16	-1606.13	**-1631.01**	328.61
18	**-1595.58**	-450.00	-568.01	**-1420.06**	-1325.65	-1125.65	**-1576.20**	-1527.34	-132.94
19	**-1551.82**	-1388.09	7586.76	**-1526.85**	-233.06	-169.78	**-1539.72**	9343.17	9875.98
20	**-1525.94**	-1324.58	-1235.45	-1462.02	-266.18	**-1614.83**	**-1540.24**	-179.82	-1536.41
21	**-1571.28**	-1317.46	-1123.46	-1547.97	**-2526.83**	-1966.08	**-1548.00**	-1132.78	-1123.89
22	**-1635.97**	-121.36	-1242.94	-1595.22	**-1703.58**	-1678.75	**-1633.88**	147.47	-524.72
23	-1358.34	**-1363.74**	7887.34	**-1630.26**	-1279.55	-285.56	**-1623.64**	-222.22	-879.12
24	**-1408.65**	-1358.48	-1236.65	**-1396.04**	-1310.98	-1291.15	**-1400.45**	-1119.04	90.55
25	**-1429.81**	-1011.30	-495.43	**-1444.68**	-255.90	-201.11	**-1425.92**	-1244.99	-1218.90
26	-1476.96	-1066.20	**-1477.01**	**-1481.68**	-153.98	21946.17	-1476.66	**-1721.39**	4418.31
27	**-1573.97**	-1105.77	-1566.84	**-1572.31**	-1020.76	2310.16	-1572.26	-314.28	**-1606.76**
28	**-1587.86**	-1398.06	-1062.99	**-1591.71**	-1542.65	-1566.50	**-1585.97**	-231.30	-248.84
29	**-1641.94**	2046.91	2061.96	**-1701.13**	640.63	8956.64	**-1643.46**	-198.40	-192.28
30	**-1613.91**	3417.81	-229.35	**-1422.72**	1188.72	844.31	**-1614.67**	-225.20	-168.05
31	**-1424.01**	-170.14	-164.25	-99.79	**-433.73**	-319.80	**-1425.13**	-1325.32	-1226.56
32	**-1373.59**	-132.00	-179.09	**-1468.46**	21013.15	19708.76	**-1372.01**	-1132.52	-1287.32
33	**-1561.82**	-470.68	-1121.24	**-1645.35**	60980.99	27615.22	**-1562.14**	-903.05	-1205.51
34	**-1559.80**	-165.96	-165.78	**-1632.16**	18203.71	31714.95	**-1555.02**	-208.05	-218.50
35	**-1474.85**	-195.73	-223.39	**-1540.45**	6503.02	33413.77	**-1473.03**	-1235.65	-1398.52
36	**-1419.31**	1521.16	638.70	**909.29**	1933.75	1741.18	**-1428.88**	-212.33	-1080.32
37	**-1587.86**	-149.29	-186.08	-1589.87	**-1711.76**	-1667.43	**-1583.46**	-861.14	-947.24
38	**-1415.57**	-174.17	-182.04	-1409.02	-1384.32	**-1445.55**	**-1408.96**	-696.29	-362.81

39	**-1425.32**	-15.41	-1534.48	-1423.95	**-3009.78**	755.29	**-1427.79**	-836.74	-1375.57
40	-1511.17	**-1511.17**	-128.19	**-1552.67**	-1519.13	-1513.55	**-1511.02**	-1471.92	-1465.98
41	-1032.24	**-1491.85**	-1010.98	-1539.61	-2713.37	**-4702.77**	**-1461.40**	-1428.35	-1131.52

Supplementary Table 5. 9) The estimated TWL return levels for 24 locations under the nonstationary environment.

Location	TWL-lower bound		TWL-median		TWL-higher bound	
	1960	2015	1960	2015	1960	2015
1	1.70	1.70	1.73	1.73	1.75	1.75
2	1.46	1.46	1.49	1.49	1.51	1.51
3	1.92	1.92	1.95	1.95	1.98	1.98
4	1.87	1.87	1.91	1.91	1.95	1.95
6	2.32	2.32	2.36	2.36	2.39	2.39
7	2.14	2.21	2.32	2.35	2.55	2.61
9	1.25	1.16	1.28	1.20	1.32	1.25
12	0.41	0.37	0.43	0.37	0.44	0.39
15	1.08	1.02	1.09	1.04	1.12	1.07
17	1.09	0.98	1.10	1.05	1.13	1.09
22	1.39	1.37	1.40	1.39	1.41	1.41
23	1.08	1.08	1.11	1.11	1.16	1.16
24	5.31	5.17	5.35	5.22	5.39	5.29
26	0.72	0.53	0.73	0.68	0.74	0.69
27	3.98	3.98	4.06	4.06	4.13	4.13
29	3.23	3.1	3.44	3.18	3.65	3.55
30	6.90	6.90	6.93	6.93	6.96	6.96
32	2.52	2.67	2.42	2.51	2.36	2.26
36	0.56	0.72	0.58	0.72	0.59	0.72
37	1.39	1.35	1.45	1.44	1.50	1.48
38	1.13	1.12	1.14	1.13	1.16	1.14
39	0.77	0.77	0.82	0.82	0.87	0.87
40	2.73	2.88	2.80	2.92	2.85	3.05
41	3.29	6.68	3.35	6.91	3.52	6.99

Supplementary Table 5. 10) The time-varying Q return levels, estimated for 24 locations.

Location	Q-lower bound		Q-median		Q-higher bound	
	1960	2015	1960	2015	1960	2015
1	190.24	190.24	190.30	190.30	190.36	190.36
2	31.25	32.37	32.11	32.54	32.98	33.10
3	13.52	13.52	19.48	19.48	26.37	26.37
4	15.24	15.24	21.23	21.23	29.21	29.21
6	536.68	541.81	538.06	543.26	539.45	549.68
7	18.69	20.26	19.48	21.04	20.26	21.83
9	20.89	23.42	24.02	24.98	27.63	28.69
12	1561.68	1561.68	1632.08	1632.08	1702.48	1702.48
15	777.35	785.35	782.44	791.08	789.53	795.65
17	190.94	190.94	196.98	196.98	203.24	203.24
22	3479.02	3479.02	3293.72	3293.72	3108.43	3108.43
23	14.67	14.67	14.73	14.73	14.79	14.79
24	774.30	779.30	778.38	785.38	783.46	793.46
26	154.47	158	162.22	168.61	167.76	174.54
27	2139.80	2139.80	2139.80	2139.80	2139.80	2139.80
29	742.85	742.85	764.16	764.16	785.47	78.47
30	971.11	971.11	988.06	988.06	1005.01	1005.01
32	27.79	28.00	29.39	30.00	31.07	33.00
36	418.18	418.18	403.57	403.57	388.96	388.96
37	634.55	634.55	633.02	633.02	631.49	631.49
38	67.11	67.11	67.14	67.14	67.17	67.17
39	62.25	63.26	64.28	65.32	66.31	67.39
40	258.23	258.23	260.78	260.78	263.34	263.34
41	261.31	261.31	264.15	264.15	266.98	266.98

Appendix B: List of supplementary Figures
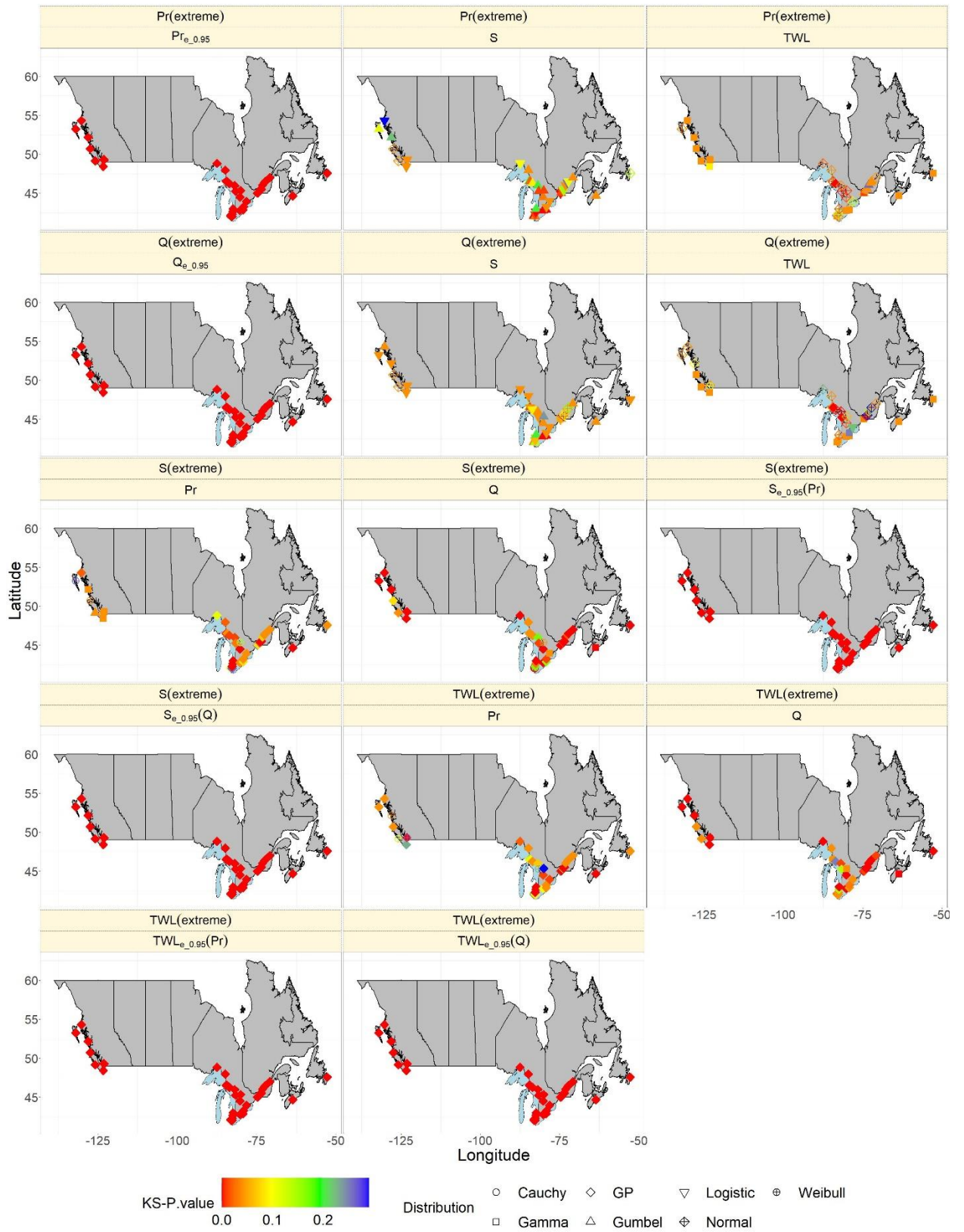
Supplementary Figure 2. 1) The best-fitted marginal distributions corresponding to the eight bivariate scenarios and the associated P-values for the Kolmogorov-Smirnov tests across different locations. For example, the subfigures entitled Pr(extreme)/Pr$_{e\_0.95}$, Pr(extreme)/S show the marginal distributions for extreme Pr and the associated surge data. As some Pr data corresponding to the scenarios (TWL$_{e\_0.95}$, Pr) and (S$_{e\_0.95}$, Pr) is zero and excluded from the analysis, there are two marginals for the extreme variable of each scenario. For instance, TWL(extreme)/ Pr$_{e\_0.95}$(Pr) and TWL(extreme)/ Pr$_{e\_0.95}$(Q) subfigures respectively, denote the marginal distributions of extreme TWL data when jointed with Pr and Q.
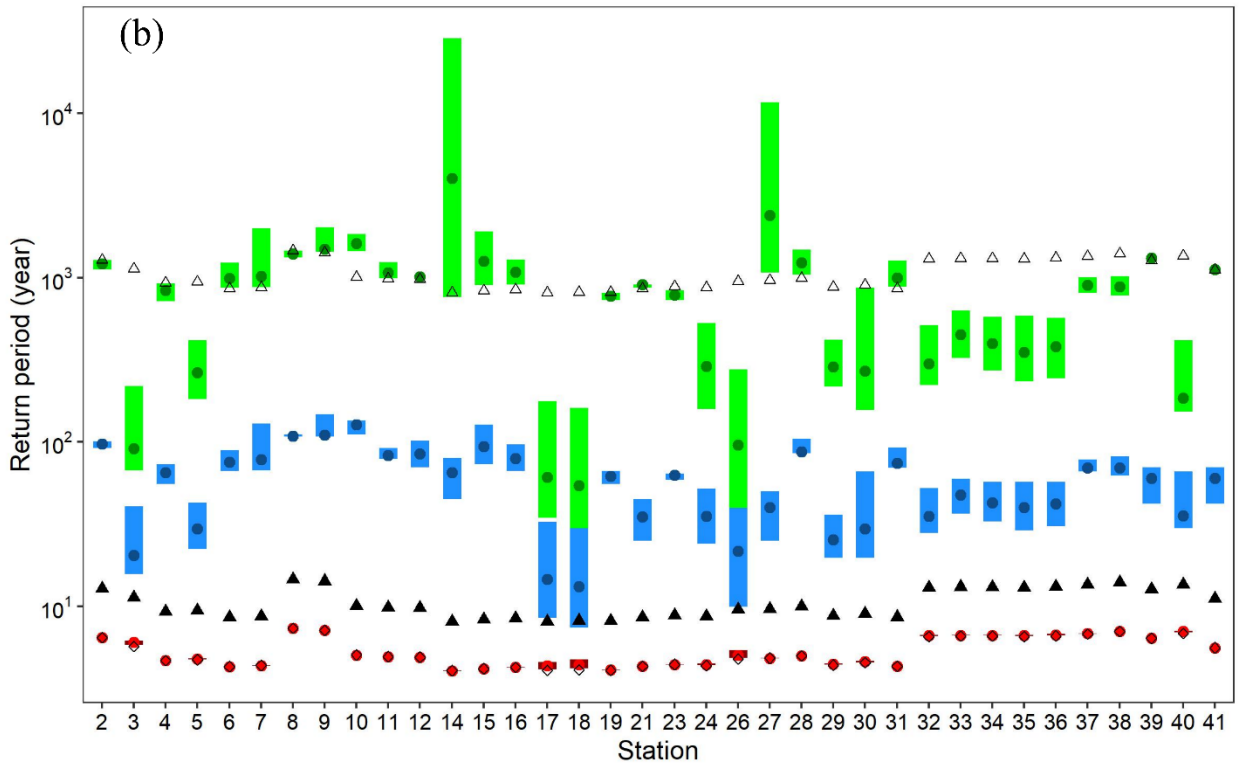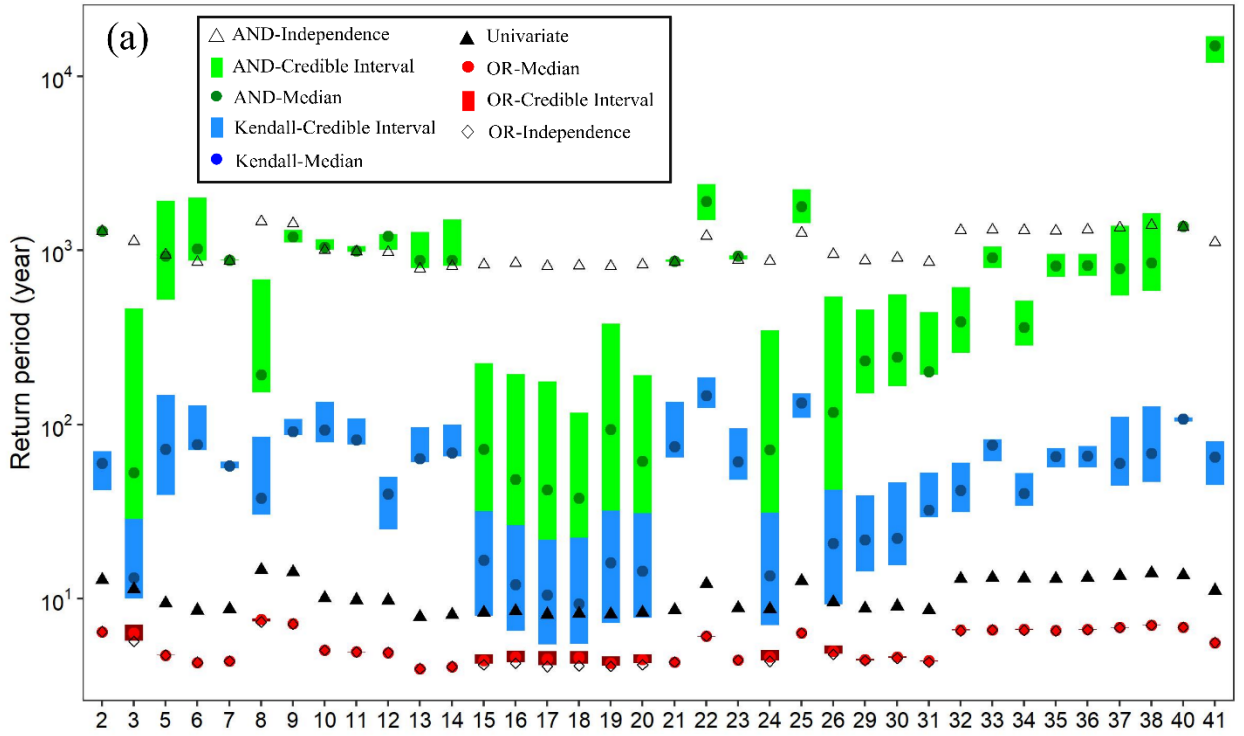
Supplementary Figure 2. 2) The estimated OR, AND, and Kendall JRPs in comparison with univariate RP and independence OR and AND JRPs for a) scenario ($Q_{e\_0.95}$, TWL) and b) scenario ($Q_{e\_0.95}$, S).
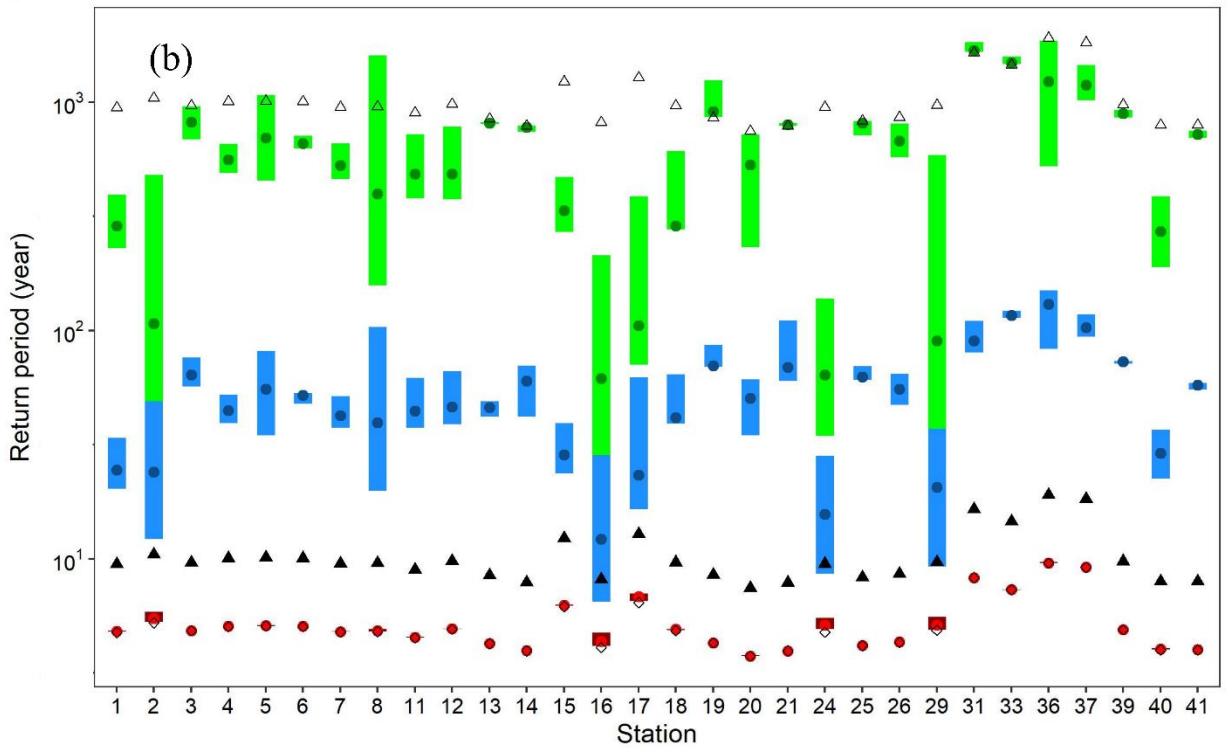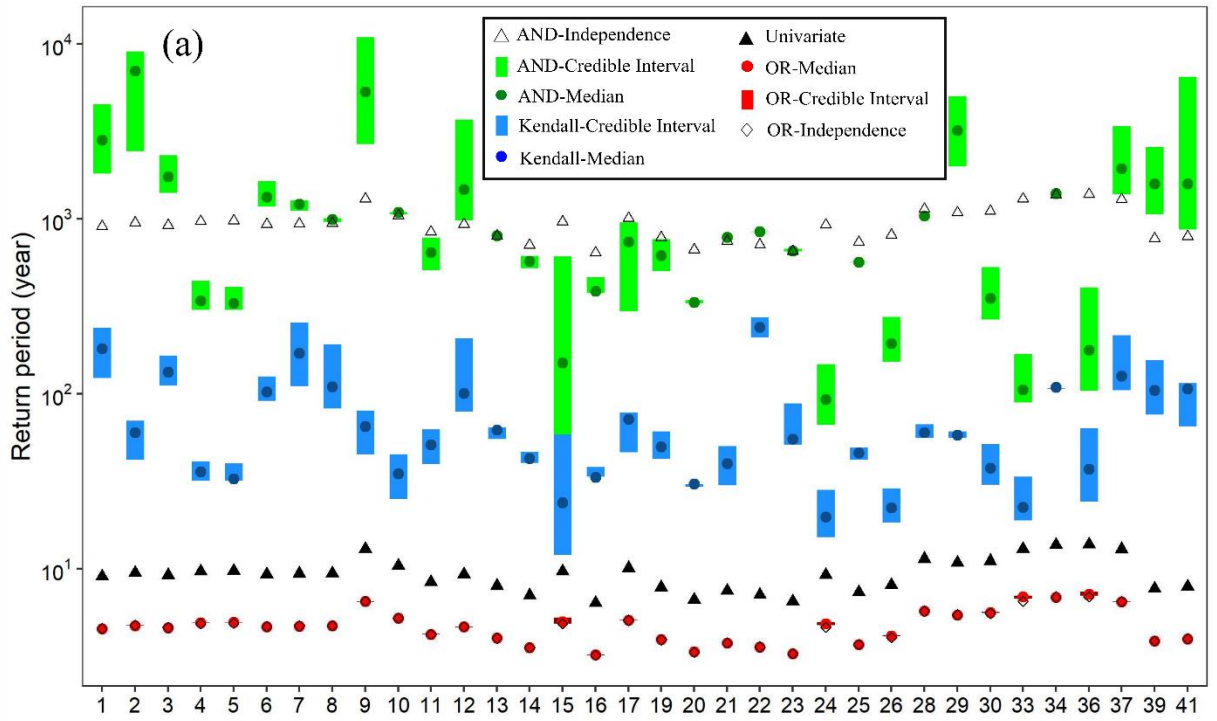
Supplementary Figure 2. 3) Similar to Figure S2 but for a) scenario (TWL$_{e\_0.95}$, Q) and b) scenario (TWL$_{e\_0.95}$, Pr).
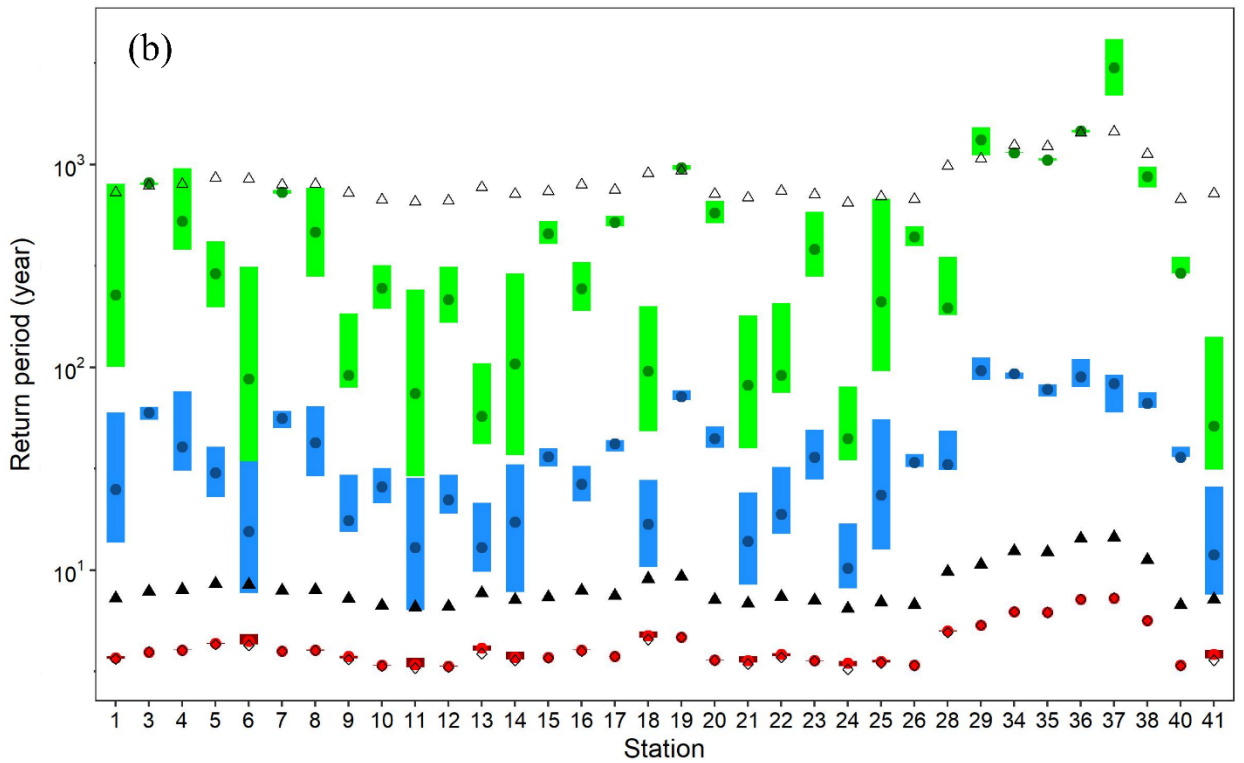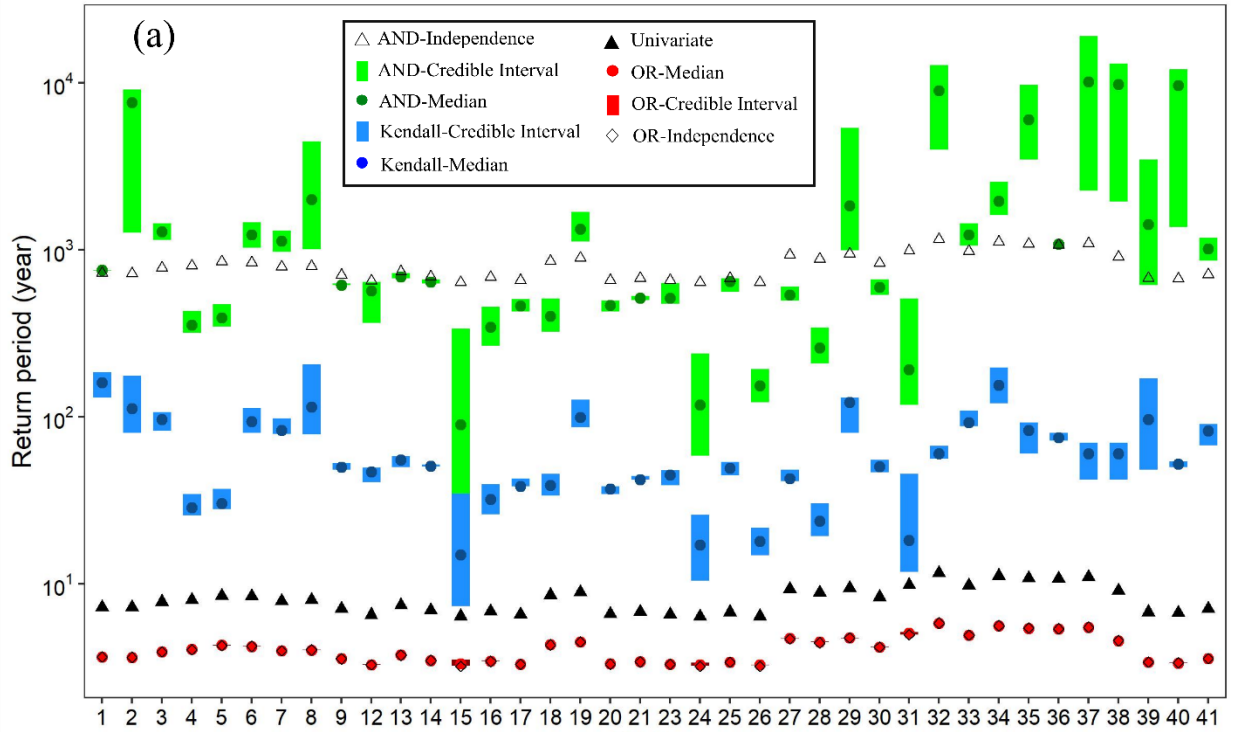
Supplementary Figure 2. 4) Similar to Table S2 but for scenario a) scenario ($S_{e\_0.95}$, Q) and b) scenario ($S_{e\_0.95}$, Pr).
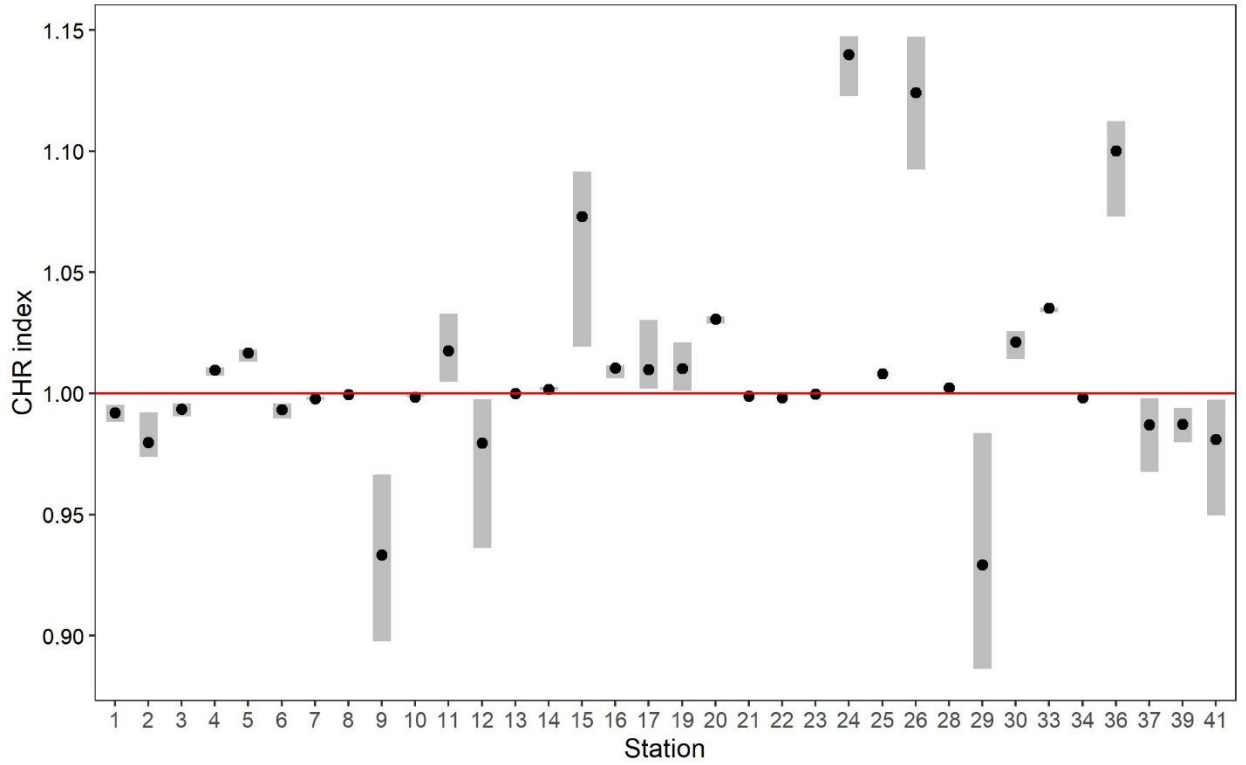
Supplementary Figure 2. 5) The CHR index values obtained for different locations regarding the scenario (TWL$_{e\_0.95}$, Q).
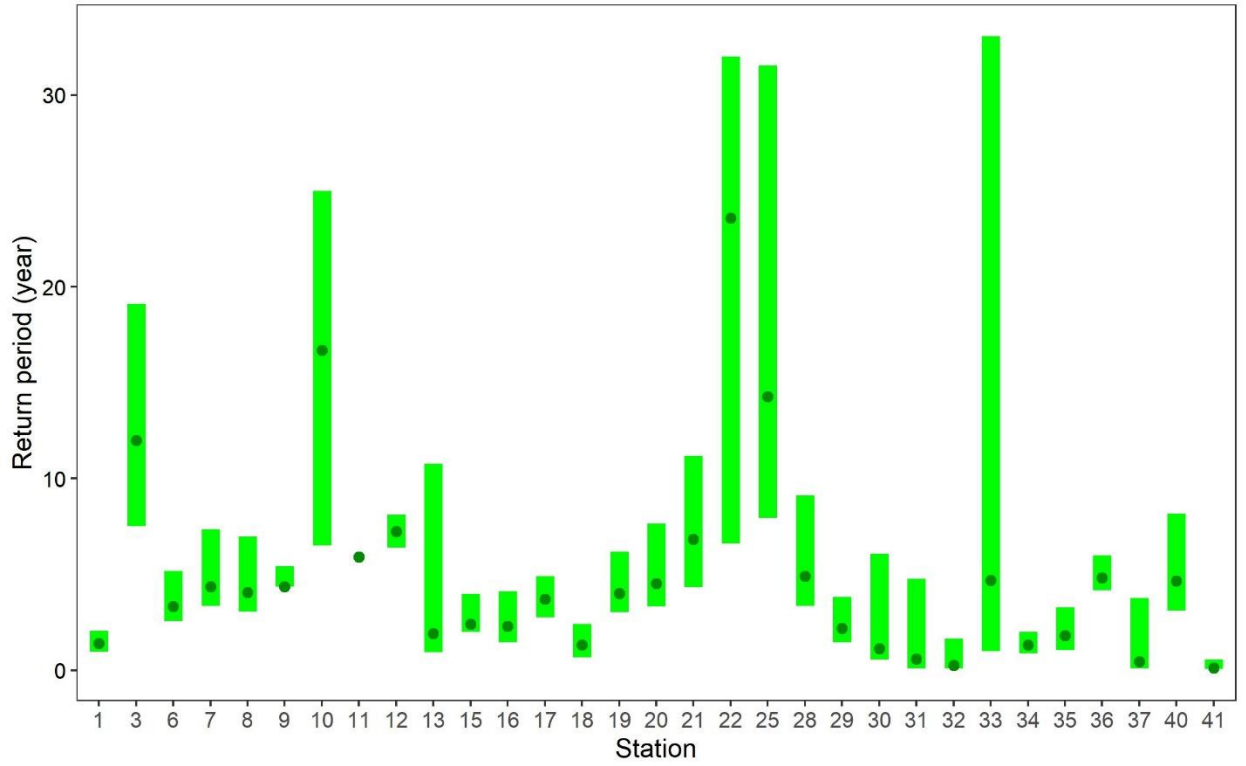
Supplementary Figure 2. 6) The measured conditional RPs across different locations for the (Pr$_{e\_0.95}$, S) bivariate scenario.
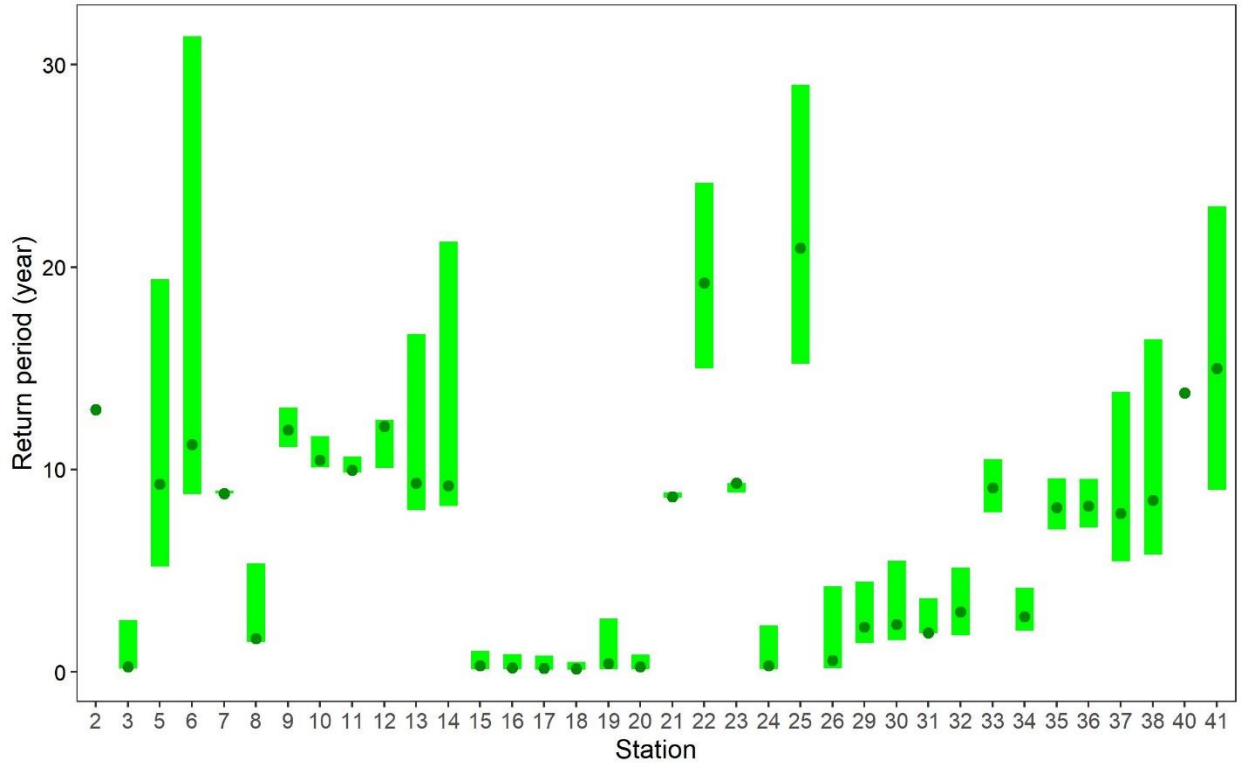
Supplementary Figure 2. 7) Similar to Figure S2.6 but for scenario ($Q_{e\_0.95}$, TWL).
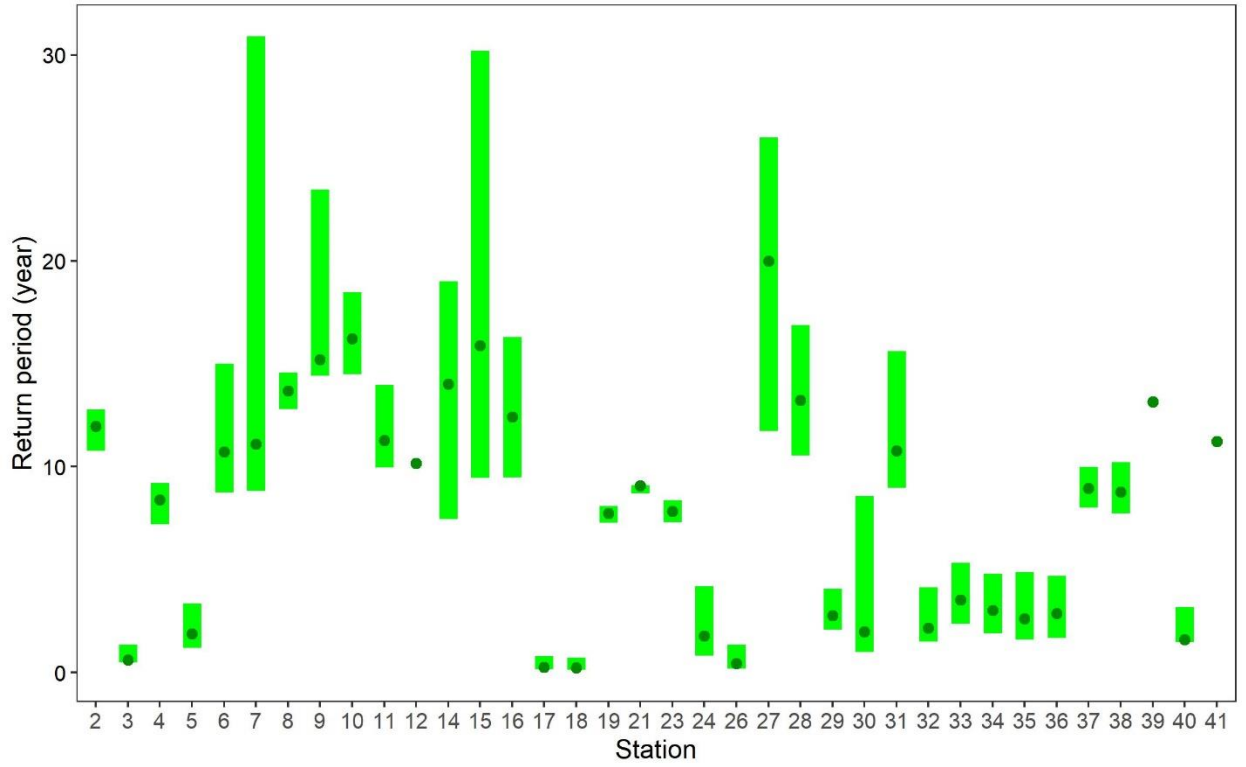
Supplementary Figure 2. 8) Similar to Figure S2.6 but for scenario ($Q_{e\_0.95}$, S).
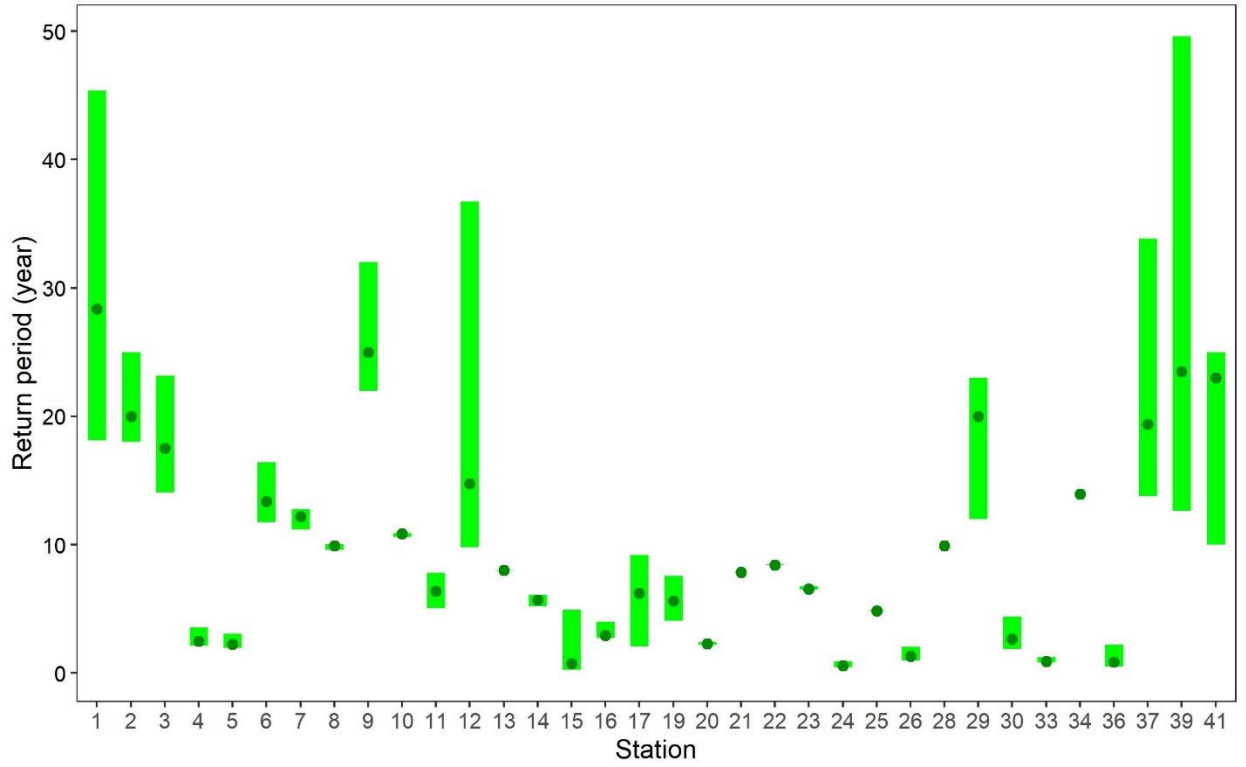
Supplementary Figure 2. 9) Similar to Figure S2.6 but for scenario (TWL$_{e\_0.95}$, Q).
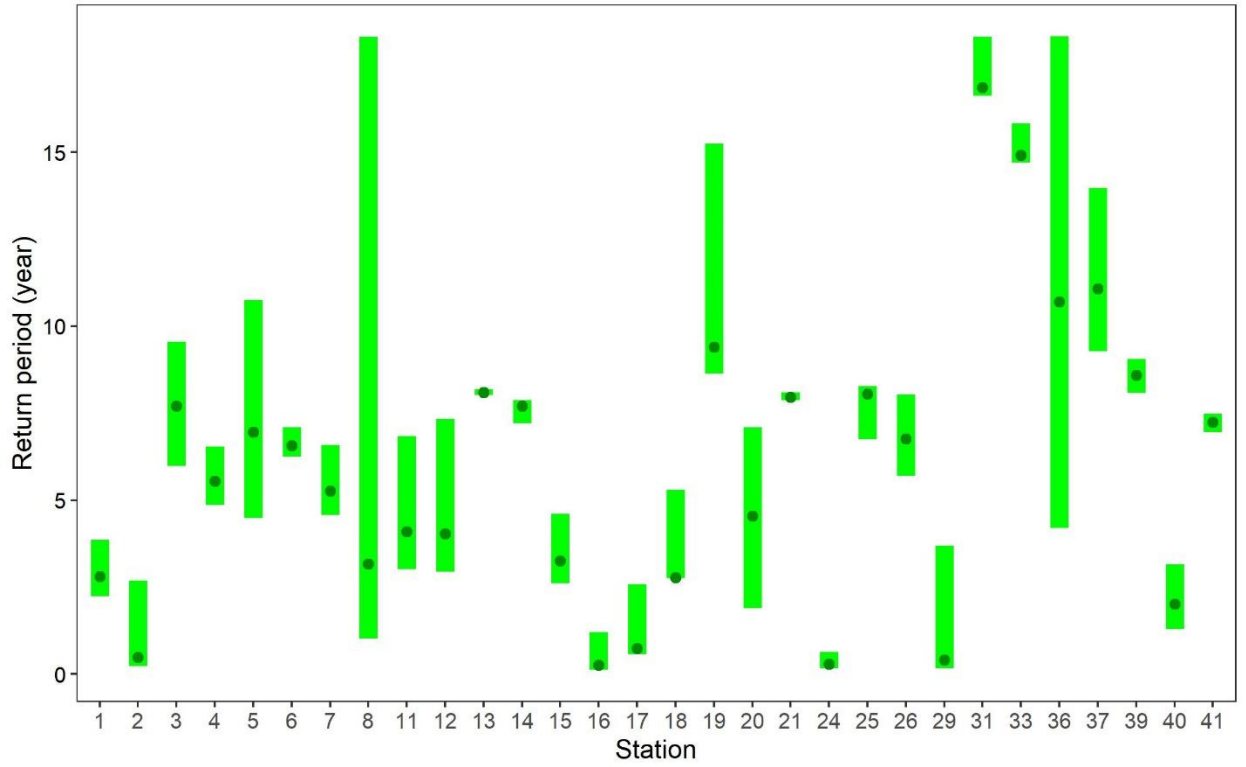
Supplementary Figure 2. 10) Similar to Figure S2.6 but for scenario (TWL$_{e\_0.95}$, Pr).
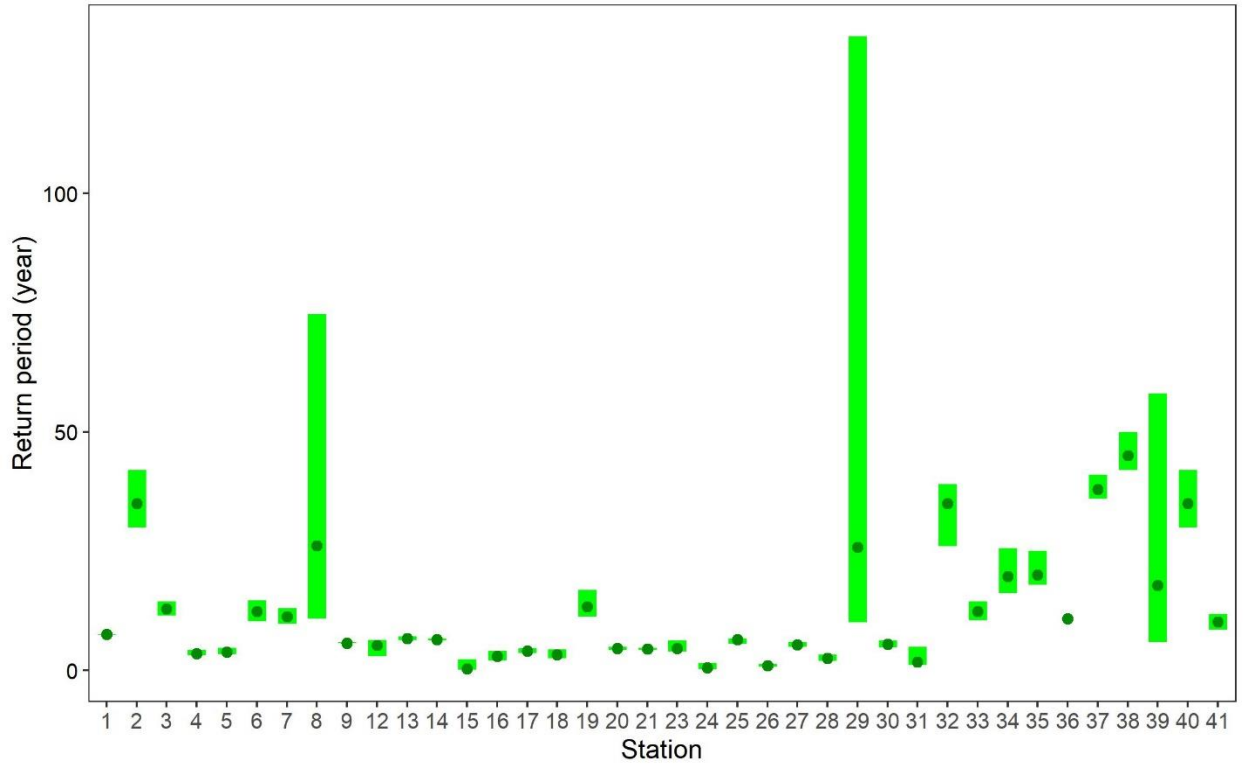
Supplementary Figure 2. 11) Similar to Figure S2.6 but for scenario ($S_{e\_0.95}$, Q).
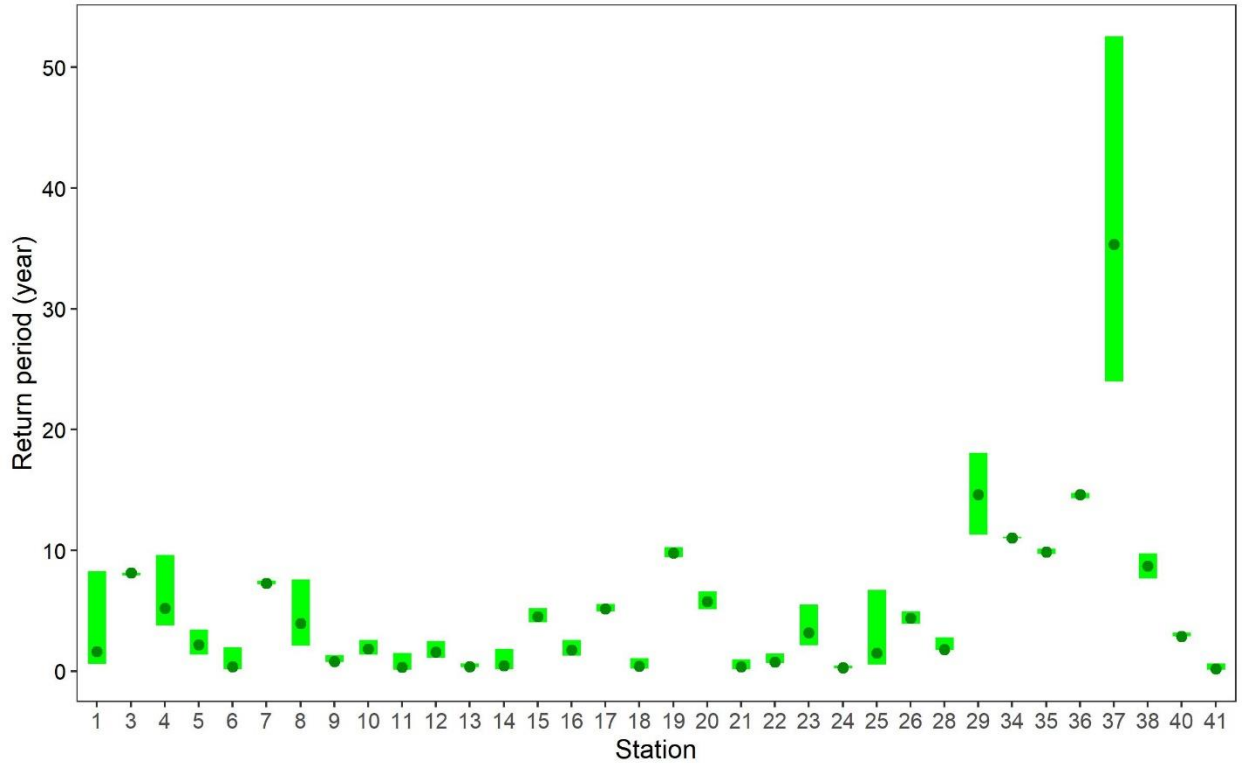
Supplementary Figure 2. 12) Similar to Figure S2.6 but for scenario (S$_{e\_0.95}$, Pr).
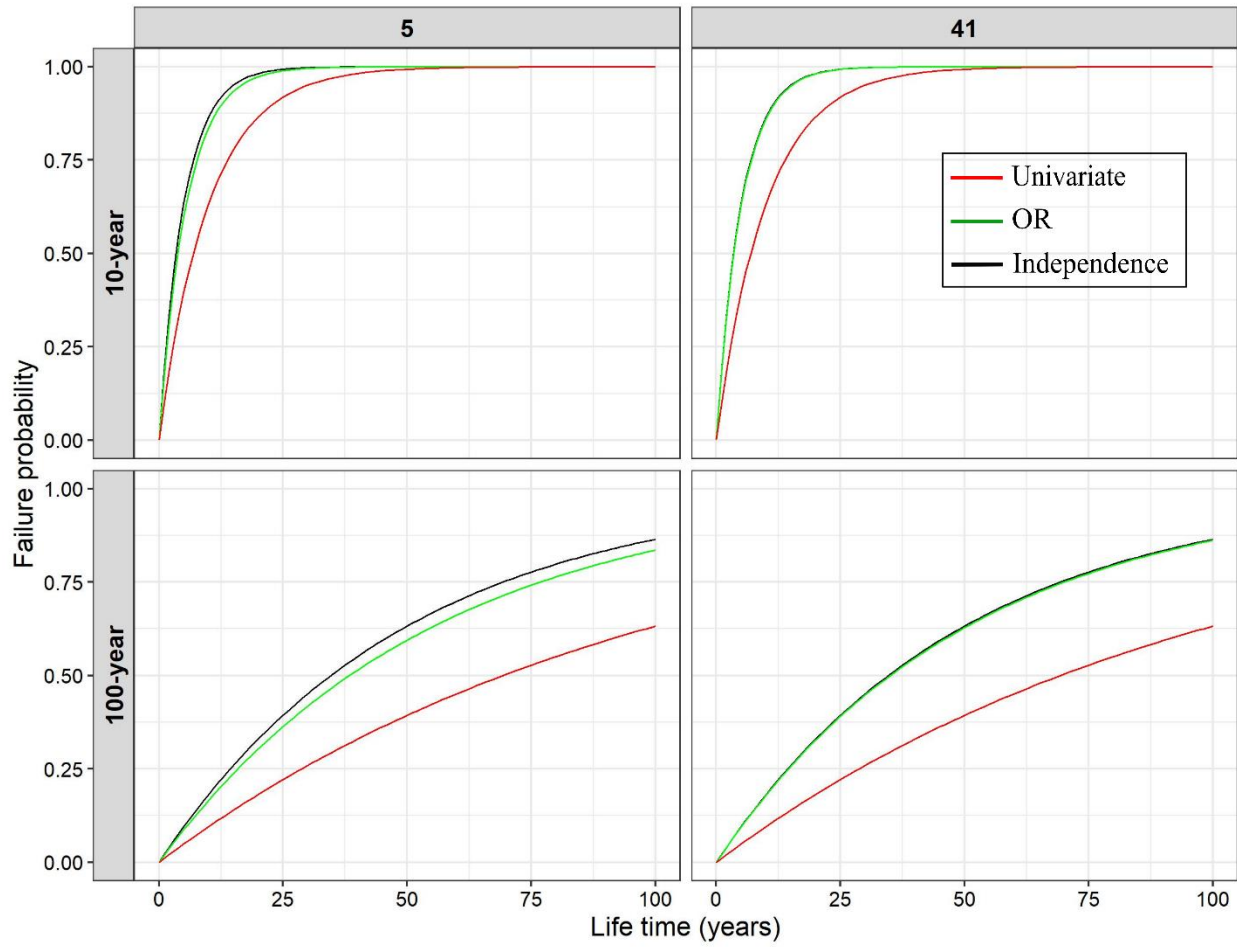
Supplementary Figure 2. 13) The estimated FPs pertaining to locations 5, and 41 for 100 and 10 years OR RP considering scenario (TWL$_{e\_0.95}$, Pr).
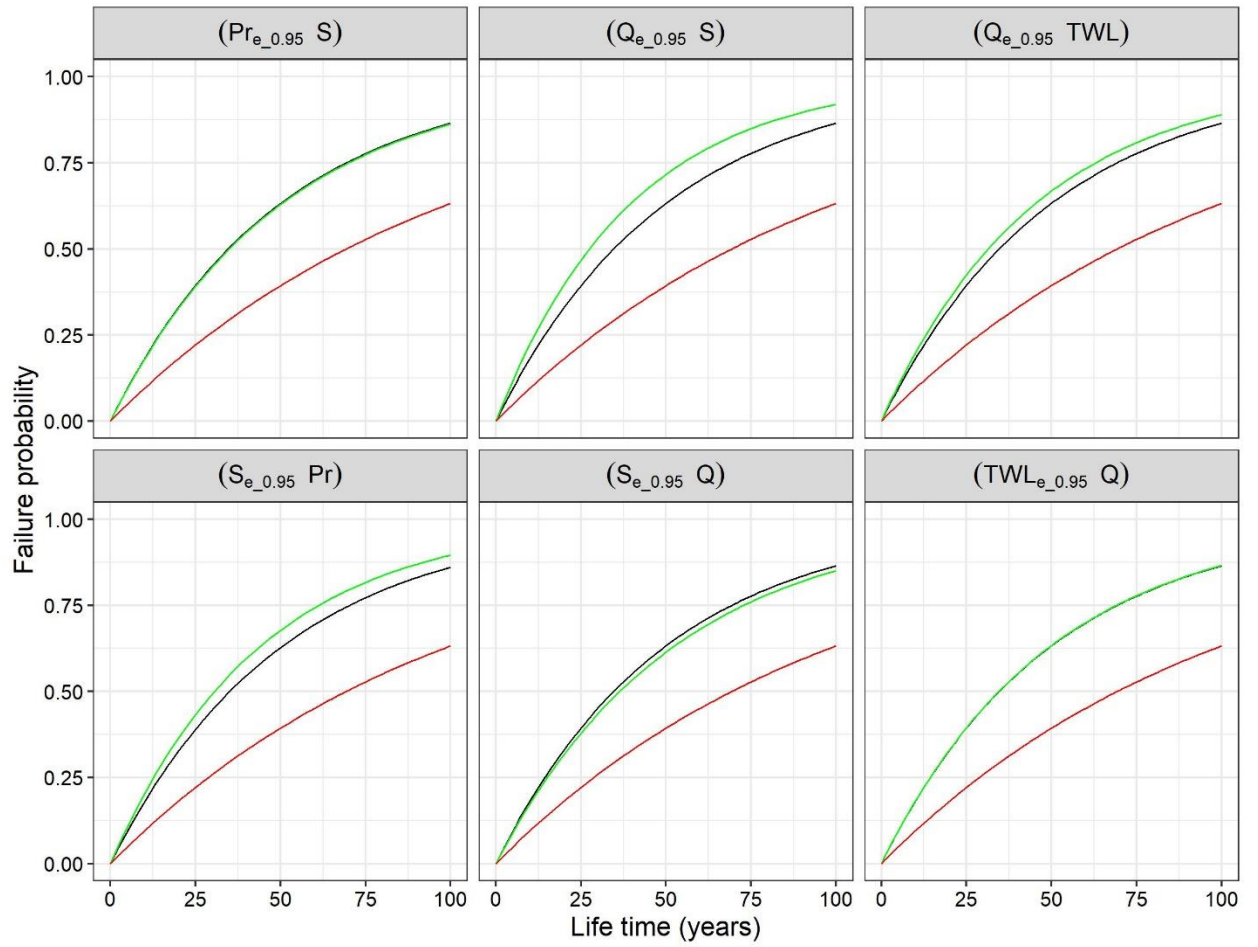
Supplementary Figure 2. 14) The estimated FPs for 100-year bivariate event of different scenarios for location # 41.
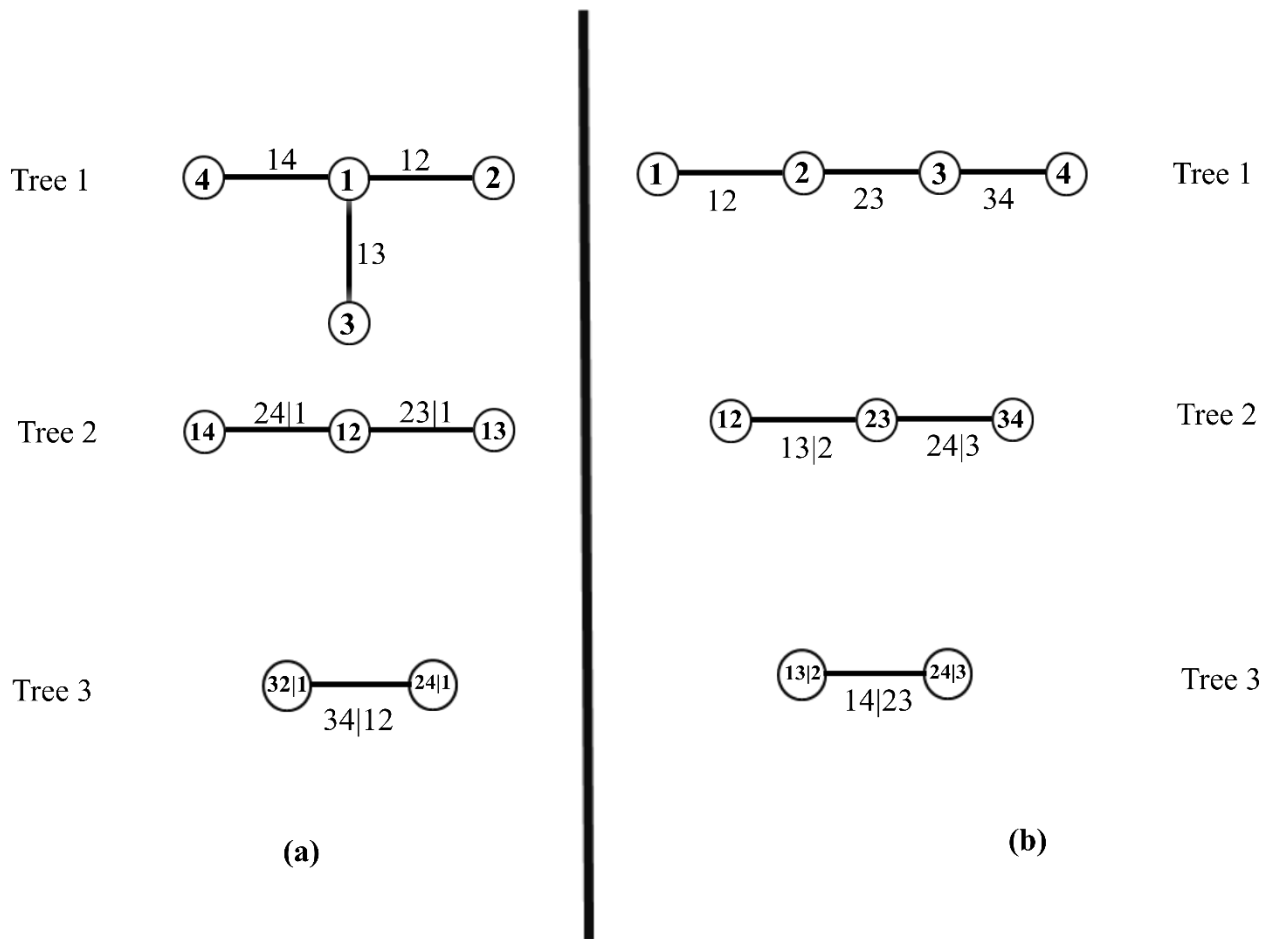
Supplementary Figure 3. 1) a) An illustration of four-dimensional C-vine copula, b) Four-dimensional D-vine copula.
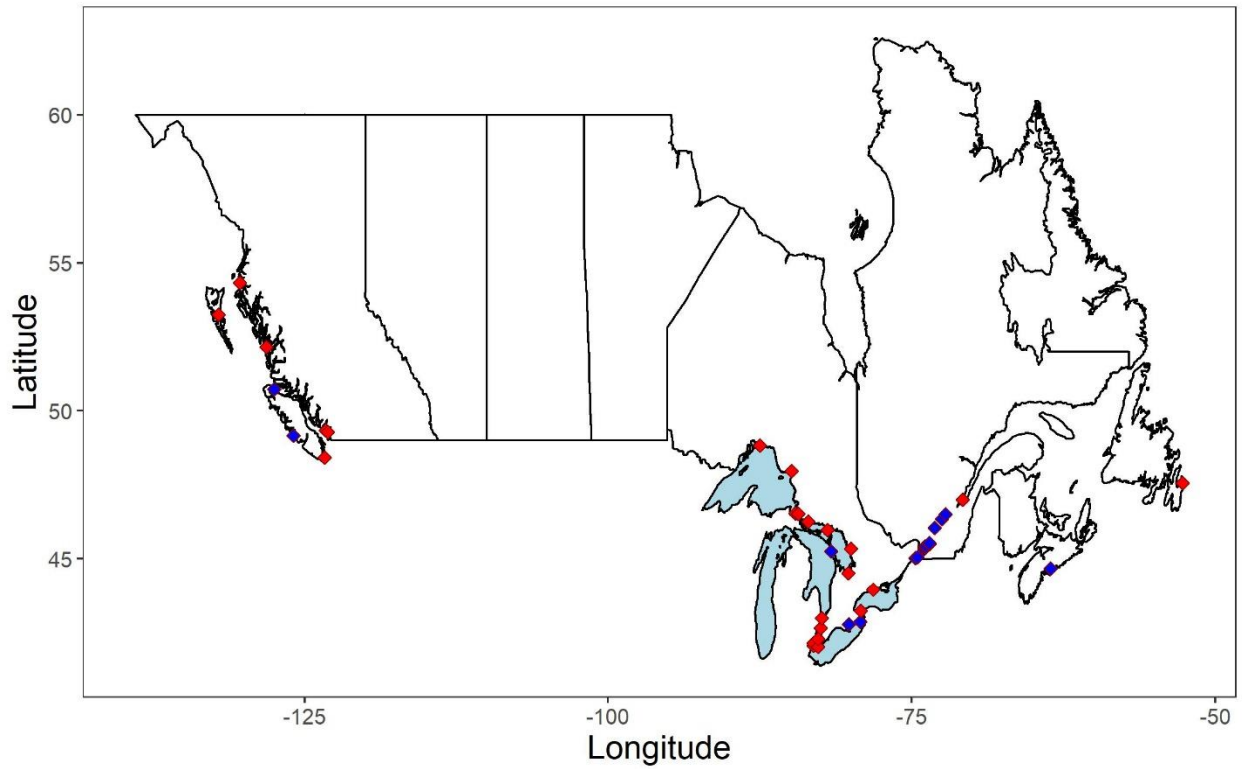
Supplementary Figure 3. 2) The locations highlighted in red show positive dependency in (Pr, TWL) which is higher than (Q, TWL), and the ones highlighted in blue show areas with larger positive dependencies in (Q, TWL) compared to (Pr, TWL).
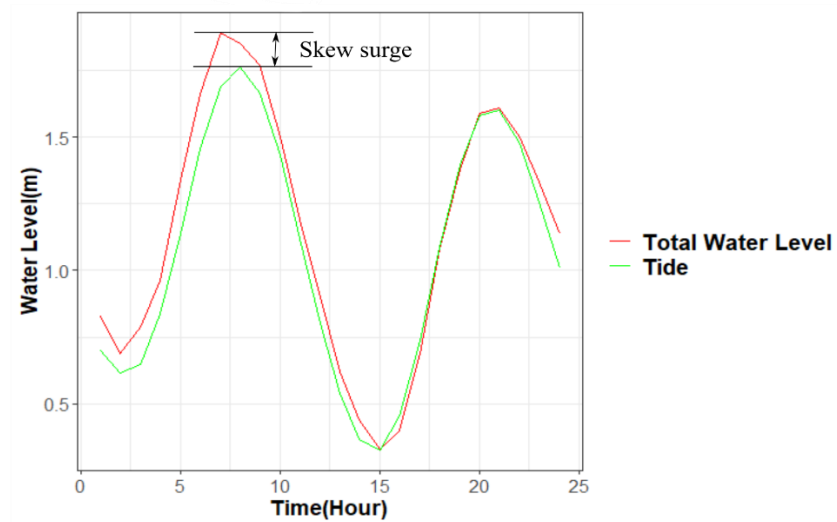
Supplementary Figure 4. 1) A graphical illustration of skew surge, which is the difference between high tide and maximum total water level over a 24-hour period regardless of their timing.
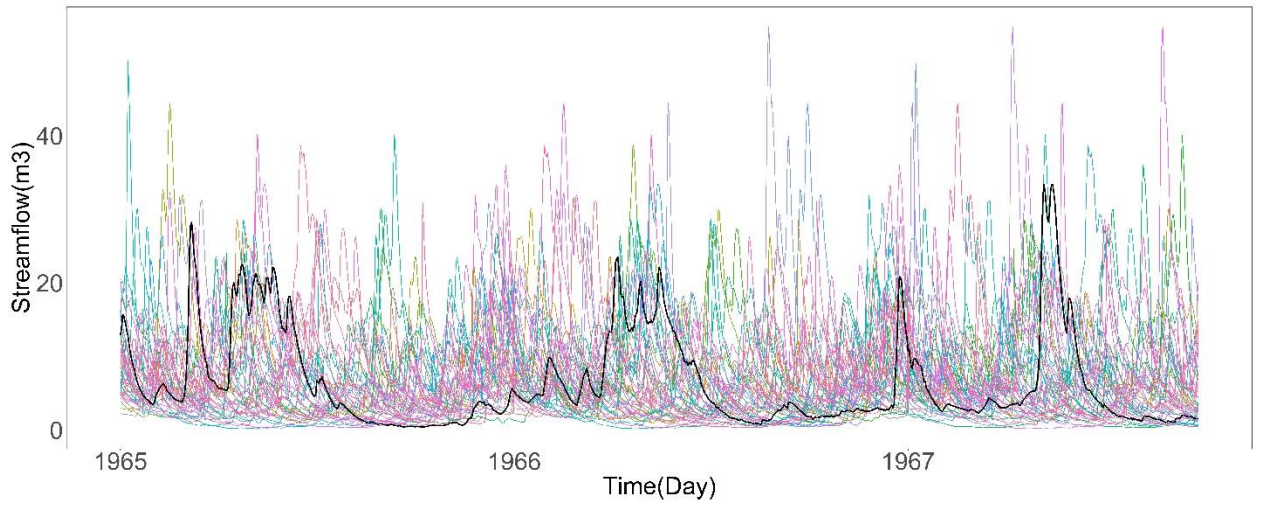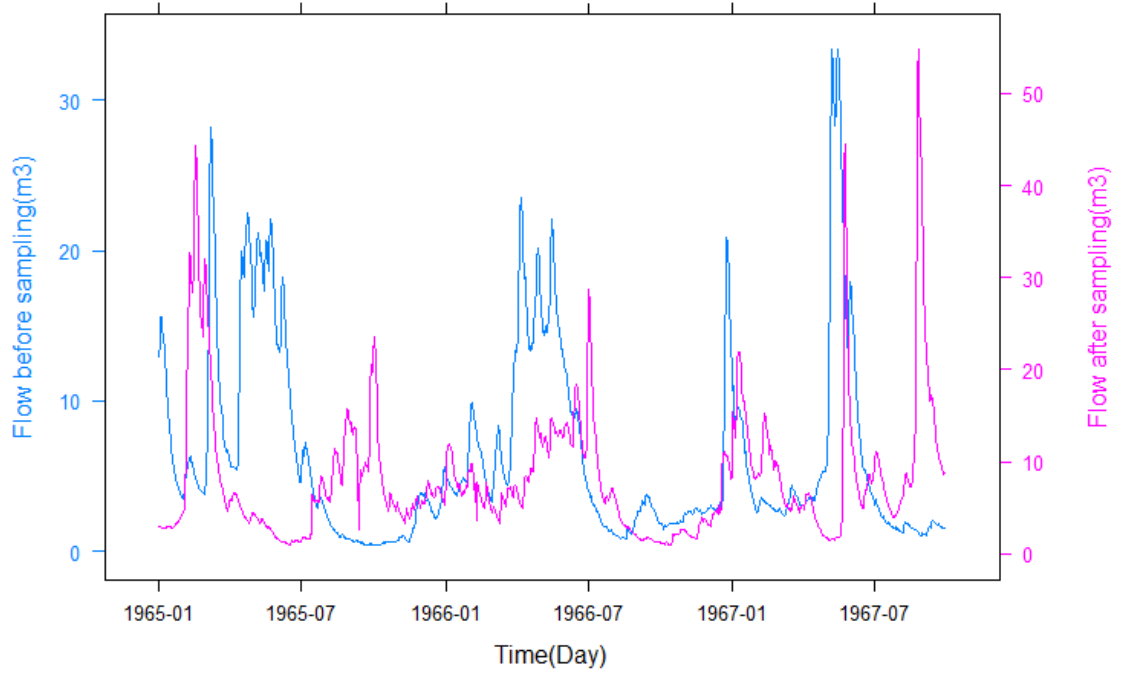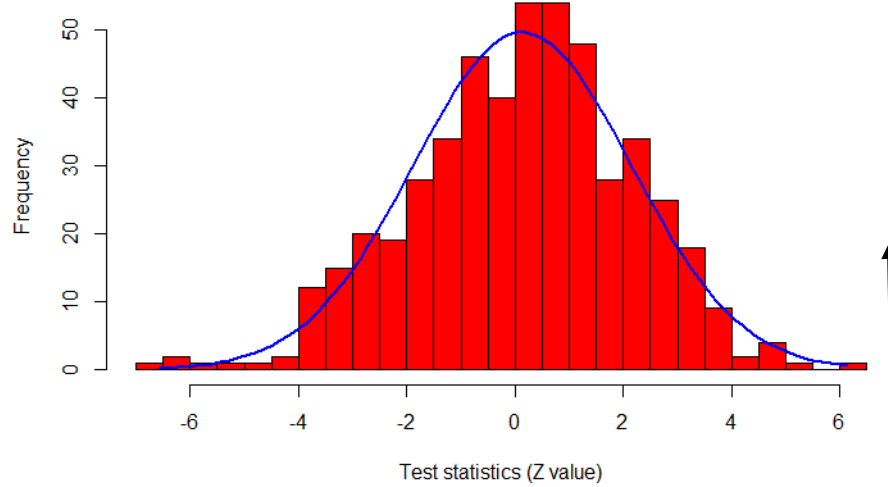
Supplementary Figure 4. 2) The streamflow time series for site # 40 before and after Block Bootstrap Sampling (block size is 1 year): a) The original and its shuffled time series (for one sample) using BBS for three years, b) The original time series highlighted in black and 500/1000 shuffled time series for three years. c) The distribution of test stats and where the observed test stat lies.

(a)

(b)
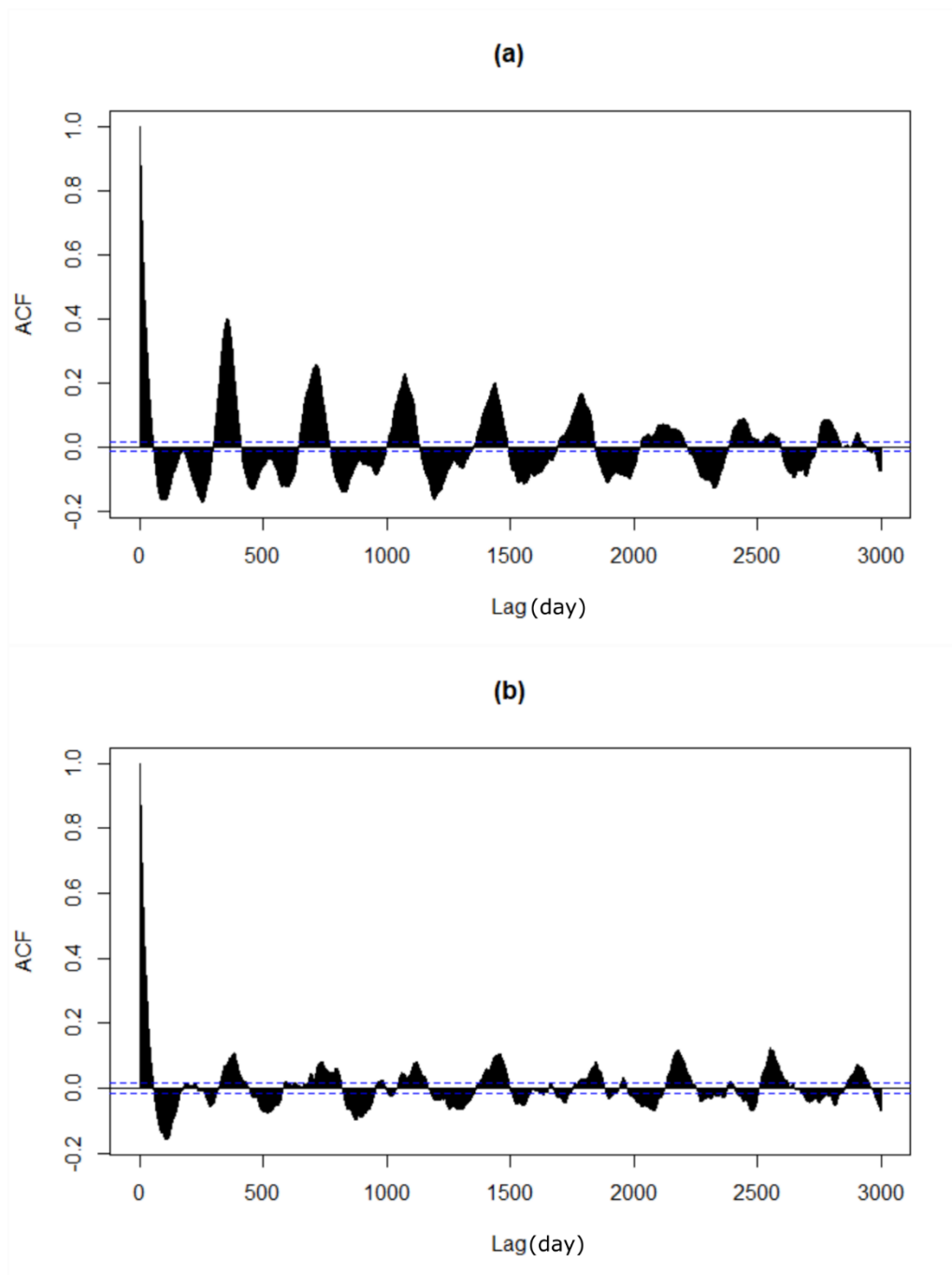
Supplementary Figure 4. 3) The autocorrelation functions of streamflow time series for site #40. a) Original time series and b) its one shuffled time series after using BBS. The time lag is one year.
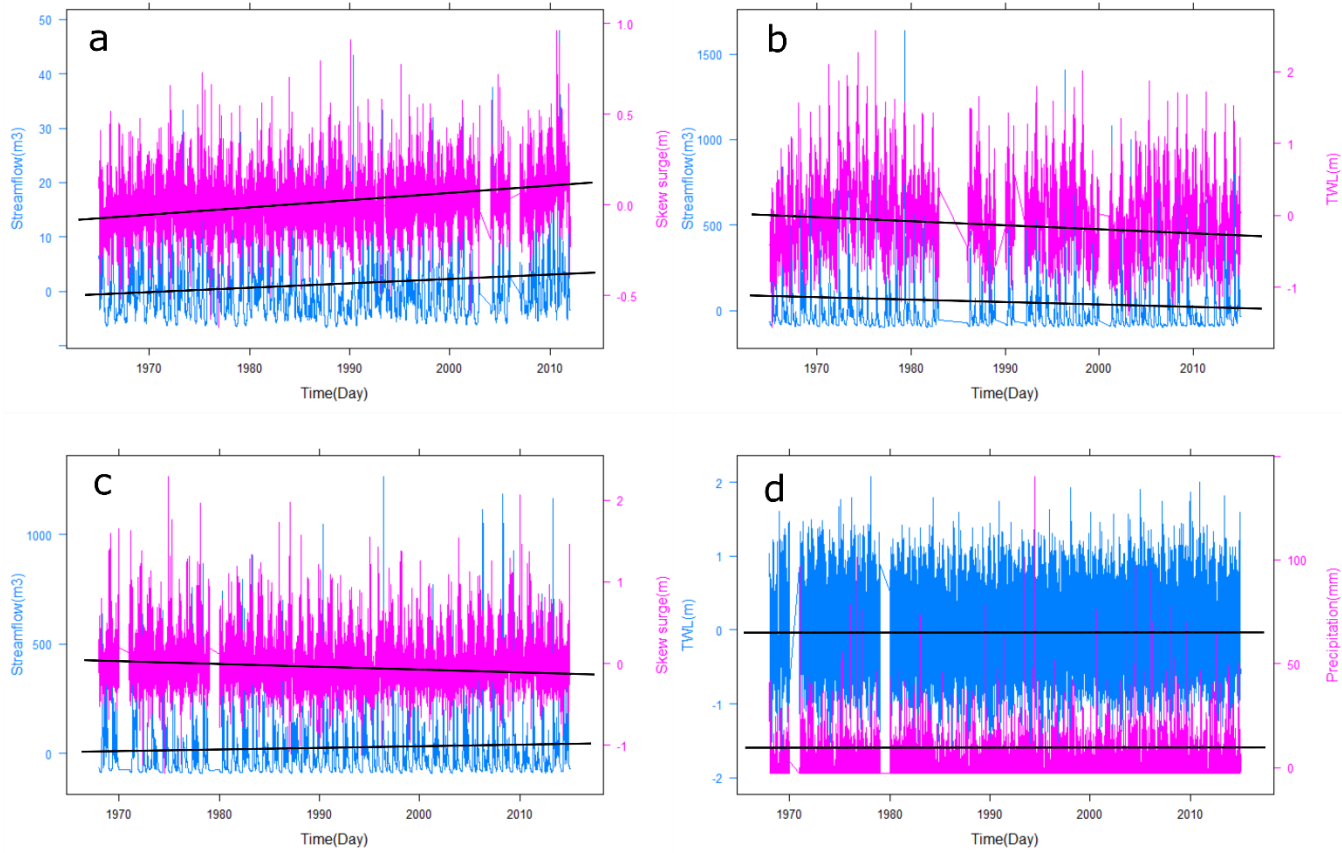
Supplementary Figure 4. 4) Different forms of the joint bivariate trends: a) both variables have increasing trends. b) both variables have decreasing trends (negative joint trend), c) the variables have increasing and decreasing trends, d) both variables are stationary.
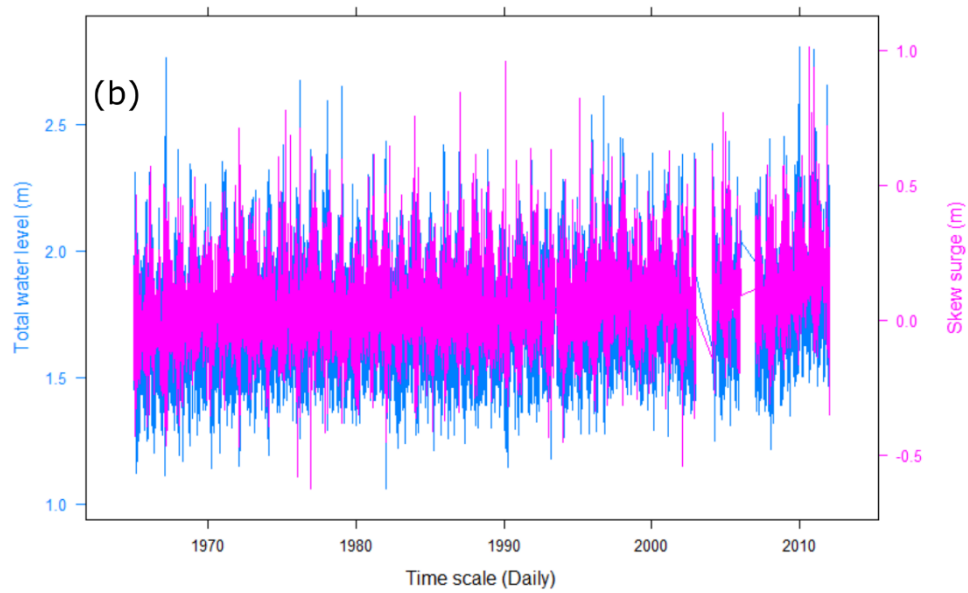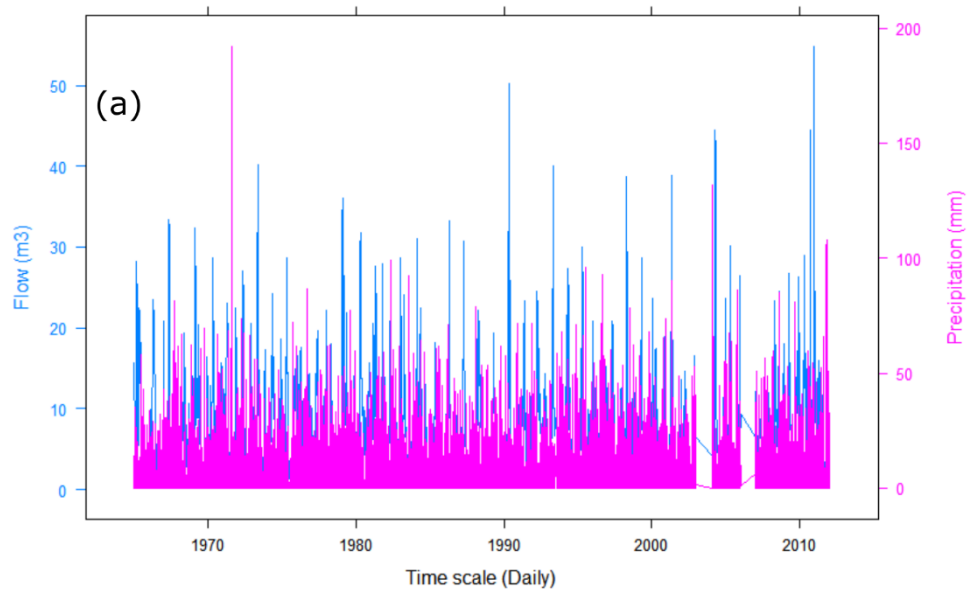
Supplementary Figure 4. 5) Daily time series of four variables for site# 40. a) Precipitation and streamflow and b) Total water level and skew surge.
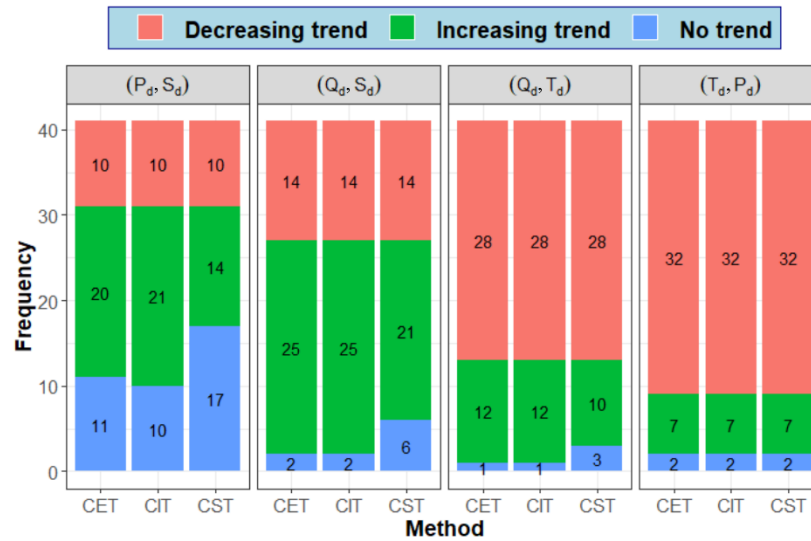
Supplementary Figure 4. 6) The number of locations with increasing, decreasing or no statistically significant trends based on the results of three non-parametric multivariate trend analysis methods (i.e. CIT, CST and CET) for (Q_d, S_d), (Q_d, T_d), (P_d, S_d) and (T_d, P_d) scenarios.
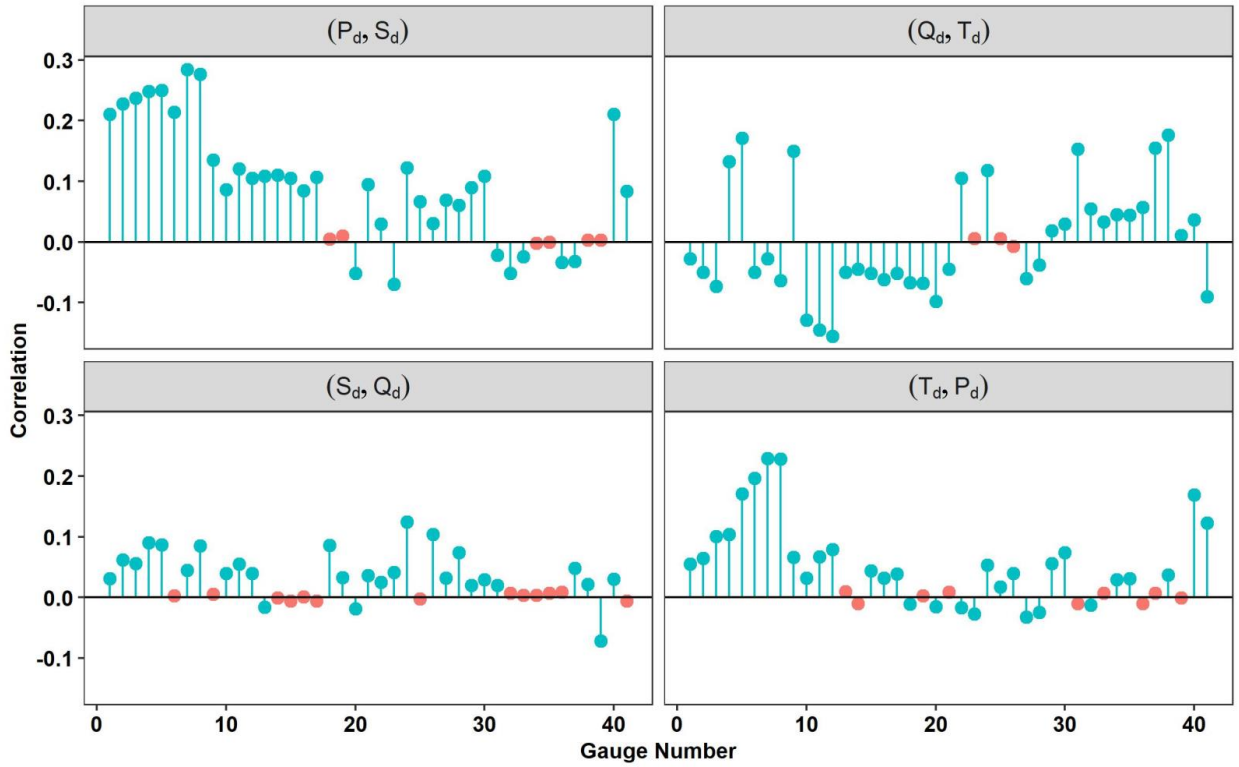
Supplementary Figure 4. 7) The Kendall's correlation coefficients of four scenarios for each gauge in daily time scale. Blue circles denote significant correlations (95% confidence).
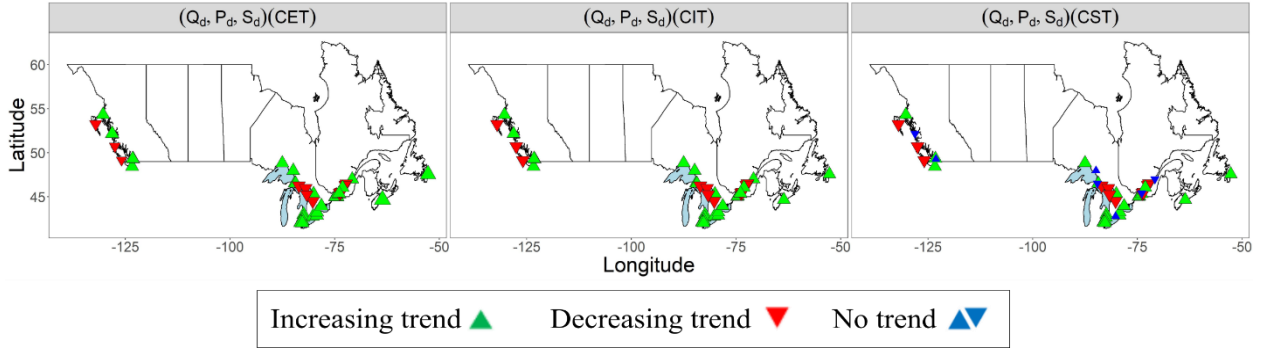
Supplementary Figure 4. 8) Trivariate daily trends of streamflow, precipitation and skew surge over the Atlantic, Pacific and the Great Lakes coasts.
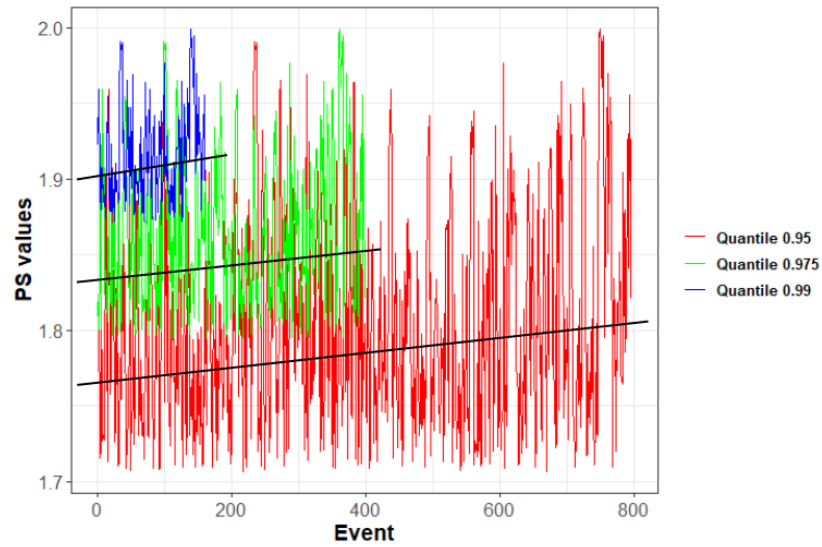
Supplementary Figure 4. 9) The trend of PS values for different quantities of gauge 40 related to the scenario (T_e, Q_1).
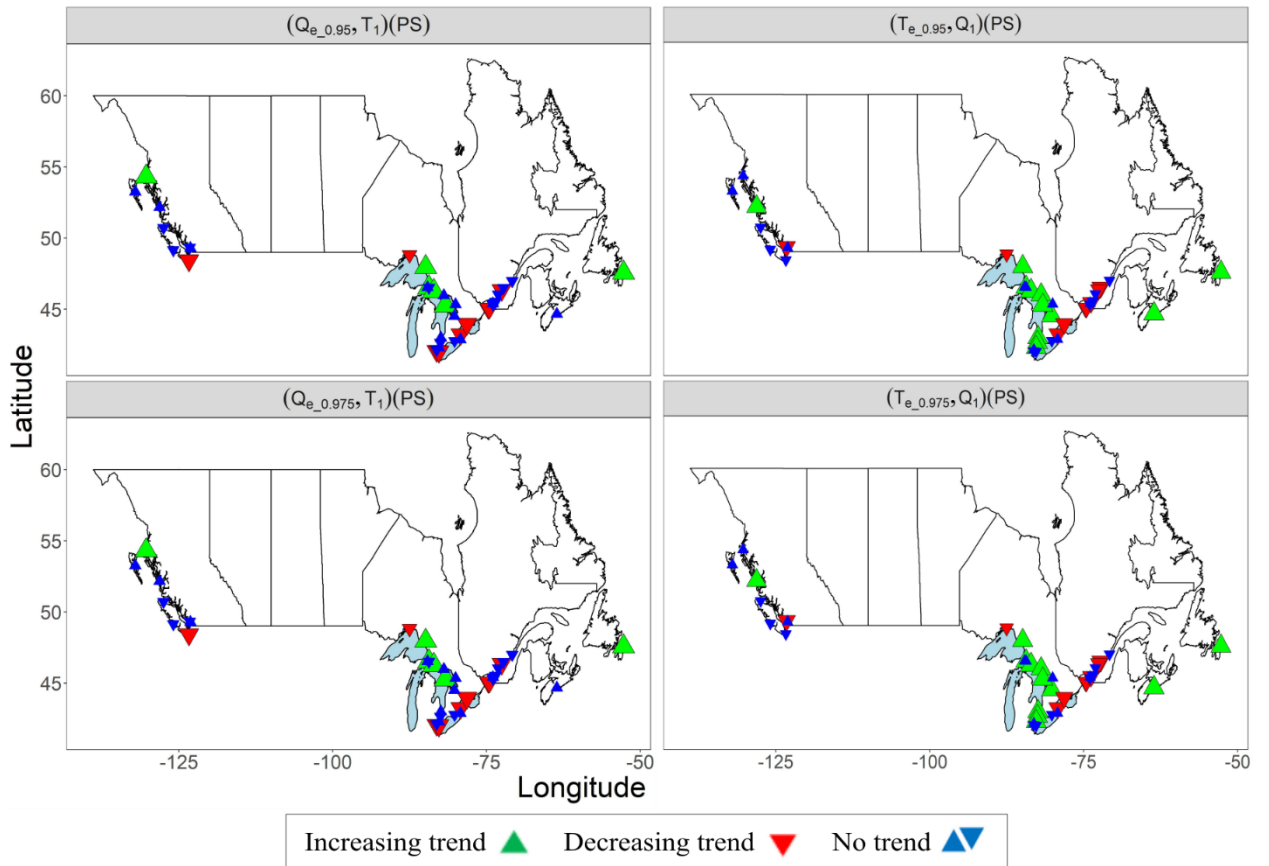
Supplementary Figure 4. 10) The trend of PS values for different $Q_{0.95}$ and $Q_{0.975}$ related to scenarios (Q_e, T_1) and (T_e, Q_1).
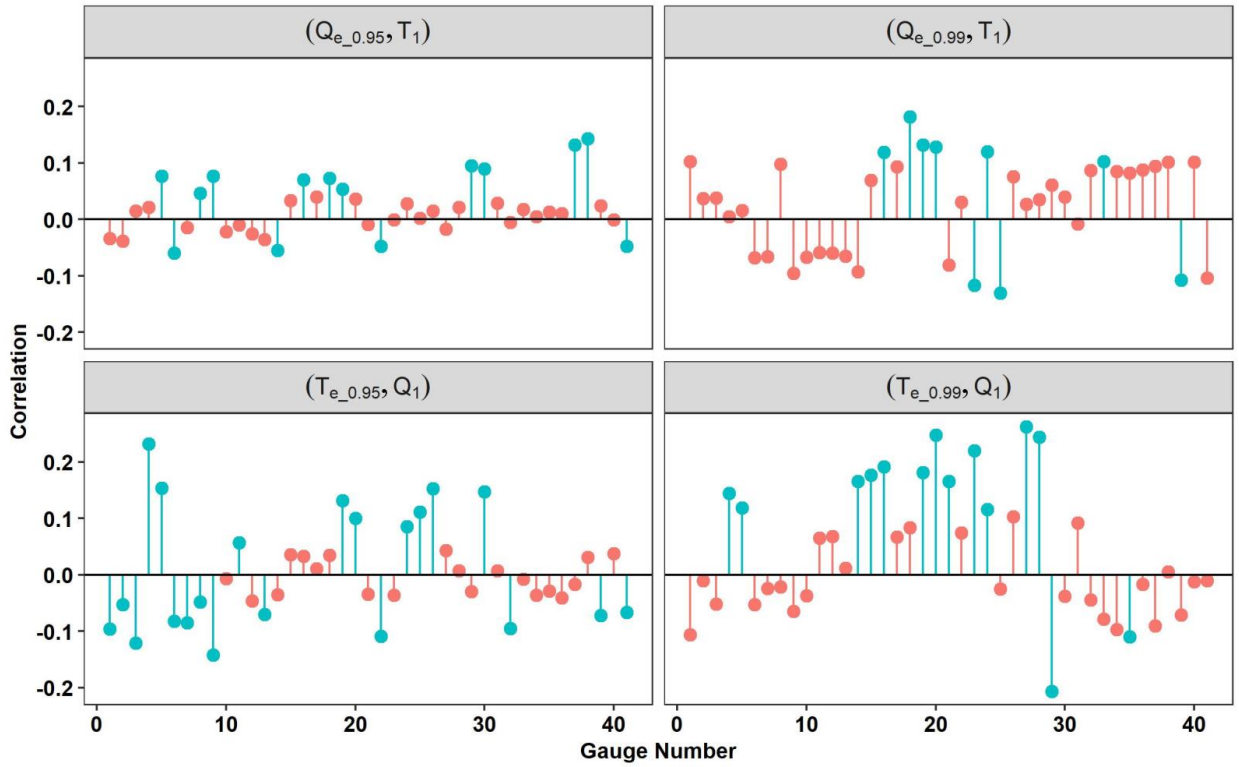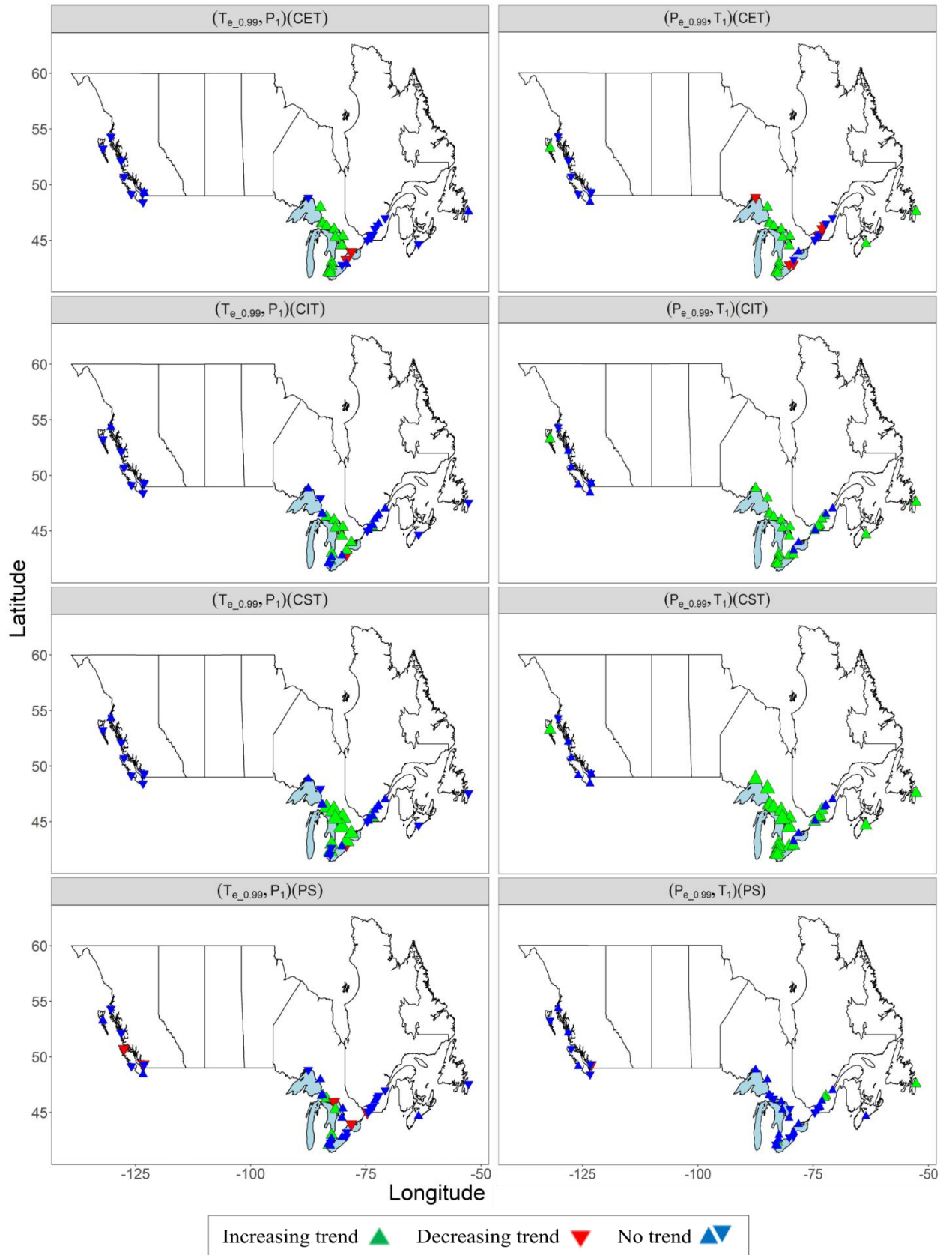
Supplementary Figure 4. 11) The Kendall's correlation coefficients of extremes ($Q_{0.95}$ and $Q_{0.99}$) of (Q, T_1) and (T, Q_1) scenarios for each gauge. Blue circles denote significant correlations (95% confidence).
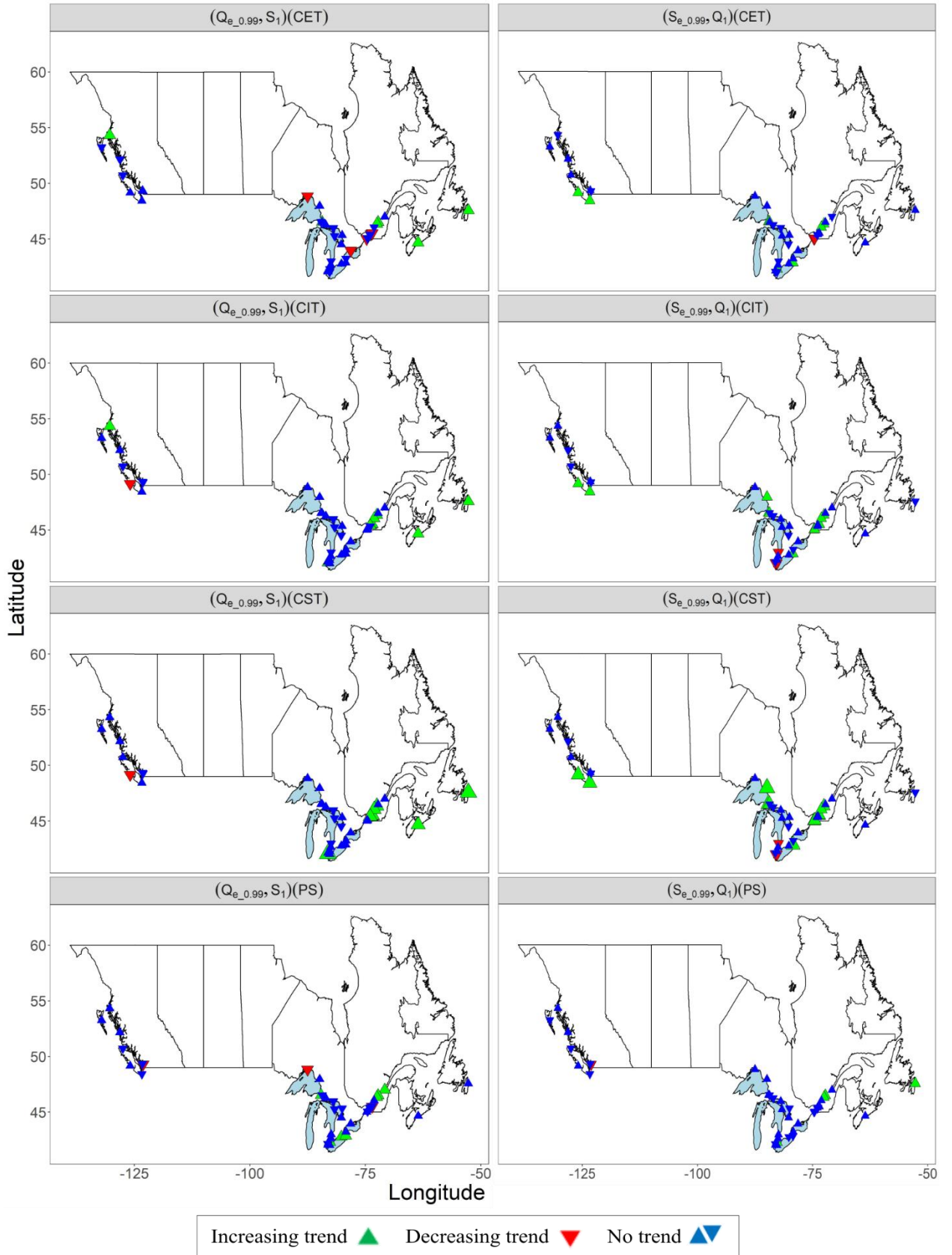
Supplementary Figure 4. 12) The bivariate trends of two extreme scenarios of $(Q_{e\_0.99}, S_1)$ (Q values above the 99th percentile threshold and maximum S values one day before or after) and $(S_{e\_0.99}, Q_1)$ for 41 locations using CIT, CST, CET and PS.
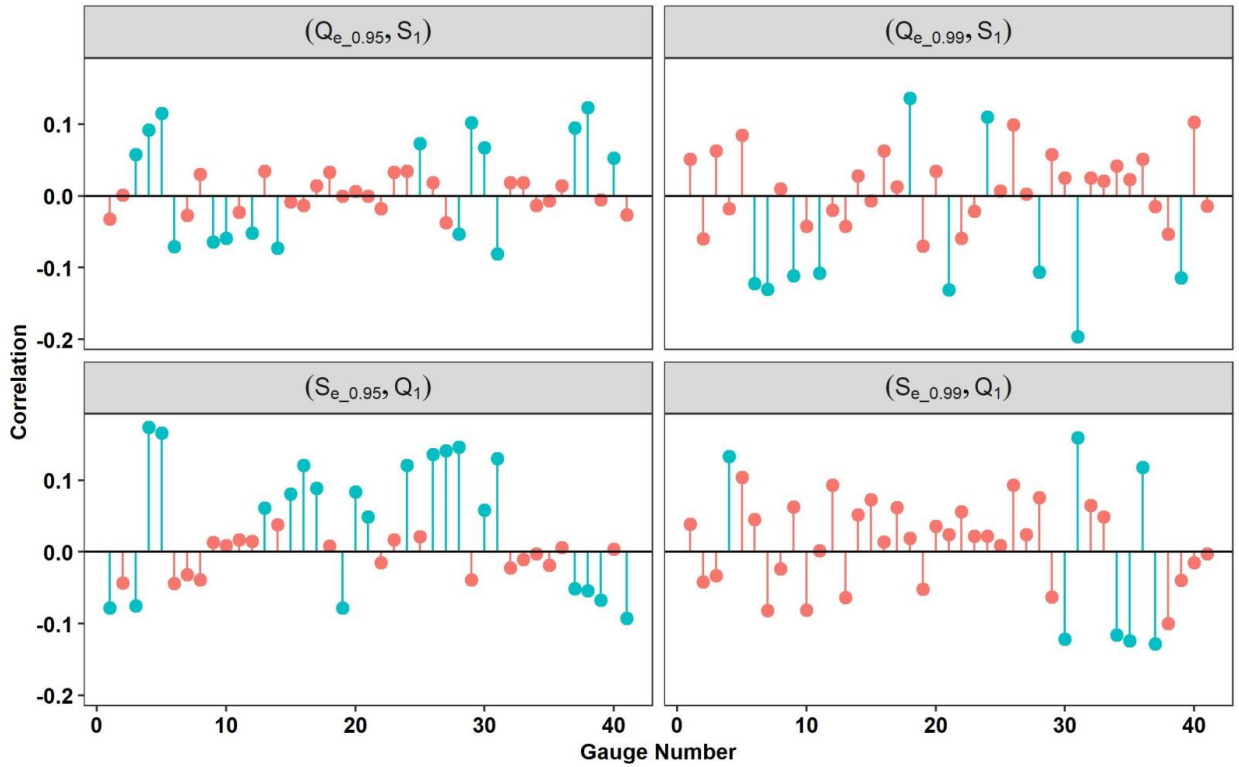
Supplementary Figure 4. 13) The Kendall's correlation coefficients of extremes ($Q_{0.95}$ and $Q_{0.99}$) of (Q, S_1) and (S, Q_1) scenarios for each gauge. Blue circles denote significant correlations (95 % confidence).
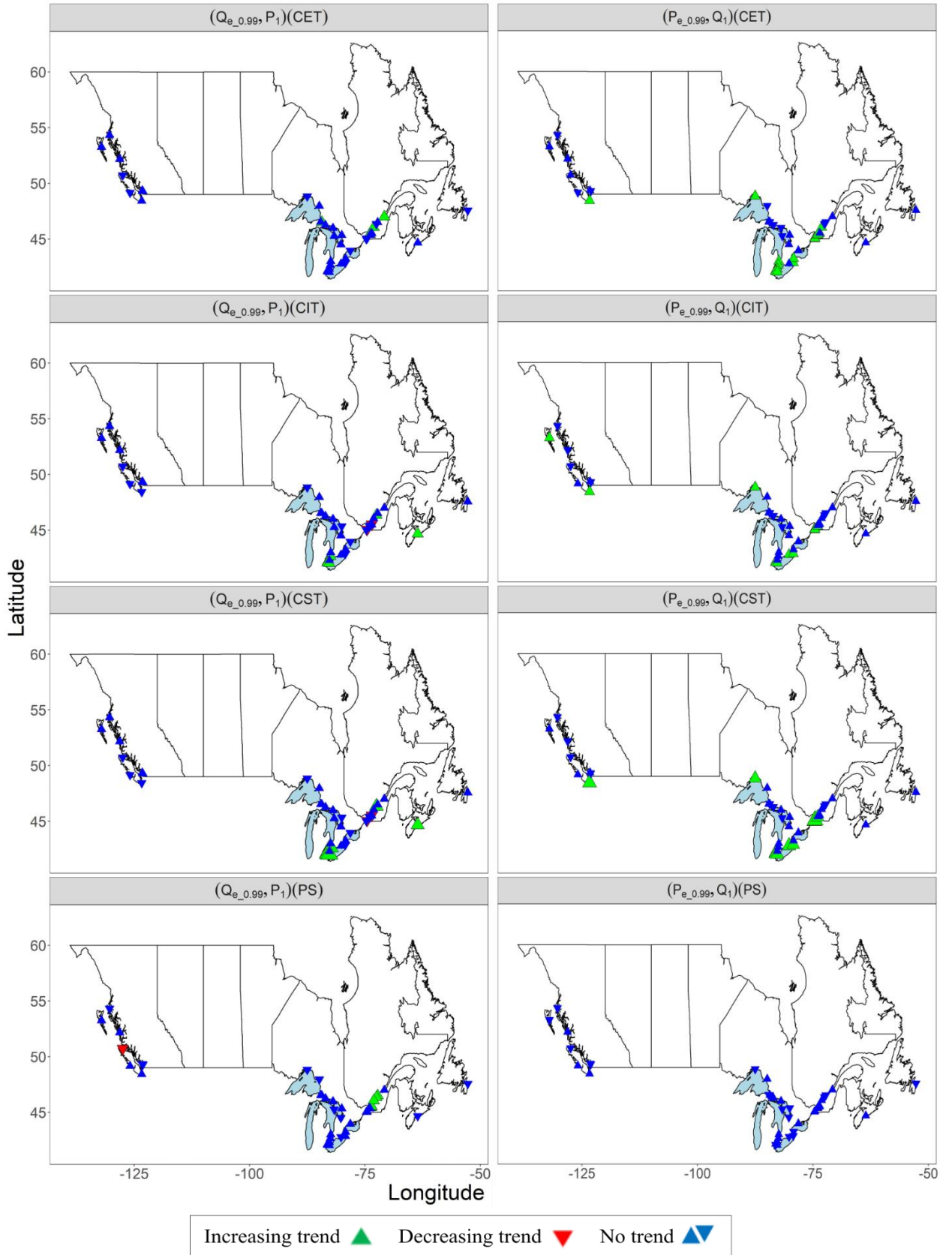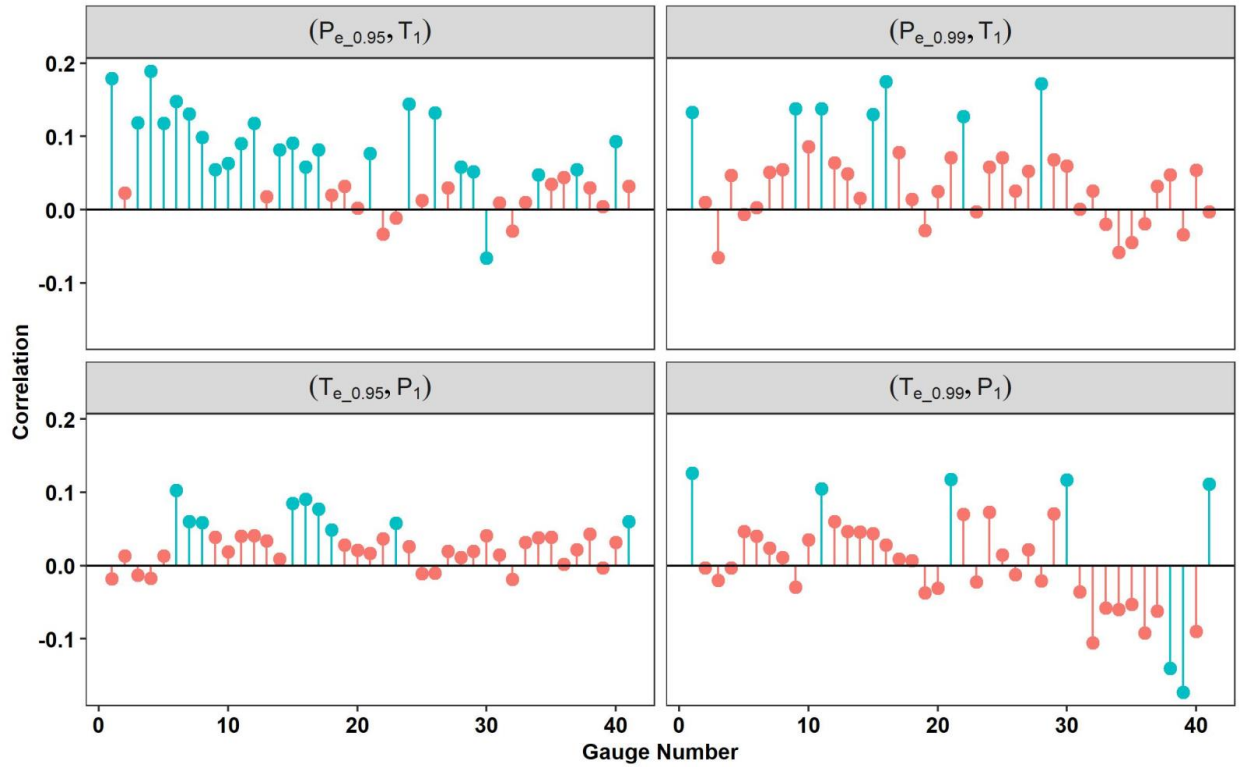
Supplementary Figure 4. 14) The bivariate trends of two extreme scenarios of $(Q_{e\_0.99}, P_1)$ (F values above the $Q_{0.99}$ threshold and maximum P values one day before or after) and $(P_{e\_0.99}, Q_1)$ for 41 locations using CIT, CST, CET and PS.
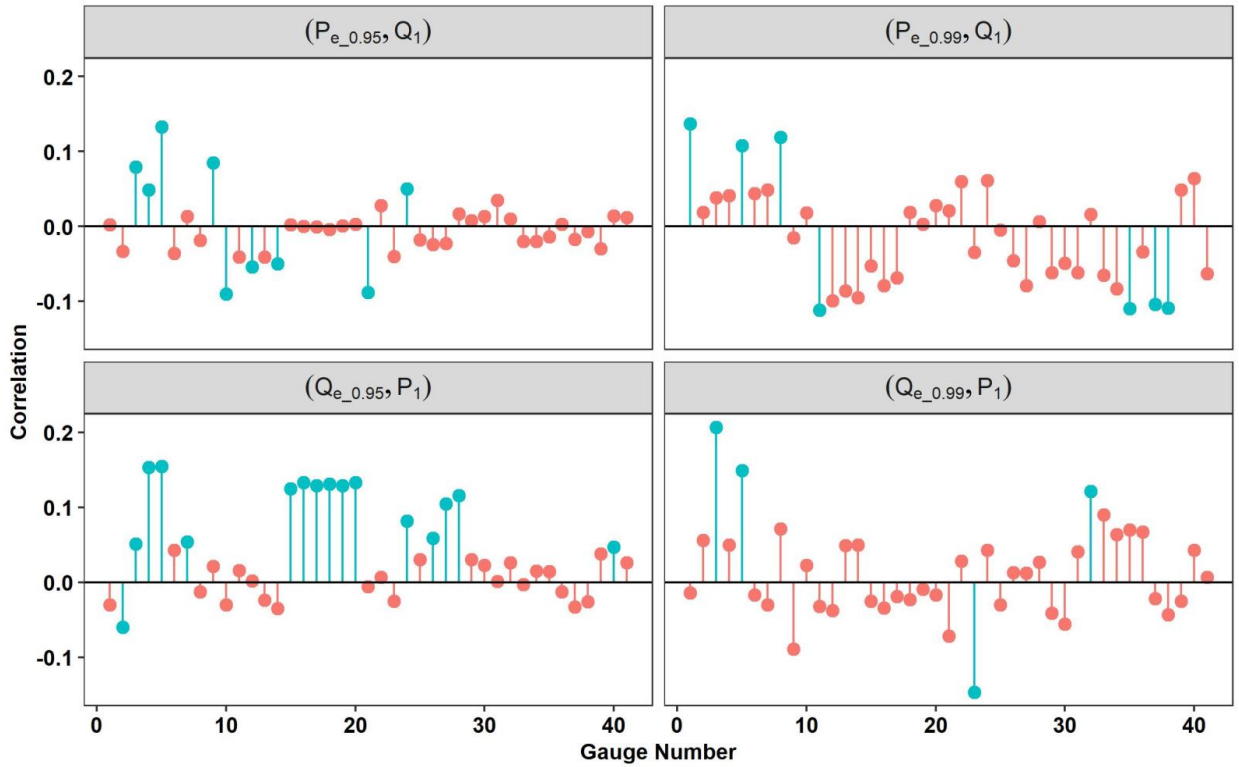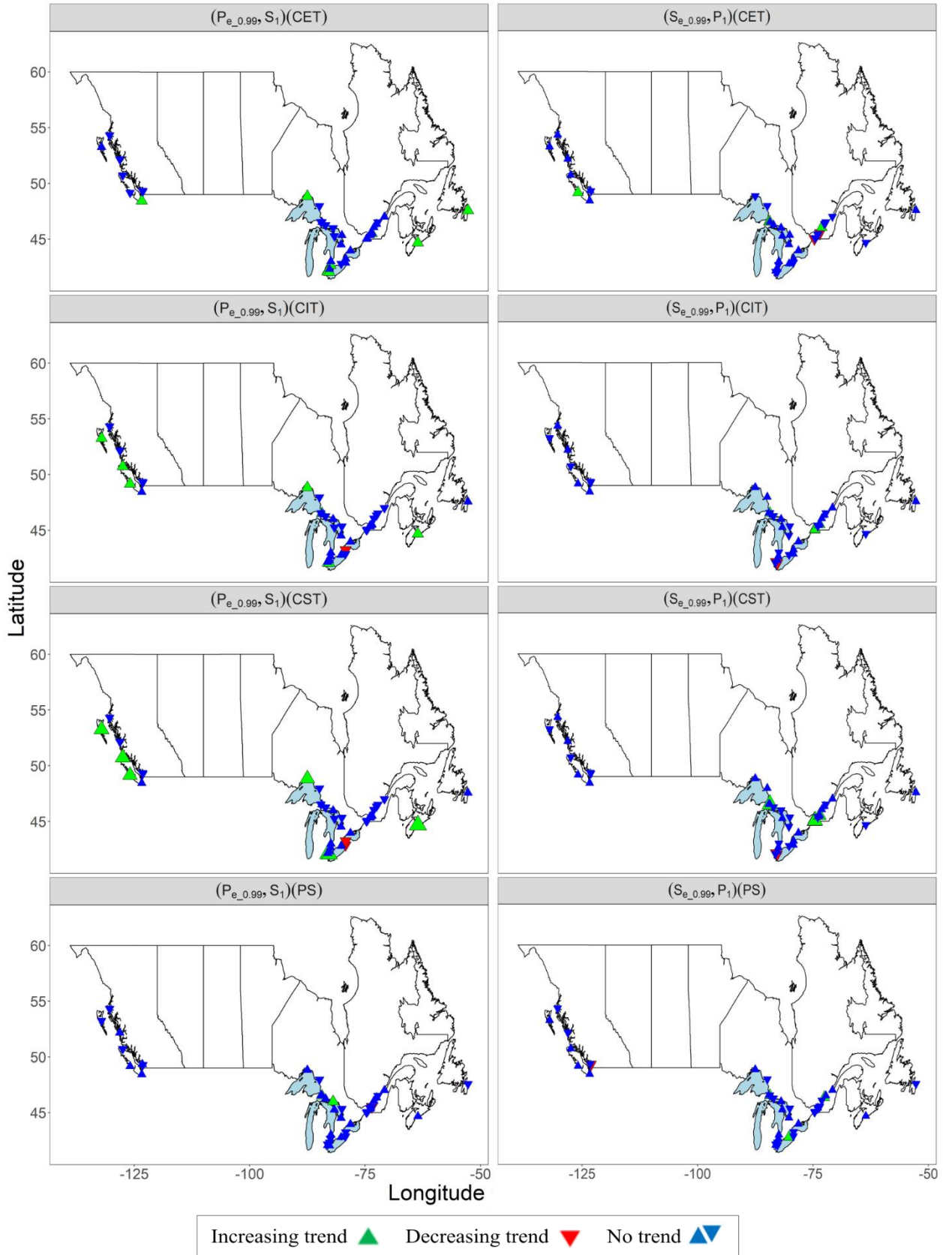

Supplementary Figure 4. 15) The Kendall's correlation coefficients of extremes $(Q_{0.95}$ and $Q_{0.99})$ of (Q, P_1) and (P, Q_1) scenarios for each gauge. Blue circles denote significant correlations (95 % confidence).

Supplementary Figure 4. 16) The bivariate trends of two extreme scenarios of ($T_{e\_0.99}$, P1) (T values above the $Q_{0.99}$ threshold and maximum P values one day before or after) and ($P_{e\_0.99}$, T1) for 41 locations using CIT, CST, CET and PS.


Supplementary Figure 4. 17) The Kendall's correlation coefficients of extremes ($Q_{0.95}$ and $Q_{0.99}$) of (P, T_1) and (T, P_1) scenarios for each gauge. Blue circles denote significant correlations (95 % confidence).

Supplementary Figure 4. 18) The bivariate trends of two extreme scenarios of $(P_{e\_0.99}, S_1)$ (P values above the $Q_{0.99}$ threshold and maximum S values one day before or after) and $(S_{e\_0.99}, P_1)$ for 41 locations using CIT, CST, CET and PS.
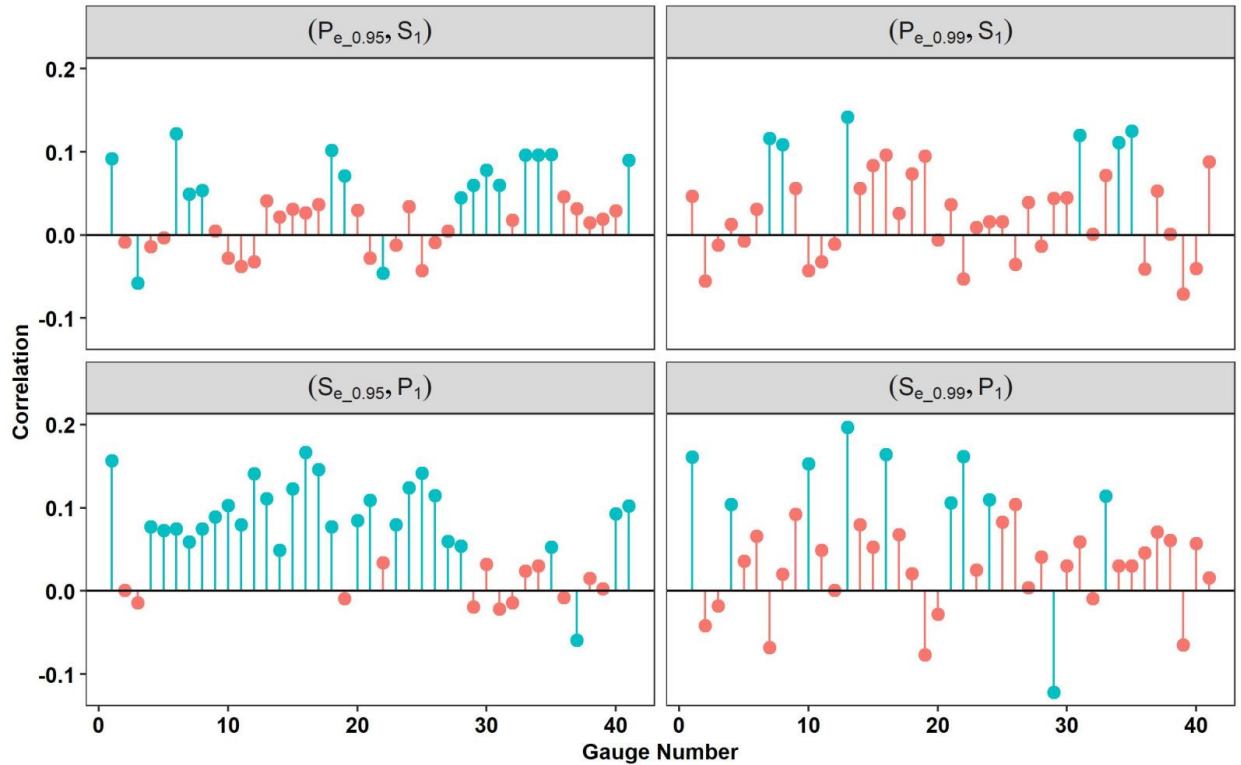
Supplementary Figure 4. 19) The Kendall's correlation coefficients of extremes ($Q_{0.95}$ and $Q_{0.99}$) of (P, S_1) and (S, P_1) scenarios for each gauge. Blue circles denote significant correlations (95 % confidence).
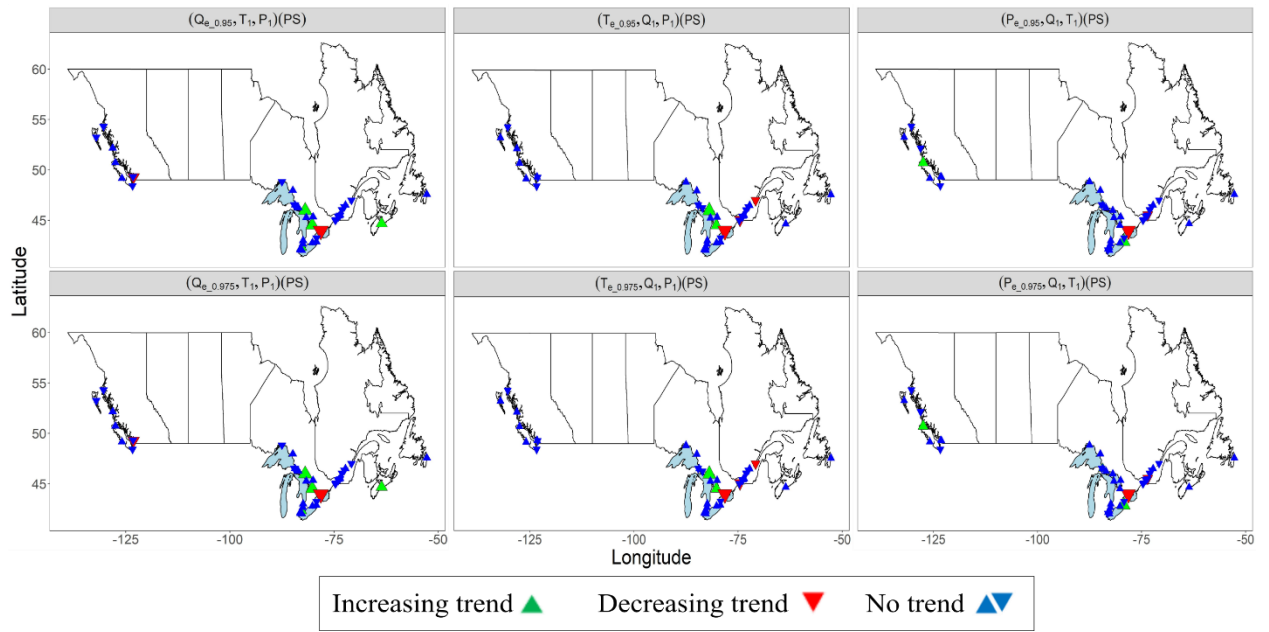
Supplementary Figure 4. 20) The trend of PS values for $Q_{0.95}$ and $Q_{0.975}$ related to scenarios (Q_e, T_1, P_1), (T_e, Q_1, P_1) and (P_e, Q_1, T_1).
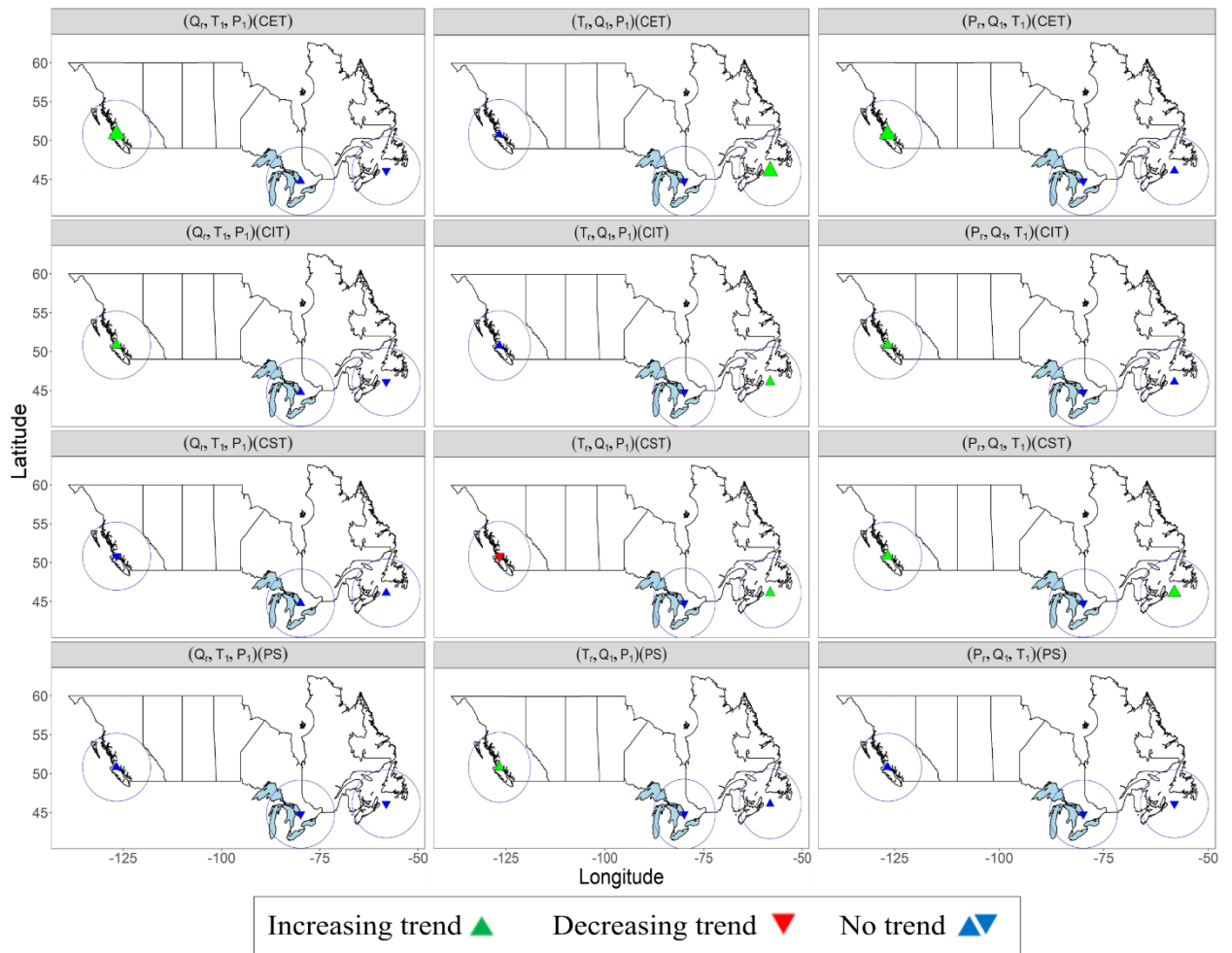
Supplementary Figure 4. 21) Regional trends of the average extremes over the Pacific, Atlantic and the Great Lakes coasts based on the PS index. Q_r indicates regional Q. The size of the triangles is proportional to the magnitude of the trends.

Curriculum Vitae

Name: Farshad Jalili Pirani

Post-secondary   Natural resource Faculty, Chamran University
Education and   Ahvaz, Iran
Degrees: 2007-2011 B.Sc.

                            Natural resource Faculty, Isfahan University of Technology
                            2012-2015 M.A.

                            The University of Western Ontario
                            London, Ontario, Canada
                            2018-2022 Ph.D.

Related Work   Teaching and Research Assistant
Experience   The University of Western Ontario
                            2018-2022

Publications:

Singh, H., Pirani, F.J. and Najafi, M.R., 2020. Characterizing the temperature and precipitation co-variability over Canada. *Theoretical and Applied Climatology*, 139(3), pp.1543-1558.

Jalili Pirani, F. and Najafi, M.R., 2020. Recent trends in individual and multivariate compound flood drivers in Canada's coasts. *Water Resources Research*, 56(8), p.e2020WR027785.

Jalili Pirani, Farshai, and Mohammad Reza Najafi. "Earth's future Multivariate analysis of compound flood hazard across Canada's Atlantic, Pacific and Great Lakes coastal areas." *Earth's Future*: e2022EF002655.

Jalili Pirani, F. and Najafi, M.R., 2022. Nonstationary frequency analysis of compound flooding across coastal environments. In preparation.

Jalili Pirani F, Bakhtiari S, Najafi MR, Shrestha RR, Nouri MS., 2021. The Effects of Climate Change on Flood-Generating Mechanisms in the Assiniboine and Red River Basins. AGU Fall Meeting 2021.

Jalili Pirani F, Najafi MR., 2021. Compound Flooding across Canada's Coasts. AGU Fall Meeting 2021.

Singh, H., Pirani, F.J., Najafi, M.R, Canon, AJ., 2020. Characterizing the Dependence Structure between Temperature and Precipitation over Canada. AGU Fall Meeting 2018.

Jalili Pirani, F. Singh, H., Najafi, M.R, Canon, AJ., 2018. Joint Variability of Precipitation and Temperature over Southern Ontario. CGU conference.

Jalili Pirani, F., Najafi, M.R., 2020. Univariate and Multivariate analysis of long-term trends in coastal flooding over Canada. IUGG conference.

Jalili Pirani, F., Najafi, M.R., 2020. Univariate and Multivariate analysis of long-term trends in coastal flooding over Canada. CMOS conference.

Jalili Pirani, F., Najafi, M.R., 2022. Compound flooding analysis over Canada's coastal zones. CMOS conference.